Transport and deformation of flexible fibers in structured environments

Ursy Makanga

INSTITUT POLYTECHNIQUE DE PARIS

NNT : 2023IPPAX080

Thèse de doctorat

Transport and deformation of flexible fibers in structured environments

Thèse de doctorat de l'Institut Polytechnique de Paris
préparée à l'École polytechnique

École doctorale n°626 École doctorale de l'Institut Polytechnique de Paris (EDIPP)
Spécialité de doctorat : Ingénierie, Mécanique et Energétique

Thèse présentée et soutenue à Palaiseau, le 11 Septembre 2023, par

M, URSY MAKANGA

Composition du Jury :

Olivia du Roure Directrice de recherche, CNRS, PMMH, ESPCI Paris	Présidente
Ian Griffiths Professeur, Université d'Oxford	Rapporteur
Thomas D. Montenegro-Johnson Professeur, Université de Warwick	Rapporteur
Basile Audoly Directeur de recherche, CNRS, LMS, École polytechnique	Examinateur
Anne Juel Professeure, Université de Manchester	Examinatrice
Camille Duprat Professeure, École polytechnique	Directrice de thèse
Blaise Delmotte Chargé de recherche, CNRS, LadHyX, École polytechnique	Co-directeur de thèse

"We all have dreams. But in order to make dreams come into reality,
it takes an awful lot of determination, dedication, self-discipline, and effort."
—Jesse Owens

Acknowledgements

This thesis marks the end of a challenging but fruitful journey. The experience of these three years has been memorable and my heart is filled with nothing but gratitude.

It would not have been possible without my two advisors, Camille Duprat and Blaise Delmotte. I want to thank Camille for teaching me experimental methods and techniques for fluid mechanics at low Reynolds number. Her support, constructive comments and helpful suggestions have allowed me to improve significantly the quality of my work. I want to thank Blaise for teaching me almost everything I know about numerical methods and analysis, but also the art of scientific investigation. His continuous support, encouragement and generosity have allowed me to explore so many avenues, but also gave me enough freedom to pursue my own ideas toward research. I am indebted to Camille and Blaise for their mentorship and kindness.

I would like to thank Ian Griffiths and Thomas (aka Tom) Montenegro-Johnson for taking the necessary time and effort to carefully review this manuscript. I sincerely appreciated all comments, recommendations and suggestions. I would also like to thank Anne Juel and Basile Audoly for accepting to be part of my thesis committee; as well as Olivia du Roure for accepting to be the president of the latter. I am grateful to all the committee members.

I would also like to express my gratitude to the department of Mechanics of École polytechnique, and its talented professors and researchers. Particular mention is due to Sébastien Michelin, who first exposed me to the world at very low Reynolds number. A world which is quite different from the one that we have developed our intuitions in. I would also like to thank Emmanuel de Langre, Christophe Josserand and Lutz Lesshafft, who welcomed me into the Hydrodynamics Lab (LadHyX) through the Ph.D Track program. And I thank the support staff of the lab for their time and assistance.

I am grateful to everyone, including people external and internal to the lab, who offered me advice and encouraged me to complete this thesis. Specifically, I would like to thank (in alphabetical order) Anaël, Cyrille, Dubon, Éric, Frère Jacques-Vincent and Romain for making these last few years less stressful.

Finally, I would like to thank my parents, who motivated me to follows my dreams and supported me through every one of my projects. I am sure none of this would have been possible without their sacrifices.

Financial support for this work came from the French Ministry of higher Education, Research and Innovation (MESRI), la Fondation de l'École polytechnique (FX) through a Ph.D Track scholarship, the French National Research Agency (ANR) under Award No. ANR-20-CE30-0006, and teaching activities at Institut Polytechnique de Paris (IP Paris).

Abstract

The transport of elastic fibers at the micron-scale often happens in complex media that are structured by obstacles whose size is similar to the one of the moving particles. This situation is ubiquitous in nature and industrial applications. In order to act against antibiotics and antimicrobial agents, bacteria often stick together in an extracellular matrix to form a *biofilm*. Their migration to secondary sites results to the formation of biofilm streamers, large elastic filaments, that can lead to clogging while transported through complex environments. In everyday life, laundry washing machines discharge a large number of microplastic fibers (around 1900 fibers per wash) into wastewaters which contain a significant amount of debris. In such complex media, flexible fibers can exhibit nontrivial conformations and different modes of transport through the surrounding obstacles. These dynamics result from the complex interplay between their elastic response, collisions and hydrodynamic interactions. Understanding of these phenomena is therefore essential to study the physics of biological, environmental and industrial systems, but also to prevent issues such as pollution or clogging.

Over the past decades, the study of the dynamics of elongated particles in a viscous fluid has been a major area of research in fluid mechanics. When settling in a free fluid, thanks to its drag anisotropy, a rigid fiber parallel to gravity will settle twice as fast as a fiber perpendicular to gravity. The drag coefficient in the direction of the minor axis of the fiber is twice as large as the one in the direction of its major axis. Therefore, a rigid fiber, initially oriented at a given angle with respect to the direction of gravity, will drift laterally and maintain its initial orientation. When the fiber is allowed to bend, owing to the inhomogeneous drag distribution along its length, it will reorient in the direction of gravity and reach an equilibrium configuration after a finite settling distance. The deformation of the fiber induces an elastic restoring torque that will counterbalance the gravitational torque. During its reorientation process, the fiber experiences a lateral displacement that affects significantly its trajectory. Accordingly, the presence of obstacles or complex environments will lead to different modes of transport/migration of the fiber based on its geometrical and/or mechanical properties.

Modeling slender particles in a viscous fluid has led researchers across different fields to develop various numerical methods that range from continuum to discrete models. These methods have since been used in applications in various domains : from biology to industrial applications. However, methodologies involving surrounding environments are scarce. The resulting complex coupling leads to a constrained formulation of the problem in addition of being stiff. Therefore, modeling fibers in complex media is challenging and can be computationally costly.

In this thesis, we will propose a methodology to model flexible fibers in different environments that are made of rigid stationary obstacles. Our implementation enables dynamic simulations of large systems in reasonable wall times on a single modern Graphics Processing Unit (GPU). Using the capabilities afforded by our method, together with simple experiments, we will investigate the sedimentation of flexible fibers in structured environments. The result-

ing findings provide physical insight into future experiments and the design of gravity-based sorting devices.

Keywords: *Flexible fibers, Structured media, Fluid-structure interactions, Stokes flow, Sedimentation, Numerical modeling.*

Résumé

Le transport des fibres élastiques à petites échelles se produit généralement dans des environnements fluidiques munis d'obstacles dont la taille est du même ordre de grandeur que celle des particules en mouvement. Ce cas de figure se rencontre dans diverses situations dans la nature et les applications industrielles. Afin de résister à la réponse immunitaire de l'hôte, les bactéries peuvent s'assembler et sécréter une matrice protectrice pour former un *biofilm*. De microcolonies filamenteuses, de 100 microns en ordre de grandeur, peuvent se détacher des biofilms et se déplacer dans des microcanaux munis d'obstacles ; conduisant ainsi à une adhésion à de nouvelles surfaces biotiques et une reformation des biofilms avec des espèces bactériennes secondaires. Quotidiennement, les lave-linge rejettent un grand nombre de fibres de microplastiques (environ 1900 fibres par lavage) dans des eaux usées contenant plusieurs débris. Dans de tels environnements complexes, les fibres peuvent adopter différentes formes non triviales et se déplacer suivant différents modes à travers les obstacles environnants. Ces différents comportements résultent du couplage complexe entre la réponse élastique des fibres, les collisions et les interactions hydrodynamiques. Leur compréhension est par conséquent essentielle pour l'étude des systèmes biologiques, environnementaux et industriels, où des phénomènes similaires sont observés, de même que pour éviter des problèmes majeurs comme la pollution ou le colmatage.

Au cours des dernières décennies, l'étude des particules élancées en interaction dans un fluide visqueux a été un domaine majeur de recherche en mécanique des fluides. Lorsqu'elle sédimente sous l'action de son propre poids, une fibre rigide, orientée parallèlement à la direction de la gravité, tombe deux fois plus vite qu'une fibre orientée perpendiculairement à la direction de la gravité. Cette dynamique résulte de l'anisotropie de la trainée de la fibre, i.e., le coefficient de trainée est deux fois plus grand dans la direction transversale de la fibre que dans sa direction longitudinale. Par conséquent, une fibre rigide, initialement inclinée d'un angle donné par rapport à la direction de la gravité, est soumise à un mouvement de dérive latérale avec une inclinaison uniforme - équivalente à son inclinaison initiale. En revanche, lorsqu'elle peut se déformer sous l'action des efforts élastiques internes, la fibre se réoriente dans la direction de la gravité et adopte une configuration d'équilibre stable. La déformation élastique de la fibre induit une inhomogénéité de la trainée le long de sa longueur et, par conséquent, un couple de rappel élastique. La réorientation de la fibre affecte significativement sa trajectoire de sédimentation. Ainsi, la présence d'obstacles ou d'un environnement complexe pourrait entrainer différents modes de déplacement/migration de la fibre en fonction de ses propriétés géométriques et/ou mécaniques.

La modélisation numérique des fibres flexibles immergées dans un fluide visqueux a été abordée sous différentes approches durant ces dernières années. Des approches continues aux discrètes, ces modèles ont permis de résoudre efficacement des dynamiques complexes d'interactions de fibres flexibles dans divers domaines : de la biologie aux applications industrielles. Cependant, le développement des modèles numériques permettant de prendre en compte des environnements munis d'obstacles a été peu abordé. Le problème raide à résoudre sous contraintes qui en résulte en est une des raisons. Modéliser des fibres dans de tels envi-

ronnements est un défi majeur pour les approches numériques actuelles.

Ainsi, dans cette thèse, nous proposerons une méthodologie pour simuler des fibres flexibles dans des environnements fluidiques munis d'obstacles. Notre implémentation permet de simuler des systèmes contenant un nombre considérable de fibres et d'obstacles en des temps raisonnables sur une seule carte graphique (GPU). Forts de cet outil, et d'expériences simples, nous étudierons ensuite le problème de sédimentation des fibres flexibles dans des environnements complexes. Nos résultats jettent les bases pour de futures expériences et fournissent des ingrédients physiques essentiels pour la conception des dispositifs de tri de particules sous l'action de la gravité.

Mots clés: *Fibres flexibles, Environnements munis d'obstacles, Interactions fluide-structure, Ecoulements de Stokes, Sédimentation, Modélisation numérique.*

Contents

List of Tables

List of Figures

Part I

Introduction and theoretical background

Chapter 1

Introduction and thesis outline

Contents

1.1 Transport of active and passive fiber-like particles in complex environments

Active elongated[1] particles such as some biological microorganisms often interact with network of obstacles in their natural habitats, e.g., soil, guts, etc. For instance, bacteria *Helicobacter pylori* swims through gastric mucus gel (Montecucco and Rappuoli, 2001; Celli et al., 2009; Mirbagheri and Fu, 2016); spermatozoa migrate through cervical mucus in their ascent through the female genital tract, see Fig.1.1(a) (Rutllant et al., 2005); the protozoan hemoflagellate *Trypanosoma brucei*, which causes a deadly sleeping sickness in both animals and humans, migrates through red blood cells (Engstler et al., 2007; Ralston et al., 2009); some invasive bacterial pathogens, known as spirochetes, move through a broad range of tissues in the mammalian body (Wolgemuth, 2015). The aforementioned surrounding environments affect significantly the locomotion performance of biological microorganisms. Experiments have shown that the swimming speed of the worm nematode *Caenorhabditis elegans* (*C. elegans*), that often swims in satured soil, is enhanced by the presence of the obstacles, see Fig.1.1(b) (Juarez et al., 2010; Jung, 2010; Majmudar et al., 2012). These findings agree with analytical results based on a mean-field approximation of the porous media (Leshansky, 2009; Jung, 2010), a Brinkman fluid (Brinkman, 1949). The latter acts as a resistance to the motion of microswimmers. In addition, recent numerical studies based on the Brinkman model, have shown that the swimming speed of a flagellar microswimmer can be enhanced, owing to emergent waveforms that are induced by the surrounding environment (Leiderman and Olson, 2016; Ho et al., 2016, 2019). These findings have provided insights into the development and study of artificial microswimmers, mainly for the purpose of biomedical applications (Nelson et al., 2010; Medina-Sánchez and Schmidt, 2017).

Over the past decade, advances in manufacturing techniques (Walther and E. Müller, 2008; Guix et al., 2018) and the development of rigorous mathematical and computational frameworks (Lauga and Powers, 2009; Du Roure et al., 2019; Lauga, 2020) have led researchers and

[1]Here by "elongated" or "fiber-like", we mean a particle whose length is much greater than its width.

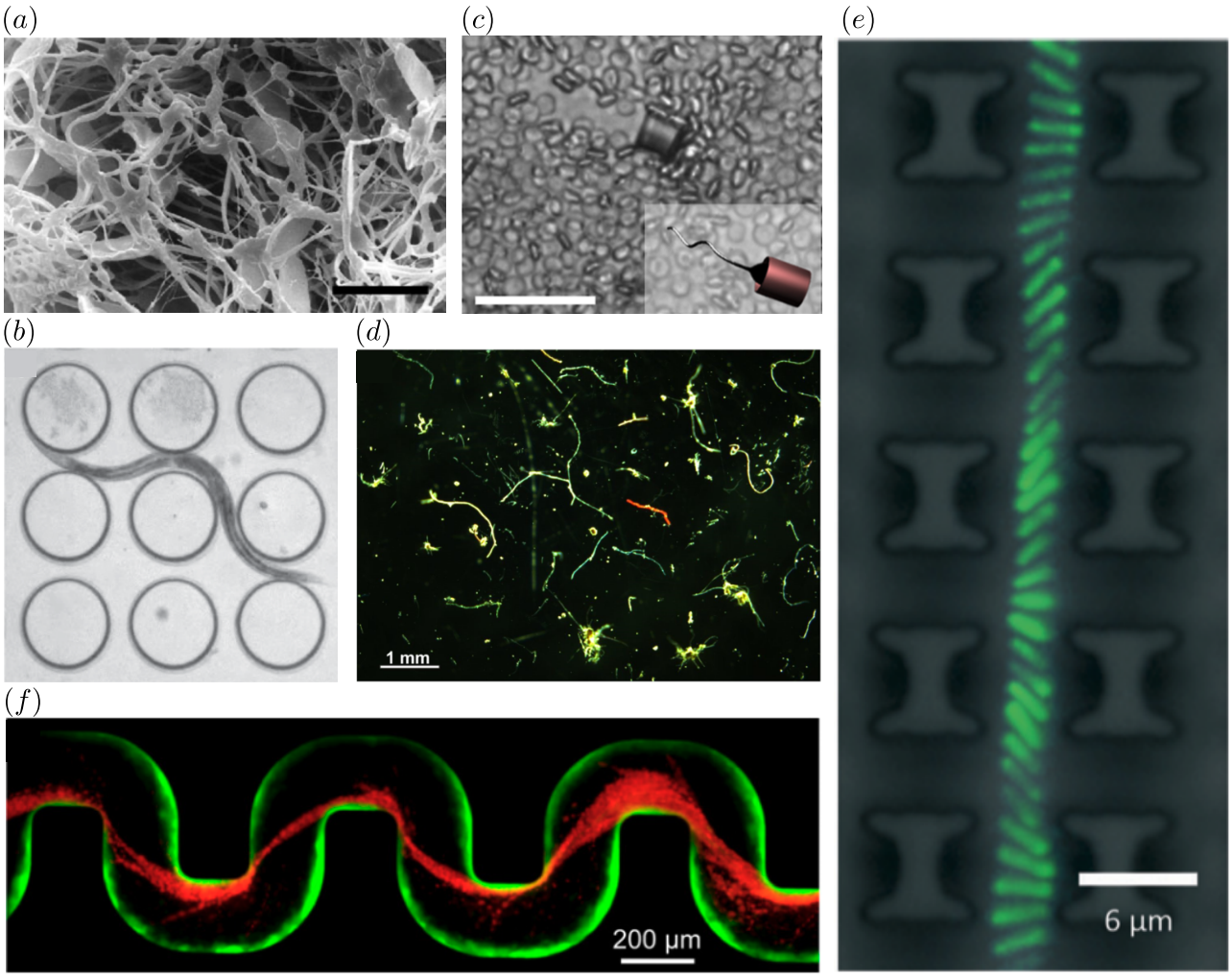

Figure 1.1: Transport of fiber-like particles in the presence of obstacles. (*a*) Photomicrograph of spermatozoa swimming in a vaginal fluid sample (Rutllant et al., 2005). Scale bar, 10 μm. (*b*) An image from experiments showing *C. elegans* in a lattice of PDMS micropillars (Majmudar et al., 2012). (*c*) An image from experiments showing a biohybrid microswimmer swimming through red blood cells (Xu et al., 2020). Scale bar, 40 μm. (*d*) Microplastic fibers in a deep-marine environment, Tyrrhenian Sea (Kane and Clare, 2019). (*e*) An image from experiments showing rod-shaped bacteria through an array of I-shaped pillars (Ranjan et al., 2014). (*f*) An image from experiments showing the clogging of a microfluidic channel by biofilm streamers (Drescher et al., 2013).

engineers across different fields to develop and design artificial microswimmers inspired by biological microorganisms. Earlier approaches rely on an external field (e.g., magnetic (Dreyfus et al., 2005; Zhang et al., 2009; Nelson et al., 2010), electric (Loget and Kuhn, 2011), light (Li et al., 2016; Sridhar et al., 2018), acoustic (Ahmed et al., 2015, 2016; Ren et al., 2017), etc.) for actuation. Although few examples of the precise navigation of such microswimmers have been demonstrated *in vivo*, recent studies show that the navigation of biohybrid fiber-like microswimmers through complex environments can be controlled *in vitro* (Magdanz et al., 2013; Medina-Sánchez et al., 2016; Xu et al., 2018, 2020). For instance, Xu et al., 2020 designed a biohybrid fiber-like microswimmer made of a sperm and a synthetic magnetic scaffold which is operated by an external magnetic field, to achieve precision navigation through red blood cells (see Fig.1.1(*c*)).

More recently, a different actuation mechanism, where microswimmers take advantage of their surrounding environment to self-propel has been promoted. The latter exploits interfacial pro-

cesses to generate propulsion from gradients of the surrounding field (e.g., chemical solute concentration (Golestanian et al., 2005), electrical charge (Nourhani et al., 2015) or temperature (Jiang et al., 2010)), namely phoretic particles; or from local gradients generated through the surface activity of the particle (e.g., heat release (P. Bregulla and Cichos, 2015) or surface-catalysis of chemical reactions (Wang et al., 2006)), namely autophoretic particles. In some applications such as cargo transport (Sundararajan et al., 2008) or drug delivery (Kagan et al., 2010), a precise trajectory control is needed during the transport of artificial microswimmers through complex environments *in vivo*. One promising navigation approach, to overcome this hurdle, is the design of autophoretic filaments (Paxton et al., 2004; Williams et al., 2014; Vutukuri et al., 2017). Indeed, autophoretic filaments driven by local chemical gradients take advantage of both, their geometric anisotropy and their chemical asymmetry to break the symmetry in order to self-propel. In addition, their flexibility allows for different conformations and modes of transport (e.g., tumbling, pumping, translating or rotating) to achieve precision transport (Montenegro-Johnson, 2018; Sharan et al., 2021).

On the other side, the transport of passive fiber-like particles through complex environments is ubiquitous in nature and industrial applications. For instance, microplastic fibers often find themselves immersed in aquatic environments with embedded obstacles, Fig.1.1(d) (Kane and Clare, 2019). In papermaking processes, fiber suspensions are collected on screens, i.e., wire meshes, for paper forming (Lundell et al., 2011; Redlinger-Pohn et al., 2021). In deterministic lateral displacement (DLD) devices, long linear polymer chains such as DNA molecules (Chou et al., 1999) or rod-shaped bacteria as shown in Fig.1.1(e) (Ranjan et al., 2014), are transported through an array of obstacles for sorting purposes. The presence of these embedded obstacles introduces additional solid surfaces, which disturb the flow field around the fibers and hence their translational and angular velocities. When passive fibers are allowed to bend, their dynamics result from the complex interplay between internal elastic stresses and interactions with their surroundings, which include long-ranged hydrodynamic interactions and short-ranged interactions such as lubrication, friction and steric interactions. This complex coupling may lead to scattering or entrapment of fibers around the surrounding obstacles, but also affect significantly the ambient flow when present. Experiments have shown that biofilm streamers, long elastic filaments (see Fig.1.1(f)), can rapidly expand, cause sudden clogging, and lead to a catastrophic disruption of the ambient flow in a microfluidic channel made of a sequence of corners (Drescher et al., 2013). Over longer time scales, thermal fluctuations together with trapping and scattering dynamics, affect the transport and dispersion of semiflexible and flexible polymers in crowded environments (Nam et al., 2010; Mokhtari and Zippelius, 2019; Chakrabarti et al., 2020).

While transported from the sea surface to the seabed, mainly by sedimentation, microplastic fibers can interact with different surroundings, from plastic debris to marine vegetation. Owing to their small size, i.e., less than 1mm, the effects of fluid inertia on microplastic fibers are negligible compared to viscous ones, leading to a low Reynolds number regime. Understanding how microplastic fibers are transported in such environments is essential for identifying and preventing pollution hotspots (Browne et al., 2011a; Kane and Clare, 2019; Re, 2019; Choi et al., 2022; Sutherland et al., 2023).
When settling in a free fluid, at low Reynolds number, a rigid fiber parallel to gravity will settle twice as fast as a fiber perpendicular to gravity; owing to its drag anisotropy, i.e., the drag coefficient in the direction of the minor axis of the fiber is twice as large as the one in the direction of its major axis (Batchelor, 1970). Therefore, a rigid fiber, initially oriented at a given nonzero angle with respect to the direction of gravity, will drift laterally at a constant velocity and maintain its initial orientation.
When the fiber is allowed to bend, owing to the inhomogeneous drag distribution along its length, it will reorient and then reach an equilibrium shape after a finite settling distance

(Li et al., 2013; Marchetti et al., 2018). This equilibrium shape is characterized by the so-called elastogravitational number. The latter is defined as the balance between gravity and elastic restoring forces, such that when the value of the elastogravitational number increases, the equilibrium shape of the fiber evolves from rod-like to U-like shapes (Marchetti et al., 2018). During its reorientation process, the fiber experiences a lateral displacement that affects strongly its trajectory. Accordingly, the presence of obstacles, together with the deformation and the orientation of the fiber, will lead to different modes of transport.

However, modeling flexible fibers in complex environments is challenging and can be numerically costly, owing to the resulting complex interactions.

1.2 Modeling moving and stationary boundaries in a viscous fluid

There are a variety of modeling approaches to handle stationary and moving boundaries in Stokes flow[2]. Such approaches can be broadly separated into those based upon (*i*) two different methods to handle both boundaries separately and (*ii*) a unique method to handle both. For category (*i*), the flow generated by stationary boundaries is precomputed and then added as a background flow to moving boundaries. Despite the fact that this approach allows fast computations, it neglects hydrodynamic interactions between moving and stationary boundaries. For instance, Chakrabarti et al., 2020 used the boundary integral method (Pozrikidis, 1992) to compute the velocity field induced by an array of obstacles on a semiflexible fiber (see Fig.1.2(*a*)) which is modeled using local slender body theory (Hancock, 1953; Keller and Rubinow, 1976). Similarly, Münch et al., 2016 and Engdahl, 2018 combined respectively the method of multiparticle collision dynamics (MPCD) (Malevanets and Kapral, 1999, 2000; Gompper et al., 2009) and the Lattice-Boltzmann method (Chen and Doolen, 1997), with a multibead model (Liu, 1989; Gauger and Stark, 2006), to investigate the transport of fiber-like particles in porous media (see Fig.1.2(*b*) and Fig.1.2(*c*), respectively).

By using a unique method to model both boundaries, approaches in category (*ii*) are more suitable to account for hydrodynamic interactions. For instance, using the immersed boundary method (Peskin, 2002), Fauci and McDonald, 1995 introduced a computational model to investigate sperm motility near rigid and elastic walls. Dillon et al., 1996 used a similar model for studying biofilm processes. However, the immersed boundary method is a grid-based approach, which requires solving the fluid problem in the entire domain, and therefore can be time consuming for large systems. The boundary integral method overcomes this hurdle, since only the immersed boundaries need to be discretized. Although being an accurate approach, the boundary integral method scales badly with the number of discrete elements. An alternative approach is the method of regularized Stokeslets (Cortez, 2001), which models the immersed boundaries as distributions of regularized point forces. This method has been used in applications to investigate the dynamics of microswimmers in complex environments such as viscoelastic media (Wróbel et al., 2016), shown in Fig.1.2(*d*), or porous media (Leiderman and Olson, 2016; Ho et al., 2019; Kamarapu et al., 2022). When the point forces are regularized and interpolated through the surface of a sphere, the method is referred to as the multibead/multiblob method (Usabiaga et al., 2016; Balboa Usabiaga and Delmotte, 2022). This method is a good compromise between efficiency, flexibility, accuracy and scalability. Recently, there has been a significant drive to apply the multiblob method on problems involving moving particles and stationary obstacles. For instance, Majmudar et al., 2012 used a multibead approach to investigate the locomotion of swimming *C. elegans* through a structured array of pillars (see

[2]In the Stokes regime, inertial effects are negligible compared to viscous ones.

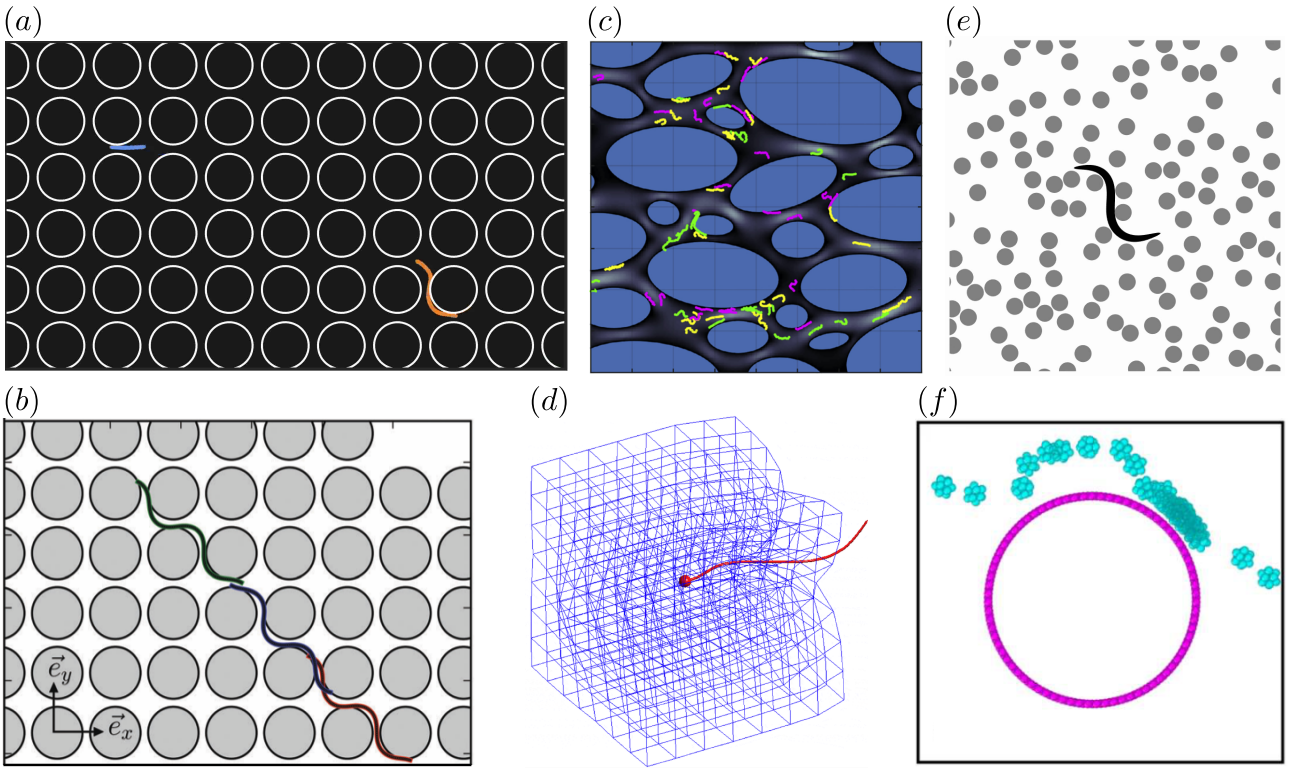

Figure 1.2: (*a*) Advection of polymers through a structured array of micropillars (Chakrabarti et al., 2020). (*b*) Chronophotographies of a swimming Taylor line through a structured array of micropillars (Münch et al., 2016). (*c*) Transport of microplastic fibers through a porous medium (Engdahl, 2018). (*d*) A flagellar microswimmer moving through a viscoelastic network (Wróbel et al., 2016). (*e*) A mechanical worm (MW) moving through a heterogeneous environment (Majmudar et al., 2012). (*f*) Chronophotographies of a microroller approaching a cylindrical obstacle (Van Der Wee et al., 2023).

Fig.1.2(*e*)). This approach has since been extended by Kamal and Keaveny, 2018 to account for randomly distributed obstacles tethered with linear springs. More recently, Van Der Wee et al., 2023 and Gidituri et al., 2023 used the rigid multiblob approach to investigate the mechanisms of trapping of microrollers by obstacles (see Fig.1.2(*f*)) and the different swimming modes of single-flagellated bacteria inside a circular pipe, respectively. To account for obstacles, in most of the aforementioned studies, kinematic constraints are introduced to prescribe the obstacle velocities to zero. Therefore, the resulting constrained problem is solved for a set of Lagrange multipliers enforcing the kinematic constraints. Solving a constrained problem can be challenging, in particular for large systems involving stationary and moving objects.

In this thesis, we aim to provide a contribution in that direction. Along this manuscript, we try to develop a modeling approach that accounts for obstacles at the scale of fibers in order to investigate the influence of different surrounding environments on the dynamics of passive flexible fibers.

1.3 Thesis outline

This thesis contains three parts, that are organized as follows:

The remainder of Part I, through Chapter 2, is devoted to the governing equations and fundamental theorems of Stokes flow, that lay the foundations of the numerical approaches

developed in the subsequent Part.

In Part II, we focus on modeling flexible fibers in complex environments.
Chapter 3 describes the commonly-used methods to simulate the dynamics of flexible fibers that are immersed in Stokes flow. The equilibrium equations for the mechanics of flexible fibers are first derived. We then discuss the different approaches to couple these equations to fluid flow. The bead-spring model is chosen from among these different approaches, for which a detailed analysis is presented. Finally, we validate our implementation against known results collected in the literature, but also address open problems such as velocity and density fluctuations in the collective sedimentation of flexible fibers.
Chapter 4 extends the bead-spring model to account for obstacles. The presence of the obstacles introduces kinematic constraints in the problem, namely that the velocity of each obstacle bead is zero. The resulting constrained formulation leads to a linear system to solve for the bead velocities and Lagrange multipliers that enforce the kinematic constraints. We propose a numerical framework to solve this problem in a computationally efficient manner, that allows to handle a large number of fibers and obstacles in the system.

In Part III, we apply our numerical framework to investigate the sedimentation of flexible fibers in structured environments.
Chapter 5 examines the effect of obstacle shapes on the settling dynamics of a single flexible fiber, by means of numerical simulations, experiments and analytical predictions. We show that the complex interplay between the fiber elastic response, gravity, contact forces and hydrodynamic interactions with the obstacle, leads to two types of events: trapping and gliding. We observe nontrivial trapping conformations on sharp obstacles that result from a subtle balance between elasticity, gravity and friction. In the gliding case, a flexible fiber reorients and drifts sideways after sliding along the obstacle. The subsequent lateral displacement is large compared to the fiber length and strongly depends on its mechanical and geometrical properties. We show how these effects can be leveraged to propose a new strategy to sort elongated particles based on their size and/or elasticity.
Chapter 6 extends the study carried out in Chapter 5 into the case of a sedimenting flexible fiber through a periodic array of pillars. By means of numerical simulations, we show that the long-time trajectory of the fiber falls into one of two modes, zigzag or displacement. In the former, there is no average displacement from the direction of gravity, therefore the fiber center of mass follows a quasi-straight line with a migration angle close to zero. In the latter, there is a net displacement from the the direction of gravity, the fiber center of mass follows a cyclical skew bumping path. The dynamics described above are dictated by the short-time scattering process of the fiber. Especially the contact angle, i.e., the angle with which the fiber collides with a given pillar in the array, and the resulting contact point. These two quantities are determined by the intrinsic properties of the fiber, i.e., its flexibility and length, as well as the topology of the array, i.e., its lattice arrangement and spacing. These findings provide physical insight into future experiments, as well as the design of gravity-based deterministic lateral displacement (DLD) devices to sort fiber-like particles for the purpose of biomedical, microfluidics and environmental applications.

Finally, we summarize at the end the results obtained throughout this thesis and suggest future directions.

Chapter 2

An overview of Stokes flow

Contents

This chapter lays the foundations of the Green's function based numerical approach used throughout this thesis to simulate the motion of particles that are immersed in Stokes flow. Here and throughout this thesis, Einstein summation is assumed for repeated indices, vectors and tensors[1] *are represented by bold symbols, and scalar quantities by unbolded symbols.*

2.1 The governing equations of fluid dynamics

We start with a rigid particle of length L, immersed in an incompressible viscous fluid with viscosity η, and subject to an external conservative force $\boldsymbol{f}$. As the particle moves, it disturbs the surrounding fluid that imparts hydrodynamic stresses. Denoting by $\boldsymbol{\sigma}$ the stress tensor, $\boldsymbol{u}$ the fluid velocity and ρ the mass density, conservation of momemtum and mass give rise to *Cauchy's incompressible equations*

$$\begin{cases} \rho\left(\dfrac{\partial \boldsymbol{u}}{\partial t} + (\boldsymbol{u}\cdot\nabla)\boldsymbol{u}\right) = \nabla\cdot\boldsymbol{\sigma} + \boldsymbol{f}, \\ \nabla\cdot\boldsymbol{u} = 0, \end{cases} . \tag{2.1}$$

For Newtonian fluids, in which viscosity is constant and the stress is defined by the following constitutive law

$$\boldsymbol{\sigma} = -p\boldsymbol{I} + 2\eta\boldsymbol{E}, \tag{2.2}$$

where p is the absolute pressure, $\boldsymbol{I}$ the identity tensor and $\boldsymbol{E}$ the rate of strain tensor, which is given by the symmetric part of the velocity gradient, $\boldsymbol{E} = (\nabla\boldsymbol{u} + \nabla\boldsymbol{u}^T)/2$. The Cauchy's incompressible equations (2.1) become the *Navier-Stokes equations*

[1] Green's functions are represented by blackboard-bold symbols.

$$\begin{cases} \rho\left(\dfrac{\partial \boldsymbol{u}}{\partial t} + (\boldsymbol{u}\cdot\nabla)\boldsymbol{u}\right) = -\nabla p + \eta\nabla^2\boldsymbol{u} + \boldsymbol{f}, \\ \nabla\cdot\boldsymbol{u} = 0, \end{cases} . \tag{2.3}$$

The solution to these equations is subject to the boundary conditions on the fluid domain, as well as the no-slip boundary condition on the surface of the immersed particle.

Now we consider a situation in which there is a time scale ω^{-1} for imposed variations in the characteristic particle velocity U. Denoting by L the characteristic length, we can rewrite the Navier-Stokes momentum balance equation in nondimensional form

$$\mathrm{St}\frac{\partial \boldsymbol{u}}{\partial t} + \mathrm{Re}(\boldsymbol{u}\cdot\nabla)\boldsymbol{u} = -\nabla p + \nabla^2\boldsymbol{u} + \boldsymbol{f}, \tag{2.4}$$

where we have used the same symbols as the dimensional equation for notation convenience. Two dimensionless numbers appear

$$\mathrm{Re} \equiv \frac{\rho U L}{\eta} \quad \text{and} \quad \mathrm{St} \equiv \frac{\rho\omega L^2}{\eta}. \tag{2.5}$$

The Reynolds number Re estimates the importance of inertial effects compared to viscous effects. The Strouhal number St is the oscillatory Reynolds number, in which the velocity scale is the local fluid velocity induced by the oscillatory motion of the particle, $L\omega$.

For the problems of interest in this thesis, both the Reynolds number and the Strouhal number will be small, i.e., $\mathrm{Re} \ll 1$ and $\mathrm{St} \ll 1$. Thus, the acceleration and the convective terms in the Navier-Stokes momentum balance equation (2.4) can be neglected, and it reduces to the *Stokes momentum balance equation*, which in dimensional form is given by

$$-\nabla p + \eta\nabla^2\boldsymbol{u} + \boldsymbol{f} = \boldsymbol{0}. \tag{2.6}$$

In numerous situations, the external conservative force is due to gravity, $\boldsymbol{f} = \rho\boldsymbol{g}$ with $\boldsymbol{g}$ the acceleration of gravity. Its only effect is to induce a hydrostatic pressure gradient, which can be included in a modified pressure field also called the dynamic pressure $\pi = p - \rho\boldsymbol{g}\cdot\boldsymbol{r}$, where $\boldsymbol{r}$ is the particle position in the material frame of reference. Thus, we can rewrite (2.6) to yield the *homogeneous* Stokes momentum balance equation

$$-\nabla\pi + \eta\nabla^2\boldsymbol{u} = \boldsymbol{0}. \tag{2.7}$$

For notation convenience, π is always replaced by p. The aforementioned equation (2.7), together with the continuity equation form the system of Stokes equations

$$\begin{cases} -\nabla p + \eta\nabla^2\boldsymbol{u} = \boldsymbol{0}, \\ \nabla\cdot\boldsymbol{u} = 0, \end{cases} . \tag{2.8}$$

The Stokes equations display numerous properties that follow from the absence of inertial effects and we refer the reader to Kim and Karrila, 2005; Graham, 2018 for a detailed description. Since there is no time derivative in the Stokes equations, the motion is said to be *quasi-static*, thus the flow field is instantaneously determined by the initial condition and prescribed boundary conditions. Taking the divergence of the Stokes momentum balance equation and knowing that the velocity field is divergence-free, it is straightforward to show that

$$\nabla^2 p = 0. \tag{2.9}$$

Thus, the pressure field is a harmonic function, it can be written as superposition of fundamental solutions of the Laplace equation. Then, taking the Laplacian of the Stokes momentum balance equation leads to

$$\nabla^4 \boldsymbol{u} \equiv \nabla^2 \nabla^2 \boldsymbol{u} = \boldsymbol{0}, \tag{2.10}$$

the velocity field is a biharmonic function, i.e., its Laplacian is harmonic. Finally, taking the curl of the Stokes momentum balance equation leads to a Laplace equation of the flow vorticity $\boldsymbol{\omega}$,

$$\nabla^2 \boldsymbol{\omega} = \boldsymbol{0}, \tag{2.11}$$

where $\boldsymbol{\omega} = \nabla \times \boldsymbol{u}$. Therefore, as the pressure field, the flow vorticity is also a harmonic function.

Note that, numerous exact and approximate solutions to the Stokes equations exist in the literature, we refer the reader to Happel and Brenner, 1981; Kim and Karrila, 2005; Leal, 2007 for a more detailed description. In this thesis, we will conduct dynamic simulations based on the Green's function formulation for Stokes flow to compute the velocity field in response to prescribed forces.

2.2 General solutions to Stokes equations

2.2.1 Fundamental solutions

Since the Stokes equations are quasi-static, the velocity field will respond instantaneously to the prescribed forces and boundary conditions. Thus, dynamic simulations are conducted by computing particle velocities due to forces that are applied on each particle. These forces are determined by the physics of the problem. Therefore, numerical methods need to compute both the velocity field induced by a given particle and the resulting motion of other particles in response to that field. Methods based on Green's function are among the widely used approaches to achieve this target. The Green's function is the fundamental solution to the Stokes equations, and derives from the velocity field induced by a point force of strength $\boldsymbol{F}$, namely $\boldsymbol{f} = \boldsymbol{F}\delta(\boldsymbol{r} - \boldsymbol{r}_0)$, where $\boldsymbol{r}$ is the *field point*, $\boldsymbol{r}_0$ the *source point* and δ the three-dimensional delta function. Thus, the Stokes equations (2.8) lead to the singularly forced Stokes equations

$$\begin{cases} -\eta \nabla^2 \boldsymbol{u} + \nabla p = \boldsymbol{F}\delta(\boldsymbol{r} - \boldsymbol{r}_0), \\ \nabla \cdot \boldsymbol{u} = 0, \end{cases} . \tag{2.12}$$

Introducing the Green's function $\mathbb{G}$, we write the velocity, pressure and stress fields, that are fundamental solutions to (2.12) in the following forms

$$\boldsymbol{u}(\boldsymbol{r}) = \mathbb{G}(\boldsymbol{r}, \boldsymbol{r}_0) \cdot \boldsymbol{F}, \tag{2.13}$$

$$\boldsymbol{p}(\boldsymbol{r}) = \mathbb{P}(\boldsymbol{r}, \boldsymbol{r}_0) \cdot \boldsymbol{F}, \tag{2.14}$$

$$\boldsymbol{\sigma}(\boldsymbol{r}) = \mathbb{T}(\boldsymbol{r}, \boldsymbol{r}_0) \cdot \boldsymbol{F}, \tag{2.15}$$

where $\mathbb{P}$ and $\mathbb{T}$ are respectively the pressure vector and stress tensor associated with the Green's function $\mathbb{G}$. In particular, the stress tensor $\mathbb{T}$ is given by

$$T_{ijk}(\boldsymbol{r}, \boldsymbol{r}_0) = -\delta_{ij} P_k(\boldsymbol{r}, \boldsymbol{r}_0) + \eta \left[\frac{\partial G_{ij}(\boldsymbol{r}, \boldsymbol{r}_0)}{\partial r_k} + \frac{\partial G_{ik}(\boldsymbol{r}, \boldsymbol{r}_0)}{\partial r_j} \right]. \tag{2.16}$$

Note that $T_{ijk} = T_{kji}$, since $\boldsymbol{\sigma}$ is symmetric as aforementioned. In an unbounded domain, the Green's function $\mathbb{G}$ is commonly called the *Stokeslet* or *Oseen-Burgers* tensor (Pozrikidis, 1992).

Due to the linearity of the Stokes equations, the velocity field in a control volume V that is bounded by a closed surface S, may be represented in terms of boundary integrals involving the boundary values of the velocity and traction fields . This formulation is known as the boundary integral representation of Stokes flow[2] (Pozrikidis, 1992; Kim and Karrila, 2005)

$$\boldsymbol{u}(\boldsymbol{r}) = -\int_S \mathbb{G}(\boldsymbol{r},\boldsymbol{r}_0)\cdot[\boldsymbol{\sigma}(\boldsymbol{r}_0)\cdot\hat{\boldsymbol{n}}(\boldsymbol{r}_0)]\mathrm{d}S(\boldsymbol{r}_0) - \int_S \mathbb{T}(\boldsymbol{r},\boldsymbol{r}_0):[\boldsymbol{u}(\boldsymbol{r}_0)\otimes\hat{\boldsymbol{n}}(\boldsymbol{r}_0)]\mathrm{d}S(\boldsymbol{r}_0), \tag{2.17}$$

where $\hat{\boldsymbol{n}}$ is the unit normal directed from S into the enclosed fluid volume V and $-\boldsymbol{\sigma}\cdot\hat{\boldsymbol{n}}$ is the traction exerted by the boundaries on the fluid. Note that S may be composed of fluid or solid surfaces (e.g., particles immersed in a viscous fluid). The two convolutions on the right hand side of (2.17) involve respectively the Green's function $\mathbb{G}$ and the associated stress tensor $\mathbb{T}$, these convolutions are known as the *single-layer* and the *double-layer* potentials, respectively.

Particles that are said to undergoing a rigid-body motion, which are the class of particles considered in this thesis[3], are characterized by the following velocity boundary condition $\boldsymbol{u}(\boldsymbol{r}) = \boldsymbol{U} + \boldsymbol{\Omega}\times\boldsymbol{r}$, for $\boldsymbol{r}\in S$, where $\boldsymbol{U}$ and $\boldsymbol{\Omega}$ are respectively the translational and angular velocities of the particle. In that case, the double-layer potential vanishes, as shown by Pozrikidis, 1992. Thus, (2.17) reduces to

$$\boldsymbol{u}(\boldsymbol{r}) = -\int_S \mathbb{G}(\boldsymbol{r},\boldsymbol{r}_0)\cdot[\boldsymbol{\sigma}(\boldsymbol{r}_0)\cdot\hat{\boldsymbol{n}}(\boldsymbol{r}_0)]\mathrm{d}S(\boldsymbol{r}_0). \tag{2.18}$$

This reduced form shows the velocity field induced by the boundary distribution of point forces.

For a collection of N rigid particles immersed in the fluid domain, it is straightforward to derive the induced velocity field as a superposition of convolutions over the sub-boundaries. Thus,

$$\boldsymbol{u}(\boldsymbol{r}) = -\sum_{i=1}^{N}\int_{S_i} \mathbb{G}(\boldsymbol{r},\boldsymbol{r}_0)\cdot[\boldsymbol{\sigma}(\boldsymbol{r}_0)\cdot\hat{\boldsymbol{n}}(\boldsymbol{r}_0)]\mathrm{d}S(\boldsymbol{r}_0), \tag{2.19}$$

where S_i is the surface of particle i.

2.2.2 The multipole expansion

The numerical evaluation of the convolutions in (2.19) can be a cumbersome task for particles of arbitrary shapes. Numerical approaches such as boundary element methods (Pozrikidis, 1992) are computationally costly and scale badly with the number of elements. A widely used approach that applies to sphere-like particles, is the *multipole expansion*. To derive the multipole expansion of the velocity field, we first Taylor expand the Green's function about the center of a rigid particle, and substitute the result into (2.18)

$$u_i(\boldsymbol{r}) = -\sum_{n=0}^{\infty}\frac{(-1)^n}{n!}\frac{\partial}{\partial r_{k_1}}\cdots\frac{\partial}{\partial r_{k_n}}G_{ij}(\boldsymbol{r},\boldsymbol{r}_0)|_{\boldsymbol{\xi}=\boldsymbol{0}}H^n_{k_1\ldots k_n j}, \tag{2.20}$$

where $\boldsymbol{\xi} = \boldsymbol{r}_0 - \boldsymbol{r}_c$, $\boldsymbol{r}_c$ being the position of the particle center. The multipole expansion of the surface traction $-\boldsymbol{\sigma}\cdot\hat{\boldsymbol{n}}$ is given by

$$H^n_{k_1\ldots k_n j} = \int_S \xi_{k_1}\ldots\xi_{k_n}[\sigma_{jp}(\boldsymbol{r}_0)\hat{n}_p(\boldsymbol{r}_0)]\mathrm{d}S(\boldsymbol{r}_0), \tag{2.21}$$

[2]This formulation gives rise to a computational approach called the *boundary integral method*, where only the boundaries need to be discretized to solve the Stokes equations instead of discretizing the fluid domain V.

[3]In discrete form, a fiber-like particle can be seen as a series of rigid spherical particles connected by stiff linkers (see Section 3.4).

where $\xi_{k_1} \dots \xi_{k_n} = 1$ for $n = 0$. In order to get some physical insight, we can write the first few terms of (2.20) as follows

$$\begin{aligned} u_i(\boldsymbol{r}) = &-G_{ij}(\boldsymbol{r}, \boldsymbol{r}_0)|_{\boldsymbol{\xi}=\boldsymbol{0}} \int_S [\sigma_{jp}(\boldsymbol{r}_0)\hat{n}_p(\boldsymbol{r}_0)] \mathrm{d}S(\boldsymbol{r}_0) \\ &+ \frac{\partial G_{ij}(\boldsymbol{r}, \boldsymbol{r}_0)}{\partial r_k}\bigg|_{\boldsymbol{\xi}=\boldsymbol{0}} \int_S \xi_k [\sigma_{jp}(\boldsymbol{r}_0)\hat{n}_p(\boldsymbol{r}_0)] \mathrm{d}S(\boldsymbol{r}_0) + \dots \end{aligned} \tag{2.22}$$

The zeroth-order moment or monopole is the force exerted on the particle by the fluid integrated over the particle surface

$$F_j = \int_S [\sigma_{jp}(\boldsymbol{r}_0)\hat{n}_p(\boldsymbol{r}_0)] \mathrm{d}S(\boldsymbol{r}_0), \tag{2.23}$$

and

$$D_{jk} = \int_S \xi_k [\sigma_{jp}(\boldsymbol{r}_0)\hat{n}_p(\boldsymbol{r}_0)] \mathrm{d}S(\boldsymbol{r}_0) \tag{2.24}$$

is the first-order moment, also called the dipole tensor or the force dipole. The traceless part of the latter[4] can be decomposed into a symmetric component known as the *stresslet*

$$\begin{aligned} S_{jk} = &\frac{1}{2} \int_S \{\xi_k [\sigma_{jp}(\boldsymbol{r}_0)\hat{n}_p(\boldsymbol{r}_0)] + \xi_j [\sigma_{kp}(\boldsymbol{r}_0)\hat{n}_p(\boldsymbol{r}_0)]\} \, \mathrm{d}S(\boldsymbol{r}_0) \\ &- \frac{2}{3} \int_S \{\delta_{jk}\xi_l [\sigma_{lp}(\boldsymbol{r}_0)\hat{n}_p(\boldsymbol{r}_0)]\} \, \mathrm{d}S(\boldsymbol{r}_0), \end{aligned} \tag{2.25}$$

and an antisymmetric component known as the *rotlet*, which is related to the total torque $\boldsymbol{L}$ exerted on the particle by the fluid integrated over the particle surface

$$\begin{aligned} R_{jk} &= \frac{1}{2} \int_S \{\xi_k [\sigma_{jp}(\boldsymbol{r}_0)\hat{n}_p(\boldsymbol{r}_0)] - \xi_j [\sigma_{kp}(\boldsymbol{r}_0)\hat{n}_p(\boldsymbol{r}_0)]\} \, \mathrm{d}S(\boldsymbol{r}_0) \\ &= \frac{1}{2} \varepsilon_{jkp} L_p, \end{aligned} \tag{2.26}$$

where

$$L_p = \int_S \{\varepsilon_{pmn}\xi_m [\sigma_{nl}(\boldsymbol{r}_0)\hat{n}_l(\boldsymbol{r}_0)]\} \, \mathrm{d}S(\boldsymbol{r}_0). \tag{2.27}$$

Now we can write the multipole expansion of the velocity field (2.22) in terms of the aforementioned quantities, we obtain

$$u_i(\boldsymbol{r}) = -G_{ij}(\boldsymbol{r}, \boldsymbol{r}_0)|_{\boldsymbol{\xi}=\boldsymbol{0}} F_j + C_{kij}(\boldsymbol{r}, \boldsymbol{r}_0)|_{\boldsymbol{\xi}=\boldsymbol{0}} R_{jk} + K_{kij}(\boldsymbol{r}, \boldsymbol{r}_0)|_{\boldsymbol{\xi}=\boldsymbol{0}} S_{jk} + \dots, \tag{2.28}$$

where

$$C_{kij}(\boldsymbol{r}, \boldsymbol{r}_0) = \frac{1}{2} \left[\frac{\partial G_{ij}(\boldsymbol{r}, \boldsymbol{r}_0)}{\partial r_k} - \frac{\partial G_{ik}(\boldsymbol{r}, \boldsymbol{r}_0)}{\partial r_j} \right], \tag{2.29}$$

and

$$K_{kij}(\boldsymbol{r}, \boldsymbol{r}_0) = \frac{1}{2} \left[\frac{\partial G_{ij}(\boldsymbol{r}, \boldsymbol{r}_0)}{\partial r_k} + \frac{\partial G_{ik}(\boldsymbol{r}, \boldsymbol{r}_0)}{\partial r_j} \right]. \tag{2.30}$$

This is the most commonly taken approach to conduct Green's function based simulations. Since the flows associated with higher-order moments decay more quickly than the one associated with the zeroth-order moment, the latter is sufficient to conduct dynamic simulations in

[4] The isotropic part of the dipole tensor is of no dynamic significance (Kim and Karrila, 2005).

the case of well-separated particles (e.g., dilute suspensions), and the formers only matter for particles that are close together (e.g., concentrated suspensions), or when lubrication effects are accounted for. Note that, for finite-size particles such as spheres, the isotropic contribution to the quadrupolar and octupolar moments contributes respectively to the coupling with the zeroth-order moment (monopole) and the first-order moment (dipole).

2.2.3 Faxén's laws

Commonly used approaches to determine the particle motion induced by the flow field are known as Faxén's laws (Kim and Karrila, 2005). For spherical particles, these laws are given by differential relations between the velocity field and gradients that derive from the multipole expansion (2.28). Accordingly, the translational and angular velocities for spherical particles are given by[5]

$$\boldsymbol{U} = \left(1 + \frac{a^2}{6}\nabla^2\right)\boldsymbol{u}(\boldsymbol{r}_0), \tag{2.31a}$$

$$\boldsymbol{\Omega} = \frac{1}{2}\nabla \times \boldsymbol{u}(\boldsymbol{r}_0). \tag{2.31b}$$

However, numerically speaking, these differential expressions suffer from regularization problems. Instead, integral expressions that are convolutions over the particle surface are employed to overcome this hurdle (Stone and Samuel, 1996; Fiore and Swan, 2019)

$$\boldsymbol{U} = \frac{1}{4\pi a^2}\int_S \boldsymbol{u}(\boldsymbol{r}_0)\mathrm{d}S(\boldsymbol{r}_0), \tag{2.32a}$$

$$\boldsymbol{\Omega} = \frac{3}{4\pi a^3}\int_S \frac{1}{2}[\boldsymbol{u}(\boldsymbol{r}_0) \times \hat{\boldsymbol{n}}(\boldsymbol{r}_0)]\mathrm{d}S(\boldsymbol{r}_0). \tag{2.32b}$$

Thus, Faxén's laws are effectively integral statements of the no-slip boundary condition for a spherical particle that undergoes a rigid-body motion.

2.3 Grand mobility tensor and Rotne-Prager-Yamakawa hydrodynamics

In the previous section, we have derived the flow due to isolated particles in the Stokes regime and seen that the particle motion induced by the flow field in the case of spherical particles can be given by Faxén's laws. However, interest is often in the motion of a collection of particles that are interacting hydrodynamically. The integral expressions of Faxén's laws (2.32) introduced at the end of the previous section are commonly used to derive equations that govern such dynamics.

Let us consider a pair of spherical particles of the same radius a, that are at positions $\boldsymbol{r}_i$ and $\boldsymbol{r}_j$ within the fluid domain, and generate a flow as they move. The flow field generated by particle j subject to the force $\boldsymbol{F}_j$ is given by

$$\boldsymbol{u}(\boldsymbol{r}) = -\frac{1}{4\pi a^2}\int_{S_j} \mathbb{G}(\boldsymbol{r}, \boldsymbol{r}_0) \cdot \boldsymbol{F}_j \mathrm{d}S(\boldsymbol{r}_0), \tag{2.33}$$

[5]These expressions derive from the Lorentz reciprocal theorem applied to the problem for translating and rotating spherical particles in Stokes flow.

and the induced motion in particle i is given by

$$\boldsymbol{U}_i = \frac{1}{4\pi a^2}\int_{S_i} \boldsymbol{u}(\boldsymbol{r})\mathrm{d}S(\boldsymbol{r}). \tag{2.34}$$

Thus, substituting (2.33) into (2.34), the expression of the translational velocity of particle i due to the force exerted on particle j reads as follows

$$\boldsymbol{U}_i = -\frac{1}{4\pi a^2}\int_{S_i} \mathrm{d}S(\boldsymbol{r})\frac{1}{4\pi a^2}\int_{S_j} \mathbb{G}(\boldsymbol{r},\boldsymbol{r}_0)\cdot\boldsymbol{F}_j\mathrm{d}S(\boldsymbol{r}_0). \tag{2.35}$$

Introducing $\boldsymbol{\mathcal{M}}^{tt}_{ij}$ as the *translational-translational mobility tensor*, such as

$$\boldsymbol{\mathcal{M}}^{tt}_{ij} = \frac{1}{4\pi a^2}\int_{S_i} \mathrm{d}S(\boldsymbol{r})\frac{1}{4\pi a^2}\int_{S_j} \mathbb{G}(\boldsymbol{r},\boldsymbol{r}_0)\mathrm{d}S(\boldsymbol{r}_0), \tag{2.36}$$

the linear coupling between forces and velocities of the particle pair can be written as

$$\boldsymbol{U}_i = -\boldsymbol{\mathcal{M}}^{tt}_{ij}\cdot\boldsymbol{F}_j. \tag{2.37}$$

We can generalize this coupling for a collection of N particles. For particle i, we have that

$$\boldsymbol{U}_i = -\sum_{j=1}^{N}\boldsymbol{\mathcal{M}}^{tt}_{ij}\cdot\boldsymbol{F}_j. \tag{2.38}$$

Letting $\boldsymbol{U} = [\boldsymbol{U}_1,\ldots,\boldsymbol{U}_N]$ and $\boldsymbol{F} = [\boldsymbol{F}_1,\ldots,\boldsymbol{F}_N]$, the vectors collecting respectively particle translational velocities and hydrodynamic forces, we can write (2.38) succinctly as

$$\boldsymbol{U} = -\boldsymbol{\mathcal{M}}^{tt}\cdot\boldsymbol{F}. \tag{2.39}$$

Using the same approach, one can derive similar relations for higher-order moments. However, as aforementioned, the predominance influence to the flow field generated by a given particle within the fluid is associated with the first terms in the multipole expansion. Hence in this thesis, we will limit our consideration to the contributions of the monopole and isotropic quadrupole moments on such flow (see Section 3.4.3). However, for the sake of completeness and because they are so prevalent in the literature, we give here the other couplings up to the first-order velocity and force moments. Thus, (2.39) can be rewritten as

$$\begin{aligned}\begin{pmatrix}\boldsymbol{U}\\ \boldsymbol{\Omega}\end{pmatrix} &= -\begin{pmatrix}\boldsymbol{\mathcal{M}}^{tt} & \boldsymbol{\mathcal{M}}^{tr}\\ \boldsymbol{\mathcal{M}}^{rt} & \boldsymbol{\mathcal{M}}^{rr}\end{pmatrix}\cdot\begin{pmatrix}\boldsymbol{F}\\ \boldsymbol{L}\end{pmatrix}\\ &= -\boldsymbol{\mathcal{M}}\cdot\begin{pmatrix}\boldsymbol{F}\\ \boldsymbol{L}\end{pmatrix},\end{aligned} \tag{2.40}$$

where $\boldsymbol{\Omega} = [\boldsymbol{\Omega}_1,\ldots,\boldsymbol{\Omega}_N]$ and $\boldsymbol{L} = [\boldsymbol{L}_1,\ldots,\boldsymbol{L}_N]$ are vectors collecting respectively particle angular velocities and hydrodynamic torques. $\boldsymbol{\mathcal{M}}^{rr}$, $\boldsymbol{\mathcal{M}}^{rt}$ and $\boldsymbol{\mathcal{M}}^{tr}$ are mobility tensors which couple respectively, angular velocities to hydrodynamic torques, angular velocities to hydrodynamic forces and translational velocities to hydrodynamic torques. In the second line of (2.40), the tensor $\boldsymbol{\mathcal{M}}$ is called the *grand mobility tensor*, and is symmetric and positive semi-definite. Both properties can be shown respectively, by the reciprocal and energy dissipation theorems (Kim and Karrila, 2005).

The relationship (2.40) is known as the *mobility problem*, and is usually employed to compute particle motions in Green's function based methods. However, in the opposite case, where translational and angular velocities are prescribed (e.g., velocity-based constraint problems, where Lagrange multipliers need to be found in order to satisfy the constraints), this problem is referred to as the *resistance problem*

$$\begin{aligned}\begin{pmatrix}\boldsymbol{F}\\ \boldsymbol{L}\end{pmatrix} &= -\begin{pmatrix}\boldsymbol{\mathcal{R}}^{tt} & \boldsymbol{\mathcal{R}}^{tr}\\ \boldsymbol{\mathcal{R}}^{rt} & \boldsymbol{\mathcal{R}}^{tr}\end{pmatrix}\cdot\begin{pmatrix}\boldsymbol{U}\\ \boldsymbol{\Omega}\end{pmatrix}\\ &= -\boldsymbol{\mathcal{R}}\cdot\begin{pmatrix}\boldsymbol{U}\\ \boldsymbol{\Omega}\end{pmatrix},\end{aligned} \tag{2.41}$$

where the *grand resistance tensor* $\boldsymbol{\mathcal{R}}$ is defined such as $\boldsymbol{\mathcal{R}} = \boldsymbol{\mathcal{M}}^{-1}$.

From Newton's third law, the hydrodynamic force $\boldsymbol{F}_i$ exerted by the fluid on a given particle i in a collection of N particles, is the negative of the force that the particle exerts on the fluid, which arises from external sources. Therefore, as aforementioned, by considering only the coupling between the zeroth-order velocity and force moments throughout this thesis, the mobility problem (2.39) can be rewritten as

$$\boldsymbol{U} = \boldsymbol{\mathcal{M}}\cdot\boldsymbol{F}, \tag{2.42}$$

where we have used the same symbols as the grand mobility tensor and the hydrodynamic forces to denote respectively the translational-translational mobility tensor and the forces that arise from external sources, for notation convenience.

The mobility tensor (2.36) derived for spherical particles can be rewritten into a form that employs the Faxén's differential operator,

$$\boldsymbol{\mathcal{M}}_{ij} = \begin{cases}\dfrac{1}{6\pi\eta a}\boldsymbol{I}, & i = j\\ \left(\boldsymbol{I} + \dfrac{a^2}{6}\nabla^2_{\boldsymbol{r}}\right)\left(\boldsymbol{I} + \dfrac{a^2}{6}\nabla^2_{\boldsymbol{r}_0}\right)\mathbb{G}(\boldsymbol{r},\boldsymbol{r}_0)\Big|^{\boldsymbol{r}=\boldsymbol{r}_i}_{\boldsymbol{r}_0=\boldsymbol{r}_j}, & i \neq j\end{cases}, \tag{2.43}$$

where $\boldsymbol{I}$ is the identity tensor. This formulation is widely used to perform dynamic simulations of hydrodynamically interacting particles in Stokes flow, and is known as the Rotne-Prager-Yamakawa (RPY) tensor (Rotne and Prager, 1969; Yamakawa, 1970). The RPY hydrodynamic tensor can be evaluated in different domains, including unbounded (Wajnryb et al., 2013), half-space above a no-slip wall (Swan and Brady, 2007), confined (Swan and Brady, 2010) and triply periodic (Fiore et al., 2017) domains. In particular, for a triply periodic domain, Fiore et al., 2017 shown that by using the appropriate Green's function, which is given by Hasimoto, 1959,

$$\mathbb{G}(\boldsymbol{r},\boldsymbol{r}_0) = \frac{1}{\eta V}\sum_{\boldsymbol{k}\neq 0}\frac{1}{k^2}\left(\boldsymbol{I} - \hat{\boldsymbol{k}}\otimes\hat{\boldsymbol{k}}\right)\exp\left(i\boldsymbol{k}\cdot\hat{\boldsymbol{x}}\right), \tag{2.44}$$

where $\hat{\boldsymbol{x}} = \boldsymbol{r} - \boldsymbol{r}_0$, V is the periodic cell volume and $\boldsymbol{k}$ are the set of reciprocal lattice vectors, with $\hat{\boldsymbol{k}} = \boldsymbol{k}/k$ for $k = |\boldsymbol{k}|$; the formulation (2.43) is symmetric and positive definite (SPD) for all particle separations, i.e., overlapping and non-overlapping configurations. The latter property is needed to conduct dynamic simulations that account for Brownian effects. In contrast, additional regularizing corrections are required for overlapping configurations in an unbounded domain (Wajnryb et al., 2013). Using the appropriate Green's function, known as the Oseen-Burgers's tensor,

$$\mathbb{G}(\boldsymbol{r},\boldsymbol{r}_0) = \frac{1}{8\pi\eta|\hat{\boldsymbol{x}}|}\left(\boldsymbol{I} + \frac{\hat{\boldsymbol{x}}\otimes\hat{\boldsymbol{x}}}{|\hat{\boldsymbol{x}}|^2}\right), \tag{2.45}$$

the formulation (2.43) takes the following form

$$\boldsymbol{\mathcal{M}}_{ij} = \frac{1}{6\pi\eta a}\begin{cases}\left(\dfrac{3a}{4|\hat{\boldsymbol{x}}|} + \dfrac{a^3}{2|\hat{\boldsymbol{x}}|^3}\right)\boldsymbol{I} + \left(\dfrac{3a}{4|\hat{\boldsymbol{x}}|^3} - \dfrac{3a^3}{2|\hat{\boldsymbol{x}}|^4}\right)\hat{\boldsymbol{x}}\otimes\hat{\boldsymbol{x}}, & |\hat{\boldsymbol{x}}| > 2a\\ \left(1 - \dfrac{9|\hat{\boldsymbol{x}}|}{32a}\right)\boldsymbol{I} + \left(\dfrac{3}{32a|\hat{\boldsymbol{x}}|}\right)\hat{\boldsymbol{x}}\otimes\hat{\boldsymbol{x}}, & |\hat{\boldsymbol{x}}| \leq 2a\end{cases}. \tag{2.46}$$

Part II

Modeling flexible fibers in complex environments

Chapter 3

Dynamics of flexible fibers in Stokes flow

Contents

This chapter describes the numerical method used throughout this thesis to conduct dynamic simulations of flexible fibers in Stokes flow. This method relies on the commonly-used bead-spring model with hydrodynamic interactions accounted for at the Rotne-Prager-Yamakawa (RPY) level of approximation.

3.1 Introduction

Various situations in biology and engineering applications exhibit interactions of elastic fiber-like particles with a surrounding fluid. For instance, in biology, numerous microswimmers such as bacteria apply stresses on the fluid through swimming strokes or sequences of shape configurations of their fiber-like appendages which include cilia and flagella, in order to induce propulsion (Boal, 2012; Lauga, 2020). In engineering applications, e.g., in industrial papermaking processes, cellulose fibers of high aspect-ratios are mixed with water to form a

suspension referred to as pulp (Lundell et al., 2011). In all the aforementioned situations, the fiber dynamics result from the complex interplay between its elastic response and hydrodynamic interactions with the surrounding fluid and fibers.

In the Stokes regime, where inertial effects are negligible compared to viscous ones, numerous mathematical and computational methods have been developed to tackle the resulting *elastohydrodynamic* coupling problem. On the numerical side, such methods follow the general pattern commonly used to simulate the dynamics of flexible fibers that are immersed in Stokes flow : an elastic model, referred to as *the theory of elastic rods*, is used to characterize the deformation of the fiber, which is subject to external forces that arise from the surrounding fluid and external fields such as gravity or steric interactions. The way to compute the forces exerted by the surrounding fluid on the fiber determines the particular numerical method. Such methods include the slender body theory (SBT) (Tornberg and Shelley, 2004), the boundary integral method (BIM) (Pozrikidis, 1992), the immersed boundary method (Peskin, 2002), the force-coupling method (FCM) (Schoeller et al., 2021), the Rotne-Prager-Yamakawa (RPY) based method (Maxian et al., 2021a; Balboa Usabiaga and Delmotte, 2022), and the method of regularized Stokeslets (Lim et al., 2008; Olson et al., 2013; Jabbarzadeh and Fu, 2020). In this chapter, we give a detailed description of the RPY-based approach used throughout this thesis to conduct dynamic simulations of flexible fibers in Stokes flow. The chapter is organized as follows. In Section 3.2, the equilibrium equations for the mechanics of flexible fibers are derived. Section 3.3 discusses the different numerical approaches to couple the mechanics of the fiber to fluid flow. Section 3.4 describes the formulation of the bead-spring model, the internal elastic forces are derived for planar deformations, as well as the mobility relation that relates bead velocities to applied forces. Finally, Section 3.5 shows various numerical test problems which validate our implementation against known results collected in the literature.

3.2 Continuum formulation for flexible fibers

In this section, we derive the equilibrium equations for flexible fibers, that are known in the literature as equations for *elastic rods*. In a very common approach, the energy functional is first derived for an arbitrary configuration of the fiber. Then, the equilibrium equations are obtained by variation of the former for given boundary conditions.

3.2.1 Kinematics

We denote by $\boldsymbol{X}(s,t)$ the space curve, which represents the position of the centerline of the fiber at a given time t, parametrized by the Lagrangian parameter[1] $s \in [0, L]$ along its length. We assume that the fiber is isotropic and has a uniform cross-section along its length.

To keep track of the deformation, we introduce the orthonormal material frame $(\hat{\boldsymbol{n}}_1(s,t), \hat{\boldsymbol{n}}_2(s,t), \hat{\boldsymbol{t}}(s,t))$, which is attached to the centerline of the fiber. The orientation of this material frame is defined such that $\hat{\boldsymbol{n}}_1$ and $\hat{\boldsymbol{n}}_2$ lie in the plane of the cross-section, while $\hat{\boldsymbol{t}}$ is the tangent to the centerline (see Fig.3.1). Upon deformation and under Euler-Bernoulli kinematic assumptions[2], these vectors are given by

$$\frac{\partial \hat{\boldsymbol{n}}_1}{\partial s} = \boldsymbol{\Omega} \times \hat{\boldsymbol{n}}_1 \qquad \frac{\partial \hat{\boldsymbol{n}}_2}{\partial s} = \boldsymbol{\Omega} \times \hat{\boldsymbol{n}}_2 \qquad \frac{\partial \hat{\boldsymbol{t}}}{\partial s} = \boldsymbol{\Omega} \times \hat{\boldsymbol{t}}, \tag{3.1}$$

where we have introduced the spatial-rate of rotation per unit length of the material frame along the centerline $\boldsymbol{\Omega}(s,t)$, also called *the Darboux vector* (Darboux, 1896)

[1] Not necessarily the arclength.

[2] Upon deformation, the plane sections remain plane and deformed centerline angles (slopes) are small. Therefore, the material frame remains approximately orthonormal.

$$\boldsymbol{\Omega}(s,t) = \kappa^{(1)}(s,t)\hat{\boldsymbol{n}}_1 + \kappa^{(2)}(s,t)\hat{\boldsymbol{n}}_2 + \tau(s,t)\hat{\boldsymbol{t}}, \tag{3.2}$$

with $\kappa^{(1)}$ and $\kappa^{(2)}$ being the curvatures of the centerline, respectively in the cross-sectional directions $\hat{\boldsymbol{n}}_1$ and $\hat{\boldsymbol{n}}_2$, and τ the twist around the centerline, i.e., around the cross-sectional direction $\hat{\boldsymbol{t}}$.

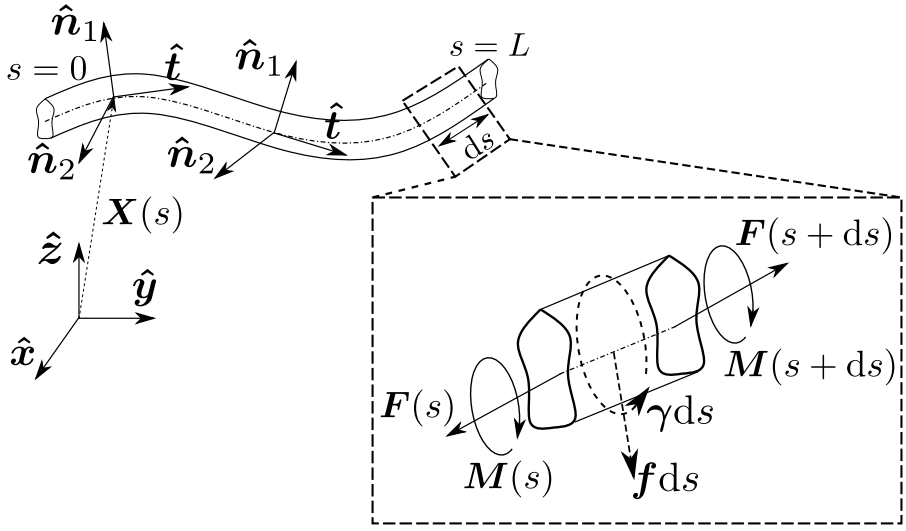

Figure 3.1: Continuous description of a flexible fiber (the explicit time dependence is omitted for notation convenience). The position of its centerline $\boldsymbol{X}(s)$ is parametrized by the Lagrange parameter $s \in [0, L]$, and the material frame $(\hat{\boldsymbol{n}}_1, \hat{\boldsymbol{n}}_2, \hat{\boldsymbol{t}})$ is attached to the former. The inset shows forces and torques acting on a small element of the fiber. $\boldsymbol{F}$ and $\boldsymbol{M}$ are the internal force and moment, that are transmitted by the neighboring elements. $\boldsymbol{f}$ and $\boldsymbol{\gamma}$ are the lineic densities of the external force and torque that arise from the surrounding fluid and other external sources.

3.2.2 Constitutive relations

3.2.2.1 Elastic energy

As mentioned earlier, the deformation of the fiber is characterized by the Darboux vector $\boldsymbol{\Omega}(s,t)$. Thus, assuming Hookean elasticity and that the deformation is invariant along the fiber, the elastic energy over the length L is a quadratic function of the components of the Darboux vector (Landau et al., 1986)

$$\mathcal{E} = \int_0^L \left(\frac{EI^{(1)}}{2}(\kappa^{(1)}(s,t))^2 + \frac{EI^{(2)}}{2}(\kappa^{(2)}(s,t))^2 + \frac{\mu J}{2}(\tau(s,t))^2 \right) \mathrm{d}s, \tag{3.3}$$

where the cross terms corresponding to coupling between flexion and twist have been set to zero, due to symmetry consideration (Landau et al., 1986; Audoly and Pomeau, 2010). The first two terms on the right hand side are the bending terms, where E is the Young's modulus, and $I^{(1)}$ and $I^{(2)}$ are the principal moments of inertia, respectively in the cross-sectional directions $\hat{\boldsymbol{n}}_1$ and $\hat{\boldsymbol{n}}_2$, for instance $I^{(1)} = I^{(2)} = \pi a^4/4$ for a circular cross-section of radius a. The last term is the twisting term, where μ is the shear modulus, and J the moment of twist, which is similar to the principal moments of inertia $I^{(i)}$ defined for bending, for instance $J = 2I^{(1)} = 2I^{(2)}$ for a circular cross-section.

The elastic energy can also be expressed only in terms of material vectors $\hat{\boldsymbol{n}}_1$, $\hat{\boldsymbol{n}}_2$ and $\hat{\boldsymbol{t}}$. Given the relations (3.1), we express the material curvatures and twist as function of the material vectors, such that

$$\frac{\partial \hat{\boldsymbol{n}}_2}{\partial s} \cdot \hat{\boldsymbol{t}} = \kappa^{(1)} \qquad \frac{\partial \hat{\boldsymbol{t}}}{\partial s} \cdot \hat{\boldsymbol{n}}_1 = \kappa^{(2)} \qquad \frac{\partial \hat{\boldsymbol{n}}_1}{\partial s} \cdot \hat{\boldsymbol{n}}_2 = \tau. \tag{3.4}$$

Thus, by substituting (3.4) into (3.3), yields

$$\mathcal{E} = \int_0^L \left[\frac{EI^{(1)}}{2} \left(\frac{\partial \hat{\boldsymbol{n}}_2}{\partial s} \cdot \hat{\boldsymbol{t}} \right) \hat{\boldsymbol{n}}_1 + \frac{EI^{(2)}}{2} \left(\frac{\partial \hat{\boldsymbol{t}}}{\partial s} \cdot \hat{\boldsymbol{n}}_1 \right) \hat{\boldsymbol{n}}_2 + \frac{\mu J}{2} \left(\frac{\partial \hat{\boldsymbol{n}}_1}{\partial s} \cdot \hat{\boldsymbol{n}}_2 \right) \hat{\boldsymbol{t}} \right] \mathrm{d}s. \tag{3.5}$$

3.2.2.2 Internal moment

The internal moment $\boldsymbol{M}(s,t)$ is defined as the moment of the contact forces transmitted across the cross-section. To derive the expression of the internal moment, we follow the same approach as done by Audoly and Pomeau, 2010. We start with the derivation of the bending part by considering the fiber clamped at its section $s = 0$ and bent by applying a moment at $s = L$. An infinitesimal change in loading will induce an infinitesimal change in curvature, denoted $\delta\kappa^{(i)}$. Therefore, the end section will experience an infinitesimal rotation by the vector $[(\delta\kappa^{(1)}\boldsymbol{n}_1 + \delta\kappa^{(2)}\boldsymbol{n}_2)L]$. The work done by the bending moment $\boldsymbol{M}_B(s,t)|_{s=L}$ upon this rotation is $[\boldsymbol{M}_B(s,t)|_{s=L} \cdot (\delta\kappa^{(1)}\boldsymbol{n}_1 + \delta\kappa^{(2)}\boldsymbol{n}_2)L]$. To maintain equilibrium, this work should balance the corresponding change in the elastic energy derived from (3.3), $[(EI^{(1)}\kappa^{(1)}\delta\kappa^{(1)} + EI^{(2)}\kappa^{(2)}\delta\kappa^{(2)})L]$. Thus, by identifying the two expressions, the internal bending moment is given by

$$\boldsymbol{M}_B(s,t) = EI^{(1)}\kappa^{(1)}(s,t)\hat{\boldsymbol{n}}_1 + EI^{(2)}\kappa^{(2)}(s,t)\hat{\boldsymbol{n}}_2 \tag{3.6}$$

Similarly, the twisting part can be derived by using an analogous argument as done for bending, thereby the internal twisting moment is given by

$$\boldsymbol{M}_T(s,t) = \mu J\tau(s,t)\hat{\boldsymbol{t}}. \tag{3.7}$$

Accordingly, the internal moment is a linear superposition of both, the internal bending and twisting moments

$$\begin{aligned} \boldsymbol{M}(s,t) &= \boldsymbol{M}_B(s,t) + \boldsymbol{M}_T(s,t) \\ &= EI^{(1)}\kappa^{(1)}(s,t)\hat{\boldsymbol{n}}_1 + EI^{(2)}\kappa^{(2)}(s,t).\hat{\boldsymbol{n}}_2 + \mu J\tau(s,t)\hat{\boldsymbol{t}}. \end{aligned} \tag{3.8}$$

As done for the elastic energy (3.5), the internal moment can also be expressed in terms of the material vectors by substituting the relations (3.4) into (3.8), thus

$$\boldsymbol{M}(s,t) = EI^{(1)} \left(\frac{\partial \hat{\boldsymbol{n}}_2}{\partial s} \cdot \hat{\boldsymbol{t}} \right) \hat{\boldsymbol{n}}_1 + EI^{(2)} \left(\frac{\partial \hat{\boldsymbol{t}}}{\partial s} \cdot \hat{\boldsymbol{n}}_1 \right) \hat{\boldsymbol{n}}_2 + \mu J \left(\frac{\partial \hat{\boldsymbol{n}}_1}{\partial s} \cdot \hat{\boldsymbol{n}}_2 \right) \hat{\boldsymbol{t}}. \tag{3.9}$$

3.2.3 Fluid-fiber coupling

In the following, we derive the equations for equilibrium of the fiber, which is subject to external forces and torques per unit length that arise from the surrounding fluid and external fields such as gravity or steric interactions. This derivation is based on the general theory of elastic rods, where the equations for equilibrium of the rod are obtained by variation of its energy functional. We first derive these equations in the case of three-dimensional deformations, known as *Kirchhoff model* (Kirchhoff, 1850), then in the case of planar deformations, known as *Euler's Elastica model* (Euler, 1744), a limit case of the general Kirchhoff equations.

3.2.3.1 Equilibrium equations : Kirchhoff model

3.2.3.1.1 Principle of virtual work

We use the principle of virtual work, which is a classical approach in the theory of elastic rods to derive the equations of equilibrium (Steigmann and Faulkner, 1993; Lim et al., 2008; Powers, 2010; Audoly and Pomeau, 2010). During a virtual displacement $\boldsymbol{X} \to \boldsymbol{X} + \delta\boldsymbol{X}$, and a virtual rotation of the material frame $(\hat{\boldsymbol{n}}_1, \hat{\boldsymbol{n}}_2, \hat{\boldsymbol{t}}) \to (\hat{\boldsymbol{n}}_1, \hat{\boldsymbol{n}}_2, \hat{\boldsymbol{t}}) + (\delta\hat{\boldsymbol{n}}_1, \delta\hat{\boldsymbol{n}}_2, \delta\hat{\boldsymbol{t}})$, the elastic energy $\mathcal{E}$ is affected and its variation is given by

$$\delta\mathcal{E} = \int_0^L \left[EI^{(1)} \left(\frac{\partial\hat{\boldsymbol{n}}_2}{\partial s}\cdot\hat{\boldsymbol{t}}\right)\delta\left(\frac{\partial\hat{\boldsymbol{n}}_2}{\partial s}\cdot\hat{\boldsymbol{t}}\right) + EI^{(2)}\left(\frac{\partial\hat{\boldsymbol{t}}}{\partial s}\cdot\hat{\boldsymbol{n}}_1\right)\delta\left(\frac{\partial\hat{\boldsymbol{t}}}{\partial s}\cdot\hat{\boldsymbol{n}}_1\right) + \mu J\left(\frac{\partial\hat{\boldsymbol{n}}_1}{\partial s}\cdot\hat{\boldsymbol{n}}_2\right)\delta\left(\frac{\partial\hat{\boldsymbol{n}}_1}{\partial s}\cdot\hat{\boldsymbol{n}}_2\right)\right] \mathrm{d}s \tag{3.10a}$$

$$= \int_0^L \boldsymbol{M}\cdot\left[\delta\left(\frac{\partial\hat{\boldsymbol{n}}_2}{\partial s}\cdot\hat{\boldsymbol{t}}\right)\hat{\boldsymbol{n}}_1 + \delta\left(\frac{\partial\hat{\boldsymbol{t}}}{\partial s}\cdot\hat{\boldsymbol{n}}_1\right)\hat{\boldsymbol{n}}_2 + \delta\left(\frac{\partial\hat{\boldsymbol{n}}_1}{\partial s}\cdot\hat{\boldsymbol{n}}_2\right)\hat{\boldsymbol{t}}\right] \mathrm{d}s \tag{3.10b}$$

where we have substituted the expression (3.9) of the internal moment $\boldsymbol{M}(s,t)$ into (3.10a) to yield (3.10b).

We introduce the variation $\delta\boldsymbol{\phi}$ to the orientation of the material frame, which is given as function of the material vectors, such that[3]

$$\delta\hat{\boldsymbol{n}}_1 = \delta\boldsymbol{\phi}\times\hat{\boldsymbol{n}}_1 \qquad \delta\hat{\boldsymbol{n}}_2 = \delta\boldsymbol{\phi}\times\hat{\boldsymbol{n}}_2 \qquad \delta\hat{\boldsymbol{t}} = \delta\boldsymbol{\phi}\times\hat{\boldsymbol{t}}. \tag{3.11}$$

Given the above relations, one can show that the first derivative of the variation $\delta\boldsymbol{\phi}$ with respect to the Lagrangian parameter s, reads as (Audoly and Pomeau, 2010)

$$\frac{\partial(\delta\boldsymbol{\phi})}{\partial s} = \delta\left(\frac{\partial\hat{\boldsymbol{n}}_2}{\partial s}\cdot\hat{\boldsymbol{t}}\right)\hat{\boldsymbol{n}}_1 + \delta\left(\frac{\partial\hat{\boldsymbol{t}}}{\partial s}\cdot\hat{\boldsymbol{n}}_1\right)\hat{\boldsymbol{n}}_2 + \delta\left(\frac{\partial\hat{\boldsymbol{n}}_1}{\partial s}\cdot\hat{\boldsymbol{n}}_2\right)\hat{\boldsymbol{t}}. \tag{3.12}$$

Thus, we can rewritte the variation of the elastic energy (3.10b) in terms of the variation $\delta\boldsymbol{\phi}$ to the orientation of the material frame,

$$\begin{aligned}\delta\mathcal{E} &= \int_0^L \boldsymbol{M}\cdot\frac{\partial(\delta\boldsymbol{\phi})}{\partial s}\mathrm{d}s \\ &= [\boldsymbol{M}\cdot\delta\boldsymbol{\phi}]_0^L - \int_0^L\left(\frac{\partial\boldsymbol{M}}{\partial s}\cdot\delta\boldsymbol{\phi}\right)\mathrm{d}s,\end{aligned} \tag{3.13}$$

where the second line is obtained after integrating by parts. The first term $[\boldsymbol{M}\cdot\delta\boldsymbol{\phi}]_0^L$ on the right hand side is the virtual work due to a virtual rotation of the ends. In the second term, the elementary contribution $(\partial\boldsymbol{M}/\partial s\cdot\delta\boldsymbol{\phi})\mathrm{d}s$ to the integral is exerted on an element of the fiber of length $\mathrm{d}s$, and corresponds to the elementary virtual work of the internal moment due to a variation $\delta\boldsymbol{\phi}$.

The external forces and torques exerted by the surrounding fluid and/or external fields to hold an arbitrary configuration of the fiber in equilibrium can be of two types : (i) points forces and torques applied at the two ends of the fiber, respectively $(\boldsymbol{F}_{EXT}(s,t)|_{s=0}, \boldsymbol{M}_{EXT}(s,t)|_{s=0})$ and $(\boldsymbol{F}_{EXT}(s,t)|_{s=L}, \boldsymbol{M}_{EXT}(s,t)|_{s=L})$, (ii) forces and torques exerted along the fiber length with linear densities denoted $\boldsymbol{f}(s,t)$ and $\boldsymbol{\gamma}(s,t)$. Thus, the work done by the aforementioned external forces and torques during a virtual displacement and rotation is given by

[3] Assuming Euler-Bernoulli assumptions.

$$\begin{aligned}\delta W = &\int_0^L (\boldsymbol{f}\cdot\delta\boldsymbol{X} + \boldsymbol{\gamma}\cdot\delta\boldsymbol{\phi})\,\mathrm{d}s \\ &+ \boldsymbol{F}_{EXT}|_{s=0}\cdot\delta\boldsymbol{X}|_{s=0} + \boldsymbol{M}_{EXT}|_{s=0}\cdot\delta\boldsymbol{\phi}|_{s=0} \\ &+ \boldsymbol{F}_{EXT}|_{s=L}\cdot\delta\boldsymbol{X}|_{s=L} + \boldsymbol{M}_{EXT}|_{s=L}\cdot\delta\boldsymbol{\phi}|_{s=L}.\end{aligned} \tag{3.14}$$

Having all the necessary ingredients, we can apply the principle of virtual work by setting $\delta\mathcal{E} - \delta W = 0$, where,

$$\begin{aligned}\delta\mathcal{E} - \delta W = [\boldsymbol{M}\cdot\delta\boldsymbol{\phi}]_0^L &- \int_0^L \left(\frac{\partial\boldsymbol{M}}{\partial s}\cdot\delta\boldsymbol{\phi}\right)\mathrm{d}s \\ &- \int_0^L (\boldsymbol{f}\cdot\delta\boldsymbol{X} + \boldsymbol{\gamma}\cdot\delta\boldsymbol{\phi})\,\mathrm{d}s \\ &- \boldsymbol{F}_{EXT}|_{s=0}\cdot\delta\boldsymbol{X}|_{s=0} - \boldsymbol{M}_{EXT}|_{s=0}\cdot\delta\boldsymbol{\phi}|_{s=0} \\ &- \boldsymbol{F}_{EXT}|_{s=L}\cdot\delta\boldsymbol{X}|_{s=L} - \boldsymbol{M}_{EXT}|_{s=L}\cdot\delta\boldsymbol{\phi}|_{s=L}.\end{aligned} \tag{3.15}$$

To calculate the above variation, we must find how the variation $\delta\boldsymbol{X}$ to the displacement is affected by the variation $\delta\boldsymbol{\phi}$ to the orientation of the material frame. To do so, we assume the centerline of the fiber to be inextensible[4], thus the following constraint holds true

$$\frac{\partial\boldsymbol{X}(s,t)}{\partial s} = \hat{\boldsymbol{t}}, \tag{3.16}$$

which can be integrated into $\boldsymbol{X}(s,t) = \boldsymbol{X}(s,t)|_{s=0} + \int_0^s \hat{\boldsymbol{t}}(s',t)\mathrm{d}s'$. By computing the variation of the latter expression, one obtains

$$\delta\boldsymbol{X} = \delta\boldsymbol{X}|_{s=0} - \int_0^s \left(\hat{\boldsymbol{t}}\times\delta\boldsymbol{\phi}\right)\mathrm{d}s', \tag{3.17}$$

where we have used the relation $\delta\hat{\boldsymbol{t}} = \delta\boldsymbol{\phi}\times\hat{\boldsymbol{t}}$ given in (3.11).

Then, after substituting (3.17) into (3.15) and introducing the force $\boldsymbol{F}$ acting on the fiber at s, such that $\partial\boldsymbol{F}/\partial s = \boldsymbol{f}$, the principle of virtual work implies the following balance of moments

$$\frac{\partial\boldsymbol{M}}{\partial s} + \hat{\boldsymbol{t}}\times\boldsymbol{F} + \boldsymbol{\gamma} = \boldsymbol{0}, \tag{3.18}$$

with the following boundary conditions at the ends, $\boldsymbol{F}|_{s=0} = -\boldsymbol{F}_{EXT}|_{s=0}$, $\boldsymbol{F}|_{s=L} = \boldsymbol{F}_{EXT}|_{s=L}$, $\boldsymbol{M}|_{s=0} = -\boldsymbol{M}_{EXT}|_{s=0}$ and $\boldsymbol{M}|_{s=L} = \boldsymbol{M}_{EXT}|_{s=L}$. These boundary conditions imply that the internal forces $\boldsymbol{F}$ and moments $\boldsymbol{M}$ are transmitted through the cross-section by the downstream part of the fiber $s > 0$ to its upstream part $s < 0$.

[4]We can justify this assumption by a scaling argument. For instance by considering an elastic fiber of length L that is immersed in a viscous fluid of viscosity η, such that inertial effects are negligible compared to viscous ones. In the absence of any external force, the only resistance to the fiber stretch will arise from the hydrodynamic force. Thus, the balance between both forces $Ea^2\,(\delta x/L) \sim \eta L\,(\delta x/\tau_s)$ yields to the stretching timescale $\tau_s \sim \eta\,(L/a)^2/E$, where δx is the fiber deformation along its major axis, E the Young's modulus, and a the characteristic length of its cross-section. Similarly, the balance between the bending moment and the hydrodynamic torque $Ea^4\,(\delta z/L^2) \sim \eta L^2\,(\delta z/\tau_b)$ yields to the bending timescale $\tau_b \sim \eta\,(L/a)^4/E$, where δz is the fiber deformation along its transverse axis. The ratio of the bending timescale to the stretching timescale leads to two powers of the fiber aspect-ratio, $\tau_b/\tau_s \sim (L/a)^2$. This implies that, assuming the slenderness assumption, $(L/a) \gg 1$, the timescale at which the fiber stretches is negligible compared to the timescale at which it bends, for long thin fibers. Thus, when the main concern is bending dynamics, long thin fibers are assumed to be inextensible.

3.2.3.1.2 Kirchhoff equations: summary

We summarize here the Kirchhoff equations, which are generally given by the force and momentum balance equations, as derived in the previous section,

$$\frac{\partial \boldsymbol{F}}{\partial s} + \boldsymbol{f} = \boldsymbol{0}, \tag{3.19a}$$

$$\frac{\partial \boldsymbol{M}}{\partial s} + \hat{\boldsymbol{t}} \times \boldsymbol{F} + \boldsymbol{\gamma} = \boldsymbol{0}. \tag{3.19b}$$

Together with the kinematic relations (3.1) and (3.2),

$$\frac{\partial \hat{\boldsymbol{n}}_1}{\partial s} = \boldsymbol{\Omega} \times \hat{\boldsymbol{n}}_1 \qquad \frac{\partial \hat{\boldsymbol{n}}_2}{\partial s} = \boldsymbol{\Omega} \times \hat{\boldsymbol{n}}_2 \qquad \frac{\partial \hat{\boldsymbol{t}}}{\partial s} = \boldsymbol{\Omega} \times \hat{\boldsymbol{t}}, \tag{3.20a}$$

$$\boldsymbol{\Omega}(s,t) = \kappa^{(1)}(s,t)\hat{\boldsymbol{n}}_1 + \kappa^{(2)}(s,t)\hat{\boldsymbol{n}}_2 + \tau(s,t)\hat{\boldsymbol{t}}, \tag{3.20b}$$

the constitutive relation (3.8),

$$\boldsymbol{M}(s,t) = EI^{(1)}\kappa^{(1)}(s,t)\hat{\boldsymbol{n}}_1 + EI^{(2)}\kappa^{(2)}(s,t)\hat{\boldsymbol{n}}_2 + \mu J\tau(s,t)\hat{\boldsymbol{t}}, \tag{3.21}$$

and the boundary conditions $\boldsymbol{F}|_{s=0} = -\boldsymbol{F}_{EXT}|_{s=0}$, $\boldsymbol{F}|_{s=L} = \boldsymbol{F}_{EXT}|_{s=L}$, $\boldsymbol{M}|_{s=0} = -\boldsymbol{M}_{EXT}|_{s=0}$ and $\boldsymbol{M}|_{s=L} = \boldsymbol{M}_{EXT}|_{s=L}$. Note that, in this thesis the fiber ends are free to move, i.e., no external forces and torques are exerted on them. This condition implies that $\boldsymbol{F}|_{s=0} = \boldsymbol{F}|_{s=L} = \boldsymbol{0}$ and $\boldsymbol{M}|_{s=0} = \boldsymbol{M}|_{s=L} = \boldsymbol{0}$.

3.2.3.2 Planar deformations : Euler's Elastica model

The Euler's Elastica model, also known as *Euler-Bernoulli rod model*, is the limit case of the general Kirchhoff equations for planar deformations. This assumption implies that the material vector $\hat{\boldsymbol{n}}_2$ is a constant vector, that is orthogonal to the plane described by $\hat{\boldsymbol{n}}_1$ and $\hat{\boldsymbol{t}}$ (see Fig.3.1). Therefore, from the kinematic equations (see Section 3.2.1), this leads to $\tau = \kappa^{(1)} = 0$, i.e., twisting of the fiber does not occur[5] and bending deformations occur in the transverse direction. Hence, by taking the first derivative of the internal moment equation (3.21), we obtain the following relation

$$\frac{\partial \boldsymbol{M}}{\partial s} = EI^{(2)}\frac{\partial \kappa^{(2)}}{\partial s}\hat{\boldsymbol{n}}_2. \tag{3.22}$$

From the equilibrium equations (3.19), one can express the internal force as function of the internal moment, by taking the cross product of the momentum balance equation (3.19b) with the material vector $\hat{\boldsymbol{t}}$

$$\begin{aligned} \boldsymbol{F} &= \hat{\boldsymbol{t}} \times \frac{\partial \boldsymbol{M}}{\partial s} + T\hat{\boldsymbol{t}} \\ &= -EI^{(2)}\frac{\partial \kappa^{(2)}}{\partial s}\hat{\boldsymbol{n}}_1 + T\hat{\boldsymbol{t}} \\ &= -EI^{(2)}\frac{\partial^2 \hat{\boldsymbol{t}}}{\partial s^2} + T\hat{\boldsymbol{t}}, \end{aligned} \tag{3.23}$$

where in the first line, T represents the line tension, a Lagrange multiplier that enforces the inextensibility condition (3.16). In the second line, we have substituted the first derivative of

[5] This assumption is valid when the dominant contribution to the fluid flow at the fiber surface is from local translation. Furthermore, the slenderness of the fiber reduces the magnitude of any twisting effect, $\left(\frac{a}{L}\right) \ll 1$.

the internal moment $\partial \boldsymbol{M}/\partial s$ by (3.22). Finally, in the third line, we end up with the expression of $\boldsymbol{F}$ as function of $\hat{\boldsymbol{t}}$, after identifying $(\partial \kappa^{(2)}/\partial s)\hat{\boldsymbol{n}}_1 = \partial^2 \hat{\boldsymbol{t}}/\partial s^2$.
Thus, the force balance equation (3.19a) takes the following form, known as Euler's Elastica model

$$\begin{aligned} \boldsymbol{f} &= -\frac{\partial \boldsymbol{F}}{\partial s} \\ &= EI^{(2)} \frac{\partial^4 \boldsymbol{X}}{\partial s^4} - \frac{\partial}{\partial s}\left(T \frac{\partial \boldsymbol{X}}{\partial s}\right), \end{aligned} \tag{3.24}$$

which relates the linear force density $\boldsymbol{f}(s,t)$ of the external forces, that arise from the surrounding fluid and/or external fields, to the deformed fiber configuration $\boldsymbol{X}(s,t)$ (Xu and Nadim, 1994; Tornberg and Shelley, 2004; Li et al., 2013; Nazockdast et al., 2017; Maxian et al., 2021a).

Note that, the Euler's Elastica model can also be derived by the principle of virtual work, as done for the Kirchhoff equations (see Section 3.2.3.1), by considering the following form of the elastic energy

$$\widetilde{\mathcal{E}} = \underbrace{\int_0^L \left[\frac{EI^{(2)}}{2}\left|\frac{\partial^2 \boldsymbol{X}}{\partial s^2}\right|^2\right] \mathrm{d}s}_{\widetilde{\mathcal{E}}^B} + \underbrace{\int_0^L \left[\frac{T}{2}\left(\frac{\partial \boldsymbol{X}}{\partial s}\cdot \hat{\boldsymbol{t}} - 1\right)^2\right] \mathrm{d}s}_{\widetilde{\mathcal{E}}^S}, \tag{3.25}$$

where the first term on the right hand side is the bending energy, namely $\widetilde{\mathcal{E}}^B$, that arises from (3.3). The second term is the stretching energy, namely $\widetilde{\mathcal{E}}^S$, that is defined in the tangential direction to the centerline, where T is the line tension, as aforementioned. T is a Lagrange multiplier for inextensible fibers (Li et al., 2013) or the stretching modulus for extensible fibers, that is $T = EA$, where E is the Young's modulus and A the area of the cross-section.

3.3 Modelisation and simulation methods

In this section, we describe how to approximately compute the forces exerted on the fiber by the surrounding fluid. Since there is no time derivative in the Stokes equations (2.8), the motion is said to be *quasi-static*. Thus at a given instant, these forces are only determined by the instantaneous velocity and configuration of the fiber. However, analytical expressions of these forces are only possible for specific geometries (Happel and Brenner, 1981). For slender bodies such as fibers, the problem can be tackled analytically and numerically by a continuum approach that exploits the smallness of the aspect-ratio of the fiber to approximate the hydrodynamic forces acting on it, this approach is known as Slender Body Theory (SBT). A numerical alternative to SBT based methods or the continuum approach is to use non-SBT based methods or a discrete approach. In the following, we summarize the two aforementioned approaches, and we refer the reader to Du Roure et al., 2019 and references therein for a more detailed description.

3.3.1 The continuum approach

The slender body theory is an asymptotic approach that relies on a superposition of fundamental solutions to construct solutions for the flow around a moving slender object. This approach was first introduced by Hancock, 1953 and later extended by Batchelor, 1970; Keller and Rubinow, 1976; Johnson, 1980 and Goetz, 2000. The core idea is that the flow produced by a moving fiber arises from distributions of Stokeslest singularities along the fiber centerline. This results in an approximation of hydrodynamic forces acting on the fiber.

On the numerical side, SBT based methods to simulate fibers immersed in Stokes flow have been in use for 20 years. Due to numerical stiffness associated with the inextensibility condition, as well as the treatment of nonlocal interactions, such methods have historically been computationally costly. The most popular and commonly used model is that of Tornberg and Shelley, 2004. In their approach, they derived an auxiliary integro-differential equation for the line tension, that acts as Lagrange multipliers in order to enforce the inextensibility condition. Combined with a stable numerical scheme based on finite differences and implicit time-stepping, this method and its extensions have since allowed the simulations of nonlocal interactions of multiple fibers in an efficient manner (Tornberg and Shelley, 2004; Gustavsson and Tornberg, 2009; Nazockdast et al., 2017). Despite these advances, imposing inextensibility via a tension boundary value problem (BVP) leads to some drawbacks such as the loss of spatial accuracy when using spectral methods (Nazockdast et al., 2017), in addition some penalty terms are still required to preserve inextensibility (Tornberg and Shelley, 2004) due to discretization errors. In order to overcome these hurdles, Maxian et al., 2021a have recently developed an accurate and robust numerical method to handle the inextensibility condition, as well as nonlocal interactions efficiently. Their approach relies on a reformulation of the classical nonlocal SBT in terms of the Rotne-Prager-Yamakawa (RPY) hydrodynamic tensor (Wajnryb et al., 2013; Zuk et al., 2014, see also Section 2.3) to regularize the local drag coefficient for cylindrical fibers, the inextensibility condition is enforced by Lagrange multipliers that are derived from the principle of virtual work, and the fiber evolution is done through a rotation of the tangent vector on a unit sphere. This framework has since been used in applications with actin filaments (Maxian et al., 2021a,b), and extended to account for Brownian motion (Maxian et al., 2023).

3.3.2 The discrete approach

In the discrete approach, the fiber is discretized by a series of marker points that are subject to regularized forces. The numerical method is determined by the type of regularization. For instance, in the immersed boundary method (Peskin, 2002), the forces are regularized by spreading them onto an Eulerian grid on which the fluid problem is solved. Thus, the marker point velocities are obtained by an interpolation of the resulting flow field. When the regularization and interpolation are done through a Gaussian kernel, the method is referred to as a Force Coupling Method (FCM)(Maxey and Patel, 2001), as done by Schoeller et al., 2021. Otherwise, when the regularization and interpolation are done through the surface of a sphere, the method is referred to as a Multibead/Multiblob method (Yamamoto and Matsuoka, 1995; Joung et al., 2001; Gauger and Stark, 2006; Swan et al., 2011; Delmotte et al., 2015; Usabiaga et al., 2016; Schoeller et al., 2021; Balboa Usabiaga and Delmotte, 2022, see also Section 3.4). The marker point velocities are coupled linearly to the forces through the Rotne-Prager-Yamakawa (RPY) hydrodynamic tensor, which is consistent with the low Reynolds number regime. Finally, when the marker point velocities are obtained without an interpolation kernel, through the exact solution to the regularized Stokes equations, the method is referred to as the method of regularized Stokeslets (Cortez, 2001; Cortez et al., 2005; Lim et al., 2008; Olson et al., 2013; Jabbarzadeh and Fu, 2020).

As highlighted for the continuum approach, the discrete approach also suffers from the stiffness associated with the inextensibility condition. For instance, in the bead-spring model (see Section 3.4) which is the model adopted in this thesis, the latter is enforced by prescribing large spring constants between successive beads, thus limiting the use of explicit temporal integrators. Other approaches use Lagrange multipliers instead of springs to effectively tackle the inextensibility condition, such approaches can be broadly separated according to whether they derive from : (i) a velocity-based formulation, meant the constraints are nonholonomic, as done by Delmotte et al., 2015; Balboa Usabiaga and Delmotte, 2022 or (ii) a position-based

formulation, meant the constraints are holonomic, as done by Schoeller et al., 2021. Finally, Jabbarzadeh and Fu, 2020 enforced rigorously the inextensibility condition through a rotation of the tangent vector. In this way, they maintained strict inextensibility of the fiber, without introducing penalty terms. Combined with the method of regularized Stokeslets, this approach has since been used in applications, for instance to investigate the dynamics of a bacteria-inspired rod-like soft robot in a viscous fluid (Bhattacharjee et al., 2022). Though scalable to multiple fibers, discrete approaches require large number of marker points to discretize a single fiber, compared to what would be needed in a continuum approach (Bringley and Peskin, 2008). Recently, hybrid continuum-discrete approaches have been developed in order to overcome the aforementioned drawbacks, as well as the bottleneck arising from the resolution of the elastohydrodynamic problem. For instance, Moreau et al., 2018 developed a coarse-grained elastohydrodynamic framework to alleviate the numerical stiffness. This does not require evaluation of Lagrange multipliers, since the inextensibility condition is satisfied by construction. In addition, their approach requires few number of maker points to discretize the fiber, that allows for faster computations, with increasingly better performance. This numerical framework has since been extended to account for nonlocal interactions of multiple fibers using the method of regularized Stokeslets (Hall-McNair et al., 2019), as well as to account for three-dimensional deformations (Walker et al., 2020).

Despite their limitations, discrete approaches based on regularized singularities are sometimes convenient to work with compared to SBT based methods, since they are nonsingular on the fiber centerline, they can therefore be efficiently evaluated there. Thus, such approaches are more suitable for modeling localized forces such as those due to electrostatics, steric interactions and friction. The latter feature is especially advantageous to capture fiber-obstacle interactions in a computationally efficient manner, which is the main concern of this work. In this thesis, the bead-spring model will be employed for the fiber model, an implicit temporal integrator with an adaptive time-step size will be used to alleviate the numerical stiffness arising from the elastohydrodynamic coupling and the springs. This approach, combined with fast methods to compute the action of the RPY hydrodynamic tensor on the applied forces in quasilinear times, allows for faster and efficient simulations of multiple fibers and obstacles, as we will show in the next sections.

3.4 The bead-spring model

Linear bead-spring models are the most commonly-used coarse-grained approaches to study the dynamics of polymer molecules in solution (Graham, 2018). They display some features, such as the extensibility of the chain that plays an important role to determine the rheological properties of polymers (Bird et al., 1987); and are "constraint-free". The latter makes them particularly efficient for carrying out Brownian dynamics simulations compared to constrained approaches such as bead-rod models, where additional $N_F - 1$ (N_F is the number of beads in the polymer chain) constraints must be satisfied to enforce the inextensibility condition. However, due to their linearity, the time-step must be taken less than the shortest intrinsic oscillating period of the springs to obey the absolute stability restriction when using explicit temporal integrators. Though various non-linear bead-spring models that allow large time step sizes have also been developed for inextensible polymers, such models usually suffer from the singular behavior of stretching forces when approaching the maximum extension (Shaqfeh et al., 2004). One commonly employed alternative that is suitable for "stiff" problems, is to use an implicit temporal integrator based on a backward differentiation formula (BDF). Throughout this thesis, the built-in variable-step, variable-coefficient ODE solver `VODE` (Brown et al., 1989), is used to alleviate the numerical stiffness arising from the springs, as well as from the elastohydrodynamic coupling problem. While not a unique or necessarily superior choice,

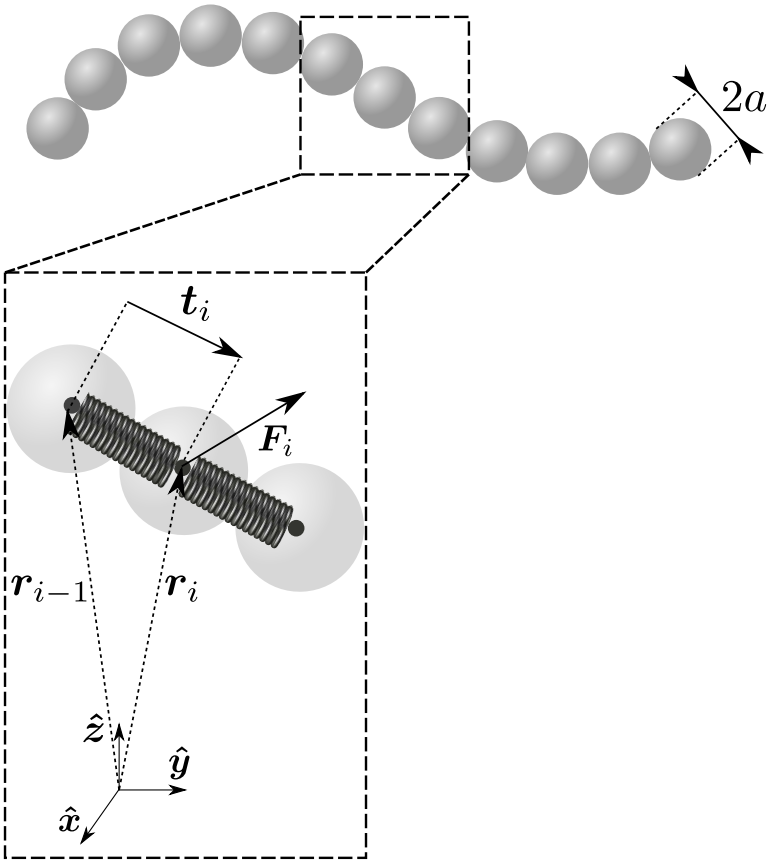

Figure 3.2: The bead-spring model of a flexible fiber. The chain is made of evenly spaced N_F beads of the same radius a that are linked by linear springs, shown in the inset. Each bead is subject to a total force $\boldsymbol{F}_i$ that includes the internal elastic and external forces. $\boldsymbol{t}_i = \boldsymbol{r}_i - \boldsymbol{r}_{i-1}$ is the tangent vector to the centerline of the chain at the bead index $i-1$.

we prefer to use a linear bead-spring model as the discrete approach to simulate the dynamics of flexible fibers that are immersed in Stokes flow, due to the fact that it reduces the number of constraints when handling obstacles in fiber-obstacle coupling problems (see Chapter 4), as well as because of its long history of use in polymer dynamics.

3.4.1 Model

As discussed in Section 3.3, the bead-spring model is one of the most discrete approaches used to model the dynamics of flexible fibers immersed in a viscous fluid. The core idea is to discretize the fiber as a series of evenly spaced N_F marker points $\boldsymbol{r}_i$ (see Fig.3.2) that are subject to internal elastic forces and external forces. These forces are thus regularized over the bead surface via the bead/delta function of width $\sim a$, that is on the order of the fiber radius. Furthermore, in the bead-spring model, two adjacent marker points are connected by stiff linkers made of springs, the tangent vector to the centerline at the position of the marker point $i-1$ is defined as $\boldsymbol{t}_i = \boldsymbol{r}_i - \boldsymbol{r}_{i-1}$(see Fig.3.2). Traditionally, the linkers are extensible in length but do not bend or twist. Since in this thesis we are interested in inextensible fibers, we made linkers inextensible by penalization. The latter is achieved by prescribing spring constants that allow small variations ΔL of the fiber length L, less than 0.35% of its initial length L_0.

3.4.2 Discrete elastic energy and forces

In Section 3.2.3.2, we have defined the elastic energy (3.25) that gives rise to Euler's Elastica model for extensible fibers. The former can be split into two parts, namely the bending and stretching energies, denoted respectively by $\widetilde{\mathcal{E}}^B$ and $\widetilde{\mathcal{E}}^S$,

$$\widetilde{\mathcal{E}} = \widetilde{\mathcal{E}}^B + \widetilde{\mathcal{E}}^S. \tag{3.26}$$

Applying forward differencing to both parts, leads to their respective discrete forms[6],

$$\begin{aligned} \widetilde{\mathcal{E}}^B &= \frac{EI}{2} \sum_{i=2}^{N_F-1} \left(\frac{\hat{\boldsymbol{t}}_i - \hat{\boldsymbol{t}}_{i-1}}{l_0} \right)^2 l_0 \\ &= \frac{EI}{l_0} \sum_{i=2}^{N_F-1} \left(1 - \hat{\boldsymbol{t}}_i \cdot \hat{\boldsymbol{t}}_{i-1} \right), \end{aligned} \tag{3.27}$$

and

$$\begin{aligned} \widetilde{\mathcal{E}}^S &= \frac{EA}{2} \sum_{i=2}^{N_F} \left(\frac{\boldsymbol{r}_i - \boldsymbol{r}_{i-1}}{l_0} \cdot \frac{\boldsymbol{t}_i}{|\boldsymbol{t}_i|} - 1 \right)^2 l_0 \\ &= \frac{EA}{2l_0} \sum_{i=2}^{N_F} \left(|\boldsymbol{t}_i| - l_0 \right)^2, \end{aligned} \tag{3.28}$$

where l_0 is the free length of the spring link. The corresponding forces are obtained by taking the gradient of each part of $\widetilde{\mathcal{E}}$ with respect to the bead positions. Thereby, the bending and stretching forces applied at the bead position $\boldsymbol{r}_i$ are given respectively by

$$\begin{aligned} \boldsymbol{F}_i^B &= -\nabla_{\boldsymbol{r}_i} \widetilde{\mathcal{E}}^B \\ &= \frac{EI}{2} \left[\frac{h_{i-1}}{|\boldsymbol{t}_i|} \hat{\boldsymbol{t}}_{i-1} - \left(\frac{h_{i-1}}{|\boldsymbol{t}_i|} \hat{\boldsymbol{t}}_{i-1} \cdot \hat{\boldsymbol{t}}_i + \frac{h_i}{|\boldsymbol{t}_{i+1}|} + \frac{h_i}{|\boldsymbol{t}_i|} \hat{\boldsymbol{t}}_i \cdot \hat{\boldsymbol{t}}_{i+1} \right) \hat{\boldsymbol{t}}_i \right. \\ &\quad \left. + \left(\frac{h_i}{|\boldsymbol{t}_{i+1}|} \hat{\boldsymbol{t}}_i \cdot \hat{\boldsymbol{t}}_{i+1} + \frac{h_i}{|\boldsymbol{t}_i|} + \frac{h_{i+1}}{|\boldsymbol{t}_{i+1}|} \hat{\boldsymbol{t}}_{i+1} \cdot \hat{\boldsymbol{t}}_{i+2} \right) \hat{\boldsymbol{t}}_{i+1} - \frac{h_{i+1}}{|\boldsymbol{t}_{i+1}|} \hat{\boldsymbol{t}}_{i+2} \right], \end{aligned} \tag{3.29}$$

and

$$\begin{aligned} \boldsymbol{F}_i^S &= -\nabla_{\boldsymbol{r}_i} \widetilde{\mathcal{E}}^S \\ &= \frac{EA}{2l_0} \left[-\left(|\boldsymbol{t}_i| - l_0 \right) h_i' \hat{\boldsymbol{t}}_i + \left(|\boldsymbol{t}_{i+1}| - l_0 \right) h_{i+1}' \hat{\boldsymbol{t}}_{i+1} \right], \end{aligned} \tag{3.30}$$

where following Gauger and Stark, 2006, to derive the explicit forms thereof, we have introduced the factors $(h_i)_{1 \le i \le N_F}$ and $(h_i')_{1 \le i \le N_F}$, that are defined as

$$h_i = \begin{cases} 1 & \text{if} \quad 2 \le i \le N_F - 1, \\ 0 & \text{otherwise}, \end{cases} \tag{3.31}$$

$$h_i' = \begin{cases} 1 & \text{if} \quad 2 \le i \le N_F, \\ 0 & \text{otherwise}, \end{cases} \tag{3.32}$$

[6] We have substituted $\left| \frac{\partial^2 \boldsymbol{X}}{\partial s^2} \right|$ by $\left| \frac{\partial \hat{\boldsymbol{t}}}{\partial s} \right|$ in (3.25) to obtain the first line of (3.27).

3.4.3 Mobility problem

The chain being immersed in a viscous fluid, in the absence of inertia, the fluid velocity $\boldsymbol{u}(\boldsymbol{r})$[7] obeys the Stokes equations forced by regularized point forces $\boldsymbol{F}_j \in \mathbb{R}^3$

$$\begin{cases} -\eta\nabla^2\boldsymbol{u} + \nabla p = \displaystyle\sum_{j=1}^{N_F} \frac{1}{4\pi a_j^2}\boldsymbol{F}_j\, \delta(|\boldsymbol{r}-\boldsymbol{r}_0| - a_j)|_{\boldsymbol{r}_0=\boldsymbol{r}_j}\,, \\ \nabla\cdot\boldsymbol{u} = 0, \end{cases} \tag{3.33}$$

where $\boldsymbol{r}_0$ is the *source point* and $\boldsymbol{r}$ is the *field point*, the distribution $(4\pi a^2)^{-1}\delta(|\boldsymbol{r}-\boldsymbol{r}_0|-a)$ is the regularized spherically-symmetric delta function or *bead function* of width $\sim a$. The forces $\boldsymbol{F} \in \mathbb{R}^{3N_F}$, $\boldsymbol{F} = \boldsymbol{F}^B + \boldsymbol{F}^S + \boldsymbol{F}^E$ that are applied at each source point, account for internal elastic forces derived in the previous section: bending and stretching forces, respectively $\boldsymbol{F}^B$ and $\boldsymbol{F}^S$; and external forces $\boldsymbol{F}^E$ such as gravity and steric interactions.

Due to the linearity of the Stokes equations, the solution $\boldsymbol{u}(\boldsymbol{r})$ to (3.33) is given analytically as a superposition of convolutions over the bead surfaces of the Green's function $\mathbb{G}(\boldsymbol{r},\boldsymbol{r}_0) \in \mathbb{R}^{3\times3}$ with regularized point forces

$$\boldsymbol{u}(\boldsymbol{r}) = \sum_{j=1}^{N_F} \frac{1}{4\pi a_j^2}\int_{S_j} \mathbb{G}(\boldsymbol{r},\boldsymbol{r}_0)\cdot\boldsymbol{F}_j\delta(|\boldsymbol{r}-\boldsymbol{r}_0|-a_j)\mathrm{d}S(\boldsymbol{r}_0), \tag{3.34}$$

where S_j is the surface of bead j.

In the multibead approach, the linear velocity of a given bead $\boldsymbol{U}_i \in \mathbb{R}^3$ is obtained as a convolution over the bead surface S_i, of the fluid velocity $\boldsymbol{u}(\boldsymbol{r})$ with the bead function

$$\boldsymbol{U}_i = \frac{1}{4\pi a_i^2}\int_{S_i} \boldsymbol{u}(\boldsymbol{r})\delta(|\boldsymbol{r}-\boldsymbol{r}_0|-a_i)\mathrm{d}S(\boldsymbol{r}). \tag{3.35}$$

Thus, by substituting (3.34) into (3.35), we obtain the so-called *mobility relation*, which gives the hydrodynamic interactions of a given bead as sum over all other beads

$$\boldsymbol{U}_i = \sum_{j=1}^{N_F} \boldsymbol{\mathcal{M}}_{ij}\cdot\boldsymbol{F}_j, \tag{3.36}$$

where $\boldsymbol{\mathcal{M}}_{ij} \in \mathbb{R}^{3\times3}$ is the widely-used Rotne-Prager-Yamakawa (RPY) tensor (Zuk et al., 2014),

$$\boldsymbol{\mathcal{M}}_{ij} = \frac{1}{4\pi a_i^2}\int_{S_i}\delta(|\boldsymbol{r}-\boldsymbol{r}_0|-a_i)\mathrm{d}S(\boldsymbol{r})\frac{1}{4\pi a_j^2}\int_{S_j}\mathbb{G}(\boldsymbol{r},\boldsymbol{r}_0)\delta(|\boldsymbol{r}-\boldsymbol{r}_0|-a_j)\mathrm{d}S(\boldsymbol{r}_0). \tag{3.37}$$

This formulation is identical to (2.36) for non-overlapping beads, but also gives a symmetric and positive definite (SPD) tensor for overlapping beads as well, and can be used for a collection of beads with different radii. As discussed in Chapter 2, the RPY tensor can be evaluated in different domains. In addition, there are fast methods to compute the action $\boldsymbol{\mathcal{M}}\cdot\boldsymbol{F}$ of the mobility matrix $\boldsymbol{\mathcal{M}} \in \mathbb{R}^{3N_F\times3N_F}$ on the applied forces $\boldsymbol{F} \in \mathbb{R}^{3N_F}$, in quasilinear time in those different domains, such methods include Fast Multipole (Yan and Shelley, 2018; Yan and Blackwell, 2021) and Positively Split Ewald (PSE) (Fiore et al., 2017, see also Appendix A).

[7] The time dependence is omitted for notation convenience.

3.5 Sedimentation of flexible fibers in a quiescent viscous fluid

In this section, we validate our bead-spring model (see Chapter 4, for the implementation details) against known dynamic results for the classical problem of flexible fibers settling under gravity in a quiescent viscous fluid. First, we investigate the deformation for a single fiber in an unbounded domain. Then, the collective dynamics that arise from fiber suspensions in a triply periodic domain are investigated.

3.5.1 Deformation under gravity

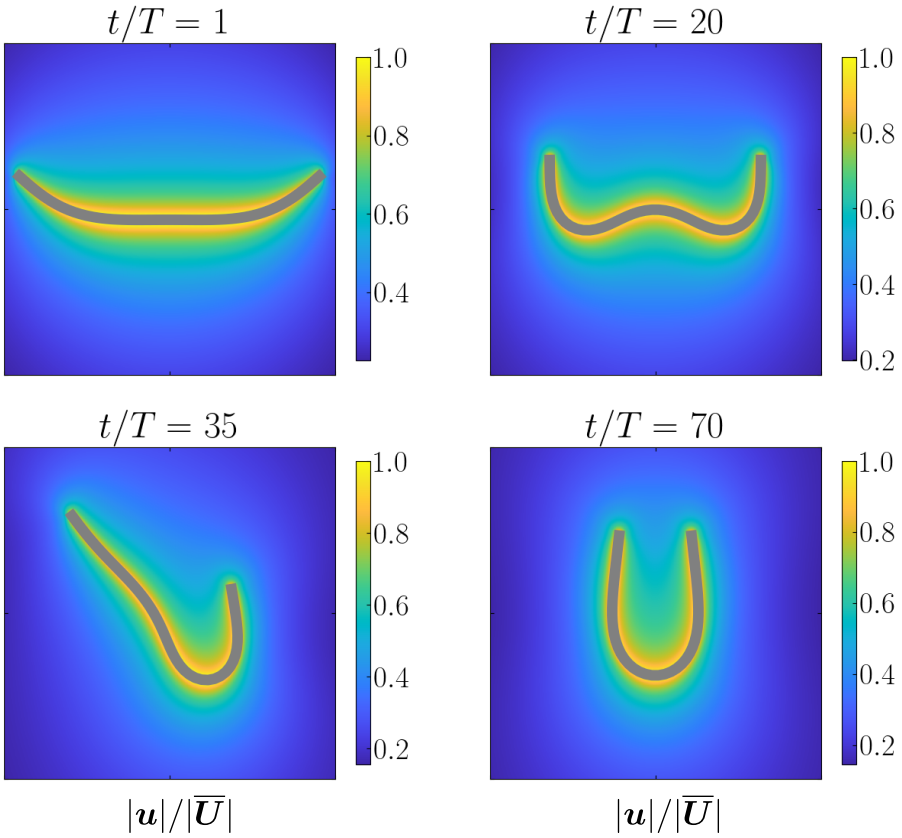

Figure 3.3: Results from numerical simulations showing a single fiber settling in a quiescent viscous fluid for $N_F = 31$ and $Be = 3800$. In each panel, axes are centered with respect to the center of mass of the fiber and normalized by its length. The color bar shows the magnitude of the velocity field normalized by the total velocity of the center of mass of the fiber $|\boldsymbol{u}|/|\overline{\boldsymbol{U}}|$. The fiber first adopts a "W" configuration also known as the metastable state that is shown at $t/T = 20$. Then, due to the inhomogeneous drag distribution along its length, the fiber reorients to reach its equilibrium state after having traveled a finite distance, that is shown at $t/T = 70$ by a "horseshoe" configuration. $T = \eta L^2/F^G$ is the characteristic settling time, defined as the time for the fiber to settle its length.

The deformation of a single flexible fiber settling under gravity in a quiescent viscous fluid has been first investigated theoretically by Xu and Nadim, 1994 for the case of small deformation amplitudes using the slender body theory (SBT), and later numerically using a bead-spring method by Lagomarsino et al., 2005 for both, small and large deformation amplitudes. Their

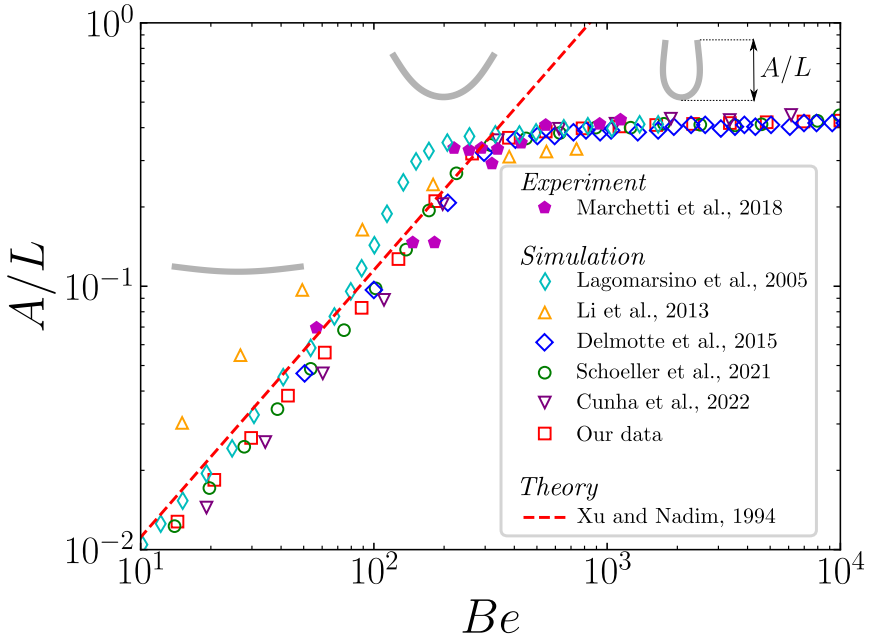

Figure 3.4: Normalized deflection A/L against the elastogravitational number Be. Our findings are compared with experimental (Marchetti et al., 2018), numerical (Lagomarsino et al., 2005; Li et al., 2013; Delmotte et al., 2015; Schoeller et al., 2021; Cunha et al., 2022) and theoretical (Xu and Nadim, 1994) results collected in the literature. The equilibrium shapes of the fiber are shown for small, intermediate and large values of Be. Our data were obtained with a fiber made of $N_F = 31$ beads.

findings were confirmed experimentally (Marchetti et al., 2018), and numerically using multi-bead (Schlagberger and Netz, 2005; Delmotte et al., 2015; Schoeller et al., 2021; Cunha et al., 2022) and SBT-based (Li et al., 2013) methods.

We conduct numerical simulations by considering a single fiber made of $N_F = 31$ beads that are evenly spaced by a distance $l_0 = 2a$. Each bead is subject to a gravitational force $\boldsymbol{F}^{\boldsymbol{G}}/N_F$ and internal elastic forces defined in Section 3.4.2. Initially, the fiber is straight and oriented perpendicularly to the direction of gravity in an unbounded domain. As it settles, the fiber first experiences a time-dependent deformation in response to viscous forces, then reaches an equilibrium state at a constant velocity. In order to characterize its equilibrium shape, we define the elastogravitational number $Be = L^2F^G/EI$, as the balance between gravitational and elastic restoring forces. The evolution of the fiber deformation in time is shown in Fig.3.3 for $Be = 3800$.

Following the previous works found in the literature, we characterize the deformation at equilibrium by measuring the normal deflection A, defined as the distance between the highest and lowest points of the fiber. We compare our numerical results with those collected in the literature, including experimental (Marchetti et al., 2018), numerical (Lagomarsino et al., 2005; Li et al., 2013; Delmotte et al., 2015; Schoeller et al., 2021; Cunha et al., 2022) and theoretical (Xu and Nadim, 1994) results (see Fig.3.4). In the weakly flexible regime ($Be \lesssim 100$), all findings exhibit the same linear growth predicted by Xu and Nadim, 1994. Numerical methods, as well as experimental ones, allow to go beyond the limit of small deflections, though experiments are limited at $Be \approx 1000$. Our "constraint-free" multibead approach agrees well with that of Cunha et al., 2022, as well as with the constrained approaches of Delmotte et al., 2015 and Schoeller et al., 2021, for small and large values of Be. In contrast, we observe discrepancies in the weakly flexible and intermediate ($100 < Be \lesssim 300$) regimes, respectively

with the SBT-based approach of Li et al., 2013, where they made the assumption of a spheroidal fiber instead of a cylindrical one; and with the multibead approach of Lagomarsino et al., 2005, where the hydrodynamic interactions between beads are approximated with point-like particles[8] instead of regularized approximations that account for the finite size of the beads.

3.5.2 Collective dynamics

We now turn to the sedimentation of a large, homogeneous and random distributed suspension of fibers in a triply periodic domain. This problem has been investigated experimentally (Anselmet, 1989; KUMAR and RAMARAO, 1991; Turney et al., 1995; Herzhaft et al., 1996; Herzhaft and Guazzelli, 1999; Metzger et al., 2005, 2007a,b), numerically (Mackaplow and Shaqfeh, 1998; Butler and Shaqfeh, 2002; Saintillan et al., 2005; Gustavsson and Tornberg, 2009; Manikantan and Saintillan, 2016), and theoretically (Koch and Shaqfeh, 1989; Manikantan et al., 2014) over the last years. In the dilute and semi-dilute regimes, most of the studies have reported the formation of floc-like inhomogeneities, i.e., small clusters of fibers, within downward streamers that are balanced by upward (back-flow) streamers of clarified fluid suspension. This leads to an enhancement of the mean settling velocity of the suspension which exceeds the velocity of a single rigid fiber settling along its major axis in an unbounded fluid domain, $U_{\parallel}$. This structural instability has been first reported by Koch and Shaqfeh, 1989. By means of theoretical predictions, they found that the complex coupling between the orientation of the fibers and hydrodynamic interactions leads to the growth of concentration fluctuations in the fiber distribution.

However, despite the various degrees of approximation of the computational studies, that range from the Stokeslet approximation to the widely used slender body theory (SBT), simulations have been found to converge into a single streamer that spans the entire height of the periodic box. This finding disagrees with experimental results (Metzger et al., 2007a), where more than one streamer has been observed[9]. Both, Saintillan et al., 2005 and Gustavsson and Tornberg, 2009 argued that the periodic boundary conditions imposed in the vertical direction of the box are at the origin of this disagreement. Furthermore, most of the numerical studies reported in the literature were carried out in the limit of rigid and weakly flexible fibers ($Be \ll 1$). To our knowledge, only the recent study of Schoeller et al., 2021 goes beyond the limit of weakly flexible fibers, up to $Be = 1000$. However, despite the fact that they captured most of the features reported in the previous studies, their simulations were restricted to a planar distribution of fibers. Here, we consider a suspension of M straight fibers, initially distributed in a triply periodic domain of size $4L \times 4L \times 25L$, where L is the fiber length. Each fiber is made of $N_F = 10$ beads, that are evenly spaced by a distance $l_0 = 2a$, where a is the bead radius. In order to characterize the regime of the suspension, we introduce the effective concentration $nl^3 = 0.5ML/V$, where V is the volume of the periodic box. We perform the simulation for $Be = 100$ and $M = 600$, that corresponds to a dilute regime[10], $nl^3 \approx 0.2$.

Fig.3.5 shows the time-evolution of the fiber distribution while settling under gravity. Qualitatively, most of the features reported in the literature (such as the formation of distinct clusters, the periodic build-up process of clusters, i.e., small clusters merge into larger clusters which later dissolve into small clusters and so on, and the orientation of the fibers toward the direction of gravity) are reproduced by our bead-spring model. In agreement with Saintillan et al., 2005, our model also captures one streamer[11] in the transverse direction of the periodic

[8] Also called the Stokeslet approximation.

[9] By increasing the horizontal dimension (in the x direction) of the periodic box, Saintillan et al., 2005 were able to observe more than one streamer.

[10] The suspension is said to be dilute when $nl^3 < 1$ (Guazzelli and Hinch, 2011).

[11] The streamer is divided into two parts, owing to the periodic boundary conditions.

box, which is composed of distinct clusters in the vertical direction. These findings confirm the adequacy of our model to accurately capture the microstructure of the suspension.

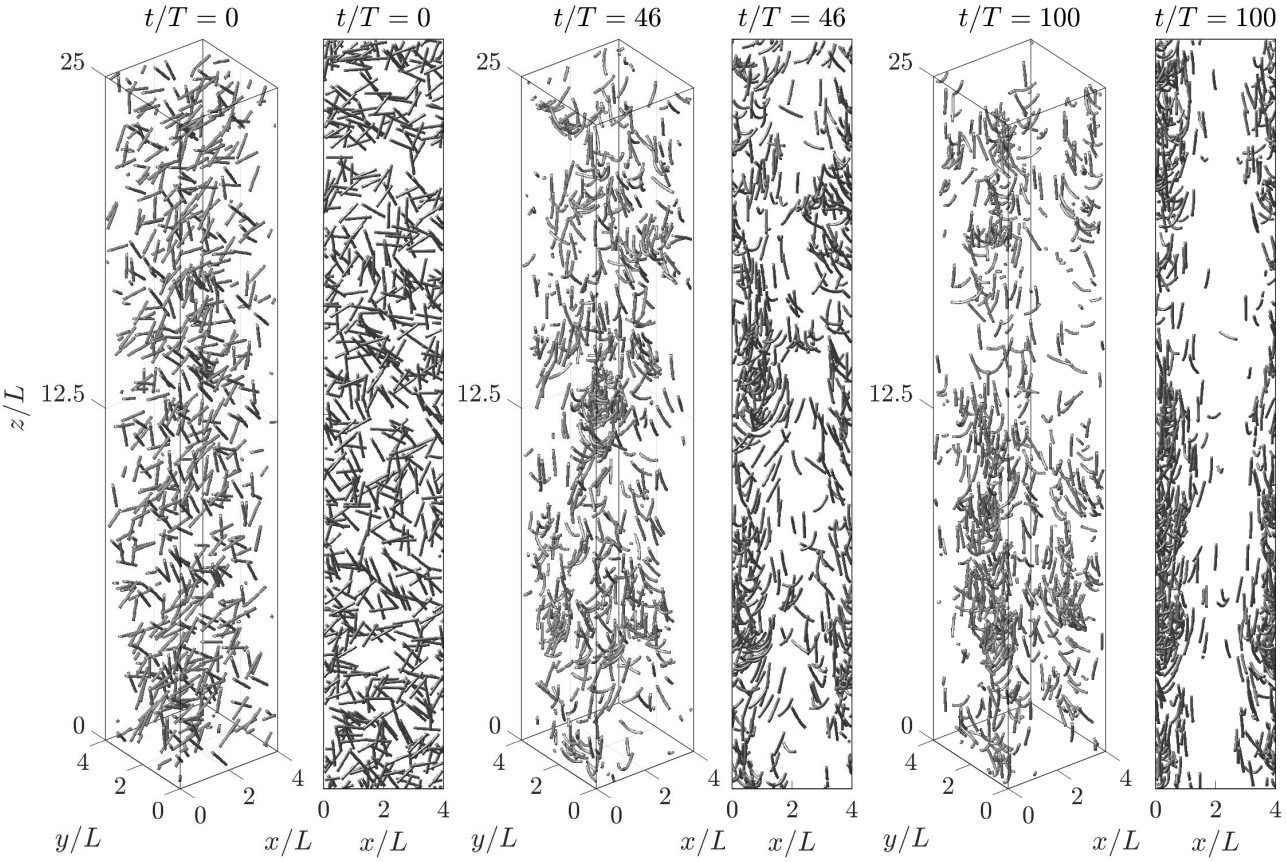

Figure 3.5: Results from numerical simulations showing the time evolution (left to right) of a sedimenting suspension of flexible fibers in a quiescent viscous fluid. The simulation has been performed for a suspension of 600 fibers, where each fiber is made of $N_F = 10$ beads. The regime is dilute with an effective concentration of $nl^3 \approx 0.2$, and the elastogravitational number is set to $Be = 100$ for each fiber.

In order to reproduce the other features, following Gustavsson and Tornberg, 2009, we introduce the mean settling velocity $\overline{w}$ and the mean orientation angle $\overline{\theta}$, that are defined by,

$$\overline{w}(t) = \frac{1}{M}\sum_{m=1}^{M} w_m(t), \tag{3.38}$$

and

$$\overline{\theta}(t) = \frac{1}{M}\sum_{m=1}^{M} \theta_m(t), \tag{3.39}$$

where w_m is the component along the $z-$axis of the center of mass velocity of fiber m, and θ_m the orientation angle between the unit tangent vector at the midpoint of fiber m and the direction of gravity ($\theta_m = \pi/2$, when the fiber is perpendicular to the direction of gravity). Fig.3.6 shows the time evolutions of the two aforementioned quantities. As expected, owing to the formation of clusters, we observe an enhancement of the mean settling velocity of the suspension, which becomes larger that the maximum possible value of a single rigid fiber, Fig.3.6(a). In the case of a sedimenting suspension of rigid fibers, experimental (Herzhaft et al., 1996; Herzhaft and Guazzelli, 1999; Metzger et al., 2007a) and numerical (Butler and Shaqfeh, 2002; Gustavsson and Tornberg, 2009) studies have reported the onset of a steady

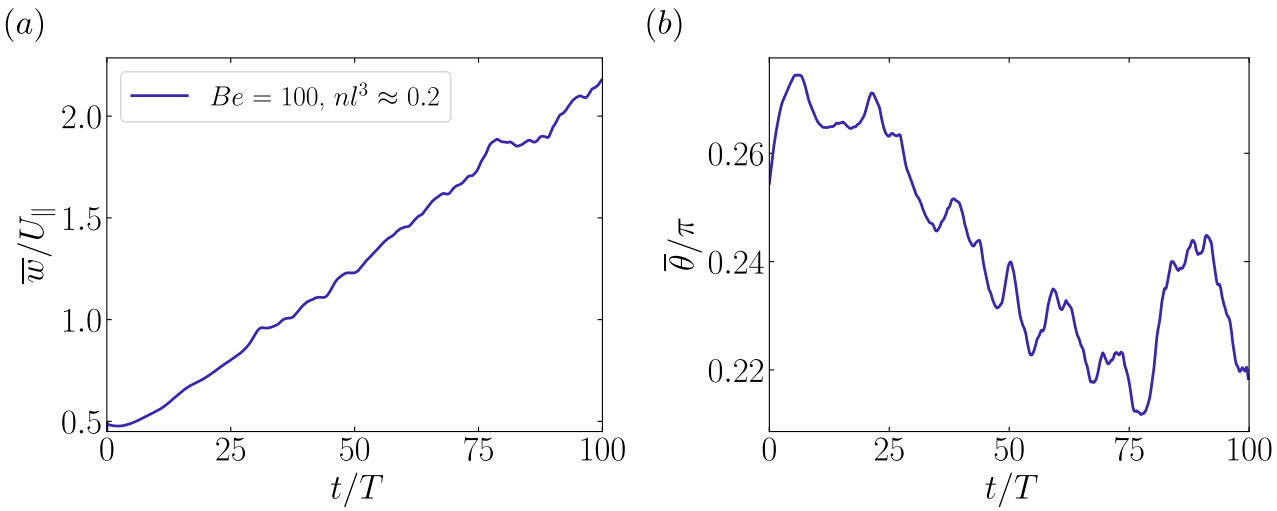

Figure 3.6: Time evolutions of the mean settling velocity of the suspension relative to the maximum velocity of an isolated rigid fiber (a), and the mean orientation of the suspension (b).

state in the mean settling velocity $\overline{w}$, when the rigid fibers tend to align in the direction of gravity with occasional flipping. However, unlike a suspension of rigid fibers, this feature is not captured in our numerical simulations that are carried out for a sedimenting suspension of flexible fibers. This finding agrees with the numerical results reported by Schoeller et al., 2021, where even after $500T$, with T being the characteristic settling time[12], the mean settling velocity continues to grow in time. This discrepancy was attributed to the larger lateral distances that the fibers have to travel in their periodic unit cell, as well as the fact that the fiber dynamics were restricted to two dimensions, in which hydrodynamic interactions are enhanced compared to three dimensions. Conversely, we suspect that this is a result of the reorientation induced by flexibility, which will continuously affect the fiber shapes and lateral displacements, thus their effective drag during the periodic build-up process of clusters, i.e., the clusters continuously capture and lose fibers. Therefore, there is no reason for the instantaneous velocities of different fibers to be statistically identical to instantaneous velocities of a single fiber, as assumed for the rigid case when the fibers are statistically aligned in the direction of gravity (Herzhaft and Guazzelli, 1999). The time evolution of the mean orientation (Fig.3.6(b)) is consistent with our assumption. However, the effect of flexibility on the collective behavior exhibited by a sedimenting suspension of fibers is an open fundamental question that will be tackled in the future.

3.6 Conclusions

In this chapter, we have described the multibead approach used throughout this thesis to carry out dynamic simulations of flexible fibers in Stokes flow. This approach relies on the commonly-used bead-spring model, which is "constraint-free" and suitable for modeling localized forces such as steric interactions and friction, as well as to carry out Brownian simulations. The hydrodynamic interactions are accounted for at the Rotne-Prager-Yamakawa (RPY) level of approximation, and can be evaluated in different geometries. Furthermore, our implementation is flexible and enables dynamic simulations of $\mathcal{O}(10^4)$ beads in reasonable wall times on a single modern Graphics Processing Unit (GPU). In addition, we have shown that our method agrees well with some relevant results collected in the literature, including experimental, numer-

[12]The time for the fiber to settle its own length.

ical and theoretical. Thus confirming, its adequacy to solve accurately the elastohydrodynamic coupling problem.

In various situations in nature and industries, fiber-like particles are transported through complex environments made of obstacles and walls. In such situations, the dynamics of fibers result from the complex coupling between internal elastic stresses, contact forces, and hydrodynamic interactions with the surrounding obstacles and walls. The resulting problem is computationally challenging, owing to the complexity of the coupling and the stiffness of the problem. There is thus a need for a numerical framework to capture fiber-obstacle interactions in a computationally efficient manner. This fundamental problem is tackled in the next chapter.

Chapter 4

A mutlibead approach to handle obstacles in Stokes flow: applications for settling fibers

Contents

In this chapter, we extend the bead-spring method to account for obstacles. We derive a constrained formulation which leads to a linear system, that we solve iteratively with a suitable preconditioner. This numerical framework allows to handle different environments involving rigid stationary obstacles.

4.1 Introduction

Fluid-structure interactions are encountered in numerous situations in biomedical, microfluidics, and environmental applications. Such situations include the locomotion of nanorobots in complex environments (Wu et al., 2020), the transport of biofilm streamers in microfluidic devices (Drescher et al., 2013) and the motion of microplastic fibers in crowded environments (Browne et al., 2011b). All these situations occur at low Reynolds number, and involve stationary and moving boundaries immersed in a fluid. These boundaries may move, deform, interact, and have complex shapes. For instance, biofilm streamers are elastic moving boundaries that can interact with stationary rigid boundaries such as obstacles or walls (Drescher et al., 2013).

Nowadays, there are various numerical approaches to handle immersed stationary and/or moving boundaries in the Stokes regime (Pozrikidis, 1992; Peskin, 2002; Cortez, 2001; Usabiaga

et al., 2016). Among those, the rigid multiblob approach offers a good compromise between flexibility, scalability, efficiency, and accuracy. This approach has been introduced by Usabiaga et al., 2016, and relies on a coarse-grained representation of the boundaries. Each boundary is built as a collection of rigidly-connected blobs that are subject to Lagrange multipliers enforcing the rigidity constraint. This framework and its extensions (Sprinkle et al., 2017; Balboa Usabiaga and Delmotte, 2022) have since been used in applications involving stationary and moving boundaries. For instance, Van Der Wee et al., 2023 used the rigid multiblob approach to simulate the dynamics of microrollers immersed in a viscous fluid with obstacles embedded. Recently, Gidituri et al., 2023 investigated different swimming modes of single-flagellated bacteria inside a circular pipe. A similar constrained formulation has also been proposed by Majmudar et al., 2012, to model the locomotion of *C. elegans* through a structured environment made of stationary rigid spheres. The authors used kinematic constraints to prescribe the velocity of each stationary sphere to zero. In the particular case of immersed elastic boundaries such as inextensible fibers, an additional set of constraints must be satisfied in order to enforce the inextensibility condition (Delmotte et al., 2015; Schoeller et al., 2021). The resulting problem involves two different sets of Lagrange multipliers: (*i*) a set to enforce the stationary condition on the obstacles and (*ii*) a set to enforce the inextensibility condition on the fibers. Thus, such problems are solved for these two types of constraints at each time step (Majmudar et al., 2012), and therefore can be computationally costly for large systems.

In an effort to reduce the number of time-consuming operations, we develop a hybrid approach that builds heavily on the methods proposed by Usabiaga et al., 2016 and Majmudar et al., 2012, to solve problems involving fibers and stationary rigid obstacles in Stokes flow. Our approach relies on the bead-spring method to model the fibers. The latter has the advantage of being "constraint-free", thus reduces the number of constraints in the system, such that only kinematic constraints need to be satisfied. Each obstacle is built as a collection of rigidly connected beads, this multibead representation allows to handle complex obstacle shapes.

This chapter is organized as follows. In Section 4.2, a constrained formulation of the bead-spring method that accounts for obstacles is derived. This formulation leads to a mixed mobility-resistance problem, a linear system to solve for the bead velocities and the Lagrange multipliers that enforce the kinematic constraints. In Section 4.3, a preconditioner is introduced to solve iteratively the mixed mobility-resistance problem, and its effectiveness is evaluated through two test problems. Finally, in Section 4.4, we explore three problems of sedimentation involving fibers and obstacles. In doing so, we show that our numerical framework is an efficient, scalable and flexible tool for studying a variety of problems that involve fiber-obstacle interactions in Stokes flow.

4.2 Constrained formulation to account for obstacles

In this section, we extend the unconstrained problem derived for flexible fibers in the previous chapter, to account for obstacles. In the following, the obstacle is made of N_O rigidly-connected beads, instead of springs as done for the fiber (see Section 3.4). For the sake of simplicity, we will consider the system $\{Fiber + Obstacle\}$ as monodispere, in which all the beads have the same hydrodynamic radius a. However, the extension to the polydisperse case is done by using the suitable RPY tensor (Zuk et al., 2014). We denote by $N = N_F + N_O$ the total number of beads in the system, by $\boldsymbol{\mathcal{M}} \in \mathbb{R}^{3N\times 3N}$ their mobility matrix, and by $\boldsymbol{U} = [\boldsymbol{U}_1, \dots, \boldsymbol{U}_{N_F}, \boldsymbol{U}_{N_F+1}, \dots \boldsymbol{U}_N] \in \mathbb{R}^{3N}$, $\boldsymbol{R} = [\boldsymbol{r}_1, \dots, \boldsymbol{r}_{N_F}, \boldsymbol{r}_{N_F+1}, \dots \boldsymbol{r}_N] \in \mathbb{R}^{3N}$ and $\boldsymbol{F} = [\boldsymbol{F}_1, \dots, \boldsymbol{F}_{N_F}, \boldsymbol{F}_{N_F+1}, \dots \boldsymbol{F}_N] \in \mathbb{R}^{3N}$, the vectors collecting respectively their linear velocities, positions and the forces that are exerted on each of them.

4.2.1 Kinematic constraints: velocity-based formulation

Our goal is to prescribe the motion of the obstacle beads, to ensure they have zero degrees of freedom (DOF). This restriction implies the following kinematic constraint equation at the velocity level

$$\boldsymbol{\Phi}(\boldsymbol{U}) \equiv \boldsymbol{\mathcal{J}} \cdot \boldsymbol{U} = \boldsymbol{0}, \tag{4.1}$$

where $\boldsymbol{\Phi} \in \mathbb{R}^{3N_O}$ denotes the set of constraints in the system, and the matrix $\boldsymbol{\mathcal{J}} \in \mathbb{R}^{3N_O \times 3N}$ maps $\mathbb{R}^{3N}$ onto $\mathbb{R}^{3N_O}$. In other words, $\boldsymbol{\mathcal{J}}$ will select the obstacle beads to prescribe their velocities to zero. It can be constructed by blocks of 3×3 sub-matrices, such that

$$\boldsymbol{\mathcal{J}}_{lk} = \begin{cases} \boldsymbol{I} & \text{for} \quad k = N_F + l \\ \boldsymbol{0} & \text{otherwise} \end{cases}, \tag{4.2}$$

where $1 \leq l \leq N_O$ and $1 \leq k \leq N$, $\boldsymbol{I} \in \mathbb{R}^{3\times 3}$ is an identity matrix.

From classical mechanics, it is well known that linear nonholonomic constraints (4.1), i.e., linear velocity-dependent constraints, give rise to constraint forces $\boldsymbol{F}^C \in \mathbb{R}^{3N}$ of the form

$$\boldsymbol{F}^C = \boldsymbol{\mathcal{J}}^T \cdot \boldsymbol{\lambda}. \tag{4.3}$$

This follows from the principle of virtual work, since the constraint forces are workless (Lanczos, 1986). The $3N_O \times 3N$ matrix $\boldsymbol{\mathcal{J}} \equiv \partial\boldsymbol{\Phi}/\partial\boldsymbol{U}$ is the constraint Jacobian, and $\boldsymbol{\lambda} \in \mathbb{R}^{3N_O}$ is a vector of Lagrange multipliers, which collects forces that are exerted on the obstacle beads to satisfy the kinematic constraints (4.1).

4.2.2 Mixed mobility-resistance problem

Due to the linearity of the Stokes equations, the solution to the constrained problem arises from the solution to the unconstrained problem $\widehat{\boldsymbol{U}} = \boldsymbol{\mathcal{M}} \cdot \boldsymbol{F} \in \mathbb{R}^{3N}$ corrected by the particle motion $\overline{\boldsymbol{U}} = \boldsymbol{\mathcal{M}} \cdot \boldsymbol{F}^C \in \mathbb{R}^{3N}$ induced by the constraint forces that are exerted on the obstacle beads. Accordingly, the constrained problem is a superposition of the two aforementioned sub-problems,

$$\begin{aligned} \boldsymbol{U} &= \widehat{\boldsymbol{U}} + \overline{\boldsymbol{U}} \\ &= \boldsymbol{\mathcal{M}} \cdot \boldsymbol{F} + \boldsymbol{\mathcal{M}} \cdot \boldsymbol{F}^C \\ &= \boldsymbol{\mathcal{M}} \cdot \boldsymbol{F} + \boldsymbol{\mathcal{M}} \cdot \boldsymbol{\mathcal{J}}^T \cdot \boldsymbol{\lambda}, \end{aligned} \tag{4.4}$$

where in the third line of (4.4), we have substituted the constraint forces $\boldsymbol{F}^C$ by (4.3). This results in a *mixed mobility-resistance problem*, as the Lagrange multipliers $\boldsymbol{\lambda}$ and the velocity of the beads $\boldsymbol{U}$ are both unknowns. This formulation is closed by the kinematic constraint equation (4.1), as defined in Section 4.2.1.

We can write the equations (4.4) and (4.1) in a compact matrix notation as a linear system to solve for the two aforementioned unknowns,

$$\underbrace{\begin{bmatrix} -\boldsymbol{\mathcal{M}} \cdot \boldsymbol{\mathcal{J}}^T & \boldsymbol{I} \\ \boldsymbol{0} & \boldsymbol{\mathcal{J}} \end{bmatrix}}_{\boldsymbol{\mathcal{A}}} \cdot \underbrace{\begin{bmatrix} \boldsymbol{\lambda} \\ \boldsymbol{U} \end{bmatrix}}_{\boldsymbol{x}} = \underbrace{\begin{bmatrix} \boldsymbol{\mathcal{M}} \cdot \boldsymbol{F} \\ \boldsymbol{0} \end{bmatrix}}_{\boldsymbol{b}}, \tag{4.5}$$

where $\boldsymbol{I} \in \mathbb{R}^{3N\times 3N}$ is an identity matrix. It is straightforward to eliminate the Lagrange multipliers $\boldsymbol{\lambda}$ in the above system, in order to derive a constrained mobility problem, i.e., with

the velocity $\boldsymbol{U}$ as the only unknown,

$$\begin{aligned}\frac{\mathrm{d}\boldsymbol{R}}{\mathrm{d}t} &\equiv \boldsymbol{U} \\ &= \left[\boldsymbol{I} - \boldsymbol{\mathcal{M}} \cdot \boldsymbol{\mathcal{J}}^T \cdot \boldsymbol{\mathcal{M}}_{OO}^{-1} \cdot \boldsymbol{\mathcal{J}}\right] \cdot \boldsymbol{\mathcal{M}} \cdot \boldsymbol{F} \\ &= \boldsymbol{\mathcal{P}} \cdot \widehat{\boldsymbol{U}} \\ &= \boldsymbol{\mathcal{N}} \cdot \boldsymbol{F},\end{aligned} \tag{4.6}$$

where in the second line of (4.6), $\boldsymbol{I} \in \mathbb{R}^{3N\times 3N}$ is an identity matrix and $\boldsymbol{\mathcal{M}}_{OO} = \left[\boldsymbol{\mathcal{J}} \cdot \boldsymbol{\mathcal{M}} \cdot \boldsymbol{\mathcal{J}}^T\right] \in \mathbb{R}^{3N_O\times 3N_O}$ is the mobility matrix between the obstacle beads. In the third line, $\boldsymbol{\mathcal{P}} = \left[\boldsymbol{I} - \boldsymbol{\mathcal{M}} \cdot \boldsymbol{\mathcal{J}}^T \cdot \boldsymbol{\mathcal{M}}_{OO}^{-1} \cdot \boldsymbol{\mathcal{J}}\right] \in \mathbb{R}^{3N\times 3N}$ is a projector, i.e., $\boldsymbol{\mathcal{P}}^2 = \boldsymbol{\mathcal{P}}$, which maps the unconstrained solution $\widehat{\boldsymbol{U}} = \boldsymbol{\mathcal{M}} \cdot \boldsymbol{F} \in \mathbb{R}^{3N}$ onto the constraint space $\mathbb{C} = \{\boldsymbol{U} \in \mathbb{R}^{3N} \mid \boldsymbol{\mathcal{J}} \cdot \boldsymbol{U} = \boldsymbol{0}\}$. Finally, the fourth line shows the action of the constraint mobility matrix $\boldsymbol{\mathcal{N}} = \boldsymbol{\mathcal{P}} \cdot \boldsymbol{\mathcal{M}} \in \mathbb{R}^{3N\times 3N}$ on the applied forces $\boldsymbol{F}$.

At first sight, it might seem easier to solve the constrained mobility problem (4.6) as done in Chapter 5 (see also the corresponding paper (Makanga et al., 2023)), instead of solving the mixed mobility-resistance problem (4.5), since one has to solve the former for $3N$ unknowns and the latter for $3N_O + 3N$. In fact, the former is attractive for small systems and if the constraint mobility matrix $\boldsymbol{\mathcal{N}}$ can be formed efficiently. The main disadvantage is that numerical instabilities may be a concern when forming $\boldsymbol{\mathcal{N}}$, especially when the mobility matrix $\boldsymbol{\mathcal{M}}_{OO}$ is ill-conditioned.

In contrast, we found that solving the mixed mobility-resistance problem (4.5) for $3N_O+3N$ unknowns, namely $(\boldsymbol{\lambda}, \boldsymbol{U})$, iteratively, using a preconditioned GMRES method, is more suitable numerically for large systems of fibers and obstacles. As a matter of fact, such approach has a computational complexity that is quadratic in the number of beads N, compared to direct methods which scale as $\mathcal{O}(N^3)$. This efficiency is mainly due to the modest number of iterations required to solve (4.5) when an appropriate preconditioner is used, as described in the next section.

4.3 Iterative solver and convergence

In this section, we solve the mixed mobility-resistance problem (4.5) iteratively, using a preconditioned GMRES method. Given the linear system $\boldsymbol{\mathcal{A}} \cdot \boldsymbol{x} = \boldsymbol{b}$, the idea behind this approach is to project this $3N$-dimensional problem onto a lower-dimensional Krylov subspace using matrix-vector products, without requiring the computation of the inverse matrix $\boldsymbol{\mathcal{A}}^{-1}$. However, due to the long-ranged nature of the hydrodynamic interactions, the condition number of $\boldsymbol{\mathcal{A}}$ will increase with the number of beads and volume fraction (e.g., large and/or concentrated systems or complex media), therefore will slow down the convergence of the iterative solver by increasing the number of iterations. This can be overcome by applying a suitable preocnditioner to (4.5). The idea of preconditioning (4.5) is the following, if $\boldsymbol{\mathcal{Q}}$ is a given non-singular $3N \times 3N$ matrix, then the linear system $\boldsymbol{\mathcal{Q}}^{-1} \cdot \boldsymbol{\mathcal{A}} \cdot \boldsymbol{x} = \boldsymbol{\mathcal{Q}}^{-1} \cdot \boldsymbol{b}$ has the same solution. If the preconditioner $\boldsymbol{\mathcal{Q}}$ is well chosen to improve the properties of $\boldsymbol{\mathcal{Q}}^{-1} \cdot \boldsymbol{\mathcal{A}}$, the new preconditioned linear system may converge quickly with a few number of iterations. Two conditions are required to set a good preconditioner: firstly it must be close to $\boldsymbol{\mathcal{A}}$, such that the eigenvalues of $\boldsymbol{\mathcal{Q}}^{-1} \cdot \boldsymbol{\mathcal{A}}$ are close to unity and $\|\boldsymbol{\mathcal{Q}}^{-1} \cdot \boldsymbol{\mathcal{A}} - \boldsymbol{I}\|_2$ is small, where $\|\cdot\|_2$ is the spectral norm and $\boldsymbol{I} \in \mathbb{R}^{3N\times 3N}$ is an identity matrix. Secondly, the preconditioner matrix must require a few number of operations to be computed.

In the following, we introduce the preconditioner that we use to solve the mixed mobility-resistance problem (4.5). Then we evaluate its effectiveness on two test problems.

4.3.1 Preconditioner

The bead mobility matrix $\boldsymbol{\mathcal{M}}$ can be decomposed into four blocks,

$$\boldsymbol{\mathcal{M}} = \begin{bmatrix} \boldsymbol{\mathcal{M}}_{FF} & \boldsymbol{\mathcal{M}}_{FO} \\ \boldsymbol{\mathcal{M}}_{OF} & \boldsymbol{\mathcal{M}}_{OO} \end{bmatrix}, \tag{4.7}$$

where F and O stand for *Fibers* and *Obstacles*, respectively. Accordingly, each block encodes hydrodynamic interactions between the subscripted bodies. Note that, the block $\boldsymbol{\mathcal{M}}_{OO}$ is the mobility matrix between the obstacle beads defined in Section 4.2.2.

Since the Lagrange multipliers $\boldsymbol{\lambda}$ apply just on the obstacle beads, a suitable preconditioner matrix for the linear system (4.5) is obtained by setting the three blocks $\boldsymbol{\mathcal{M}}_{FF}$, $\boldsymbol{\mathcal{M}}_{FO}$ and $\boldsymbol{\mathcal{M}}_{OF}$ as null matrices and neglecting hydrodynamic interactions between different obstacles, i.e., setting the elements of $\boldsymbol{\mathcal{M}}_{OO}$ corresponding to pairs of beads on distinct obstacles to zero, as done by Usabiaga et al., 2016; Balboa Usabiaga and Delmotte, 2022. This results in a sparse matrix $\widetilde{\boldsymbol{\mathcal{M}}}$ and a block-diagonal approximation $\widetilde{\boldsymbol{\mathcal{M}}}_{OO}$ for $\boldsymbol{\mathcal{M}}_{OO}$,

$$\widetilde{\boldsymbol{\mathcal{M}}}_{OO}^{(pq)} = \delta_{pq} \boldsymbol{\mathcal{M}}_{OO}^{(pp)}, \tag{4.8}$$

where p and q are two distinct bodies defined as *obstacles*, and δ_{pq} is the Kronecker delta.

Accordingly, applying the preconditioner matrix to (4.5) amounts to solving the following linear system

$$\begin{bmatrix} -\widetilde{\boldsymbol{\mathcal{M}}} \cdot \boldsymbol{\mathcal{J}}^T & \boldsymbol{I} \\ \boldsymbol{0} & \boldsymbol{\mathcal{J}} \end{bmatrix} \cdot \begin{bmatrix} \boldsymbol{\lambda} \\ \boldsymbol{U} \end{bmatrix} = \begin{bmatrix} \boldsymbol{\mathcal{M}} \cdot \boldsymbol{F} \\ \boldsymbol{0} \end{bmatrix}. \tag{4.9}$$

The corresponding approximation of the constraint mobility matrix is $\widetilde{\boldsymbol{\mathcal{N}}} = \widetilde{\boldsymbol{\mathcal{P}}} \cdot \boldsymbol{\mathcal{M}}$, where the projector $\widetilde{\boldsymbol{\mathcal{P}}}$ is a block-diagonal matrix, which each block refers to an identity matrix for each body defined as *fiber* and to a sub-matrix neglecting all hydrodynamic interactions with the other bodies for each body defined as *obstacle*

$$\widetilde{\boldsymbol{\mathcal{P}}}^{(pq)} = \begin{cases} \delta_{pq} \boldsymbol{I}^{(p)} & \text{for fibers} \\ \delta_{pq} \left[\boldsymbol{I}^{(p)} - \boldsymbol{\mathcal{M}}^{(pp)} \cdot \left(\boldsymbol{\mathcal{J}}^{(p)} \right)^T \cdot \left(\boldsymbol{\mathcal{M}}_{OO}^{(pp)} \right)^{-1} \cdot \boldsymbol{\mathcal{J}}^{(p)} \right] & \text{for obstacles} \end{cases}. \tag{4.10}$$

The construction of $\widetilde{\boldsymbol{\mathcal{P}}}$ requires the computation of both $\widetilde{\boldsymbol{\mathcal{M}}}_{OO}$ and its inverse $\widetilde{\boldsymbol{\mathcal{M}}}_{OO}^{-1}$, which depend on the boundaries of the domain. We compute the latter by Cholesky factorization and iteratively, respectively in unbounded and periodic domains. Since the obstacles are not moving over time, $\widetilde{\boldsymbol{\mathcal{M}}}_{OO}$ and its inverse never change. Therefore, both are precomputed once before the time loop and reused during the simulation.

4.3.2 Convergence

In the following, we test the robustness of our preconditioner with respect to the number of obstacle beads N_O. We consider two types of tests, that are similar to the study carried out in Chapter 5 (see also the corresponding paper (Makanga et al., 2023)). Where we investigated the sedimentation of a single flexible fiber of length L against a rigid obstacle of width ω in a quiescent viscous fluid. The fiber is discretized as a series of N_F beads connected by springs and subject to a constant weight per unit length, as described in Section 3.4. The obstacle has a different shape for each test:

1. Cylindrical shape of depth D_O (see Fig.4.1(i)), built with a hexagonal close-packing arrangement of rings, where each ring is discretized as a series of 20 rigidly connected beads so that the number of obstacle beads is given as $N_O = 20 N_{\text{rings}}$, where N_{rings} is the number of rings.

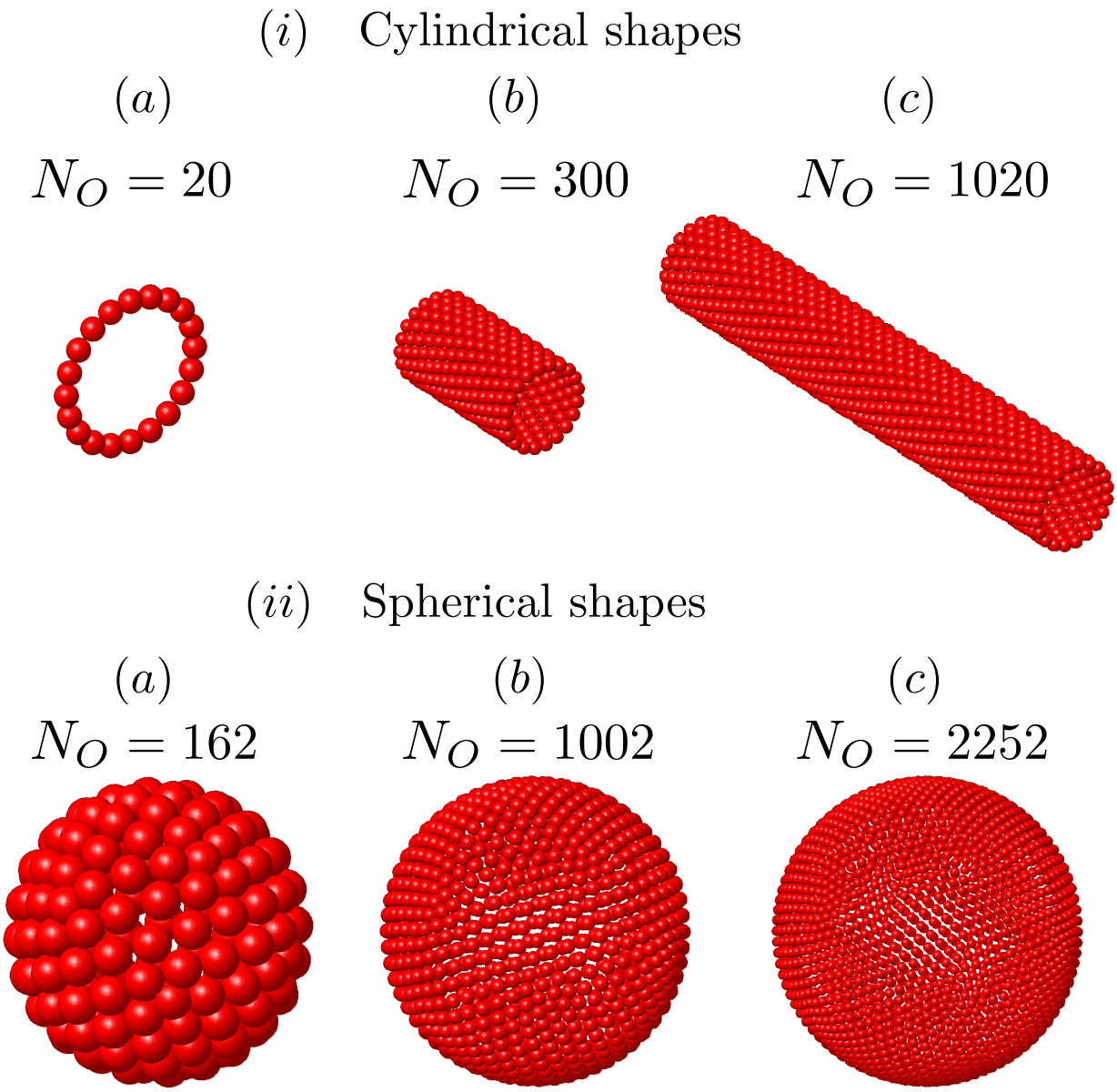

Figure 4.1: Multibead models of obstacles used to evaluate the effectiveness of our preconditioner. Each obstacle is made of N_O beads. (i) Cylindrical obstacles of different depths. (ii) Spherical obstacles of different resolutions.

2. Spherical shape (see Fig.4.1(ii)), built as a rigid geodesic polyhedron with icosahedral symmetry made of N_O beads sitting on the nodes of the different geodesic grids.

Initially, the fiber midpoint is positioned at a given horizontal ($Dx/L = 0.05$) and vertical ($Dz/L = 4$) distance from the obstacle center of mass. The tests are investigated in an unbounded domain for $Be = 1000$, $L/\omega = 3.1$ and 1.5 respectively for cylindrical and spherical obstacles. The simulations are performed with right preconditioned GMRES of residual tolerance $\varepsilon = 10^{-8}$, using the implementation described in Section 4.4.

We evaluate the performance of the preconditioned GMRES solver for two different approximations of the mobility matrix $\boldsymbol{\mathcal{M}}_{OO}$, the first one (Fig.4.2, dashed lines) neglects hydrodynamic interactions between obstacle beads, i.e., the elements of $\boldsymbol{\mathcal{M}}_{OO}$ corresponding to pair interactions are null; and the second approximation of $\boldsymbol{\mathcal{M}}_{OO}$ (Fig.4.2, solid lines) does not.

First, we test the robustness for cylindrical obstacles with increasing N_O (i.e., the obstacle depth D_O). The panels $(a) - (c)$ of Fig.4.2 show that the iterative solver converges within

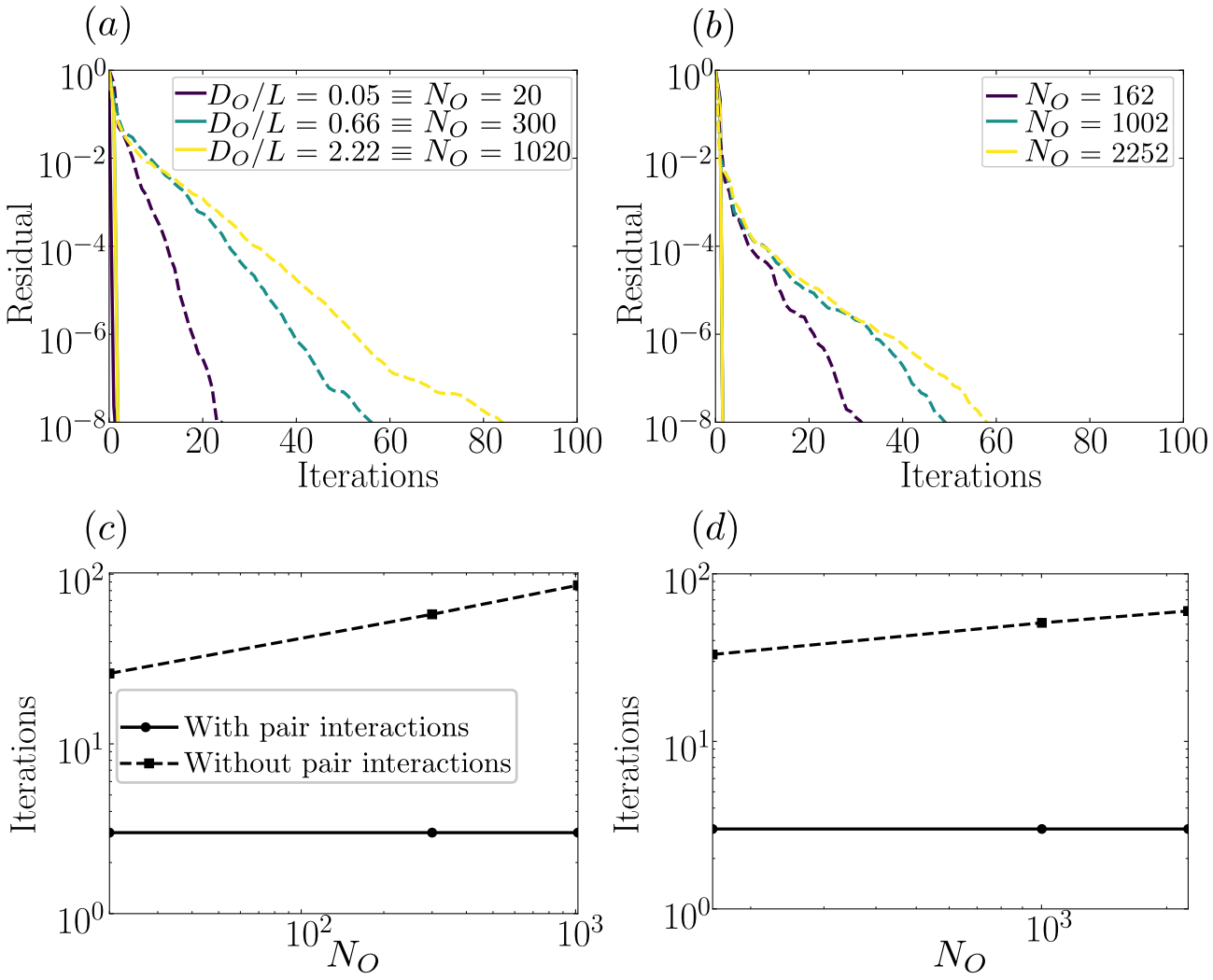

Figure 4.2: Linear solver convergence for different number of obstacle beads, N_O, of the two types of obstacle shapes: cylindrical [panels (a) and (c)] and spherical [panels (b) and (d)]. The different values of N_O correspond respectively to different depths for cylindrical shapes and different resolutions for spherical shapes. Panels (c) and (d) show the number of iterations required to reach a tolerance $\varepsilon = 10^{-8}$. The dashed lines correspond to identical models which do not account for pairwise hydrodynamic interactions to form $\boldsymbol{\mathcal{M}}_{OO}$.

3 iterations independently of the number of obstacle beads N_O when considering pair interactions. Without pair interactions, the preconditioner performance is expected to deteriorate with increasing N_O as the obstacle beads are relatively close to no longer neglect hydrodynamic interactions between neighbouring beads to form $\boldsymbol{\mathcal{M}}_{OO}$. Figure 4.2 (a) shows that without pair interactions, the number of iterations to reach the GMRES residual tolerance ($\varepsilon = 10^{-8}$) depends strongly on the number of obstacle beads. However, even though the number of iterations scales logarithmically with N_O, as shown in Fig.4.2(c), our preconditioner should not be formed by neglecting pairwise hydrodynamic interactions between beads that belong to the same obstacle, since it does not improve significantly the properties of the iterative matrix $\boldsymbol{\mathcal{A}}$ (4.5).

Next, we test the robustness for spherical obstacles with increasing N_O. Figure 4.2 (b) shows the convergence rate with (solid lines) and without (dashed lines) pair interactions. As in the case of cylindrical shapes, the iterative solver converges within 3 iterations independently of the number of obstacle beads N_O. Without pair interactions, the number of iterations also scales logarithmically with N_O (see Fig.4.2(d), dashed line).

Accordingly, the aforementioned results demonstrate the effectiveness of our preconditioner to solve the mixed mobility-resistance problem (4.5). The main feature of our preconditioner seems to be its ability to improve significantly the properties of the iterative matrix $\boldsymbol{\mathcal{A}}$ such that the rate of convergence becomes independent of the obstacle shape and the number of obstacle beads.

4.4 Implementations and simulations

In this section, we apply the numerical framework described above to problems involving fibers and obstacles that are immersed in a quiescent viscous fluid. In all simulations presented here, the fibers are driven by gravity and the obstacles are rigid and stationary.

4.4.1 Implementations

The code used to perform simulations throughout this thesis is written in Python. Time-consuming operations such as matrix-vector products, are implemented on a Graphics Processing Unit (GPU) using PyCUDA.

As mentioned earlier, the cost of each GMRES iteration while solving the deterministic mixed mobility-resistance problem (4.5) will be related to the action $\boldsymbol{\mathcal{M}} \cdot (\bullet)$ of the mobility matrix on a given vector. The computation of the latter depends on the geometry of the domain and the construction of $\boldsymbol{\mathcal{M}}$. In what follow, we perform simulations in two kinds of geometry: unbounded and triply periodic domains. For unbounded domains, we use a GPU implementation based on a direct summation of $\boldsymbol{\mathcal{M}} \cdot (\bullet)$ (Usabiaga et al., 2016), where $\boldsymbol{\mathcal{M}}$ is based on the free-space Green's function for Stokes flow (2.46). This implementation scales as $\mathcal{O}(N^2)$, however thanks to their large number of threads, this computation is relatively fast on modern GPUs, allowing large number of beads to be handled with a low computational cost. For triply periodic domains, we use a GPU implementation of the Positively-Split-Ewald (PSE) method (Fiore et al., 2017; Pérez Peláez, 2022) based on the periodic Green's function for Stokes flow (Hasimoto, 1959). The PSE method is briefly described in Appendix A.

4.4.2 Simulations

4.4.2.1 Sedimenting a fiber square against an obstacle

At low Reynolds number, the sedimentation of a finite number of fiber-like particles that are in an initially symmetric configuration, has been investigated experimentally (Jung et al., 2006), numerically (Claeys and Brady, 1993; Llopis et al., 2007; Gustavsson and Tornberg, 2009; Saggiorato et al., 2015; Bukowicki and L. Ekiel-Jeżewska, 2019; Hall-McNair et al., 2019; Schoeller et al., 2021) and theoretically (Wakiya, 1965; Kim, 1985). Most of the studies have reported the periodic tumbling-like motion exhibited by rigid and semi-flexible particles, as well as in the case of flexible fibers, the onset of chaotic or more complex dynamics that arise in the long term. Here, we investigate how the presence of a rigid obstacle can affect the dynamics described above.

Following Schoeller et al., 2021, we consider four fibers evenly distributed at the corners of a horizontal square of side length relative to fiber length, $d/L = 0.268$. Each fiber is made of $N_F = 20$ beads that are evenly spaced by a distance $l_0 = 2.2a$, where a is the bead radius. The obstacle is a rigid cylindrical tube of width $\omega/d \approx 1$ and depth $D_O/d = \sqrt{2}$ (Fig.4.1(i)) that is made of $N_O = 200$ beads of radius a. Initially, the center of mass of the fiber configuration is aligned and positioned vertically at $D_z/L \approx 40$ with respect to the obstacle center of mass.

One quantity of interest to characterize the dynamics is the mean settling velocity, $\overline{U}(t)$, which we define as follows

$$\overline{U}(t) = \frac{1}{4}\sum_{m=1}^{4} U_m(t) \tag{4.11}$$

where U_m is the center of mass velocity of fiber m. We perform simulations in an unbounded domain for various values of the elastogravitational number Be ($10 \leq Be \leq 1000$).

When settling toward the obstacle, most of the features (e.g., the tumbling orbits for $Be = 10$ and $Be = 100$, the repulsion and convergence toward a stationary state for $Be = 1000$) reported in the literature (Bukowicki and L. Ekiel-Jeżewska, 2019; Schoeller et al., 2021) are observed in our simulations (Fig.4.3(a)). During the collision with the obstacle, the fiber configuration is disturbed, the distance between the fibers increases (Fig.4.3(b), panels (i)). This perturbation is reflected by a decrease in the mean settling velocity, its minimum value is lower than the one attained by an identical sedimenting configuration without the obstacle (Fig.4.3(b), panels (ii)). Downstream the obstacle, for $Be = 10$ and $Be = 100$, at early times the dynamics are similar to those observed upstream, then become unstable, we observe the onset of complex dynamics. However, at very long times, the mean settling velocity displays a steady state, in which the instantaneous fiber configuration is such that three fibers form a bundle that settles faster than the fourth fiber that is left behind (Fig.4.3(c)). Finally, for $Be = 1000$, the collective behavior is found to converge toward a stable state.

4.4.2.2 Obstacle-induced separation of a fiber pair

In this study, we discuss the effect of an array of obstacles on a sedimenting pair of flexible fibers. Our goal here is to illustrate the flexibility of our numerical approach rather than a detailed investigation of the problem. In the following, we consider a pair of fibers of identical length L and different flexibilities such that their elastogravitational numbers are $Be = 10$ and $Be = 100$. Each fiber is made of $N_F = 15$ beads of radius a. The array is immersed in a quiescent viscous fluid, and is made of rigid cylindrical pillars (Fig.4.1(i)) of infinite depth, that are arranged in a hexagonal lattice. The fibers are initially straight, oriented perpendicularly to the direction of gravity. Initially, the fibers are well separated along their minor axis by a distance $D = |\overline{\boldsymbol{r}}^{(1)} - \overline{\boldsymbol{r}}^{(2)}| = 12a$, where $\overline{\boldsymbol{r}}^{(1)}$ and $\overline{\boldsymbol{r}}^{(2)}$ are their respective center of mass (Fig.4.4(a)). The computational domain consists of $2 \times 1 \times 2$ unit cells (Fig.4.4(a)), where each unit cell contains the equivalent to two pillars of depth $D_O \approx L$. In order to characterize the fiber dynamics, we introduce the mean displacement $\boldsymbol{\sigma}(\tau)$, which we define as follows

$$\boldsymbol{\sigma}(\tau) = \langle [\overline{\boldsymbol{r}}(t+\tau) - \overline{\boldsymbol{r}}(t)] \rangle \,, \tag{4.12}$$

where $\langle \cdot \rangle$ denotes the ensemble average, and $\overline{\boldsymbol{r}}$ is the position of the fiber center of mass. We perform simulations with periodic boundary conditions in the three directions of the domain.

Panel (i) of Fig.4.4(b) shows the center of mass trajectories of the fibers. At early times, hydrodynamic interactions affect the fiber trajectories, and therefore lead to a complex scattering dynamics. At long times, the fibers separate laterally, their trajectories fall in quasi-straight lines. This long-time behavior is reflected in the x-component of their mean displacement by the onset of a steady state, as shown in panel (i) of Fig.4.4(c). However, when the fibers are sufficiently close, such that $D = 4a$, they strongly interact hydrodynamically. As a result, the fibers continuously attract each other and form a bundle, which later dissolves when it collides with a pillar. This process persists over a longer period of time ($0 \leq t/T \leq 150$), and therefore the fibers do not separate laterally at long times (Figs.4.4(b)-(c), panels (ii)). These findings provide physical insight into how collective behavior can significantly affect the dynamics of a sedimenting suspension of fibers through an array of pillars.

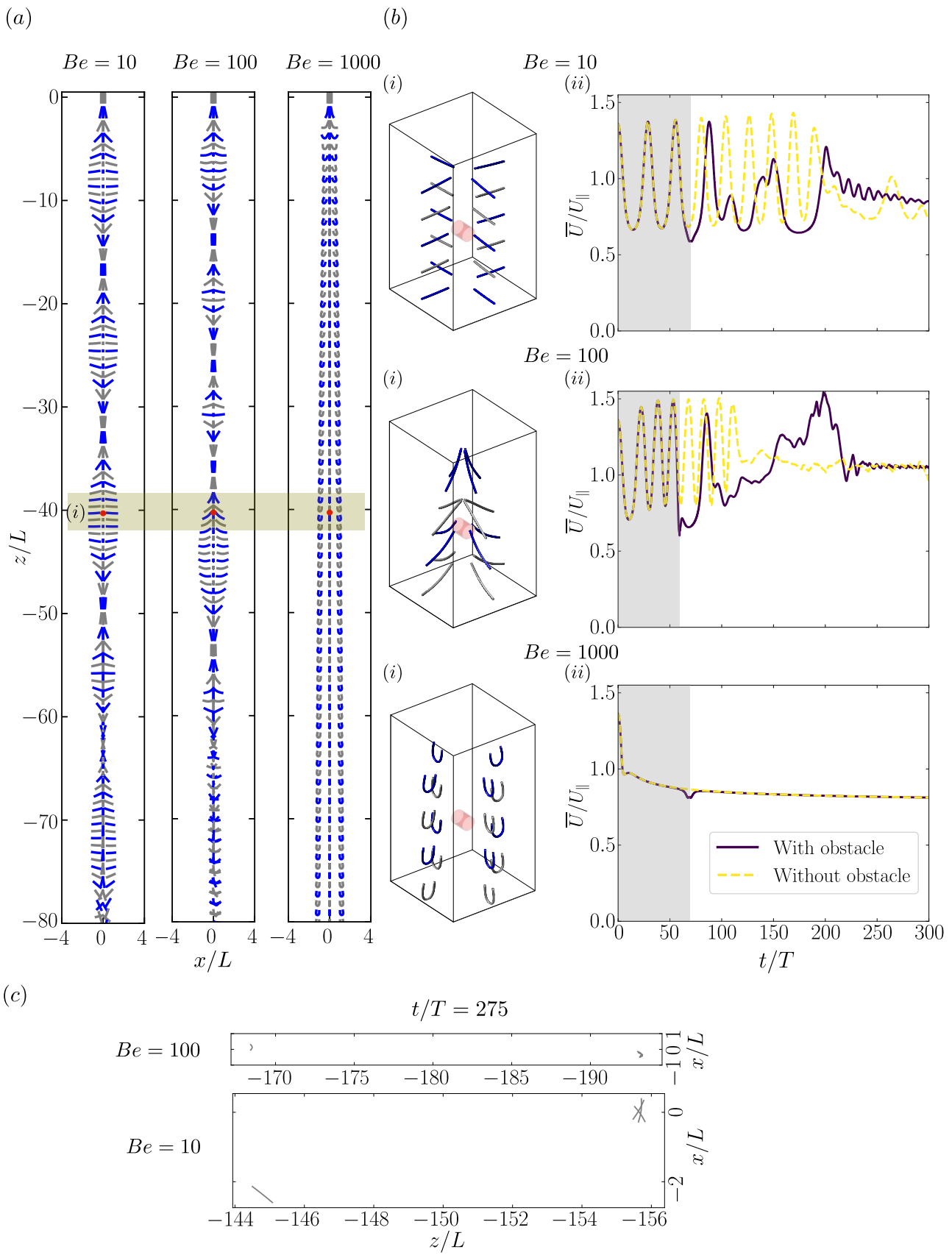

Figure 4.3: Sedimenting four fibers against a rigid obstacle. The fibers are initially in a symmetric configuration. (a) Chronophotographs, the time step between two consecutive frames (shown with alternating colors: blue and gray) is $\Delta t = 1.7T$, where T is the characteristic settling time. (b) The panels (i) show the settling dynamics close to the obstacle. the panels (ii) show the time evolution of the mean settling velocity relative to the maximum velocity of an isolated rigid fiber, $U_{\parallel}$. The gray-shaded zone corresponds to the dynamics before the collision. (c) Long-time dynamics at $t = 275T$.

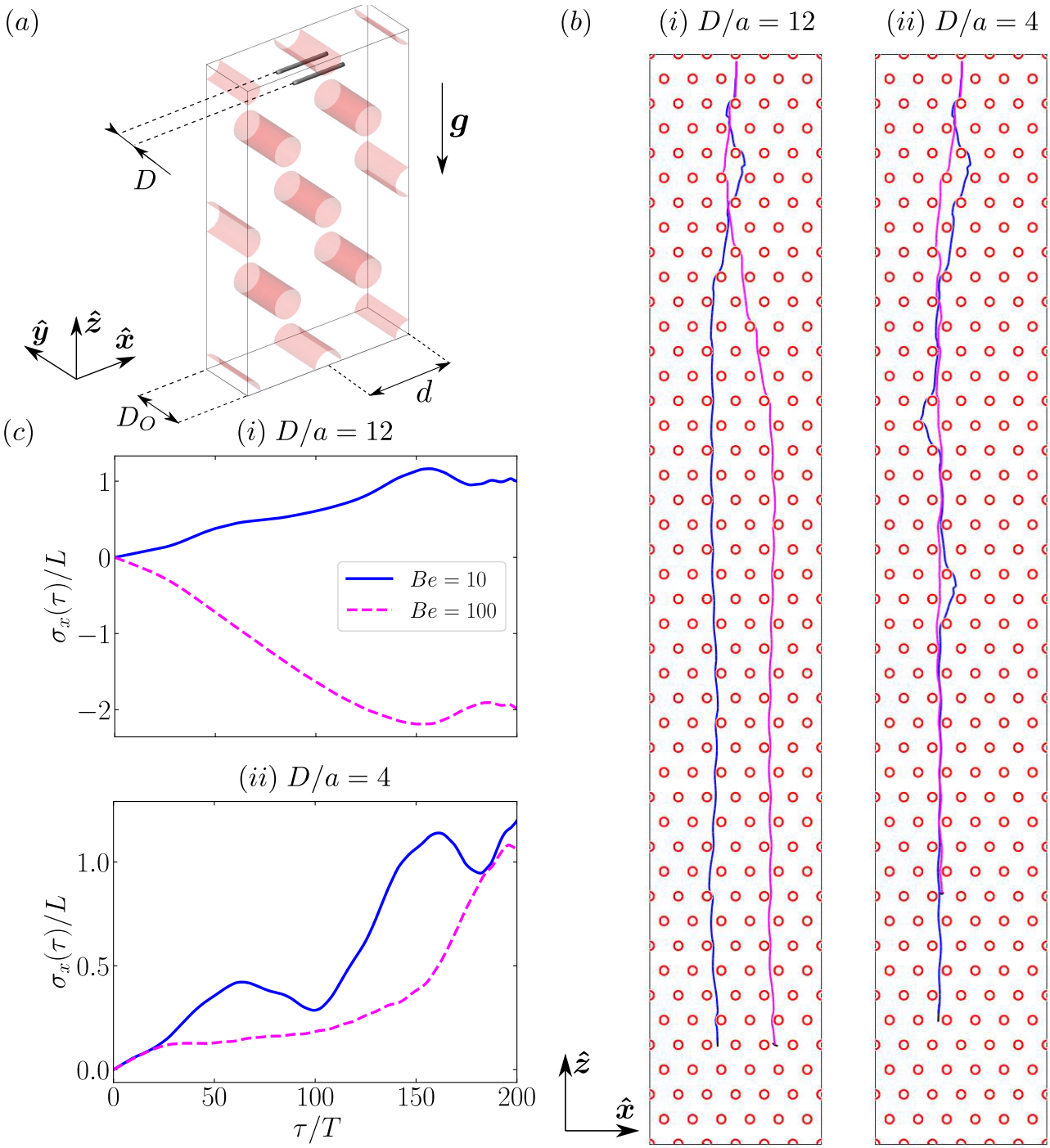

Figure 4.4: Sedimenting pairs of flexible fibers through an array of rigid pillars. (a) A 3D representation of the computational domain, which is made of $2 \times 1 \times 2$ unit hexagonal cells. The computational domain contains the equivalent to 8 pillars of depth D_O, plus the pair of fibers. The center-to-center distance between two adjacent pillars d is defined such that $L/d \approx 0.67$. (b) Trajectories of the center of mass of the fibers, that are initially separated by a distance $D = 12a$ (i) or $D = 4a$ (ii). The two fibers have different elastogravitational numbers, $Be = 10$ (blue) and $Be = 100$ (magenta). (c) Time-evolutions of the x-component of the mean displacement of each fiber center of mass. Panels (i) and (ii) correspond to $D = 12a$ and $D = 4a$, respectively.

4.4.2.3 Sedimenting a fiber suspension through an array of obstacles

Here, we investigate the sedimentation of a dilute suspension of M fibers through an array of obstacles. Initially, the fibers are straight and randomly distributed within the array of obstacles. The latter, as well as the computational domain, are defined in the same way as in the previous problem (see Section 4.4.2.2). Each fiber is made of $N = 15$ beads, that are evenly spaced by a distance $2a$, where a is the bead radius. We perform numerical simulations for $Be = 100$ and two different values of the effective concentration of the fiber suspension, $nl^3 = [0.3, 0.5]$.

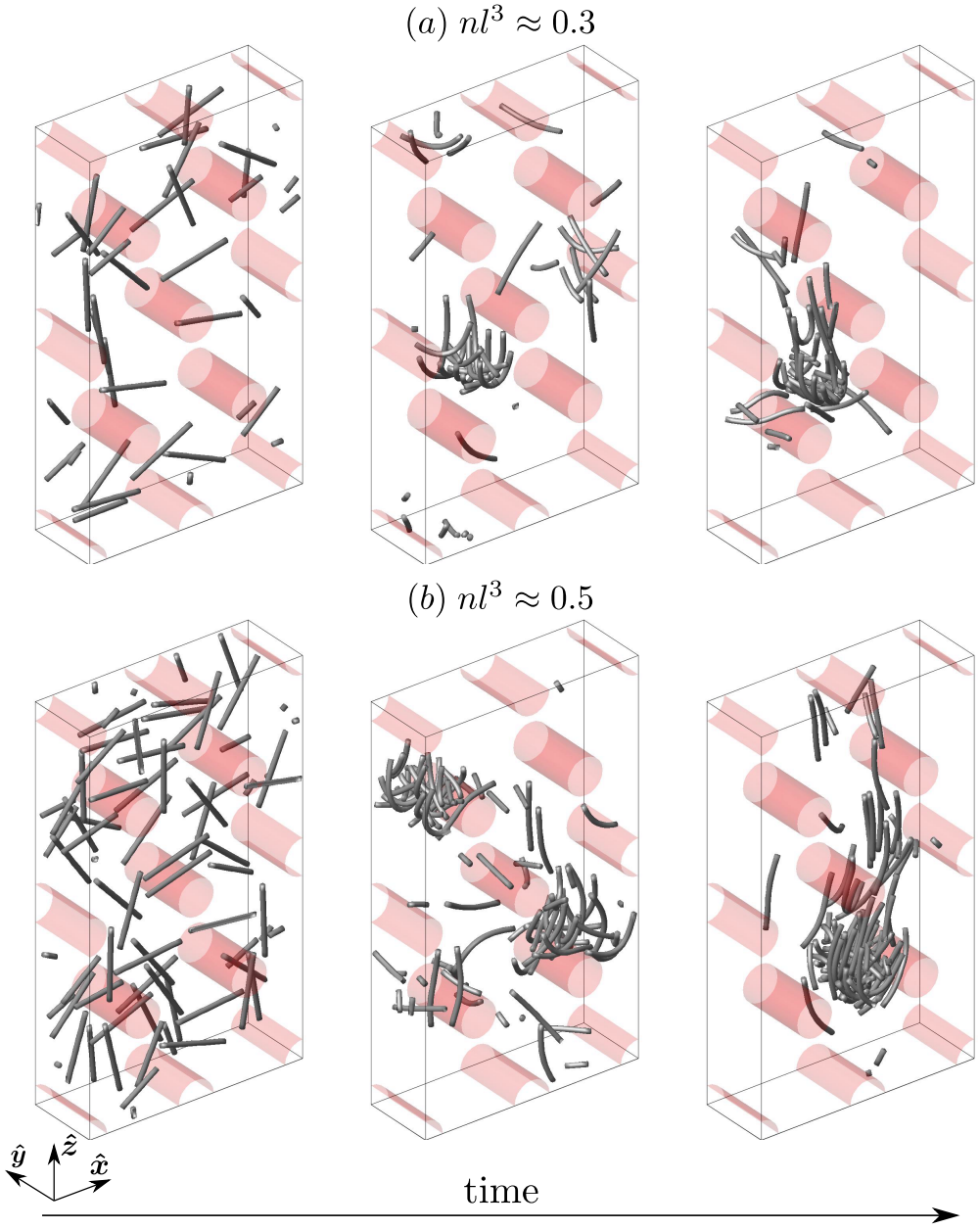

Figure 4.5: Results from numerical simulations showing the time evolution (from left to right) of a sedimenting suspension of fibers through an array of obstacles. The snapshots are shown for two different values of the effective concentration: $nl^3 = 0.3$ (a) and $nl^3 = 0.5$ (b).

Figure 4.5 shows some snapshots of the time evolution of the fiber suspension through the array of obstacles. In contrast to the case of a sedimenting suspension of fibers in a free fluid, where the formation of clusters within downward streamers has been observed at long times (see Section 3.5.2), the presence of obstacles leads to the formation of a single cloud of fibers. The

latter undergoes a zigzag motion with no average displacement from the direction of gravity, i.e., the migration angle of the cloud through the array is close to zero.

While interacting with the obstacles, the cloud continuously loses and captures fibers. As a result, it remains a cohesive entity with a quasi-stable shape. This finding contrasts with the settling dynamic of a cloud of fibers in a free fluid (Park et al., 2010), where, at long times, the cloud evolves into a torus that subsequently becomes unstable and breaks up into secondary clouds which themselves later break up and so on. However, this cascade behavior has been observed for a very large number of fibers (more than 500 fibers) which has not been explored in this thesis.

As done in Section 4.4.2.2, for each simulation, we measure the mean settling velocity $\overline{w}$ of the fiber suspension. The time evolution of the resulting values is shown in Fig.4.6. For each effective concentration nl^3, the mean settling velocity increases as the cloud forms and becomes even larger than the maximum possible value of a single rigid fiber for $nl^3 = 0.5$. At long times, the mean settling velocity reaches a plateau when the cloud adopts a quasi-stable shape. This steady state occurs earlier as the value of the effective concentration decreases.

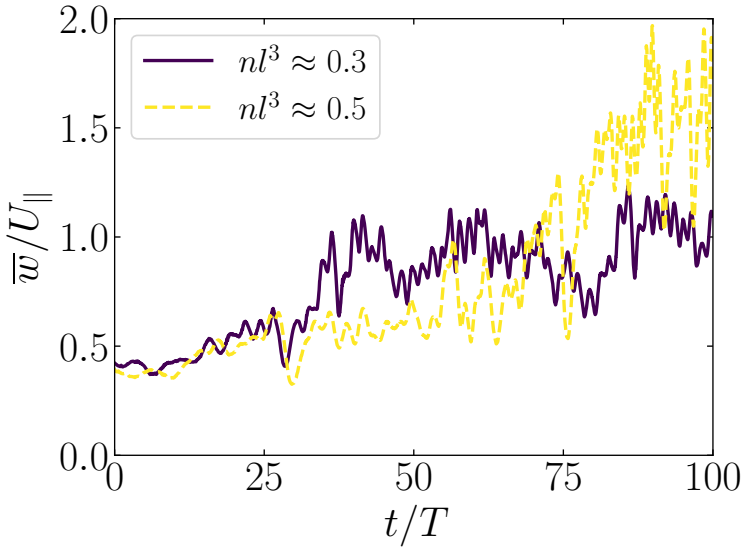

Figure 4.6: Time evolution of the mean settling velocity $\overline{w}$ of the fiber suspension for various values of the effective concentration nl^3. The mean settling velocity is normalized by the maximum velocity of an isolated rigid fiber $U_{\parallel}$.

4.5 Conclusions

In this chapter, we have introduced a methodology to solve problems involving fiber and rigid stationary obstacles of arbitrary shapes in Stokes flow. Especially, we have shown how our methodology reduces the number of constraints in the system compared to the approach proposed by Majmudar et al., 2012, in which the inextensibility condition gives rise to additional constraints. We have proposed an effective preconditioner to solve iteratively the resulting mixed mobility-resistance problem in reasonable wall times on a single modern Graphics Processing Unit (GPU). This framework has been used to investigate three problems involving sedimentation of flexible fibers against obstacles, in which we have observed interesting phenomena owing to the complex coupling between the elastic response of the fibers, gravity, contact forces and hydrodynamic interactions.

Although in this chapter, we focused on passive fiber-like particles, our methodology can be extended to active fiber-like particles, and to account for more complex shapes.

Owing to the capabilities afforded by our methodology, in the next part, we use numerical simulations, experiments and analytical tools to investigate in detail the effects of obstacles on the settling dynamics of flexible fibers.

Part III

Sedimenting flexible fibers against rigid obstacles

Chapter 5

Obstacle-induced lateral dispersion and nontrivial trapping of flexible fibers settling in a viscous fluid

Contents

Remark: the content of this chapter is directly extracted from the eponymous paper (Makanga et al., 2023), published in Physical Review Fluids.

The motion of flexible fibers through structured fluidic environments is ubiquitous in nature and industrial applications. Most often, their dynamics results from the complex interplay between internal elastic stresses, contact forces and hydrodynamic interactions with the walls and obstacles. By means of numerical simulations, experiments and analytical predictions, we investigate the dynamics of flexible fibers settling in a viscous fluid embedded with obstacles of arbitrary shapes. We identify and characterize two types of events: trapping and gliding, for which we detail the mechanisms at play. We observe nontrivial trapping conformations on sharp obstacles that result from a subtle balance between elasticity, gravity and friction. In the gliding case, a flexible fiber reorients and drifts sideways after sliding along the obstacle. The subsequent lateral displacement is large compared to the fiber length and strongly depends on its mechanical and geometrical properties. We show how these effects can be leveraged to propose a new strategy to sort particles based on their size and/or elasticity. This approach has the major advantage of being simple to implement and fully passive, since no external source of energy is needed.

5.1 Introduction

The transport and trapping of fibers through complex environments, such as porous media, occurs in a variety of systems. Small fibers, e.g., microplastic fibers, may propagate in soil and cause pollution of groundwater (Re, 2019; Engdahl, 2018). When flowed through small cracks in natural rocks, such flexible fibers may buckle, leading eventually to clogging and thus closing of small paths (D'Angelo et al., 2010), which is for example used to prevent proppant flowback in petroleum engineering (Howard et al., 1995). Similar clogging may happen in the vascular system, where biofilm streamers may form in irregular channels, detach, transport and ultimately remain attached and clog small vessels or structures such as stents (Rusconi et al., 2010). The characterization of the interaction of flexible fibers with obstacles can further be used to design chromatographic devices to separate DNA filaments by size by transporting them through periodic arrays of posts in microfluidic devices (Chou et al., 1999). Other industrial processes rely on the trapping of the fibers on the obstacles, e.g., in papermaking where the fibers accumulates on the wires of a fabric through which a suspension is drained in order to form the paper sheet (Vakil and Green, 2011). In all these situations, the velocity, deformation or trapping of the fiber is determined by a complex interplay between elasticity, viscosity, and interactions with the obstacles.

When a rigid fiber is freely transported in a viscous flow, the trajectory of its center of mass globally follows the streamlines. The fiber may further interact hydrodynamically with the bounding walls of the channel, causing rotations and reorientations (Nagel et al., 2018; Cappello et al., 2019). When freely transported fibers encounter obstacles, they will thus glide around them (López et al., 2015). When the fiber is flexible, it may deform in response to viscous forces (Du Roure et al., 2019). These deformations help the fiber escape and migrate through the flow streamlines, e.g., through buckling (Wandersman et al., 2010; Quennouz et al., 2015), bending or coiling (Xue et al., 2022). In the presence of obstacles, flexible fibers may thus deform, stretch, buckle, vault and tumble due to the flow generated by the obstacles, which will affect their trajectory as well as their transport time (Sabrio and Rasoulzadeh, 2022; Kawale et al., 2017; Chakrabarti et al., 2020); indeed, these dynamics increase the path taken by the fiber, and may further lead to prolonged trapping periods or fibers remaining trapped on the obstacles (Vakil and Green, 2011). The presence of obstacles thus affects the long-time transport properties of fibers, such as dispersion, and since the collision times and the associated transport velocity are size-dependent, this can serve as a base for sorting devices. However, in these cases the overall lateral displacement remains small, as freely transported fibers globally tend to align with the flow.

Conversely, when moving thanks to external forces such as gravity or in a centrifuge, without an external driving flow, the trajectories of a fiber strongly depends on its orientation with respect to the direction of the force. In particular, a rigid fiber settling in a quiescent fluid oriented at an angle neither perpendicularly nor aligned with the force will drift as it settles down, leading to large lateral displacements. During settling, flexible fibers experience deformations and reorientations that strongly affect their transport (Saggiorato et al., 2015; Marchetti et al., 2018; Cunha et al., 2022). Indeed, a flexible fiber bends due to its own hydrodynamic disturbances; this deformation leads to a torque that re-orients the fiber perpendicularly to gravity, thus reducing its lateral drift (Xu and Nadim, 1994; Li et al., 2013), which also affects their collective dynamics (Manikantan et al., 2014; Schoeller et al., 2021). In this situation, the presence of an obstacle, by modifying the deformation and orientation of the fiber, will thus directly affect its trajectory. Here, we consider the prototypal case of a single flexible fiber settling in a quiescent fluid embedded with fixed obstacles of various shapes. We show that the fiber interacts with the obstacle both hydrodynamically and through friction. The presence of the obstacle induces a reorientation with an angle that depends on the fiber characteristics, in

particular its flexibility, and the obstacle shape. The fiber then reorients to reach its equilibrium shape after having travelled a finite distance; the magnitude of this lateral displacement is large (typically several fiber lengths) and depends on the fiber characteristics, an effect we leverage on to propose a sensitive sorting solution. Furthermore, we examine the conditions under which a fiber may remain trapped on the obstacle, and identify non-trivial trapping events, providing design clues for optimal sorting/filtration.

5.2 Problem description and relevant parameters

We study the dynamics of a flexible fiber settling in a viscous fluid, with viscosity η, embedded with a rigid obstacle, as shown in Fig. 5.1. The flexible fiber is an elastic rod of length L and circular cross-section of radius a, with centerline characterized by its arc length $s \in [0, L]$. The fiber is settling at a velocity U such that the Reynolds number $\mathrm{Re} = \rho U L/\eta$ is always small and viscous effects dominate the hydrodynamics. The obstacle is defined as a rigid tube of width ω and depth D_O. The cross-section of the tube is generated by an area-preserving conformal mapping of the unit circle (Avron et al., 2004; Alonso-Matilla et al., 2019) (see Appendix D.1). The obstacle shape and symmetry are controlled by a geometric parameter $\mathcal{K}$: $\mathcal{K} = 0$ corresponds to a circular cross-section while $\mathcal{K} = \pm 0.6$ is a triangle with negative curvature pointing upward (downward respectively). The fiber starts at equilibrium with its midpoint initially positioned at a given horizontal and vertical distance, D_x and D_y, from the obstacle center of mass.

In the absence of obstacles, the equilibrium shape of a fiber subject to gravity in a viscous fluid results from the balance between viscous and internal elastic stresses, which is quantified by the so-called elasto-gravitational number $Be = F^G L^2/EI = WL^3/EI$, where $F^G = WL$ is the gravity force, W the weight per unit length of the fiber, E its Young's modulus and $I = \pi a^4/4$ its second moment of inertia. In the rigid case, $Be \ll 1$, the fiber keeps its initial shape, while in the flexible regime, $Be \gg 1$, it bends due to its own hydrodynamic disturbances. The fiber will thus adopt a more or less pronounced "U" shape, depending on Be, oriented perpendicularly with the direction of gravity, independently of its initial configuration, as sketched in Fig. 5.1. As we will show below, the presence of an obstacle destabilizes this equilibrium shape and affects its trajectory. These changes depend on two additional parameters: the relative length of the fiber with respect to the obstacle width $\xi = L/\omega$ and the obstacle shape $\mathcal{K}$.

5.3 Experimental and numerical methods

5.3.1 Experimental methods

Experiments are carried out using a slightly modified version of the experimental setup and protocol described in Marchetti et al., 2018. We fabricate elastic fibers of controlled properties by molding liquid poly-vinyl siloxane (PVS 8, Elite double Zhermack) mixed with iron powder (from 10 to 20%) into a capillary tube of radius $a = 510$ μm; after degassing and cross-linking at room temperature, the fibers are extracted from the tubes. We work with two solutions: 10% Fe, for which $\rho_f = 1107 \pm 40$ kg/m^3 and $E = 141 \pm 50$ kPa, and 20% Fe for which $\rho_f = 1143 \pm 13$ kg/m^3 and $E = 180 \pm 75$ kPa. The fibers are then released in a large tank which has a rectangular cross-section ($L_1 = 60$ cm, $L_2 = 40$ cm) and height $H = 80$ cm, filled with silicone oil ($\rho = 970$ kg/m^3, $\eta = 0.97$ Pa.s). A 3D-printed obstacle of width 1 cm and spanning the entire depth of the tank is held against the walls in the center of the tank (Fig. 5.2(a)). Fibers are initially held in the upper part of the tank by tweezers in a shape close to their equilibrium configuration. It ensures that equilibrium is reach before interacting with the

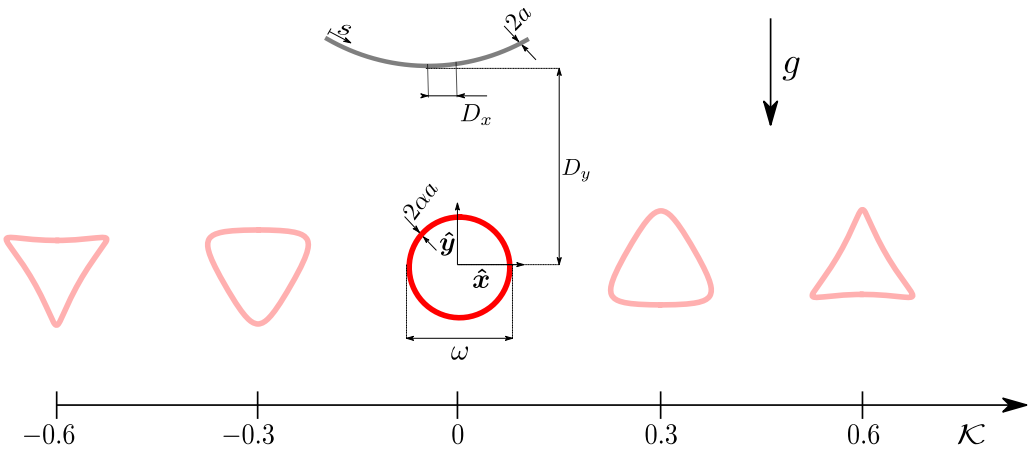

Figure 5.1: Schematic of the problem considered: a fiber sediments with its equilibrium shape towards an obstacle of cross-section controlled by the parameter $\mathcal{K}$ ranging between $\mathcal{K} = -0.6$ to $\mathcal{K} = 0.6$.

obstacles. Fibers are released by slightly opening the tweezers simultaneously to avoid large flow disturbances. We track the shape and position of the fiber using a high-resolution DSLR camera with a wide 20 mm lens. Typically, the fiber settling velocity is 0.5 mm/s, corresponding to Reynolds numbers $Re \sim 10^{-2}$, and images are taken every 10s.

5.3.2 Numerical simulations

The numerical method relies on the bead model (see Section 3.4) to solve the elasto-hydrodynamic couplings and contact interactions between fibers and obstacles. Below we briefly outline the method, more details are provided in Chapter 4. The fiber is modelled as a chain of N_F spherical beads of radius a connected by Hookean springs (Fig. 5.2(b)). The fiber beads are subject to a gravitational force $\boldsymbol{F}^G/N_F$, where $F^G = \|\boldsymbol{F}^G\|$ is the weight of the whole fiber. Mechanical interactions between the fiber beads are governed by elastic forces, $\boldsymbol{F}^E$, that derive from the stretching and bending free energies (see Section 3.4.2). Since we are considering plane deformations, twisting of the fiber is neglected. The obstacle surface is discretized with N_O beads of radius a_O stacked in slices. Each slice is discretized with a uniform distribution of beads in contact along its contour $\mathcal{C}$. The total number of beads in the system is $N = N_F + N_O$. The contact forces between the obstacle and fiber beads, $\boldsymbol{F}^R$, are pairwise, short-ranged and repulsive. The repulsion between bead i and j is given by Dance et al., 2004

$$\boldsymbol{F}^R_{ij} = \begin{cases} -\dfrac{F_R}{(a_i + a_j)} \left[\dfrac{R_c^2 - r_{ij}^2}{R_c^2 - (a_i + a_j)^2} \right]^4 \boldsymbol{r}_{ij}, & \text{for } r_{ij} < R_c \\ \boldsymbol{0}, & \text{otherwise} \end{cases} \tag{5.1}$$

where $\boldsymbol{r}_{ij} = \boldsymbol{r}_j - \boldsymbol{r}_i$ is the vector between the bead centers and $r_{ij} = |\boldsymbol{r}_{ij}|$. The repulsion strength is chosen to prevent bead overlaps, $F_R = 4F^G$, and $R_c = 1.1(a_i + a_j)$ sets the cutoff distance over which the force acts, here 10% of the contact distance between a pair of beads. Owing the spherical shape of the beads, and to the discrete nature of the bead model, the repulsive force (5.1) can exert tangential efforts along the fiber centerline. The tangential component of $\boldsymbol{F}^R$, denoted $\boldsymbol{F}^R_\tau$ hereinafter, therefore acts as a friction force between the fiber and obstacle surface. For a given obstacle shape and fiber conformation, the relative magnitude of this friction force is controlled by the relative size of the obstacle beads with respect to the

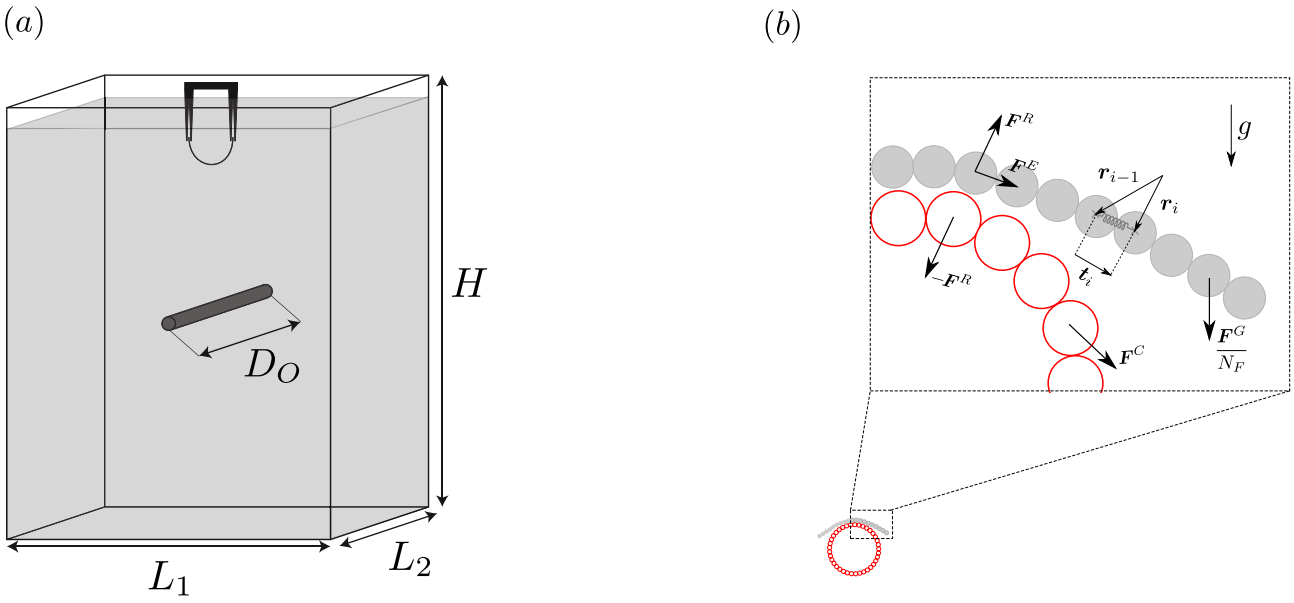

Figure 5.2: (a) Experimental setup, showing a fiber initially held with tweezers under the free-surface of the tank, with an obstacle of circular cross-section and depth D_O held at the center of the tank. (b) Numerical model, showing the fiber (gray), represented by a chain of N_F spherical beads linked elastically by Hookean springs, and an obstacle slice (red), discretized by a series of N_O beads along its contour. Both fiber and obstacle beads are subject to external and internal forces: $\boldsymbol{F}^R$ is the repulsive contact barrier force between the fiber and obstacle beads, $\boldsymbol{F}^C$ is the constraint force applied to obstacle beads in order to prescribe their motion, $\boldsymbol{F}^E$ and $\boldsymbol{F}^G/N_F$ are respectively the internal elastic and gravitational forces experienced by the fiber beads. $\boldsymbol{t}_i = \boldsymbol{r}_i - \boldsymbol{r}_{i-1}$ is tangent vector to the fiber centerline at the position of bead $i-1$.

fiber beads, $\alpha = a_O/a$. The maximum penetration of the obstacle bead in the void between fiber beads is given by $\delta/a = 1 + \alpha - \sqrt{\alpha(2+\alpha)}$, which is an upper bound of the effective roughness between the two surfaces. This maximum value is reached when the local radius of curvature of the obstacle is equal to a_O, i.e., when the obstacle has cusps and the beads are touching. In the following we choose $\alpha = 0.61 - 2$, which sets the maximum interpenetration to $\delta/a = 0.17 - 0.35$.

Because the Reynolds number associated with the fiber motion is relatively small ($Re \ll 1$), the kinematic equation of motion of the beads, in the absence of background flow, is given by the constrained mobility problem (4.6), which we reproduce here for the sake of clarity

$$\frac{\mathrm{d}\boldsymbol{R}}{\mathrm{d}t} \equiv \boldsymbol{U} = \boldsymbol{\mathcal{N}} \cdot \left(\boldsymbol{F}^G/N_F + \boldsymbol{F}^E + \boldsymbol{F}^R \right), \tag{5.2}$$

where $\boldsymbol{R} = [\boldsymbol{r}_1, \cdots, \boldsymbol{r}_{N_F}, \boldsymbol{r}_{N_F+1}, \cdots, \boldsymbol{r}_N]$ and $\boldsymbol{U} = [\boldsymbol{U}_1, \cdots, \boldsymbol{U}_{N_F}, \boldsymbol{U}_{N_F+1}, \cdots, \boldsymbol{U}_N]$ are $3N$ vectors collecting the bead positions and translational velocities. $\boldsymbol{\mathcal{N}}$ is the $3N \times 3N$ constraint mobility matrix[1], as defined in Section 4.2.2. Long-ranged hydrodynamic interactions, namely the bead mobility matrix $\boldsymbol{\mathcal{M}}$, to construct $\boldsymbol{\mathcal{N}}$, is defined in an infinite fluid domain (Zuk et al., 2014). Here the choice of an unbounded geometry is justified by the fact that the tank dimensions are approximately one order of magnitude larger than the fiber length in experiments, and also because the fiber relaxes to equilibrium long before reaching the bottom of the tank. After computing $\boldsymbol{U}$ we then integrate the bead positions in the equation of motion (5.2) using an implicit time integrator based on Backward Differentiation Formula (BDF) with adaptive time-stepping (Brown et al., 1989).

[1]The constraint mobility matrix $\boldsymbol{\mathcal{N}}$ includes the constraint forces $\boldsymbol{F}^C$ by construction.

5.4 Results and discussion

The presence of the obstacle leads to two main outcomes that depend on the mechanical and geometrical properties of the system: the fiber can either glide along the obstacle (see Fig. 5.3(a)) or remain trapped around it (see Fig. 5.3(b)). These events results from the complex interplay between internal elastic stresses, contact forces and hydrodynamic interactions with the embedded rigid obstacle.

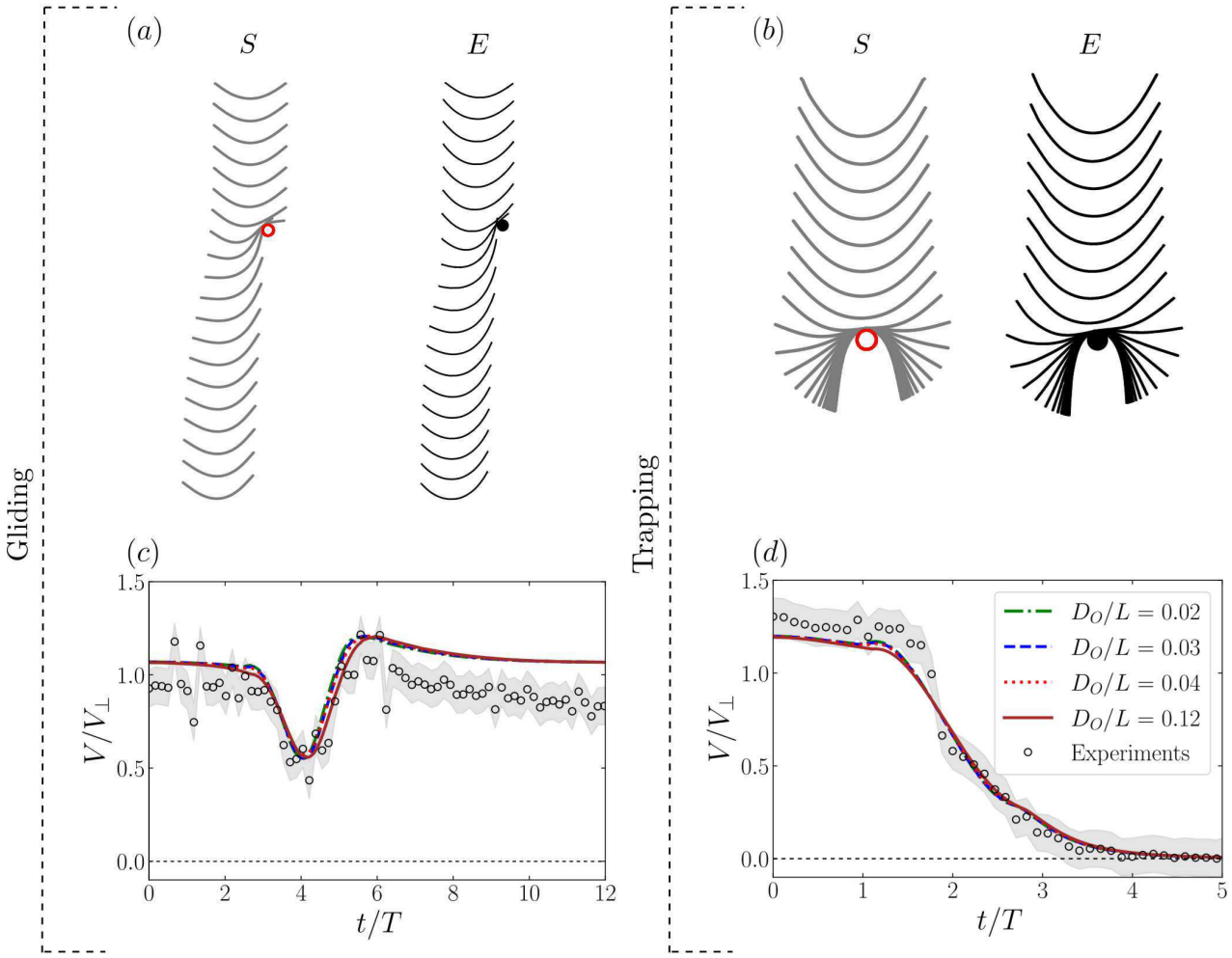

Figure 5.3: ($a-b$) Numerical (S) and experimental (E) chronophotographies of a flexible fiber settling against an obstacle in a viscous fluid. The time step between two consecutive frames is taken as $\Delta t = 10s$. The initial fiber configuration in numerical simulations is taken from the first experimental frame (see also movies 1 and 2 in supplementary material (Makanga et al., 2023)). (a) Gliding event: parameter values are $Be = 200$, $\xi = 7.71$ and $D_x/L = 0.25$. The gliding event is characterized by a short trapping period around the obstacle followed by a drift motion. (b) Trapping event: parameter values are $Be = 210$, $\xi = 9.35$ and $D_x/L = 0.03$. The trapping event is characterized by a prolonged trapping period of the fiber around the obstacle. ($c-d$) Evolution of the total velocity of the center of mass of the fiber as function of time in experiments (circles with grey shaded error bars) and numerical simulations (lines) for various depths of the obstacle, respectively for (c) gliding and (d) trapping events. The velocity and the time are scaled respectively by the settling velocity of the corresponding rigid fiber oriented perpendicularly to the direction of gravity, $V_\perp$, and the characteristic settling time $T = L\eta/W$.

Before addressing the role of each of these mechanisms on the fiber trajectory, we characterize these two situations and use them to validate our numerical method. Fig. 5.3 shows

numerical and experimental realizations of the gliding and trapping events for a semi-flexible fiber ($Be \sim 200$) settling against an obstacle (the complete set of parameters is provided in Appendix D.2). In the simulations, the initial position of the fiber centerline and its mechanical properties are directly extracted from the experiments. Note that to compute the elasto-gravitational number Be in our multibead approach, we have used the volume of the object as a continuous fiber and not as a chain of beads, which is smaller by a factor 2/3 (Marchetti et al., 2018).

As shown by the chronophotographies in panels $(a) - (b)$, the simulations agree qualitatively well with experiments for both events. In addition, the time evolution of the settling speed, reported in panels $(c) - (d)$, shows excellent quantitative agreement, thus confirming the adequacy of our method to capture fiber-obstacle interactions in a viscous fluid. In the gliding case, the fiber starts close to its equilibrium shape with a settling speed larger than a rigid one ($V > V_\perp$), (see panels (a) and (c)). As it settles, it progressively slows down until it partially hits the obstacle and reaches its minimum speed. The speed increases again as the fiber glides along the obstacle. Upon release, it is more aligned with gravity and reaches its maximum velocity ($V/V_\perp \approx 1.2$). Eventually it slowly relaxes to its equilibrium shape: the velocity decreases to its initial value and the fiber drifts sideways as it reorients perpendicular to gravity. In the trapping case, the initial lateral distance between the fiber and obstacle, D_x, is smaller. As a result the fiber slows down continuously, wraps around the obstacle and finally remains in a trapped configuration indefinitely (see Fig. 5.3(b) and (d)). The decrease in the settling speed is more pronounced when the fiber touches and wraps around the obstacle in the interval $1.3 < t/T < 4$, where $T = L\eta/W$ is the characteristic settling time. The trapped configuration in the steady regime is asymmetric with respect to the obstacle center of mass. Such stable asymmetric configuration is only permitted by the tangential contact forces and results from an equilibrium configuration that minimizes the total energy due to external (gravity and contact) and internal elastic forces.

We note that the settling velocity of the fiber weakly depends on the obstacle depth D_O in numerical simulations, and is close to the experimental value, for which the obstacle is spanning the entire depth of the tank, with typical value $D_O/L \approx 4$ (see Fig. 5.3$(c - d)$). This weak dependence can be understood by the fact that the fluid in the tank is at rest and the dominant portion of the flow induced by the fiber decays as r^{-1}. Therefore, the response of the obstacle, to maintain its position, is weak for large separation distances. As a result the extremities of the obstacle that are far from the fiber barely affect its motion. That is why we only observe a slight decrease in the velocity of fiber close to the obstacle when D_O increases. We note that in the case of a fiber transported by a convective, e.g., plug or Poiseuille flow, the fiber velocity would be strongly correlated to the obstacle depth as its response to the ambient flow (which is no longer zero) has a magnitude close to the fiber speed.

Now that the gliding and trapping events have been described, and the numerical method validated, we use numerical simulations and analytical tools to explain their mechanical origin, identify their key parameters and to explore their potential for sorting applications.

5.4.1 Gliding events: tilting and lateral displacement induced by fiber-obstacle interactions

The gliding motion along the obstacle induces a tilt of the fiber centerline with respect to gravity, measured at the midpoint, denoted $\theta(t)$ (see Fig. 5.4(a)). Here, the origin of time ($t = 0$) is taken when the fiber leaves the obstacle, i.e., when there is no contact anymore. As mentioned earlier, this tilt induces a lateral drift as the fiber reorients back to its horizontal equilibrium shape. We define this lateral shift, $\tilde{\delta x} = \delta x/L$, as the lateral displacement of the fiber center of mass between a given starting time, here $t = 0$, and the final equilibrium state.

In the elongated limit ($\varepsilon = 2a/L \ll 1$), the velocity and lateral displacement of weakly flexible fibers ($Be \ll 1$) with initial orientation $\theta(0)$, and negative curvature, has been computed analytically by Li et al., 2013 using slender body theory (Keller and Rubinow, 1976; Johnson, 1980; Tornberg and Shelley, 2004). Their approach is based on a multiple-scale analysis (Hinch, 1991; Bender and Orszag, 1999), where they identify two relevant independent timescales in the fiber dynamic: the time for the fiber to settle its length L, of order $\mathcal{O}(1)$, and the time to reorient toward its equilibrium configuration, which is much slower and of order $\mathcal{O}(Be^{-1})$. In the case of a fiber with uniform thickness, mass and bending stiffness, they found that the leading order settling velocity is given by $\boldsymbol{U} = 2c_0\cos(\theta)\hat{\boldsymbol{t}}(\theta) - c_0\sin(\theta)\hat{\boldsymbol{n}}(\theta)$, where $(\hat{\boldsymbol{t}}, \hat{\boldsymbol{n}})$ are the tangent and normal vector at the midpoint of the centerline, and $c_0 = \ln(1/\varepsilon^2 e)$. Therefore, the velocity components in the lab frame, U_x and U_y, are obtained by dotting separately with the unit vectors $\hat{\boldsymbol{x}}$ and $\hat{\boldsymbol{y}}$:

$$U_x = \boldsymbol{U}\cdot\hat{\boldsymbol{x}} = \frac{c_0 h}{1+h^2}, \tag{5.3}$$

$$U_y = \boldsymbol{U}\cdot\hat{\boldsymbol{y}} = -c_0\left(1+\frac{1}{1+h^2}\right), \tag{5.4}$$

where

$$h(t) = \tan(\theta(0))\exp((2CBe)t), \tag{5.5}$$

with

$$C = \frac{7}{400} + c_0^{-1}\left(\frac{1813 - 300\pi^2 + 630\ln(2)}{18000}\right). \tag{5.6}$$

Finally, the lateral shift can be deduced by integrating Eq.(5.3) and assuming $0 < \theta(0) \leq \pi/2$

$$\tilde{\delta}x = \int_0^\infty (\boldsymbol{U}\cdot\hat{\boldsymbol{x}})\mathrm{d}t = \frac{c_0}{2CBe}\beta_0, \tag{5.7}$$

where

$$\beta_0 = \frac{\pi}{2} - \theta(0). \tag{5.8}$$

Eq.(5.7) is valid in the slender body regime if $C > 0$, i.e., when $\varepsilon = 2a/L < 0.196$. Holding β_0 constant in Eq.(5.7), we observe that, the lateral shift is inversely proportional to the elasto-gravitational number Be and the larger displacements are achieved for very stiff fibers, $Be \to 0$. The lateral shift is also proportional to the initial angle β_0 by holding Be constant. We also notice that, $\tilde{\delta}x = 0$ when $\theta(0) = \pi/2$: a fiber whose unit tangent at the midpoint is initially oriented perpendicular to the direction of gravity, will not experience a drift motion, as expected.

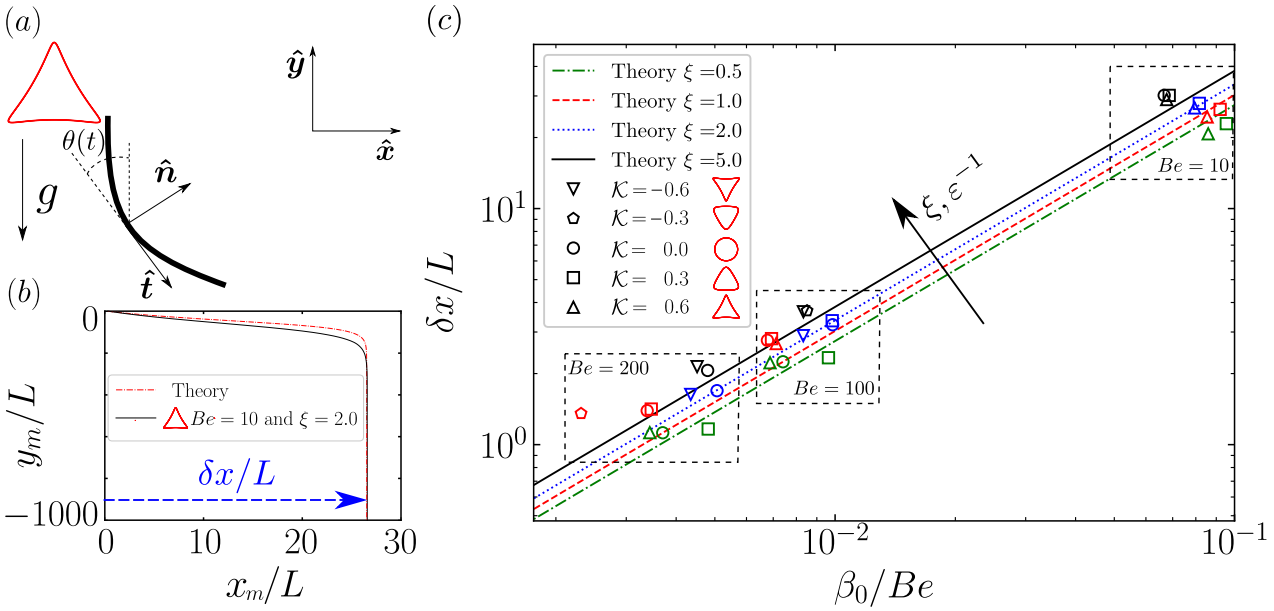

Figure 5.4: (a) Illustration of a fiber at the edge of the obstacle (downstream). $\hat{\boldsymbol{t}}$ and $\hat{\boldsymbol{n}}$ are respectively the unit tangent and unit normal vectors. The orientation angle $\theta(t)$ is defined between $\hat{\boldsymbol{t}}$ and the direction of gravity $-\hat{\boldsymbol{y}}$. (b) Results from numerical simulations (solid line) and from theoretical predictions (dash-dot line) showing the trajectory of the center of mass of the fiber for $Be = 10$ and $\xi = 2$. The initial configuration of the fiber is considered at the edge of the obstacle (downstream), with an initial orientation $\theta(0)$ induced by its shape, here for $\mathcal{K} = 0.6$. (c) Scaled lateral shift $\delta x/L$ versus β_0/Be. Comparison of the theoretical predictions (lines) with numerical results (symbols) done with one slice on the obstacle, for various values of the geometrical parameter ξ and the conformal mapping parameter $\mathcal{K}$. The corresponding values of ε are $0.031, 0.016, 0.008$ and 0.0032, respectively for $\xi = 0.5, 1, 2$ and 5. The showed numerical results (symbols) correspond to three sets of data for $Be = 10, 100$ and 200. The initial offset of the fiber midpoint is set horizontally at $D_x/L = 0.005$. Parameter values: $\Delta s/\mathcal{C} = 0.01$, $\alpha = 2$, and $D_y/L = 5$.

Figure 5.4(b) shows a typical trajectory of the midpoint of a rigid fiber with $Be = 10$, $\xi = 2$, after it has hit an upward-pointing triangular obstacle ($\mathcal{K} = 0.6$). The black solid line corresponds to the numerical simulation of the full system and the red dashed line to the theoretical prediction obtained by integrating (5.3) and (5.4) in time with the initial tilt angle taken from the numerics (here $\theta(0) = 0.38$). While the two curves show some discrepancies at short time when the fiber reorients, probably due to the fact that hydrodynamic interactions with the obstacle are not taken into account in the theoretical approach, their lateral shift matches exactly at long times when equilibrium is reached. Fig. 5.4(c) compares the predicted lateral shift in Eq. (5.7) with numerical simulations for a large range of realizations involving different obstacle shapes $\mathcal{K} = -0.6, \ldots, 0, 6$, relative length $\xi = 0.5, \ldots, 5$. As before, the initial tilt angle in Eq. (5.8) is taken from the simulations after hitting the obstacle. Since the theoretical approach is valid only for weakly flexible fibers, we used relatively small values of $Be = 10, 100, 200$ in the simulations. As expected, the simulated lateral shift $\tilde{\delta}x$ is monotonic in β_0/Be. Its values is maximal the most rigid case, i.e. the largest β_0/Be. Similarly to the theoretical prediction we observe a slow increase of $\tilde{\delta}x$ with ξ (i.e. ε^{-1}) for a given value of β_0/Be: for the same mechanical properties and a given obstacle shape, elongated fibers exhibit larger displacements than short ones. While theory and numerics agree reasonably well for $\xi > 1$ ($\varepsilon \ll 1$), a slight shift appears for $\xi = 5$ (black symbols vs. black solid line) due to the fact that the fiber has a positive curvature at its midpoint in the simulations when it leaves

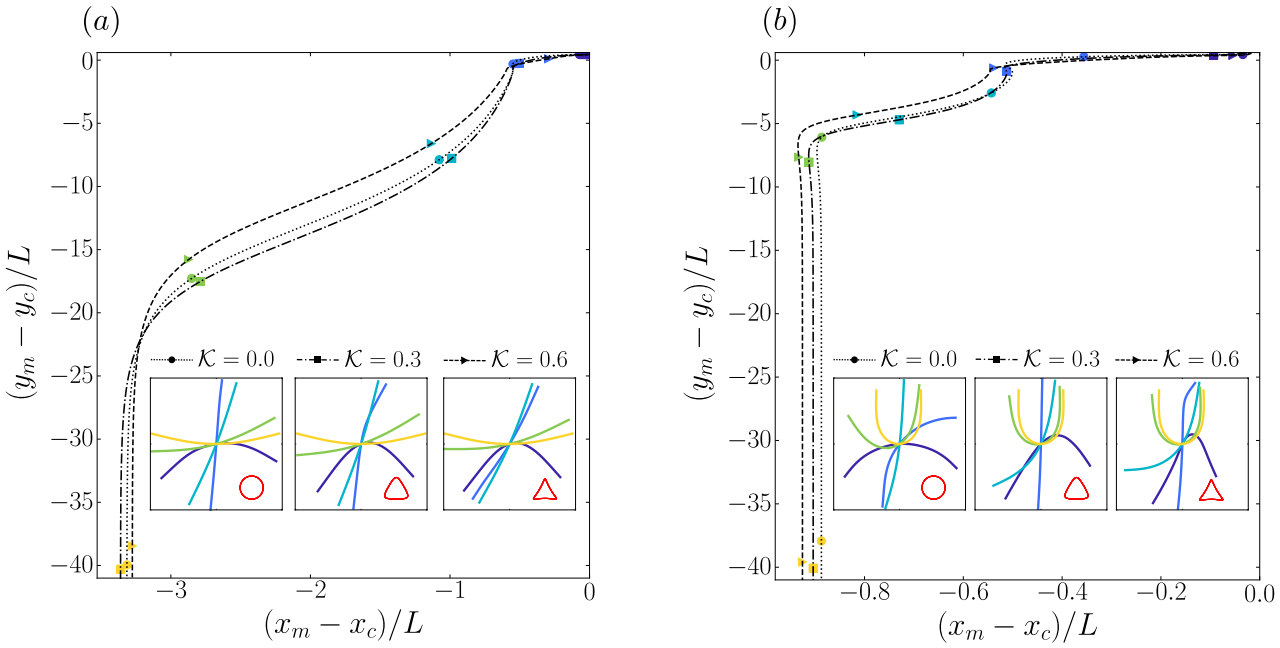

Figure 5.5: Results from numerical simulations of the trajectory of the center of mass of the fiber for $\xi = 1$ and three different shapes of the obstacle ($\mathcal{K} = 0, 0.3$ and 0.6). The snapshots show the configurations of the fiber under sedimentation in a frame moving with its midpoint, each configuration corresponds to the point having the same color on the trajectory. The initial offset of the fiber midpoint is set horizontally at $D_x/L = 0.05$ with respect to the center of mass of the obstacle. (a) With an intermediate value of the elasto-gravitational number $Be = 100$. (b) With a large value of the elasto-gravitational number $Be = 1000$. Note that x_c and y_c represent the position of the center of mass of the obstacle in xy plane. Parameter values are as in Fig. 5.4.

the obstacle (see movie 3 in the supplementary material (Makanga et al., 2023)), which violates the hypothesis of negative initial curvature in the theoretical approach. This error is decreased if the initial angle is taken at a later time in the simulations when the curvature at the midpoint becomes negative. For $\xi \leq 1$, the numerical simulations (red and green symbols) present some scatters which reflect the effects of hydrodynamic interactions of order $\mathcal{O}(1/d)$ induced by the obstacle, d being the fiber-obstacle distance. Note that, these effects are not taken into account in the theoretical approach where the fiber is isolated. In addition to the dependence of the lateral shift on ξ, we observe also the dependence of the lateral shift on the initial orientation angle induced by the obstacle shape. Before embarking in a detailed explanation on the dependence of $\tilde{\delta}x$ on the obstacle shape, we notice that for large values of ξ, i.e. $\xi = 5$, the lateral shift is quasi-independent of the obstacle shape. For instance, for $\beta_0/Be \approx 10^{-1}$, the induced local deflection along the fiber is lower than in the other cases ($\xi < 5$), therefore the initial fiber configurations are quasi-straight and have the same initial orientation angles at the edge of the obstacle (downstream) for all $\mathcal{K}$ (see movies 4-6 in the supplementary material (Makanga et al., 2023)). However, at smaller ξ, we observe a slight dependence of $\tilde{\delta}x$ on the obstacle shape. This dependence is due to the different curvatures of the obstacle sides, i.e. negative curvature ($\mathcal{K} = -0.6$ and $\mathcal{K} = 0.6$) or positive curvature ($\mathcal{K} = -0.3$, $\mathcal{K} = 0$ and $\mathcal{K} = 0.3$), and depends on the fiber flexibility. Finally, the increased discrepancies between simulations and theory at $Be = 200$ provide an upper bound for the range of validity of the theory which relies on an expansion at small Be. To include larger values outside the small Be constraint, we perform numerical simulations for $\xi = 1$ with $Be = 1000$. Typical trajectories for $Be = 100$ and $Be = 1000$ are presented in Fig. 5.5 for three shapes. In Fig. 5.5(a) for $Be = 100$, we observe that the lateral shift is maximized where the curvature of the obstacle

shape has a positive sign ($\mathcal{K} = 0$ and $\mathcal{K} = 0.3$) and minimized where it is negative ($\mathcal{K} = 0.6$) as observed in Fig. 5.4. However, for a large value of Be ($Be = 1000$) shown in Fig. 5.5(b), the trend is different, the lateral shift is maximized for $\mathcal{K} = 0.6$ compared to the other cases $\mathcal{K} = 0$ and $\mathcal{K} = 0.3$. This difference can be explained by the fact that for $\mathcal{K} = 0.6$, the fiber takes longer to release from the obstacle (characterized by the plateau region) than for $\mathcal{K} = 0$ and $\mathcal{K} = 0.3$, due its high flexibility which promotes higher adherence to the obstacle curvature. Nevertheless, for all shapes the angle at which the fiber leaves the obstacle is always small (typically $\theta < \pi/6$) and only slightly depends on the obstacle shape. The obstacle thus always tends to align the fiber with the direction of gravity; from there, the fibers have to reorient towards their equilibrium shape while drifting laterally; the magnitude of the lateral drift then strongly depends on the fiber's length and flexibility through Be, which offers opportunities for sorting fibers according to their characteristics.

Finally, we systematically explore the influence of the parameters on the lateral shift with a large set of simulations in the range $-0.6 \leq \mathcal{K} \leq 0.6$, $10 \leq Be \leq 1000$, $1 \leq \xi \leq 5$, for a given initial lateral offset $D_x/L = 0.05$. The results, reported in Fig. 5.6, show the coexistence of the gliding and trapping states, the latter corresponding to the purple symbols ($\delta x/L = 0$). Before undertaking a detailed investigation of the trapping events in Section 5.4.2, we qualitatively highlight the features of the resulting phase diagram (Fig. 5.6(a)) for each value of Be. Firstly, we observe that the maximum value of the lateral displacement $\delta x/L$ starts to saturates with Be^{-1} in the flexible regime $Be \geq 200$, which clearly indicates where the linear relationship obtained from the theory (5.7) breaks down.

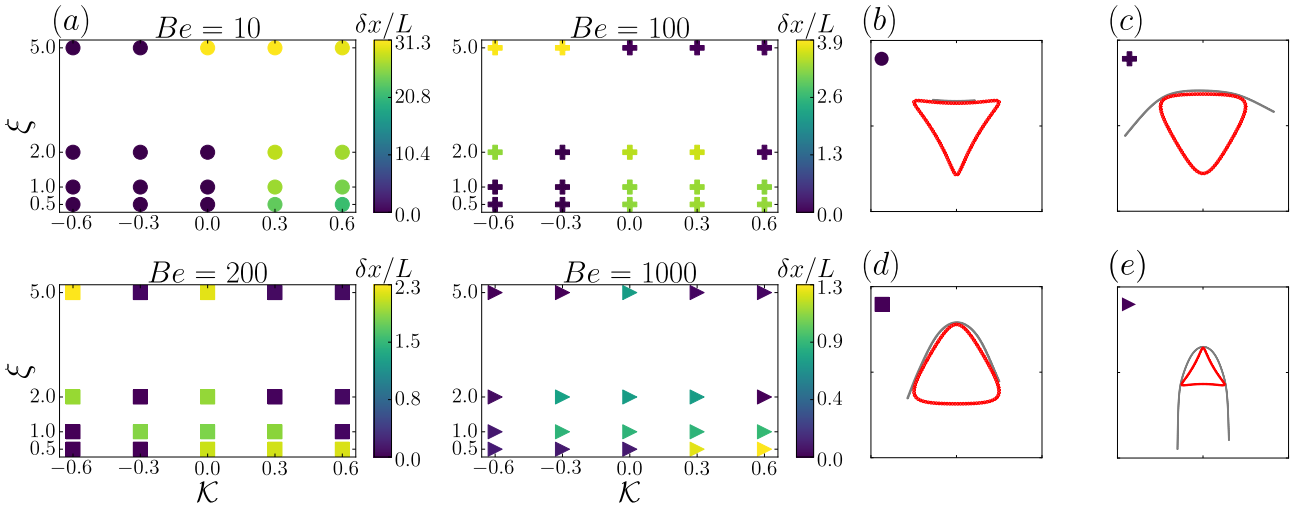

Figure 5.6: Results from numerical simulations computed with one slice on the obstacle. The initial offset of the fiber midpoint is set horizontally at $D_x/L = 0.05$ with respect to the center of mass of the obstacle. (a) Phase diagram, showing the scaled lateral shift $\delta x/L$ for various values of the elasto-gravitational number Be, the relative length ξ and the conformal mapping parameter $\mathcal{K}$. The purple symbols ($\delta x/L \sim 0$), denote the trapping events. ($b - e$) Trapping events resulting from the phase diagram (see also movies 7-10 in supplementary material (Makanga et al., 2023)). (b) $Be = 10$, $\xi = 0.5$ and $\mathcal{K} = -0.6$. (c) $Be = 100$, $\xi = 2$ and $\mathcal{K} = -0.3$. (d) $Be = 200$, $\xi = 2$ and $\mathcal{K} = 0.3$. (e) $Be = 1000$, $\xi = 5$ and $\mathcal{K} = 0.6$. Parameter values are as in Fig. 5.4.

Secondly, we notice that in the flexible regime ($Be = 1000$), for a given obstacle shape $\mathcal{K}$, the lateral shift in the gliding events is inversely proportional to the fiber length ξ (and thus proportional to ε). This trend contrasts with the rigid and semi-flexible regimes ($10 \leq Be \leq 200$) where the opposite is observed and predicted by the theory (5.7). Indeed as the flexibility

increases, local deformations happen near the tip of the longest fibers as they exit the obstacle, which tends to reorient them earlier than shorter ones and therefore reduce their lateral displacement. Thirdly, trapping states are mostly localized in the bottom left (short fibers on downward-pointing triangles) and upper right (long fibers on upward-pointing triangles) corners of the $(\mathcal{K}, \xi)$ plane for $Be \geq 100$. In the most rigid regime $Be = 10$ trapping only occurs on obstacles with a large incident contact surface ($\mathcal{K} \leq 0$).

5.4.2 Investigation of trapping events

As shown in Fig. 5.6$(b-e)$, for a given initial lateral offset (here $D_x = 0.05L$), the fiber can be trapped in many different ways depending on the obstacle shape $\mathcal{K}$, elasto-gravitational number Be, and relative length ξ. Some of these configurations might not seem intuitive at first sight and need to be rationalized.
The goal of this section is to systematically explore the wide diversity of trapping states in order to connect them to the geometric and mechanical parameters of the system.

In the absence of surface roughness, steric forces with the obstacle are exclusively directed along the normal of the fiber centerline. In this regime, trapping is only possible for symmetric configurations i.e., with zero lateral offset ($D_x/L = 0$), where the gravity forces balance on both sides of the fiber. However, surface asperities appear both in experiments and simulations: even though the crosslinked fibers are smooth, the 3D-printer has a finite resolution and defects might occur, while the simulated obstacles and fibers have a maximum interpenetration length $\delta/a \approx 0.17$ (see Section 5.3.2). Surface roughness generates friction directed along the fiber centerline. These tangential forces can balance asymmetric gravity forces and thus prevent the fiber from slipping away from the obstacle. In numerical simulations, friction forces correspond to the tangential component of the steric forces between obstacle and fiber beads F_τ^R. The trapping probability and trapping configurations are obviously highly sensitive to the details of the surface roughness. However, we did not try to match the experimental roughness in the simulations. The focus of this section is, for a given roughness value, to understand the mechanisms that lead to the observed trapping states.

To do so, we systematically explored the four-dimensional parameter space $(\xi, \mathcal{K}, Be, D_x/L)$. For each simulation, the fiber is released at a fixed height $D_y/L = 5$ with its equilibrium shape and the initial lateral offset is varied between $D_x/L = \pm 0.5$ with steps of size 0.01. Figure 5.7 shows the probability density function (PDF) of finding the trapped fiber centerline, with relative length $\xi = 2$, as a function of the elasto-gravitational number Be and obstacle shape $\mathcal{K}$. Owing to the symmetry of the problem, the PDF is computed only for the trapping events (TE in the figure) happening in the range $D_x/L = [0, 0.5]$, which represents 51 simulations for each panel. The range of initial offsets that correspond to the trapping events is shown at the bottom of each panel.

In the stiff limit, $Be = 10$ (Fig. 5.7i), the fiber barely deforms and cannot fit the obstacle shape. The trapping configurations result from the balance between the tilt induced by the lever arm due to gravity and the friction forces at the contact points with the obstacle. The trapping probability of the fiber therefore decreases as the tip of the obstacle narrows, as shown by the drop in the number of trapping events (TE) between $\mathcal{K} = -0.6$ and $\mathcal{K} = 0.6$ (panels $i(a-e)$). This competition between lever arm and friction at the tips obstacle leads to surprising trapping states for upward pointing triangles $i(d-e)$. In the highly flexible regime, $Be = 1000$ (Fig. 5.7iv), the fiber better fits the obstacle shape and its freely hanging extremities are aligned with the gravitational field. Such alignment with gravity induces a tangential load along the fiber centerline, which competes with friction in the high curvature regions of the obstacle. As a result, the fiber is mostly trapped by obstacles with high curvatures, i.e., for $\mathcal{K} = \pm 0.6$ (panels $iv(a)$ and $iv(e)$), and easily slips away from smooth obstacles (panels $iv(b-d)$).

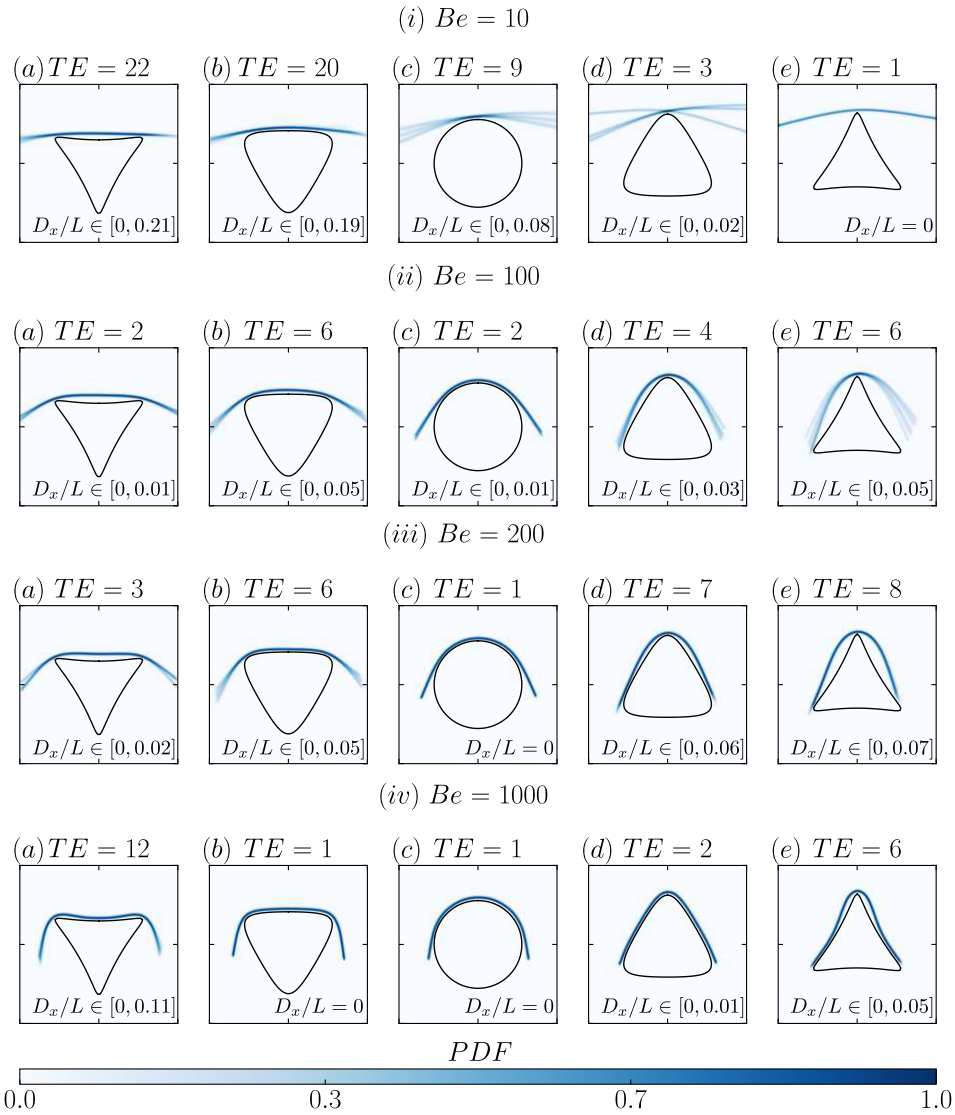

Figure 5.7: Probability distribution of the trapping configurations of the fiber around the obstacle, for $\xi = 2$ and various values of Be and $\mathcal{K}$. TE stands for the number of trapping events. Note that we used 10^2 initial configurations per shape and for a given value of Be, generated by varying the initial offset D_x/L between -0.5 and 0.5 with a step size of 10^{-2}. For the sake of clarity, the initial offsets of the showed configurations fall between 0 and 0.5, since the remaining configurations are the same by symmetry. The range of initial offsets corresponding to the trapping events is shown at the bottom of each panel. Parameter values are as in Fig. 5.4.

To further quantify the main differences between the stiff and flexible limits, we measure the total tangential (i.e., frictional) component of the resultant steric force, F_τ^R, acting on the fiber against an obstacle with a high trapping probability, $\mathcal{K} = -0.6$, as a function of the relative length ξ, for a small initial offset $D_x/L = 0.05$ (see Fig. 5.8(a)). First we notice that, regardless of the rigidity, the friction force is small for short relative lengths $\xi \leq 1$, where the fiber fully rests on the base of the triangle. When $\xi > 1$, the rigidity makes a big difference since the contact line with the obstacle becomes more and more localized along the fiber. In the rigid case ($Be = 10$), the tilt induced by the lever arm effect increases with ξ and so does the friction force to counterbalance the resulting tangential motion. In the flexible regime ($Be = 1000$), as soon as the fiber extremities stick out of the obstacle ($\xi > 1$), they align with gravity and generate a strong tangential load (i.e., a pulley effect). As a result the friction force jumps suddenly, by a factor 24, between $\xi = 1$ and $\xi = 2$ and is at least twice larger than the friction

on the rigid fiber. This is illustrated for $\xi = 2$ in the close-up views of Fig. 5.8(a), where the larger compliance of the flexible fiber leads to an extra frictional contact near the right edge of the triangle compared to the rigid one. For longer flexible fibers ($\xi = 5$), the curvature near the edges of the obstacle saturates and so does the friction force.

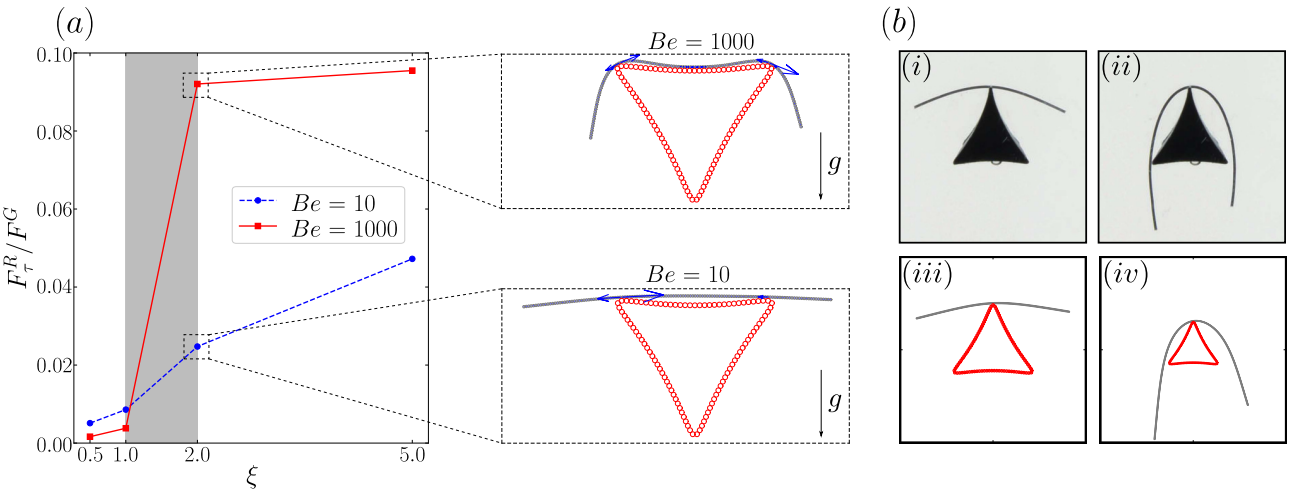

Figure 5.8: (a) Evolution of the tangential component (frictional force) of the steric force scaled by the gravitational force for two different values of Be and various values of ξ, $D_x = 0.05L$ and $\mathcal{K} = -0.6$. The close-up views show the corresponding distributions of the tangential component of the steric force along the fiber centerline, for $\xi = 2$. (b) Trapping events from experimental $(i - ii)$ and numerical $(iii - iv)$ results obtained for $\mathcal{K} = 0.6$. (i) $Be = 36$ and $\xi = 2$. (ii) $Be = 210$ and $\xi = 4$. (iii) $Be = 10$ and $\xi = 2$. (iv) $Be = 200$ and $\xi = 5$.

In the intermediate semi-flexible regime ($Be = 100$, 200, see Fig. 5.7$ii - iii$), the increasing flexibility promotes alignment of the extremities with gravity but the fiber cannot fit obstacles with high curvatures. As a result fibers are much less trapped for $\mathcal{K} = -0.6$ because the strong tangential motion induced by the hanging extremities beats the friction with the pointy vertices of the triangle, while the increased contact area with a smooth inverted triangle, $\mathcal{K} = -0.3$, allows for more trapping configurations. For the upward pointing triangles, the fiber can bend enough so that friction at the tip can beat tangential motion. Fiber flexibility also allows one of its extremities to touch one of the sides of the triangle. The vertical component of the steric force between the obstacle side and the fiber extremity, which acts against gravity, increases as the obstacle curvature becomes negative, leading to higher trapping probability for $\mathcal{K} = 0.6$ than for $\mathcal{K} = 0.3$.

Some of the exotic, asymmetric, trapping states observed in numerical simulations with non-circular obstacles have also been reported in experiments. Figure 5.8$(b)i - ii$ shows two occurrences of relatively long fibers being trapped on a curved triangle ($\mathcal{K} = 0.6$) in the stiff ($Be \approx 36$ and $\xi = 2$) and semi-flexible ($Be \approx 210$ and $\xi = 4$) regimes. The two panels below (Fig. 5.8$(b)iii - iv$) show qualitatively similar trapping states from numerical simulations in the explored parameter state ($Be = 10$ and $\xi = 2$ for the stiff regime and $Be = 200$ and $\xi = 5$ for the semi-flexible case), thus confirming the relevance of our parametric exploration, and more importantly, showing that even a small amount of friction can lead to nontrivial trapping configurations. This good agreement with experiments suggests that the effective friction coefficient in our simulations is at least equal or larger than the experimental one. Finally, for the range of parameters considered, our analysis shows that trapping is overall minimized with smooth obstacles ($\mathcal{K} = 0, 0.3$). These findings could be used in the design of fiber sorting devices where trapping or long residence times are undesired.

5.4.3 Toward a sorting device

We have shown that an obstacle can reorient a settling fiber, and thus deviate its trajectory. This reorientation and its subsequent lateral motion strongly depend on the geometrical and mechanical properties of the fiber (Be, ξ) and the obstacle shape ($\mathcal{K}$).

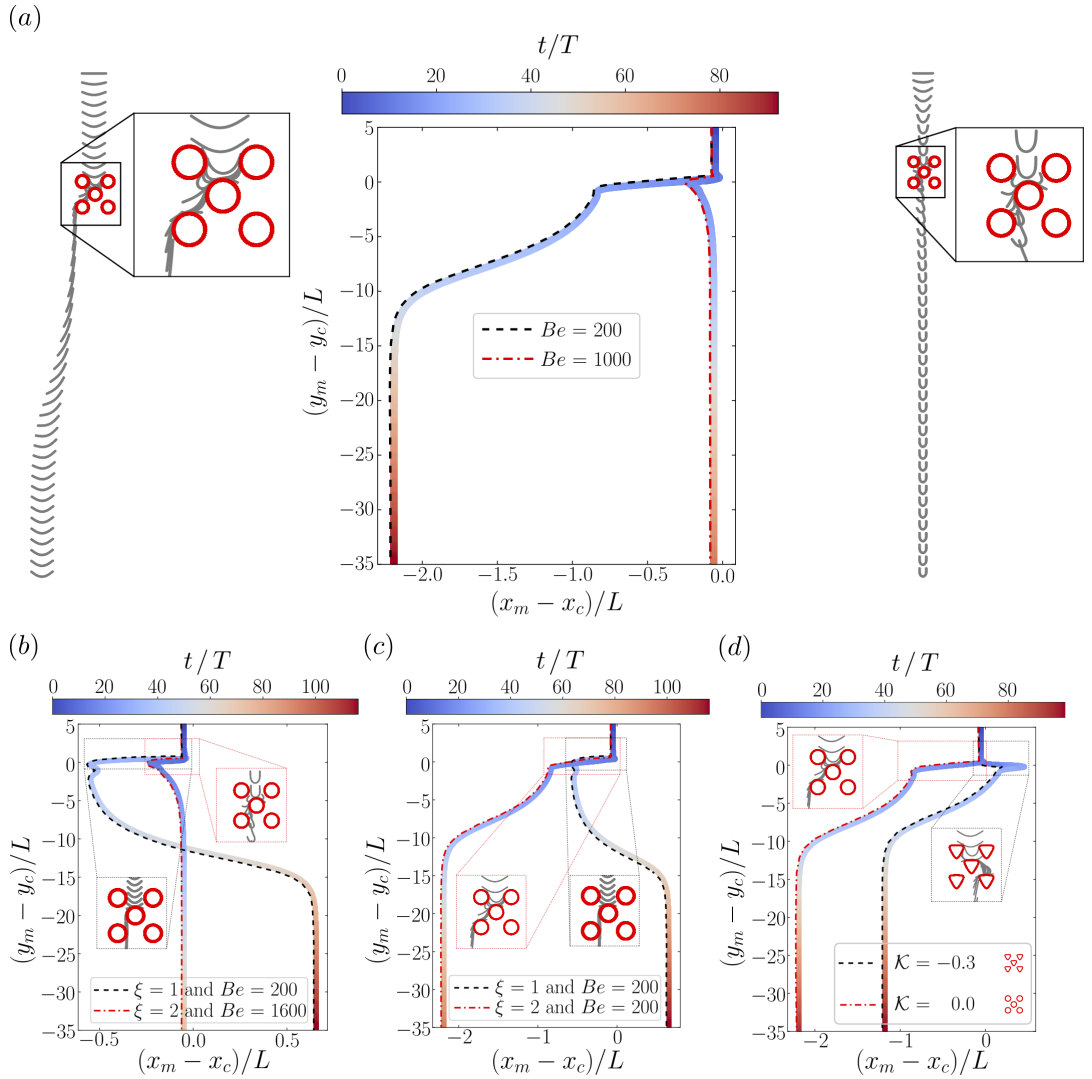

Figure 5.9: (a) The central panel shows the trajectories of the center of mass of two fibers with the same length $\xi = 2$ and different elasto-gravitational number, respectively $Be = 200$ and $Be = 1000$. The side to side panels show the corresponding chronophotographies of the fiber centerline settling through the unit cell, respectively on the left and right of the central panel (see also movies 11 and 12 in supplementary material (Makanga et al., 2023)). (b) Trajectories of the center of mass of two fibers with the same rigidity EI and different length, respectively $\xi = 1$ and $\xi = 2$. (c) Trajectories of the center of mass of two fibers with the same elasto-gravitational number $Be = 200$ and different length, respectively $\xi = 1$ and $\xi = 2$. (d) Trajectories of the center of mass of two fibers with the same elasto-gravitational number $Be = 200$ and length $\xi = 2$, settling through two different unit cells, respectively $\mathcal{K} = -0.3$ and $\mathcal{K} = 0$. In all cases studies, the initial offset of the fiber midpoint is set horizontally at $D_x/L = 0.05$ with respect to the center of the unit cell. Parameter values: $\Delta s/\mathcal{C} = 0.02$, $\alpha = 2$ and $D_y/L = 5$.

We now discuss how to leverage and guide such lateral dispersion with obstacles arranged in a lattice to sort fibers according to their flexibility and/or length. Our goal here is to provide

the proof of concept of a new, passive, sorting strategy rather than a systematic parametric exploration or optimization of the system. In the following, we analyze the motion of a fiber settling towards a unit cell of a centered square lattice of circular obstacles ($\mathcal{K} = 0$). The lattice spacing between nearest obstacles is $d = 1.5\omega$, which leaves a gap of $d - \omega = 0.5\omega$ for the fiber to go through. The fiber is initially released horizontally with a lateral offset $D_x = 0.05L$ with respect to the center obstacle. We consider two different sorting strategies: 1) sorting fibers by rigidity EI for a given length L, 2) sorting by length for a given rigidity.

To showcase the first sorting strategy, we consider two fibers with the same relative length $\xi = 2$ that differ by a factor 5 in their rigidity, so that their elasto-gravitational number are $Be = 200$ and $Be = 1000$ respectively. Figure 5.9(a) shows their conformation and trajectory over time. The most flexible fiber ($Be = 1000$) approaches the lattice with an equilibrium "U" shape such that its end-to-end width is smaller than the spacing between the obstacles in the first row of the lattice. As a result it directly falls onto the center obstacle, zigzags around it and escapes from the center of the lattice. Due to its high elasto-gravitational number, the fiber quickly readjusts to find its equilibrium "U" shape with almost no lateral displacement ($\delta x/L = 0.01$). On the other hand, the more rigid fiber approaches the lattice with a "V" shape that is wider than the entrance. It therefore interacts with the first two obstacles and migrates to the left side of the lattice. It thus lands on the outer side of the left obstacle, allowing it to exit vertically from the diagonal of the lattice and slowly reorient back to its equilibrium shape while drifting leftward. As a result, the fibers are separated by a distance $2.13L$ after passing only through one unit cell of the lattice, which clearly illustrates the potential efficiency of the first strategy with a larger lattice.

In the second scenario, only the fiber length changes. The shortest one has a relative length $\xi = 1$ and an elasto-gravitational number $Be = 200$. The second one is twice longer ($\xi = 2$), and thus has an elasto-gravitational number 8 times higher ($Be = 1600$). Due to its small size, the short fiber directly lands on the center obstacle (see Fig. 5.9($b-c$)). After wrapping around it, it aligns with gravity, and exits from the center of the lattice. It finally slowly reorients while drifting sideways which results in a lateral displacement of $\delta x/L = 0.7$. The second fiber is twice longer and 8 times more deformable, which allows it to bend between the pores (see Fig. 5.9(b)). It therefore follows a very similar trajectory to the first scenario ($Be = 1000$ and $\xi = 2$) shown in Fig. 5.9(a), where very little lateral displacement ($\delta x/L = 5 \times 10^{-4}$) is observed due to the short reorientation time. If the fibers were rigid regardless of their length, (i.e., $EI \gg 1$ so that $Be < 1$ for all L), then they would barely deform and the separation would be more efficient because the pore size would differentiate them: short fibers ($L/d < 0.5$) would fall vertically through the pores while long fibers ($L/d > 0.5$) would travel along the diagonals. However, our simulations suggest that non-rigid fibers tend to fall vertically and exit from the same location in the lattice regardless of their length. Indeed, long fibers ($\xi > 1$) are much more deformable than short ones (because of the L^3 factor in the elasto-gravitational number Be), and therefore bend and squeeze between the pores to fall in a zig-zag motion. Even though these fibers are not sorted inside the network, the lattice is still useful to reorient them so that the difference in their reorientation dynamics, and the subsequent lateral drift, separates them in the obstacle-free area underneath.

Although in most practical cases, the fibers would be sorted by length and/or rigidity, i.e. with coupled variations in both ξ and Be, we can isolate the mechanisms at play by varying ξ and keeping Be constant (i.e. by adjusting the rigidity EI) in order to identify the effect of changing the fiber length only. In that case, sorting becomes easier. Indeed, Fig. 5.9(c) shows the trajectory of two fibers of different length ($\xi = 1$ and $\xi = 2$ resp.) with the same elasto-gravitational number $Be = 200$. Because the longest fiber has the same deformability as the small one, it is now rigid enough to travel along the diagonal of the lattice. The final separation, here $2.84L$, is four times greater than in the previous scenario.

Finally, one may wish to optimize sorting by tuning the obstacle shape. In Figure 5.9(c) we compare the trajectory of a semi-flexible fiber ($Be = 200$ and $\xi = 2$) crossing a unit cell made of circles (already analysed above) and of smooth inverted triangles ($\mathcal{K} = -0.3$). The triangular obstacles have two main effect on the fiber trajectory: 1) the fiber follows a much more complex path across the lattice, leading to a different exit location (through the center instead of the diagonal); 2) due to prolonged contacts with the flat base of the triangles, the residence time of the fiber is increased by 50% ($15T$ instead of $10T$ for $\mathcal{K} = 0$), as expected from our analysis in Section 5.4.2. These effects may not be particularly desirable or easy to comprehend for the design of an efficient sorting platform. Furthermore, obstacles with circular cross-sections also minimize fiber trapping, and may thus provide a simple, easy to manufacture solution for optimal sorting.

5.5 Conclusions

The dynamics of a flexible fiber sedimenting in a structured medium is dictated by complex and intricate couplings, combining long-ranged hydrodynamic interactions, internal elastic stresses and contact forces (steric and/or friction) between the fiber and the surface of obstacles of arbitrary shape. With a combination of theory, numerical simulations and experiments, all of which show excellent quantitative agreement, we explain how these various mechanisms lead to lateral migration or trapping by obstacles.

Indeed, in a large tank, in the absence of obstacles, flexible fibers adopt an horizontal, curved, equilibrium shape and settle vertically. Upon hitting an obstacle, a fiber changes its orientation by an amount that depends on the obstacle shape $\mathcal{K}$, relative length ξ, fiber deformability Be and initial lateral offset D_x. As it relaxes back to its equilibrium shape the fiber drifts laterally due to its elongated shape. In the limit of small Be, the relaxation time scale and the resulting lateral displacement are inversely proportional to Be. This obstacle-induced lateral displacement under gravity can be used to passively sort fibers according to their Be and thus their mechanical properties E and/or length L. Preliminary simulations show that fibers can indeed be efficiently sorted by length and/or rigidity in a lattice of circular obstacles. This system has the major advantage of being fully passive, since no energy is needed, low-tech and simple to implement. The design of a sorting device only requires a tank and 3D-printed obstacles. However, even a small amount of friction (due to roughness) between the fiber and obstacle surfaces can lead to the trapping of the fiber. The trapping configurations and their likelihood depend on the obstacle shape and Be, and we find that the obstacle shape that best avoids trapping is a circular cross-section.

When transported by a background flow, a flexible fiber can migrate across the streamlines by dynamically changing its shape in the velocity gradients induced by the obstacle. However, even if the fiber undergoes drastic deformations (buckling, rotation, coiling, snaking,...), the resulting lateral displacement remains small compared to the fiber length ($\delta x/L < 1$) (Vakil and Green, 2011). In our system, the reorientation induced by the obstacle generates a lateral shift one to two orders of magnitude larger ($\delta x/L \sim O(1-100)$). We therefore believe our approach could be a complementary and promising alternative to the traditional deterministic lateral displacement (DLD) methods used to sort elongated particle in microfluidics (McGrath et al., 2014). In some practical situations (wastewater treatment, textile and micro-plastic clean-up, separation of pathogen populations), and in order to increase the throughput of our method, a whole fiber suspension would be injected in the device. If the fiber concentration is high enough, fiber-fiber hydrodynamic and contact interactions would probably affect their lateral displacement and their trapping likelihood. In the absence of obstacles, sedimenting fiber suspensions are known to exhibit clustering and large scale density fluctuations (Saintillan et al., 2005; Guazzelli and Hinch, 2011; Schoeller et al., 2021; Du Roure et al., 2019). The effect of

obstacles and porosity on these collective effects is an open fundamental question that we will tackle in the future to further develop our sorting strategy.

Chapter 6

Sedimentation of a flexible fiber in a structured environment

Contents

Remark: this chapter is written as a standalone article for publication.

The motion of flexible fibers often happens in complex environments that are structured by obstacles. Examples range from the transport of biofilm streamers through porous media to the design of sorting devices for DNA molecules. For large number of such problems, the dynamics of the fibers result from the complex interplay between internal elastic stresses, contact forces and hydrodynamic interactions with the obstacles. By means of numerical simulations, we investigate the dynamics of flexible fibers settling through a periodic array of pillars that is immersed in a quiescent viscous fluid. We show that the fiber trajectory falls at long times into one of two modes of migration, zigzag or displacement, that are determined by the short-time scattering dynamics induced by fiber-pillar interactions. In the zigzag mode, there is no average displacement from the direction of gravity, the fiber center of mass follows a quasi-straight line. Conversely, in the displacement mode, there is a net displacement from the direction of gravity, the fiber center of mass follows a cyclical skew bumping path. We show how this long-time behavior can be predicted through a theoretical model based on minimal ingredients. These findings, together with the long-time transport properties of the fiber, provide physical insight into future experiments, as well as the design of gravity-based sorting devices to sort elongated particles based on their size and/or elasticity.

6.1 Introduction

The motion of fibers in a fluid is ubiquitous in various situations. Examples include the process of making pulp in paper industries (Lundell et al., 2011), where cellulose fibers are mixed with water; and the transport of microplastic fibers through fluidic environments (Browne et al., 2011b; Engdahl, 2018; Re, 2019; Kane and Clare, 2019; Sutherland et al., 2023). Over the last

20 years, several studies focused on fluid-fiber interactions in different fluid domains, and resulted to numerous well known conclusions (Du Roure et al., 2019). However, there are many instances in nature and engineering applications where fiber-like particles must make their way through a fluidic environment embedded with obstacles, whose size is similar to the fiber characteristic length. In nature, bacteria often live in biofilms, which act as antibiotic-resistant and may lead to undesirable effects. Their migration to secondary sites results to the formation of biofilm streamers, large elastic filaments, that can lead to clogging while transported through complex environments (Dykaar and Kitanidis, 1996; Drescher et al., 2013). Understanding their navigation is essential for biomedical applications, for instance to prevent infections. In engineering applications, especially for particle sorting purposes, fiber-obstacle interactions are relevant to deterministic lateral displacement (DLD) device design, as the obstacles affect the long-time transport properties of fiber-like particles (e.g., long linear polymer chains such as DNA molecules) through repetitive collisions (Chou et al., 1999; Kulrattanarak et al., 2011a,b). In all the aforementioned situations, the dynamics of the fiber result from the complex interplay between internal elastic stresses, contact forces and hydrodynamic interactions with the surrounding obstacles.

To our knowledge, the transport of flexible fibers through structured environments has been the subject of few analytical (Doi and Edwards, 1988; Sevick and Williams, 2001; de Gennes, 2003), experimental (Chou et al., 1999; Dorfman et al., 2013) and numerical studies (Muthukumar and Baumgaertner, 1989; Patel and Shaqfeh, 2003; Nam et al., 2010; Kurzthaler et al., 2021). Recently, Chakrabarti et al., 2020 analyzed numerically the dynamics of semi-flexible polymers moving through a structured two-dimensional array of pillars, under the influence of an imposed flow. They reported three modes of transport: trapping, gliding, and vaulting, governed by the balance between dynamic buckling instabilities and steric interactions with the pillars. However, although the presence of thermal fluctuations affects the modes of migration, the magnitude of the overall lateral displacement remains small compared to the fiber length, as the fiber tends to align in the direction of the imposed flow. Therefore, the trajectory of the center of mass of the fiber generally follows the streamlines.

In contrast, while settling under gravity at low Reynolds number, due to its drag anisotropy, a rigid fiber drift laterally at a constant velocity and maintains its initial orientation with respect to the direction of gravity (Batchelor, 1970). When the fiber is allowed to bend, owing to the inhomogeneous drag distribution along its length, the fiber reorients to reach an equilibrium state after having traveled a finite distance (Li et al., 2013; Marchetti et al., 2018). Accordingly, the presence of an obstacle is expected to affect significantly the trajectory of the fiber. In our recent study (Makanga et al., 2023, see also Chapter 5), we showed that, while settling against a rigid obstacle of arbitrary shape, a flexible fiber can either glide or remain trapped on it. The trapping states lead to nontrivial conformations of the fiber that result from the balance between elastic stresses, gravity, and friction on the obstacle surface. On the other hand, gliding cases lead to a lateral displacement, whose the magnitude is large (typically several fiber lengths) and depends on the mechanical and geometrical properties of the fiber. In an array of rigid obstacles, it is clear that the repetitive collisions with the obstacles, as well as hydrodynamic interactions, will qualitatively change the dynamics described above, and therefore the trajectory of the fiber. Here, we investigate the dynamics of a single flexible fiber settling through a periodic array of pillars that is immersed in a quiescent viscous fluid. We show that the fiber trajectory falls at long times into one of two modes of migration, zigzag or displacement, that are determined by the short-time scattering dynamics. Furthermore, we examine the effect of mechanical and geometrical properties of the fiber on its long-time transport behavior. These findings provide physical insight into future experiments, as well as the design of sorting devices for the purpose of biomedical, microfluidics and environmental applications.

6.2 Problem description

We study the dynamics of a single flexible fiber settling under gravity through a periodic array of pillars that is immersed in a quiescent viscous fluid, of viscosity η. The fiber is an elastic rod of length L and has a circular cross-section of radius a. The fiber is settling at a characteristic velocity U such that the Reynolds number $\mathrm{Re} = \rho UL/\eta$ is always small, where ρ is the mass density of the fluid. Therefore, inertial effects are negligible compared to viscous ones. The array is made of rigid cylindrical pillars of infinite depth and width ω, see Fig.6.1. The geometry of the array is generated following the commonly-used convention for the design of *deterministic lateral displacement* (DLD) devices, used to sort particles in biological and microfluidic applications (Long et al., 2008; Kim et al., 2017). We denote by d the center-to-center distance between two adjacent pillars, see Fig.6.1. Starting from row (i), the subsequent row $(i+1)$ is placed downstream at a distance $\alpha_z d$ from the former, where $\alpha_z \in \mathbb{R}_+^*$. The pillars in this subsequent row are then shifted by a distance $\alpha_x d$ along the transverse direction, where α_x is known as the row-shift fraction. Following the same process, the n-th nearest row will be shifted by a distance $n\alpha_x d$ from row (i), $n \in \mathbb{N}^*$. Thus, a periodic array is obtained for $\alpha_x = 1/n$, and its structural angle ϕ_s is given by $\tan(\phi_s) = 1/(n\alpha_z)$. In this study, we set $\alpha_z = \sqrt{3}/2$ and $n = 2$. This setting leads to an array of pillars arranged in a hexagonal lattice, which we characterize by the structural angle, $\phi_s = \pi/6$, and the lattice spacing relative to the width of the pillars, d/ω.

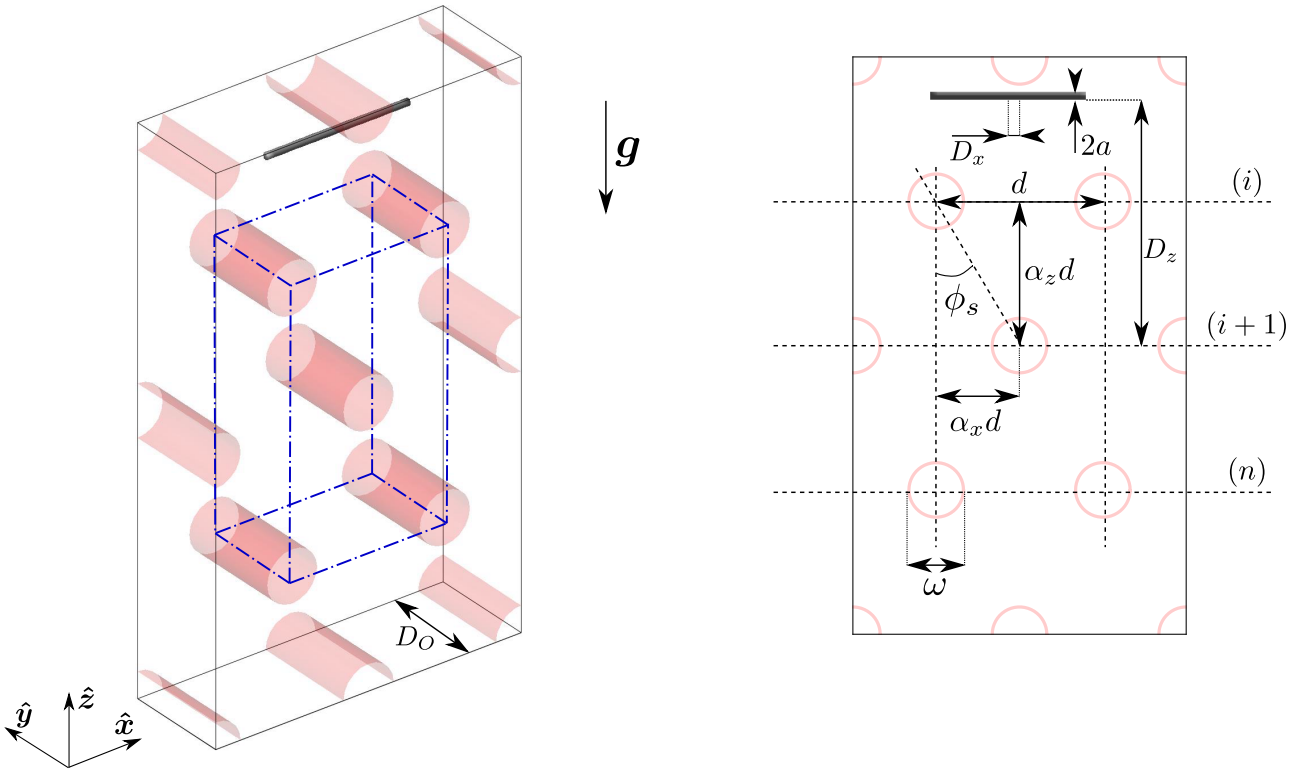

Figure 6.1: Schematic of the problem considered: A flexible fiber, initially straight, sediments under gravity in an array of rigid pillars, that is arranged in a hexagonal lattice, and immersed in a quiescent viscous fluid. **Left:** A 3D representation of the computational domain made of $2 \times 1 \times 2$ unit cells. A unit cell (indicated in blue) contains the equivalent to two pillars of depth D_O. **Right:** A planar representation of the computational domain, that shows an array of pillars, whose geometry is characterized by its topological parameters $\alpha_x = 1/2$ and $\alpha_z = \sqrt{3}/2$.

As done in Chapter 5, in addition to the aforementioned geometrical parameters to describe

the dynamics of the fiber through the array, we introduce the relative length of the fiber with respect to the width of the pillars, denoted as $\xi = L/\omega$, as well as the elastogravitational number $Be = F^G L^2/EI$, where $F^G = WL$ is the gravity force, W is the weight per unit length of the fiber, E its Young's modulus, and $I = \pi a^4/2$ the second moment of inertia of its cross-section. The elastogravitational number characterizes the deformation of the fiber at equilibrium, when settling under gravity in a viscous fluid. It results from the balance between gravitational and elastic restoring forces. When the value of Be increases, the equilibrium shape of the fiber evolves from rod-like to U-like shapes.

6.3 Model and numerical method

Simulations are performed using the method described in Chapter 4. We summarize the method here and we refer the reader to the aforementioned chapter for a more detailed description. The fiber model relies on the commonly-used bead-spring model. Accordingly, the fiber is discretized as a series of evenly spaced N_F beads $(\boldsymbol{r}_i)_{1\leq i\leq N_F}$ connected by stiff linkers made of springs, which do not bend or twist. Each bead of radius a is subject to two types of forces : (i) a gravitational force $\boldsymbol{F}^G/N_F$, where $F^G = |\boldsymbol{F}^G|$ is the weight of the whole fiber; and (ii) an internal elastic force $\boldsymbol{F}_i^E = -\nabla_{\boldsymbol{r}_i}\widetilde{\mathcal{E}}$, where $\widetilde{\mathcal{E}}$ is the elastic potential[1] and is given by

$$\widetilde{\mathcal{E}} = \underbrace{\frac{S}{4a}\sum_{i=2}^{N_F}\left(|\boldsymbol{t}_i| - 2a\right)^2}_{\widetilde{\mathcal{E}}^S} + \underbrace{\frac{B}{2a}\sum_{i=2}^{N_F-1}\left(1 - \hat{\boldsymbol{t}}_{i+1}\cdot\hat{\boldsymbol{t}}_i\right)}_{\widetilde{\mathcal{E}}^B}, \tag{6.1}$$

where $S = \pi E a^2$ and $B = \pi E a^4/4$ are respectively the stretching and the bending moduli, with E being the Young's modulus. The tangential vector between two neighboring beads is defined as $\boldsymbol{t}_i = \boldsymbol{r}_i - \boldsymbol{r}_{i-1}$, and $\hat{\boldsymbol{t}}_i = \boldsymbol{t}_i/|\boldsymbol{t}_i|$ is the corresponding unit vector. The first term on the right hand side of (6.1) is the stretching energy, namely $\widetilde{\mathcal{E}}^S$, and the second term is the bending energy, namely $\widetilde{\mathcal{E}}^B$. Similarly, each pillar of the array is discretized with N_O beads of radius a that are rigidly-connected. Since pillars are not moving, their beads must have zero velocity. This kinematic constraint is enforced with a set of constraint forces $\boldsymbol{F}^C$ applied on each bead that belongs to the pillars. Finally, owing to fiber-pillar contacts, a pairwise-repulsive force $\boldsymbol{F}^R$ is applied between the beads of pillars and the ones of the fiber, in order to prevent overlaps (see Chapter 5).

In our model, a unit lattice cell contains the equivalent to two pillars of depth D_O (see Fig.6.1), while the computational domain consists of $2\times 1\times 2$ unit cells, thus including the equivalent to 8 pillars of depth D_O, plus the fiber. Therefore the total number of beads in the computational domain is $N = N_F + 8N_O$. Due to the lack of inertia ($\mathrm{Re} \ll 1$), and in the absence of background flow, the kinematic equation of motion of the beads is given by the following linear mobility relation between velocities and forces

$$\frac{\mathrm{d}\boldsymbol{R}}{\mathrm{d}t} \equiv \boldsymbol{U} = \boldsymbol{\mathcal{M}}\cdot\left(\boldsymbol{F}^C + \boldsymbol{F}^G/N_F + \boldsymbol{F}^E + \boldsymbol{F}^R\right), \tag{6.2}$$

where $\boldsymbol{R} = [\boldsymbol{r}_1, \ldots, \boldsymbol{r}_{N_F}, \boldsymbol{r}_{N_F+1}, \ldots, \boldsymbol{r}_N]$ and $\boldsymbol{U} = [\boldsymbol{U}_1, \ldots, \boldsymbol{U}_{N_F}, \boldsymbol{U}_{N_F+1}, \ldots, \boldsymbol{U}_N]$, are $3N$ vectors collecting respectively bead positions and translational velocities. $\boldsymbol{\mathcal{M}}$ is their $3N\times 3N$ mobility matrix that encodes hydrodynamic interactions between all beads in the domain. This mobility matrix is given by the Rotne-Prager-Yamakawa (RPY) hydrodynamic tensor evaluated in a triply periodic domain (Fiore et al., 2017, see also Section 2.3), and we use the Positively-Split-Ewald (PSE) method (Fiore et al., 2017; Pérez Peláez, 2022, see also Appendix A) for a fast

[1] We are considering planar deformations, i.e., twisting of the fiber is neglected.

computation of its action $\boldsymbol{\mathcal{M}}\cdot(\cdot)$ on a given vector. Once $\boldsymbol{U}$ is computed, the bead positions are updated by a temporal integration of (6.2). We use an implicit integrator based on a backward differentiation formula (BDF) with adaptive time stepping (Brown et al., 1989), to alleviate the numerical stiffness arising from the springs, as well as from the elastohydrodynamic coupling problem.

In our simulations, the fiber is initially straight and oriented perpendicularly to the direction of gravity. It is positioned halfway the depth of the computational domain, with its midpoint at a given horizontal and vertical distance, D_x and D_z, from the center, see Fig.6.1.

6.4 Results and discussion

We start by a characterization of the long-time dynamics of the fiber through the array. The considered time interval is $100 \leq t/T \leq 300$, where $T = L\eta/W$ is the characteristic settling time. The dynamics of a single flexible fiber settling under gravity in a quiescent viscous fluid embedded with a rigid obstacle have been described and analyzed in detail in Chapter 5. The resulting findings provide a basis to investigate the dynamics in the present work. While settling against an obstacle of arbitrary shape, a flexible fiber can either glide or remain trapped around the latter. These two outcomes result from the complex interplay between internal elastic stresses, contact forces and hydrodynamic interactions with the obstacle, as well as the surrounding fluid. The trapping states lead to nontrivial conformations of the fiber that result from the balance between its elastic response, gravity, and friction on the obstacle surface. While in the gliding case, the fiber experiences a drift motion, leading to a lateral displacement whose the magnitude depends on its mechanical and geometrical properties, as well as on its initial orientation that is induced by the obstacle. In an array of rigid pillars, the lattice arrangement and spacing may influence the lateral displacement of the fiber, thus its migration through the former. Accordingly, we explore the two-dimensional parameter space ($10 \leq Be \leq 1000$, $2.36 \leq \xi \leq 6.28$) for a given lattice spacing $d/\omega \approx 3.53$ and depth $D_O/\omega \approx 2.36$. For each simulation, the fiber is released at $D_x/\omega \approx 0.12$ and $D_z/\omega \approx 5.22$, from the center of the computational domain.

Figure 6.2 shows the probability distribution (PDF) of the fiber centerline inside the computational domain at long times, where only the representative cases of the explored parameter space are illustrated, for the sake of clarity.
We identify two modes of migration of the fiber through the array, "zigzag" and "displacement" modes, for which the mechanisms at play will be detailed in Section 6.4.1. These two modes are respectively denoted (ZM) and (DM) in Fig.6.2, and can be characterized as follows. We denote by ϕ the migration angle of the fiber through the array. In the zigzag mode (see Fig.6.2(a), panels (ii) and (iii); Fig.6.2(b), panels (i) and (iii)), there is no average displacement from the direction of gravity, the trajectory of the fiber falls in a quasi-straight line with a migration angle close to zero, $\phi \approx 0$. In contrast, in the displacement mode (see Fig.6.2(a), panel (i); Fig.6.2(b), panel (ii)), there is a net displacement from the direction of gravity, the trajectory of the fiber falls in a cyclical skew bumping path with a cyclic period $n' = 3$, i.e., the number of rows of pillars after which the bumping pattern repeats itself. Thus, the resulting nonzero migration angle is given by $\tan(\phi) \approx 1/(n'n\alpha_z)$, and can be related to the structural angle of the array, $\tan(\phi) \approx \tan(\phi_s)/n'$. The latter relation implies that $\phi < \phi_s$, thus the fiber is always traveling with an angle that is less than the structural angle of the array. This finding is illustrated in Fig.6.3, that shows the migration angle relative to the structural angle, ϕ/ϕ_s, as function of the elastogravitational number Be ($10 \leq Be \leq 100$) for a fixed value of the relative length $\xi = 2.36$ (Fig.6.3(a)), and as function of the relative length ξ ($2.36 \leq \xi \leq 6.28$) for a fixed value of the elastogravitational number $Be = 100$ (Fig.6.3(b)). In addition, the migration angle is found to be the same $\phi \approx 0.36\phi_s$ for all displacement modes (DM), that are shown

by the gray-shaded zones in Fig.6.3. Therefore, for a given topology of the array, when its trajectory does not fall in a quasi-straight line at long times, the fiber will travel laterally with a constant angle, regardless of its mechanical and geometrical properties.

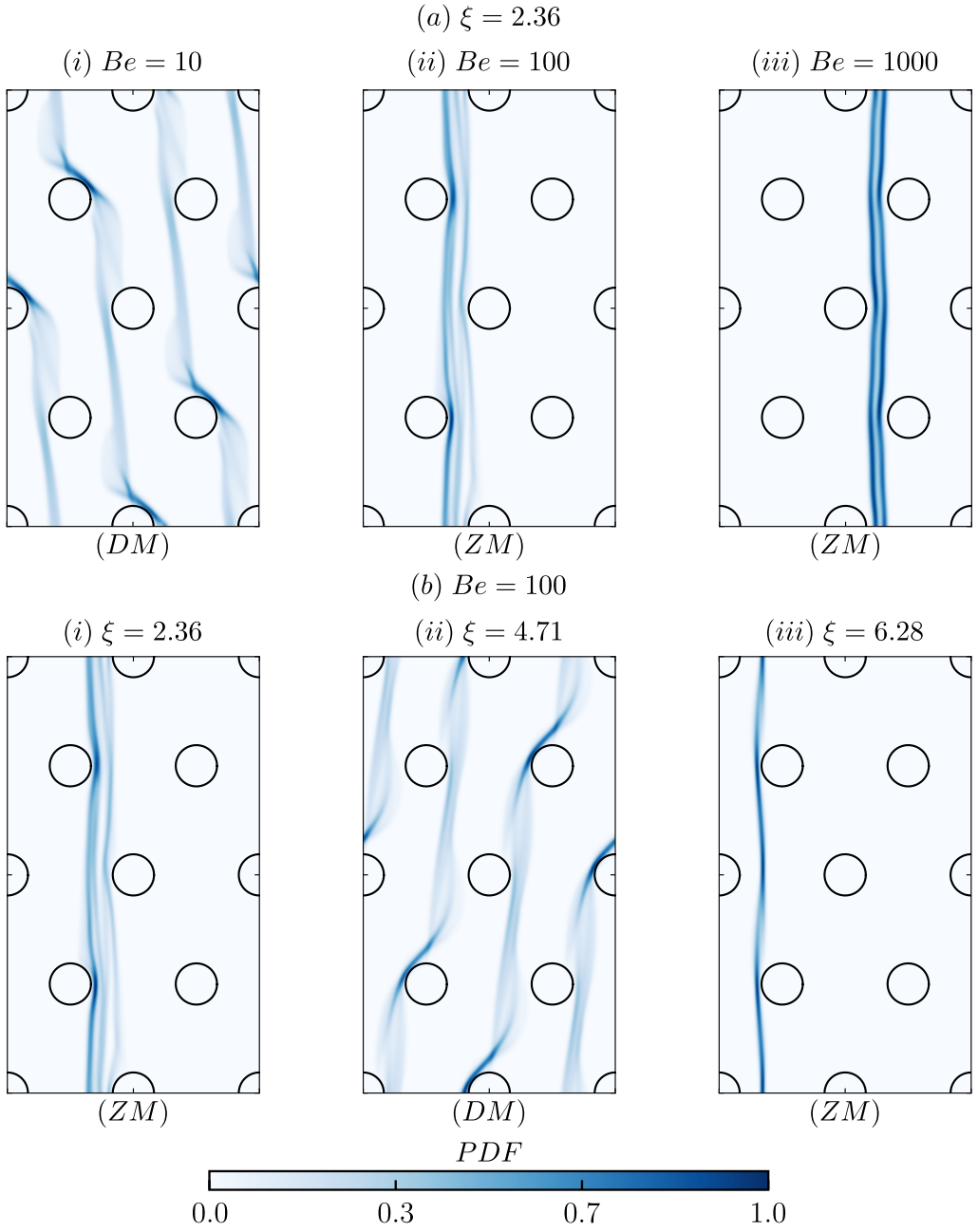

Figure 6.2: Probability distribution of the fiber centerline inside the computational domain at long times ($100 \leq t/T \leq 300$), where $T = L\eta/W$ is the characteristic settling time. These results are obtained from the explored two-dimensional parameter space ($10 \leq Be \leq 1000$, $2.36 \leq \xi \leq 6.28$). (ZM) and (DM) stand for "Zigzag Mode" and "Displacement Mode", respectively. Parameter values: $d/\omega \approx 3.53$, $D_O/\omega \approx 2.36$, $D_x/\omega \approx 0.12$ and $D_z/\omega \approx 5.22$.

Now that we have characterized the long-time trajectory of the fiber through the array, we discuss the mechanisms at play at short times ($0 \leq t/T < 100$) that lead to the two aforementioned modes of migration, namely the zigzag and displacement modes.

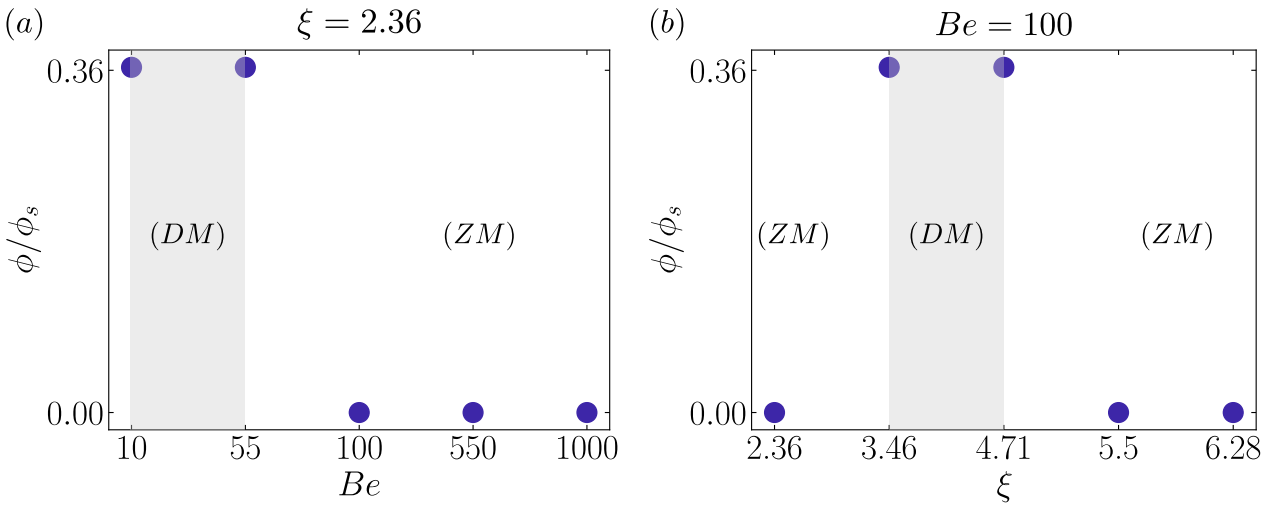

Figure 6.3: Migration angle normalized by the structural angle of the array, ϕ/ϕ_s. (a) As function of the elastogravitational number Be ($10 \leq Be \leq 100$) for a fixed value of the relative fiber length $\xi = 2.36$. (b) As function of the relative fiber length ($2.36 \leq \xi \leq 6.28$) for a fixed value of the elastogravitational number $Be = 100$. (ZM) and (DM) stand for "Zigzag Mode" and "Displacement Mode", respectively. Parameter values are as in Fig.6.2.

6.4.1 Short-time dynamics : scattering induced by fiber-pillar interactions

The behavior of the fiber at long times follows a reptation picture, which was first proposed by de Gennes, 2003, to describe the thermal motion of a long linear polymer chain through an array of fixed obstacles. The key assumption of the reptation theory is that, after short-time dynamics, the polymer chain experiences a snake-like motion through an imaginary tube formed by the surrounding obstacles, which prevent it from undergoing transverse displacements.

Unlike a long polymer chain that is driven by thermal fluctuations, the short-time dynamics of a non-Brownian flexible fiber under sedimentation through an array of rigid pillars, result from repetitive steric collisions and hydrodynamic interactions with nearby pillars. These lead to a scattering process, which determines the mode of migration of the fiber at long times. The scattering process can be decomposed into three steps: (i) the migration toward a given pillar of the array, (ii) the collision and the subsequent gliding along the pillar surface, and (iii) the escape. In the following, we focus on the collision events (step (ii)) to characterize the short-time dynamics. We denote by x_c, the contact point between one end of the fiber and the surface of the pillar; and by θ_c, the corresponding contact angle defined between the direction of gravity and the tangent vector directed outward at the end of the fiber. Fig.6.4 shows the two modes of scattering induced by fiber-pillar interactions, for which we define qualitative features by analogy with electromagnetic interactions:

- *In-scattering*: the contact angle and the contact point are unlike-charged, i.e., (θ_c^+, x_c^-) or (θ_c^-, x_c^+), referred to as "In" events in Fig.6.4.

- *Out-scattering*: the contact angle and the contact point are like-charged, i.e., (θ_c^+, x_c^+) or (θ_c^-, x_c^-), referred to as "Out" events in Fig.6.4.

With these pictures in mind, we now proceed to discuss the features of the scattering process before the limit of reptation. To do so, we track the end of the fiber that collides with a given pillar in the array at short times ($0 \leq t/T < 100$). We plot the corresponding path, from

the migration toward the pillar to the escape (steps $(i) - (iii)$), and we describe the different modes of scattering that occur at each collision event. These results are shown in Fig.6.5 for the explored parameter space ($10 \leq Be \leq 1000$, $2.36 \leq \xi \leq 6.28$).

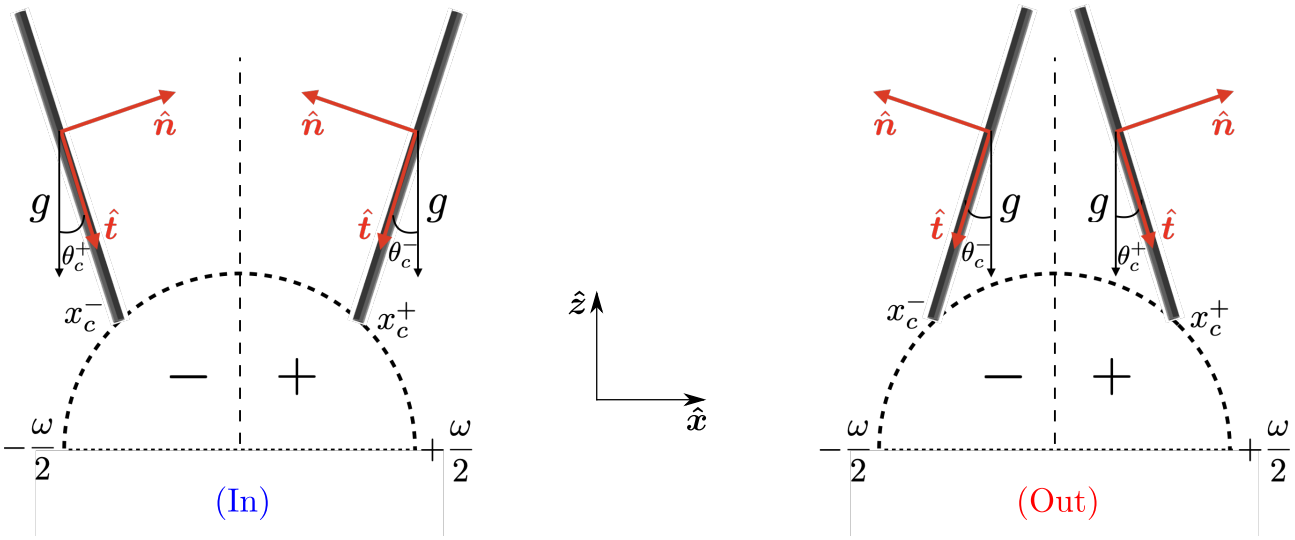

Figure 6.4: Schematic of the two modes of scattering induced by fiber-pillar interactions, which we define by analogy with electromagnetic interactions. **Left:** In-scattering mode, the contact point and the contact angle are unlike-charged, (θ_c^+, x_c^-) or (θ_c^-, x_c^+). **Right:** Out-scattering mode, the contact point and the contact angle are like-charged, (θ_c^+, x_c^+) or (θ_c^-, x_c^-). Note that, the contact angle θ_c is defined between the direction of gravity $-\hat{\boldsymbol{z}}$ and the unit tangent vector $\hat{\boldsymbol{t}}$ (directed outward) at the end of the fiber that is in contact with the surface of the pillar.

We first investigate the effect of flexibility ($10 \leq Be \leq 1000$) for a fixed fiber length, $\xi = 2.36$ (Fig.6.5(a)). In the stiff limit, $Be = 10$ (see Fig.6.5(a), panel (i)), after its first interaction with a pillar ($t/T = 17$), which is dictated by its initial configuration, the fiber follows a scattering process. The latter first falls two times consecutively in the "In" scattering mode, then alternates in a cyclic manner between "Out" and "In" scattering modes. This cyclic scattering pattern is a signature of a migration in a displacement mode (DM) at long times (see Fig.6.2(a), panel (i)). Owing to its long elastic relaxation time scale [$\mathcal{O}(Be^{-1})$], the fiber drifts rightward in a skew configuration after escaping from the surface of the pillar with which it collided. The subsequent lateral displacement is large and increases with the settling distance (see Fig.6.5(a), top panel of (i)). In the "In" scattering events, during its migration toward a pillar, the fiber settles a finite vertical distance less than d, the center-to-center distance between two adjacent pillars; such that its escape angle is close to its contact angle. Since the angle at which the fiber leaves a pillar is always smaller than $\pi/6$ (Makanga et al., 2023), the contact point at the surface of the pillar with which the fiber collides is such that $x_c \in [-\omega/2, 0)$. Therefore all collision events occur with positive contact angles on the left side of the collided pillars, (θ_c^+, x_c^-). Unlike the "In" scattering events, the fiber settles a vertical distance larger than d when approaching a pillar in the "Out" scattering events, such that its lateral displacement exceeds $\omega/2$ and leads to $x_c \in (0, +\omega/2]$. Therefore all collision events occur with positive contact angles on the right side of the collided pillars, (θ_c^+, x_c^+). On the other hand, in the flexible regime, $Be = 1000$, the fiber quickly relaxes to a U-like shape. As a result, it escapes from its first interaction ($t/T = 12$) with a hook-like shape while drifting rightward. This leads to a large orientation of its end compared to the structural angle of the array, typically larger than $2\phi_s$, where ϕ_s is the structural angle of the array (see Fig.6.5(a), top panel of (iii)).

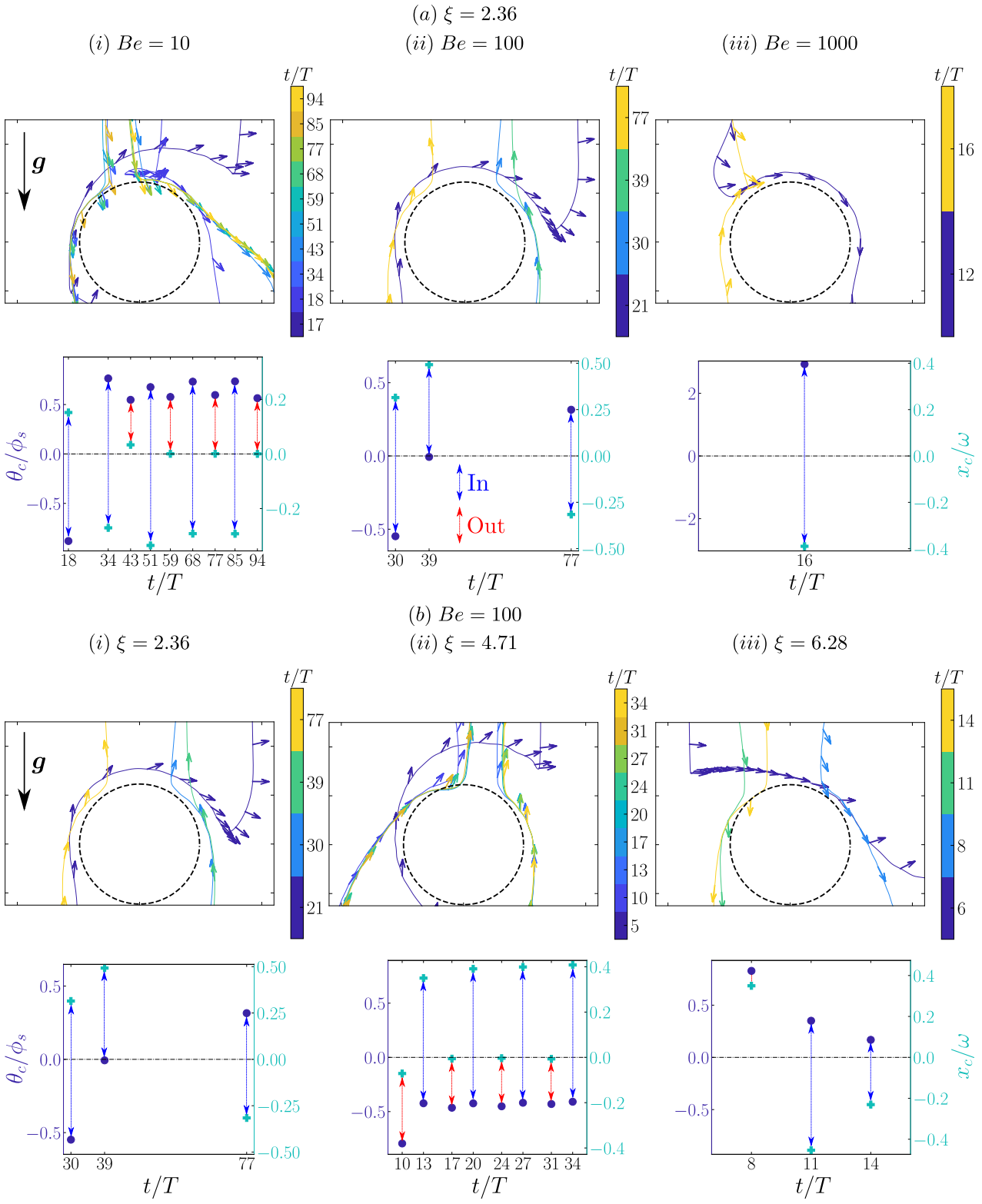

Figure 6.5: Results from numerical simulations showing the scattering process at short times. The trajectories represent the scattering of the fiber end which collides with a given pillar in the array, and the arrows represent the unit tangent vectors that define its orientation. The scattering events are represented from the migration toward the pillar to the escape. The corresponding scattering modes are shown in the subsequent row. (a) As function of the elastogravitational number Be ($10 \leq Be \leq 1000$), for a fixed value of the relative fiber length $\xi = 2.36$. (b) As function of the relative fiber length ξ ($2.36 \leq \xi \leq 6.28$), for a fixed value of the elastogravitational number $Be = 100$. Parameter values are as in Fig.6.2.

Since the allowed vertical distance for the fiber to settle until collision is smaller than d, the resulting contact angle θ_c^+ will be close to the escape angle, as well as the resulting contact point will fall on the left side of the collided pillar, x_c^-. This leads to a "In" scattering event, as shown in the scattering process (Fig.6.5(a), bottom panel of (iii)). The latter corrects the trajectory of the fiber, that results to a quick readjustment of its shape into a U-like shape, such that its end-to-end width is smaller than the lattice spacing. Thus, the trajectory of the fiber falls in a quasi-straight line with no average displacement from the direction of gravity (Fig.6.2(a), panel (iii)).

Finally, the effect of the fiber length ($2.36 \leq \xi \leq 6.28$) in the semi-flexible regime, $Be = 100$ (Fig.6.5(b)), affects the short-time dynamics as follows. For $\xi = 2.36$, the fiber length is smaller than the lattice spacing, $L/d \approx 0.67$. All the scattering modes fall in "In" events (see Fig.6.5(b), bottom panel of (i)), the surrounding pillars prevent the fiber from undergoing lateral displacements. As a result, the fiber migrates through the array in a quasi-straight line (Fig.6.2(b), panel (i)). Owing to its semi-flexibility, the fiber ends tend to align in the direction of gravity while escaping from the surface of the collided pillars (see Fig.6.5(b), top panel of (i)). Therefore, due to its near-zero escape angle and its slow reorientation toward its equilibrium configuration, the fiber exhibits small transverse displacements, less than $\omega/2$, while settling toward a pillar. These dynamics lead to the two types of "In" events shown in the scattering process (Fig.6.5(b), bottom panel of (i)), namely (θ_c^-, x_c^+) and (θ_c^+, x_c^-). When the fiber length is larger than the lattice spacing, $L/d > 1$, after its first interaction, the fiber cannot align with the direction of gravity while escaping from the surface of the pillar. As a result, the fiber end hits the subsequent pillar with a contact angle close to ϕ_s while its other end still gliding on the surface of the upstream pillar. This leads to the two "Out" scattering events shown at $t/T = 10$ and $t/T = 8$ in Fig.6.5(b) (bottom panel of (ii) and (iii)), respectively for $\xi = 4.71$ and $\xi = 6.28$. For each of these "Out" scattering events, the fiber bends significantly while escaping from the collided pillar, such that its lower end tends to align with the direction of gravity. In addition, its escape angle becomes smaller than ϕ_s, when the fiber end is close to the surface of the subsequent nearby pillar. Therefore, the collision event occurs with a negative angle on the right side of the collided pillar, (θ_c^-, x_c^+), for $\xi = 4.71$ (see Fig.6.5(b), bottom panel of (ii)); and with a positive angle on the left side of the collided pillar, (θ_c^+, x_c^-), for $\xi = 6.28$ (see Fig.6.5(b), bottom panel of (iii)). In these two cases, the resulting escape angle, together with the vertical distance that the fiber end has to settle before the next collision event, determine the subsequent scattering events. The shortest fiber, $\xi = 4.71$, escapes with a large angle at $t/T = 13$ (see Fig.6.5(b), top panel of (ii)), compared to the longest fiber ($\xi = 6.18$) at $t/T = 11$ (see Fig.6.5(b), top panel of (iii)). As a result, the former exhibits a large lateral displacement while drifting leftward, such as its contact point falls on the left side of the collided pillar, that leads to the "Out" scattering event (θ_c^-, x_c^-) shown at $t/T = 17$ in the scattering process (Fig.6.5(b), bottom panel of (ii)); and the latter is less laterally displaced than the former while drifting rightward, such as its contact point falls on the left side of the collided pillar, that leads to the "In" scattering event (θ_c^+, x_c^-) shown at $t/T = 14$ in the scattering process (Fig.6.5(b), bottom panel of (iii)). Thus, once a steady state is achieved, the trajectory of the shortest fiber ($\xi = 4.71$) falls in a cyclical skew bumping path, which is a signature of a migration in a displacement mode (DM) at long times (see Fig.6.2(b), panel (ii)); and the one of longest fiber ($\xi = 6.28$) falls in a quasi-straight line, which is a signature of a migration in a zigzag mode (ZM) at long times (see Fig.6.2(b), panel (iii)).

Now that we have a clear understanding on how the scattering process at short times leads to the two aforementioned modes of migration at long times, namely the zigzag and the displacement modes, we use analytical tools to predict in which mode of migration the trajectory of the fiber will fall according to its intrinsic properties, i.e., geometrical and mechanical properties, as well as to the geometry of the array, i.e., the lattice arrangement and spacing.

We consider the limit of large lattice spacings, $d/L \gg 1$, where the scattering modes are determined by the escape configuration, i.e., when the fiber is no longer in contact with the collided pillar; and by the vertical distance that the fiber has to settle for the subsequent collision event to occur. We denote by θ_0 the escape angle of the fiber, that is its incident angle for the subsequent collision event; and by $h_x d$ and $h_z d$, the lateral shift and the vertical distance, at which the center of the pillar is initially positioned with respect to the nearest end of the fiber, see Fig.6.6(a). In the limit of small deformation amplitudes, $Be \ll 1$, the time-dependent parametric equation of the path $\mathcal{L}$ of the lower end of the fiber $(X(t), Z(t))$, while sedimenting without interacting with the pillars, is given by

$$\mathcal{L}: \begin{cases} \tan\left[(2CBe/c_0)X + \theta_0\right] = \tan\left(\theta_0\right)\exp\left[(2CBe)t\right], \\ Z = -c_0 t - \dfrac{c_0}{4CBe}\ln\left\{\dfrac{\left[1+\tan^2\left(\theta_0\right)\right]\exp\left[(4CBe)t\right]}{1+\tan^2\left(\theta_0\right)\exp\left[(4CBe)t\right]}\right\}, \end{cases} \quad t \in [0, +\infty) \tag{6.3}$$

with

$$C = \frac{7}{400} + c_0^{-1}\left(\frac{1813 - 300\pi^2 + 630\ln\left(2\right)}{18000}\right), \tag{6.4}$$

where c_0 is related to the aspect-ratio of the fiber $\varepsilon^{-1} = L/2a$ as follows, $c_0 = \ln\left(1/\varepsilon^2 e\right)$. This parametric equation is derived for a slender fiber with uniform thickness, following the approach described in Appendix B of Li et al., 2013. We refer the reader to Appendix C of this thesis for a more detailed description.

The settling trajectory is obtained by eliminating t in (6.3), this leads to the following implicit formulation

$$\begin{aligned} \mathcal{L}: \quad &\left\{(X, Z) \in \mathbb{R}^2, \right. \\ &\left. \tan\left(\theta_0\right)\sin^2\left(\theta_0\right)\exp\left[-(2CBe/c_0)Z\right] = \tan\left[(2CBe/c_0)X + \theta_0\right]\sin^2\left[(2CBe/c_0)X + \theta_0\right]\right\}. \end{aligned} \tag{6.5}$$

Linearizing (6.5) about $X = 0$ (the fiber exhibits small lateral displacements compared to its length), we obtain

$$\begin{aligned} \tan\left(\theta_0\right)\sin^2\left(\theta_0\right)\exp\left[-(2CBe/c_0)Z\right] = &\tan\left(\theta_0\right)\sin^2\left(\theta_0\right) \\ &+ (2CBe/c_0)[2\sin^2\left(\theta_0\right) + \tan^2\left(\theta_0\right)]X + \mathcal{O}(X^2), \end{aligned} \tag{6.6}$$

thus

$$X \sim \frac{c_0\tan\left(\theta_0\right)\left\{\exp\left[-(2CBe/c_0)Z\right] - 1\right\}}{2CBe[3 + \tan^2\left(\theta_0\right)]}, \tag{6.7}$$

linearizing (6.7) about $\theta_0 = 0$ (the fiber ends tend to align in the direction of gravity), leads to

$$X \sim \frac{c_0}{6CBe}\theta_0\left\{\exp\left[-(2CBe/c_0)Z\right] - 1\right\}. \tag{6.8}$$

Holding CBe/c_0 constant in (6.8), we observe that the lateral displacement is monotonic in the incident angle θ_0 for a small longitudinal displacement, i.e., vertical motion in the direction of gravity.

For a given incident angle θ_0, the contact point between the lower end of the fiber and the surface of the pillar, is any point of $\mathcal{L}$ that lies on the latter. We denote by $\boldsymbol{R}_O$, the time-dependent position of the center of the pillar with respect to the lower end of the fiber, see Fig.6.6(a). Thus, the set of contact points $\mathcal{C}$ is given by

$$\mathcal{C} = \{X \in \mathcal{L} \text{ such that } |\boldsymbol{R}_O| = \omega/2\}, \tag{6.9}$$

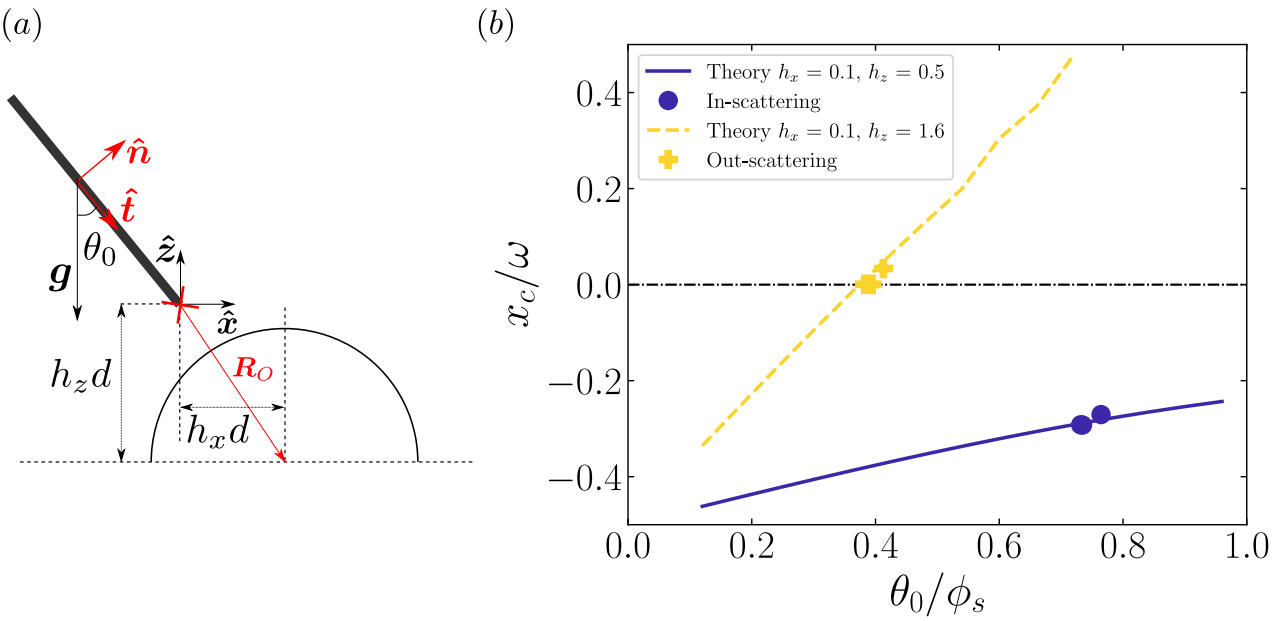

Figure 6.6: (a) Illustration of the migration of the fiber toward the pillar. The center of the pillar is positioned initially at a given lateral shift $h_x d$ and vertical distance $h_z d$, from the nearest end of the fiber. $\hat{\boldsymbol{t}}$ and $\hat{\boldsymbol{n}}$ are the unit tangent and unit normal vectors, respectively. The incident angle θ_0 is defined between $\hat{\boldsymbol{t}}$ and the direction of gravity -$\hat{\boldsymbol{z}}$. (b) Scaled contact points x_c/ω vs θ_0/ϕ_s. Comparison of the theoretical predictions (lines) and numerical results (markers). These results are obtained for $Be = 10$ and $\xi = 2.36$, the latter corresponds to $\varepsilon^{-1} = 15$. Parameter values are as in Fig.6.2.

where ω is the width of the pillar. Fig.6.6(b) shows two sets of contact points for various values of θ_0 ($\pi/50 \leq \theta_0 \leq \pi/6$). These two sets are obtained for $Be = 10$ and $\varepsilon^{-1} = 15$ ($\xi = 2.36$), where the corresponding parameters (h_x, h_z) are extracted from numerical simulations for the two modes of scattering (see Fig.6.5(a), panel (i)), In-scattering (solid line) and Out-scattering (dashed line).

In the limit of small incident angles, the two sets of contact points exhibit a linear growth, that agrees with (6.8). Furthermore, numerical results are in good agreement with theoretical predictions, thus confirming the adequacy of our simple theoretical model to predict the scattering process that the fiber will experience at short times; in the limit of small deformations and large lattice spacings. These findings may be used to predict in which mode of migration the trajectory of a fiber-like particle will fall at long times, according to the geometry of the array, i.e., the lattice arrangement and spacing. For instance, array geometries that are designed such that $h_x \leq 0.1$ and $h_z \leq 0.5$ hold for most of the scattering events at short times, will lead to a migration of the fiber in a zigzag mode, see Fig.6.6(b).

6.4.2 Long-time transport properties

We now set out to describe the long-time transport properties of the fiber. To do so, we introduce the mean square displacement (MSD) and rotation (MSR), that are defined respectively as

$$\boldsymbol{\Xi}(\tau) = \langle [\overline{\boldsymbol{r}}(t+\tau) - \overline{\boldsymbol{r}}(t)]\,[\overline{\boldsymbol{r}}(t+\tau) - \overline{\boldsymbol{r}}(t)] \rangle\,, \tag{6.10}$$

and

$$\Theta(\tau) = \langle [\theta(t+\tau) - \theta(t)]\,[\theta(t+\tau) - \theta(t)] \rangle\,, \tag{6.11}$$

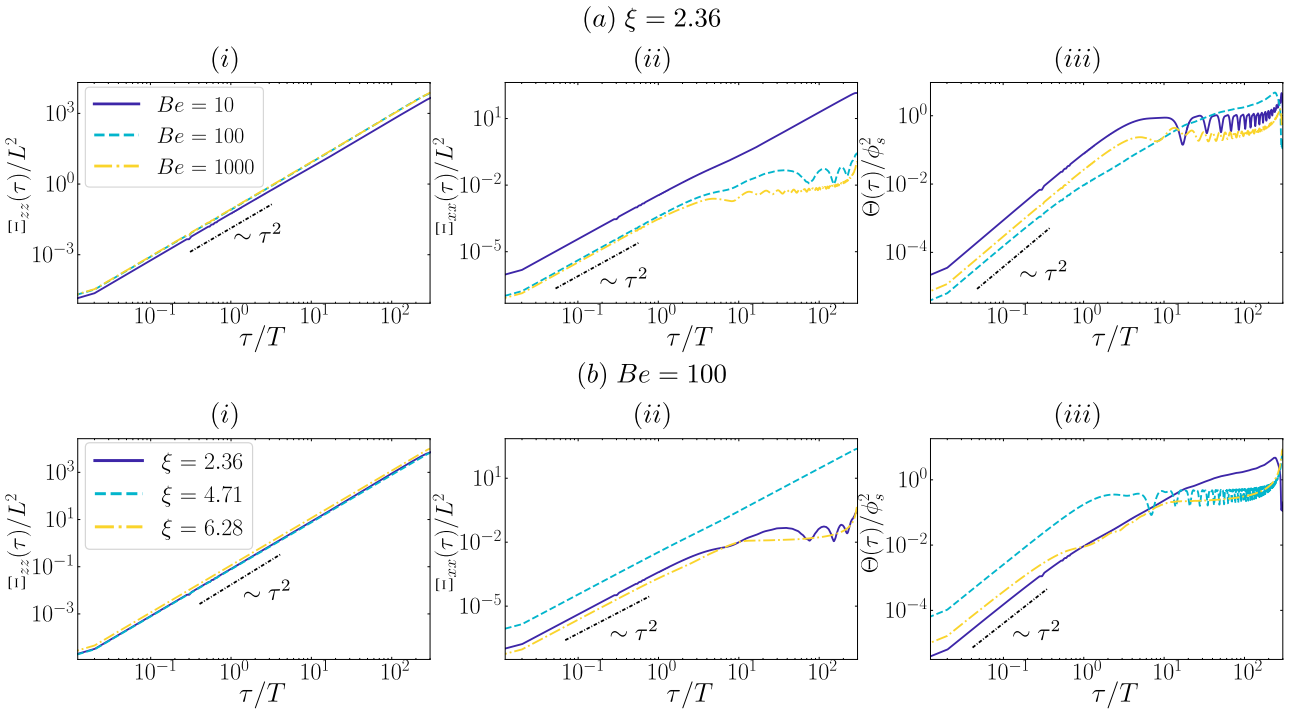

Figure 6.7: Results from numerical simulations showing the time evolutions of the two relevant components of the mean square displacement tensor (MSD) relative to the fiber length square, Ξ_{zz}/L^2 and Ξ_{xx}/L^2; and the mean square rotation (MSR) relative to the structural angle of the array square, Θ/ϕ_s^2. (a) As function of the elastogravitational number Be ($10 \leq Be \leq 1000$), for a fixed value of the relative fiber length $\xi = 2.36$. (b) As function of the relative fiber length ξ ($2.36 \leq \xi \leq 6.28$), for a fixed value of the elastogravitational number $Be = 100$. Parameter values are as in Fig.6.2.

where $\langle\cdot\rangle$ denotes the ensemble average. The mean square displacement $\boldsymbol{\Xi}$ is dyadic and measured at the center of mass of the fiber, $\overline{\boldsymbol{r}}$. While the mean square rotation Θ is obtained from the angle θ, measured between the direction of gravity and the unit tangent vector at the fiber midpoint. These two quantities are shown in Fig.6.7 for the explored parameter space ($10 \leq Be \leq 1000$, $2.36 \leq \xi \leq 6.28$); where only the two relevant components of $\boldsymbol{\Xi}$ are represented, Ξ_{zz} and Ξ_{xx}.

The fiber dynamics display a short-time regime, in which the effect of flexibility and length are reflected on both, Ξ_{xx} (panels (ii) in Fig.6.7(a) and Fig.6.7(b)) and Θ (panels (iii) in Fig.6.7(a) and Fig.6.7(b)) . This regime is followed by a ballistic regime at intermediate times, that is characterized by a linear increase of slope two, $\sim \tau^2$. The short and intermediate regimes are dominated by the scattering process, as discussed in the previous section. Since the longitudinal behavior of the fiber, i.e., its vertical motion in the direction of gravity, is also ballistic at long times (panels (i) in Fig.6.7(a) and Fig.6.7(b)), regardless of its flexibility and length, i.e., the fibers move longitudinally at the same velocity, we focus on the time-evolution of Ξ_{xx}, as the latter displays features that will determine the mode of migration of the fiber through the array.

For the stiff case, $Be = 10$, as well as for the intermediate length with $Be = 100$, the long-time regime is also ballistic: Ξ_{xx} maintains the same increase as in the intermediate regime (panels (ii) in Fig.6.7(a) and Fig.6.7(b)) which is indicative of a migration in a displacement mode. Conversely, in the other cases, the ballistic regime is followed by a caged regime, where Ξ_{xx} displays a plateau. This saturation of Ξ_{xx} reflects the formation of an imaginary tube by the surrounding pillars, which prevent the fiber from undergoing lateral displacements. This is indicative of a migration in a zigzag mode. At later times, however, we observe that Ξ_{xx} sud-

denly increases and gradually decreases after, regardless of the flexibility and the length of the fiber. This sudden variation results from the reorientation of the fiber in the less topologically constrained direction, which is well reflected by the change in Θ observed at long times (panels (iii) in Fig.6.7(a) and Fig.6.7(b)). We expect that at very long-time dynamics, though not captured owing to the finite duration of our simulations, Ξ_{xx} and Θ will display a plateau, as the fiber will reach its equilibrium shape in the less topologically constrained direction. Therefore, all the trajectories will fall in quasi-straight lines with migration angles close to zero, regardless of the flexibility and the length of the fiber.

To further characterize its long-time reorientation, we investigate the deformation of the fiber. To do so, we introduce the gyration tensor $\boldsymbol{Q} \in \mathbb{R}^{3\times3}$ of the fiber (Blavatska and Janke, 2010; Arkın and Janke, 2013), whose components are given by

$$Q_{jk} = \frac{1}{N_F}\sum_{i=1}^{N_F}[x_i^{(j)} - x_M^{(j)}][x_i^{(k)} - x_M^{(k)}], \quad j,k = 1,2,3, \tag{6.12}$$

where $x_i^{(j)}$ and $x_M^{(j)}$ are respectively the components of the fiber bead position $\boldsymbol{r}_i \in \mathbb{R}^3$, and the fiber midpoint $\boldsymbol{r}_M \in \mathbb{R}^3$. Since the gyration tensor is symmetric, there exists a basis in which it can be diagonalized. Its eigenvalues also known as *moments* can be combined to characterize the fiber shape. Let $(\lambda_i)_{1\leq i\leq 3}$ be the eigenvalues of $\boldsymbol{Q}$ and $\overline{\lambda} \equiv \mathrm{Tr}\boldsymbol{Q}/3$ their average. Thus, the relative shape anisotropy of the fiber, denoted κ^2, is given by

$$\kappa^2 = \frac{1}{6}\sum_{i=1}^{3}\frac{(\lambda_i - \overline{\lambda})}{\overline{\lambda}^2} = \frac{3}{2}\frac{\mathrm{Tr}\hat{\boldsymbol{Q}}^2}{(\mathrm{Tr}\boldsymbol{Q})^2}, \tag{6.13}$$

where $\hat{\boldsymbol{Q}} \equiv \boldsymbol{Q} - \overline{\lambda}\boldsymbol{I}$, with $\boldsymbol{I} \in \mathbb{R}^{3\times3}$ being the identity matrix. This quantity evolves from zero to one, where its lower bound corresponds to an isotropic shape, i.e., all the eigenvalues are equal; and its upper bound to a rod-like shape, i.e all the eigenvalues are zero except for one. Furthermore, the dominant eigenvalue of the gyration tensor determines the orientation θ of the fiber with respect to the direction of gravity. Figure 6.8 shows the long-time evolutions of the relative shape anisotropy, κ^2; and the orientation of the fiber at its midpoint relative to the structural angle of the array, θ/ϕ_s. These both quantities are represented for various values of the elastogravitational number Be ($10 \leq Be \leq 1000$) at a fixed value of the relative length $\xi = 2.36$, Fig.6.8(a); and for various values of the relative length ξ ($2.36 \leq \xi \leq 6.28$) at a fixed value of the elastogravitational number $Be = 100$, Fig.6.8(b).

In the semi-flexible regime ($10 \leq Be \leq 100$), the fiber weakly deforms, its shape remains quasi-straight $\kappa^2 \approx 1$, while its orientation θ varies in the two modes of migration. The time-periodic evolutions of θ characterize a cyclical skew bumping trajectory, that is a signature of a migration in a displacement mode (DM). Conversely, when $\theta \approx 0$ the fiber is nearly oriented to the direction of gravity, while moving through the array, that is a signature of a migration in a zigzag mode (ZM). However for $\xi = 2.36$ and $Be = 100$, we observe a sudden jump in the orientation angle from $\theta \approx 0$ to $\theta \approx 2.5\phi_s$ (see the gray-shaded zones in Fig.6.8(a)-(b), panels (ii)), while the fiber still roughly straight $\kappa^2 \approx 1$, and executes a zigzag motion through the array. During this transition, the fiber rotates around the x-axis to roughly aligned perpendicularly with the direction of gravity in the yz-plane, which is the less topologically constrained direction of the array. This reorientation is shown in Fig.6.9, and leads to a lateral displacement of the fiber along the y direction.

Finally, in the highly flexible regime ($Be \geq 1000$), the fiber adopts a roughly U-like shape $\kappa^2 \approx 0.5$, while traveling quasi-periodically through the array, with a mean orientation angle $\theta \approx 2\phi_s$, i.e., the fiber is oriented quasi-perpendicularly to the direction of gravity.

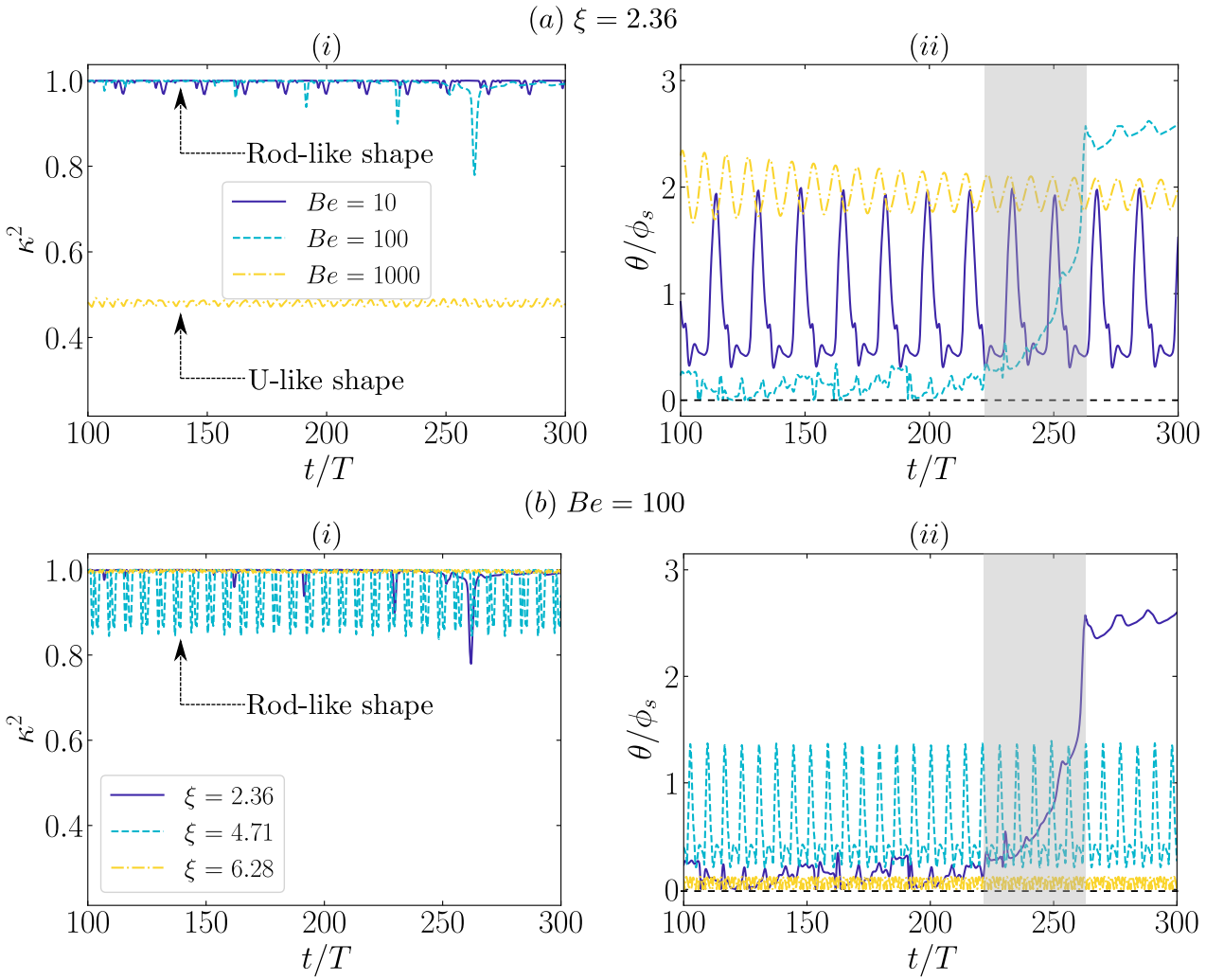

Figure 6.8: Long-time evolutions of the relative shape anisotropy κ^2 of the fiber and its orientation (measured at its midpoint) with respect to the direction of gravity. The latter is normalized by the structural angle of the array, θ/ϕ_s. These results are obtained from the explored two-dimensional parameter space ($10 \leq Be \leq 1000$, $2.36 \leq \xi \leq 6.28$). Parameter values are as in Fig.6.2.

6.5 Conclusions

The dynamics of flexible fibers in a periodic array of pillars, result from the complex interplay between internal elastic stresses, contact forces, and hydrodynamic interactions with the pillars, as well as the surrounding fluid. By means of numerical simulations, we have investigated the long-time behavior of a single flexible fiber settling under gravity through a periodic array of pillars, that is immersed in a quiescent viscous fluid. Our findings show that the long-time trajectory of the fiber falls into one of two modes, zigzag (ZM) or displacement (DM). In the former, there is no average displacement from the direction of gravity, therefore the center of mass of the fiber follows a quasi-straight line with a migration angle close to zero. In the latter, there is a net displacement from the direction of gravity, the center of mass of the fiber follows a cyclical skew bumping path.

The short-time scattering of the fiber by the stationary pillars was found to dictate the aforementioned behavior. Especially the contact angle, i.e., the angle with which the fiber collides with a given pillar in the array, and the resulting contact point. These two quantities are determined by the intrinsic properties of the fiber, i.e., its flexibility and length, as well as the

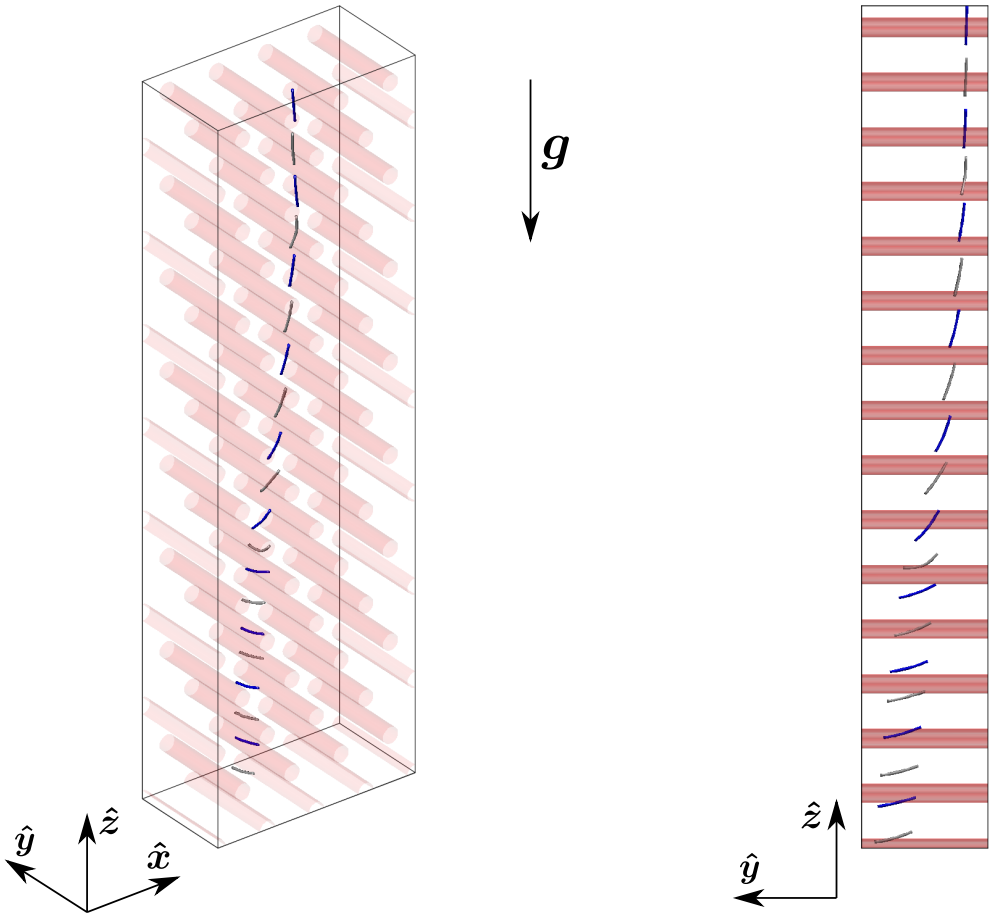

Figure 6.9: Chronophotographs showing the long-time reorientation of the fiber for $\xi = 2.36$ and $Be = 100$, while settling through the array of pillars. The results are shown for the time interval $215 \leq t/T \leq 300$, where $T = L\eta/W$ is the characteristic settling time. The time step between two consecutive frames (shown with alternating colors: blue and gray) is $\Delta t \approx 9T$. **Left:** A 3D representation. **Right:** A planar representation in the yz-plane.

topology of the array, i.e., its lattice arrangement and spacing. In the limit of small deformations ($Be \ll 1$) and large lattice spacings ($d/L \gg 1$), we propose a toy model to predict the scattering process that the fiber will experience at short times, and therefore in which mode of migration its trajectory will fall at long times. These findings, together with the long-time transport properties of the fiber, provide physical insight into future experiments, as well as the design of gravity-based deterministic lateral displacement (DLD) devices to sort fiber-like particles for the purpose of biomedical, microfluidics and environmental applications. In practical situations such as wastewater treatment, a suspension of fiber-like particles is released from the top of a vessel which contains an array of stationary obstacles, the fibers will eventually clump together to form clusters (Metzger et al., 2007a; Saintillan et al., 2006; Manikantan and Saintillan, 2016) which will interact hydrodynamically and collide with the surrounding obstacles. From this complex coupling, may emerge unexpected collective dynamics whose understanding will inspire future works on the transport of fiber suspensions in structured environments.

Conclusions and future directions

Conclusions and future directions

Conclusions

In this thesis, we have proposed a methodology to conduct numerical simulations for problems involving flexible fibers and obstacles. Our method relies on a multibead approach to solve Stokes flow with stationary and moving boundaries. Such problems require to prescribe the motion of stationary boundaries, such that their velocities are always zero. We used a set of Lagrange multipliers to enforce these kinematic constraints, and solved the resulting constrained problem iteratively with a preconditioned GMRES solver. We have shown that this problem can converge quickly with a suitable preconditioner, such that the rate of convergence becomes independent of the obstacle shape and the number of obstacle beads. This feature allows to reduce significantly the computational cost, and therefore to carry out simulations of large systems. By doing so, we provide an effective tool for studying a variety of problems involving fibers and obstacles.

Using this numerical framework, together with simple experiments, we have investigated the settling dynamics of flexible fibers in a viscous fluid with embedded obstacles. In particular, we have found that fiber-obstacle interactions may lead to trapping or scattering events, owing to the complex coupling between internal elastic stresses, gravity, contact forces, and hydrodynamic interactions. The trapping events result from the balance between frictional forces along the fiber centerline and gravity. As a result, in the flexible regime, the fibers easily escape from smooth obstacle shapes since the fiber ends tend to align in the direction of gravity. This finding provides insight into the design of microfluidic devices. For instance, in some applications such as sorting processes, the circular cross-section obstacles are particularly interesting to avoid trapping events hence to prevent microfluidic devices from clogging. In addition, we have found that the scattering dynamics govern the long-time behavior of the fibers, such that they can undergo lateral displacements from the direction of gravity. We leveraged these findings to propose a strategy to sort fiber-like particles based on their size and/or flexibility. This strategy resulted in an invention that is patent pending.

Our invention consists of a sorting device made of a large tank which contains a periodic array of obstacles. The array is immersed in a quiescent viscous fluid, and its geometry is characterized by the lattice arrangement and spacing, i.e., the distance between two adjacent obstacles in the array; as described in Chapter 6. A heterogeneous suspension of fiber-like particles is released from the upper side of the tank, such that the particles are transported under gravity through the array of obstacles. Owing to the resulting interactions between particles, obstacles, and the surrounding fluid; the particles migrate laterally after a finite settling distance. The resulting lateral displacement, $\delta x/L \sim EI/WL^3$, depends on their size L and flexibility EI, where W is the weight per unit length. Hence, at the lower side of the tank, the particles are sorted with respect to their mechanical and/or geometrical properties. This strategy of sorting has the main advantage of being passive or "energy-free" since the particles are transported under the effect of gravity, no external energy is required. In addition, this

device also has the advantages of low manufacturing and maintenance costs.
Our invention is useful for environmental, biological, and microfluidic applications. In particular, it could be used for wastewater treatment purposes, to prevent important issues such as the pollution of the oceans by microplastic fibers. Indeed, more than 5250 billion of microplastic debris are found in the marine environment, i.e., nearly 270000 tonnes. According to Eriksen et al., 2014, the amount of microplastic fibers is estimated to 2.9 millions tonnes. Owing to their small size, less than 1 mm, microplastic fibers are not captured by conventional filters and wastewater treatment plants (Browne et al., 2011a), therefore, they end up most of the time in the oceans, leading to adverse effects on aquatic environments and human well-being. Our device could be installed downstream of wastewater treatment plants to increase filtration efficiency. In biology, many parasites, such as those responsible for meningitis, develop in the form of chains of cells of various size and rigidity (Barratt et al., 2016). The size and rigidity of these chains vary between species of pathogens, between dead and living cells, depending on their virulence or under the action of antibiotics. Accordingly, our device could be used for the separation of pathogens based on their morphology, to study their virulence.

During this thesis, we have also discussed some features of a sedimenting suspension of flexible fibers in a quiescent viscous fluid. In particular, we have shown that the mean settling velocity of the suspension will increase continuously in time, owing to the effect of flexibility. This finding disagrees with the rigid case, where some experimental (Herzhaft et al., 1996; Herzhaft and Guazzelli, 1999; Metzger et al., 2007a) and numerical (Butler and Shaqfeh, 2002; Saintillan et al., 2005; Gustavsson and Tornberg, 2009) studies have reported the onset of a steady state in the mean settling velocity. We hope that this outcome will provide physical insight into future experimental and numerical studies.

Finally, it is my sincere hope that our methodology, together with the studies carried out in this thesis, will provide a launching point into future experiments and applications.

Future directions

The numerical framework developed during this thesis lends itself to a wide range of relevant extensions. One avenue to tackle in the future is to account for thermal fluctuations. Indeed, at very small scale, i.e., less than 1 μm, thermal fluctuations become an important aspect of the fiber dynamics. In complex environments, thermal fluctuations may allow fiber-like particles to escape from obstacles, thus avoiding trapping events (Chakrabarti et al., 2020). However, the resulting interplay between internal elastic stresses, contact forces, hydrodynamic interactions, and thermal fluctuations is challenging to tackle numerically. Especially to account for the random increments and the stochastic drift term, that turn the deterministic equation of motion into a stochastic one. In Appendix B, inspired by the work of Bao et al., 2018, we propose an approach to account efficiently for the random increments.

Our framework could also be extended to account for active particles, such as autophoretic fiber-like particles. These particles self-propel owing to local gradients generated through their surface activity (e.g., heat release (P. Bregulla and Cichos, 2015) or surface-catalysis of chemical reactions (Wang et al., 2006)). The most popular design consists of half-coated spherical or fiber-like particles that catalyze through surface activity on the solute (e.g., the catalytic decomposition of hydrogen peroxide in aqueous solution), and thus lead to their self-propulsion resulting from local chemical gradients (Paxton et al., 2004; Guix et al., 2018). While transported through complex environments, the trajectory of autophoretic fibers results from the complex interplay between the surrounding fluid and solute, internal elastic stresses, contact forces, and hydrodynamic interactions with the boundaries of the domain and the embedded obstacles. The resulting chemoelastohydrodynamic problem can be challenging to tackle analytically and numerically. Recently, there has been a significant drive to develop efficient theoretical and numerical frameworks for autophoretic fiber-like particles. The most systematic and rigorous approach is the Slender Phoretic Theory (SPT) developed by Katsamba et al., 2020 to investigate the dynamics of chemically active fibers with arbitrary three dimensional shapes and surface activities. Their approach asymptotically reduces the phoretic problem from three dimensions to one by assuming a certain distribution of singularities along the fiber centerline. This result is then combined with the Slender Body Theory (SBT) of Koens and Lauga, 2018 to evaluate the swimming velocity. However, to our knowledge, the current SPT framework is limited to stiff fibers, and accounting for pairwise interactions is challenging. Our approach could be used to overcome the aforementioned hurdles while achieving a similar numerical efficiency to SPT. The key idea is to introduce a non-standard boundary condition on the fiber surface. The latter will be a superposition of the no-slip boundary condition, namely the passive part; and the slip boundary condition that arises from the phoretic flow due to the non-uniform solute distribution on the fiber surface, namely the active part. The passive part could be computed by our current framework, i.e., a multibead approach; and the active part by the diffusio-phoretic force coupling method (DFCM) of Rojas-Pérez et al., 2021.

Regarding the settling dynamics of flexible fibers through structured environments, one clear avenue to tackle in the future is to consider a suspension of multiple fibers. Indeed, in the absence of obstacles, it has been shown that a sedimenting suspension of fibers exhibits a structural instability (Guazzelli and Hinch, 2011; Manikantan et al., 2014; Manikantan and Saintillan, 2016). Vertical inhomogeneities develop through the formation of clusters within downward streamers that are balanced by upward streamers of clarified fluid, and therefore enhance the mean settling velocity of the suspension (typically larger than the maximum velocity of an isolated fiber). The repetitive collisions with the obstacles will clearly affect the formation of clusters, and therefore may lead to hindered or enhanced settling. In Chapter 4, for a dilute suspension of fibers, we have shown that the presence of obstacles leads to the formation of

a single cloud of fibers. The latter undergoes a zigzag motion through the array of obstacles. However, this study is limited to a given geometry of the array, i.e., a hexagonal arrangement with a fixed lattice spacing. A detailed study of this problem through a parametric study should therefore be carried out. Furthermore, this study will provide additional physical insight into the design of gravity-based sorting devices, since in such systems a whole fiber suspension is sorted rather than an isolated fiber. Our current methodology allows to handle a large number of fibers and obstacles. However, the use of fast algorithms (Kalantari and McDonald, 1983; Tasora and Anitescu, 2013; Yan et al., 2019; Broms and Tornberg, 2023) to detect and compute collisions might enable an efficient simulation of larger systems in reasonable wall times.

Regarding our sorting strategy, one avenue for future direction is to investigate the effects of the array geometry on the fiber dynamics. Indeed, the numerical studies carried out through this thesis are limited to a hexagonal arrangement of the array. Since the lattice spacing affects the fiber dynamics at long times, as shown in Chapter 6, it is clear that the lattice arrangement will have a similar effect on the lateral displacement. For instance, to avoid the out-of-plane motions observed during the reorientation process of the fiber, in Chapter 6, one can use a grid-like arrangement to constrain the fiber motion to a 2D plane. Accordingly, a detailed parametric investigation of the system is necessary to propose a complete gravity-based sorting device.

Finally, in the two applications investigated in Chapters 5 and 6, the theoretical approach, built heavily on the work of Li et al., 2013, does not account for the interactions with the obstacles. An avenue for future work is therefore to develop a theory that overcomes this hurdle. One might consider for instance, a mean field approach that is built upon the solutions of Stokes flow through an array of obstacles. Leshansky, 2009 used a similar approach to investigate theoretically the effect of an array of obstacles on the locomotion of a microswimmer. The author modeled the array as a Brinkman fluid that acts as a resistance to the motion of the microswimmer. Although limited to sparse arrays, i.e., the obstacles are well separated from each other and from the microswimmer, this model provided physical grounds into the understanding of the enhancement of propulsion of some microswimmers in gel-like polymer environments (Berg and Turner, 1979).

Appendix A

The Positively-Split-Ewald method

A key idea for achieving quasilinear scaling with the total number of beads N in a triply periodic domain, is to use an Ewald splitting strategy as described in Fiore et al., 2017.

Starting from the periodic Green's function for Stokes flow as derived in Hasimoto, 1959,

$$\mathbb{G}(\boldsymbol{r}, \boldsymbol{r}_0) = \frac{1}{\eta V} \sum_{\boldsymbol{k} \neq 0} \frac{1}{k^2} \left(\boldsymbol{I} - \hat{\boldsymbol{k}} \otimes \hat{\boldsymbol{k}} \right) \exp\left(i \boldsymbol{k} \cdot \hat{\boldsymbol{x}}\right), \tag{A.1}$$

where $\hat{\boldsymbol{x}} = \boldsymbol{r} - \boldsymbol{r}_0$, η is the fluid viscosity, V is the periodic cell volume, $\boldsymbol{I}$ is the identity tensor, and $\boldsymbol{k}$ are the set of reciprocal lattice vectors, with $\hat{\boldsymbol{k}} = \boldsymbol{k}/k$ for $k = |\boldsymbol{k}|$.

We derive the periodic RPY tensor, which amounts to plug (A.1) into the Fourier representation of (3.37)

$$\boldsymbol{\mathcal{M}}_{ij} = \frac{1}{\eta V} \sum_{\boldsymbol{k} \neq 0} \frac{\operatorname{sinc}^2(ka)}{k^2} \left(\boldsymbol{I} - \hat{\boldsymbol{k}} \otimes \hat{\boldsymbol{k}} \right) \exp\left(i \boldsymbol{k} \cdot \hat{\boldsymbol{x}}\right), \tag{A.2}$$

given here for a pair of beads with equal finite hydrodynamic radius a.

Using the Ewald sum splitting of Hasimoto (Hasimoto, 1959), we decompose (A.2) into a sum of two symmetric positive definite (SPD) operators

$$\boldsymbol{\mathcal{M}}_{ij} = \boldsymbol{\mathcal{M}}_{ij}^{(w)} + \boldsymbol{\mathcal{M}}_{ij}^{(r)}, \tag{A.3}$$

where the long-ranged wave-space part $\boldsymbol{\mathcal{M}}_{ij}^{(w)}$ is given by

$$\boldsymbol{\mathcal{M}}_{ij}^{(w)} = \frac{1}{\eta V} \sum_{\boldsymbol{k} \neq 0} \frac{\operatorname{sinc}^2(ka)}{k^2} H(k, \xi) \left(\boldsymbol{I} - \hat{\boldsymbol{k}} \otimes \hat{\boldsymbol{k}} \right) \exp\left(i \boldsymbol{k} \cdot \hat{\boldsymbol{x}}\right), \tag{A.4}$$

with $H(k, \xi)$ being the Hasimoto splitting function defined as

$$H(k, \xi) = \left(1 + \frac{k^2}{4\xi^2} \right) e^{-k^2/4\xi^2}, \tag{A.5}$$

where ξ is the splitting parameter that controls the rate of exponential decay. The short-ranged real-space part $\boldsymbol{\mathcal{M}}_{ij}^{(r)}$ in (A.3) is given by the following expression, after performing analytically the integral for the inverse Fourier transform

$$\boldsymbol{\mathcal{M}}_{ij}^{(r)} = F(|\hat{\boldsymbol{x}}|, \xi) \left(\boldsymbol{I} + \frac{\hat{\boldsymbol{x}} \otimes \hat{\boldsymbol{x}}}{|\hat{\boldsymbol{x}}|^2} \right) + G(|\hat{\boldsymbol{x}}|, \xi) \left(\frac{\hat{\boldsymbol{x}} \otimes \hat{\boldsymbol{x}}}{|\hat{\boldsymbol{x}}|^2} \right), \tag{A.6}$$

where $F(|\hat{\boldsymbol{x}}|, \xi)$ and $G(|\hat{\boldsymbol{x}}|, \xi)$ are two rapidly decaying scalar functions that are given in Appendix A of Fiore et al., 2017.

Thus, the action $\boldsymbol{\mathcal{M}}\cdot(\cdot)$ of the mobility matrix on a given vector, can be computed efficiently by a superposition of the actions of the long-ranged wave-space part $\boldsymbol{\mathcal{M}}_{ij}^{(w)}\cdot(\cdot)$ and the short-ranged real-space part $\boldsymbol{\mathcal{M}}_{ij}^{(r)}\cdot(\cdot)$. In the case of Brownian dynamics, the stochastic displacements $\boldsymbol{\mathcal{M}}^{1/2}\cdot\boldsymbol{\mathcal{W}}(t)$ in triply periodic domains are computed by a superposition of two independent samples (Fiore et al., 2017):

$$\boldsymbol{\mathcal{M}}^{1/2}\cdot\boldsymbol{\mathcal{W}}(t)\overset{d}{=}\left(\boldsymbol{\mathcal{M}}^{(w)}\right)^{1/2}\cdot\boldsymbol{\mathcal{W}}^{(w)}(t)+\left(\boldsymbol{\mathcal{M}}^{(r)}\right)^{1/2}\cdot\boldsymbol{\mathcal{W}}^{(r)}(t), \tag{A.7}$$

where $\boldsymbol{\mathcal{W}}^{(w)}(t)$ and $\boldsymbol{\mathcal{W}}^{(r)}(t)$ are two uncorrelated Wiener processes. The long-ranged wave-space contribution is computed using fluctuating hydrodynamics (Bao et al., 2018) and the short-ranged real-space contribution by a Lanczos iterative method (Chow and Saad, 2014).

Appendix B

Constrained Brownian dynamics: Itô stochastic differential equation

By considering Brownian motion, bodies that are allowed to move, i.e the fibers, will experience a random motion due to the thermal fluctuations of the surrounding fluid in addition to the deterministic motion due to the conservative external and internal forces. In the overdamped limit, the effect of thermal fluctuations turns the deterministic equation of motion (4.6) into the Itô stochastic differential equation (SDE) describing the evolution of the bead positions (Graham, 2018)

$$\frac{\mathrm{d}\boldsymbol{R}}{\mathrm{d}t} \equiv \boldsymbol{U} = \boldsymbol{\mathcal{N}} \cdot \boldsymbol{F} + \sqrt{2k_BT}\boldsymbol{\mathcal{N}}^{1/2} \cdot \boldsymbol{\mathcal{W}}(t) + k_BT(\nabla \cdot \boldsymbol{\mathcal{N}}), \tag{B.1}$$

where k_B and T are respectively the Boltzmann constant and the temperature. The first term on the right hand side is the deterministic motion. The second term represents the random increments, with $\boldsymbol{\mathcal{W}}(t) \in \mathbb{R}^{3N}$ being a vector of independent Wiener processes (Graham, 2018). The square root of the constraint mobility matrix $\boldsymbol{\mathcal{N}}^{1/2}$ is any matrix, not necessarily square that ensures that the fluctuation-dissipation balance is satisfied

$$\boldsymbol{\mathcal{N}}^{1/2} \cdot (\boldsymbol{\mathcal{N}}^{1/2})^T = \boldsymbol{\mathcal{N}}. \tag{B.2}$$

The third term on the right hand side of (B.1) is the stochastic drift term, which ensures that the SDE with an Itô interpretation of the stochastic integral leads to an equilibrium Gibbs-Boltzmann distribution.

In practice, as mentioned in Section 4.2.2, direct computation of the constraint mobility matrix $\boldsymbol{\mathcal{N}}$ is not attractive for large systems due to numerical instabilities which may be a concern when forming $\boldsymbol{\mathcal{N}}$. Therefore, direct computation of its square root $\boldsymbol{\mathcal{N}}^{1/2}$ is less convenient too. This can be overcome by following the same approach as in fluctuating hydrodynamics (Bao et al., 2018) to incorporate the random displacements $\sqrt{2k_BT}\boldsymbol{\mathcal{N}}^{1/2} \cdot \boldsymbol{\mathcal{W}}(t)$ into the deterministic motion $\boldsymbol{\mathcal{N}} \cdot \boldsymbol{F}$. The key idea, based on the linearity of Stokes flow, is to introduce a random slip velocity $\tilde{\boldsymbol{v}}(t) = \sqrt{2k_BT}\boldsymbol{\mathcal{M}}^{1/2} \cdot \boldsymbol{\mathcal{W}}(t)$, that has zero mean and covariance

$$\langle \tilde{\boldsymbol{v}}(t)\tilde{\boldsymbol{v}}^T(t')\rangle = 2k_BT\boldsymbol{\mathcal{M}}, \tag{B.3}$$

into the right hand side of the mixed mobility-resistance problem (4.5). Where the square root of the mobility matrix $\boldsymbol{\mathcal{M}}^{1/2}$ satisfies the fluctuation dissipation balance $\boldsymbol{\mathcal{M}}^{1/2} \cdot (\boldsymbol{\mathcal{M}}^{1/2})^T = \boldsymbol{\mathcal{M}}$. Specifically, the deterministic linear system (4.5) turns into the following stochastic linear system to solve for the Lagrange multipliers and the stochastic bead velocities $(\boldsymbol{\lambda}, \widetilde{\boldsymbol{U}})$

$$\begin{bmatrix} -\boldsymbol{\mathcal{M}} \cdot \boldsymbol{\mathcal{J}}^T & \boldsymbol{I} \\ \boldsymbol{0} & \boldsymbol{\mathcal{J}} \end{bmatrix} \cdot \begin{bmatrix} \boldsymbol{\lambda} \\ \widetilde{\boldsymbol{U}} \end{bmatrix} = \begin{bmatrix} \boldsymbol{\mathcal{M}} \cdot \boldsymbol{F} + \sqrt{2k_BT}\boldsymbol{\mathcal{M}}^{1/2} \cdot \boldsymbol{\mathcal{W}}(t) \\ \boldsymbol{0} \end{bmatrix}. \tag{B.4}$$

We can eliminate the Lagrange multipliers from this system and write the solution for $\widetilde{\boldsymbol{U}} \in \mathbb{R}^{3N}$,

$$\begin{aligned}\widetilde{\boldsymbol{U}} &= \boldsymbol{\mathcal{N}} \cdot \boldsymbol{F} + \sqrt{2k_BT}\boldsymbol{\mathcal{P}}^{1/2} \cdot \boldsymbol{\mathcal{M}}^{1/2} \cdot \boldsymbol{\mathcal{W}}(t) \\ &= \boldsymbol{\mathcal{N}} \cdot \boldsymbol{F} + \sqrt{2k_BT}\boldsymbol{\mathcal{N}}^{1/2} \cdot \boldsymbol{\mathcal{W}}(t),\end{aligned} \tag{B.5}$$

which defines $\boldsymbol{\mathcal{N}}^{1/2}$ with correct covariance

$$\begin{aligned}\boldsymbol{\mathcal{N}}^{1/2} \cdot (\boldsymbol{\mathcal{N}}^{1/2})^T &= \boldsymbol{\mathcal{P}}^{1/2} \cdot \boldsymbol{\mathcal{M}}^{1/2} \cdot (\boldsymbol{\mathcal{P}}^{1/2})^T \cdot (\boldsymbol{\mathcal{M}}^{1/2})^T \\ &= \boldsymbol{\mathcal{P}} \cdot \boldsymbol{\mathcal{M}} \\ &= \boldsymbol{\mathcal{N}}.\end{aligned} \tag{B.6}$$

Hence, the stochastic bead velocities (without taking into account the stochastic drift term) can be computed by solving the stochastic mixed mobility-resistance problem (B.4). As shown for the deterministic case (see Section 4.3), we can solve efficiently this linear system iteratively, using a preconditioned GMRES method. In addition to the action $\boldsymbol{\mathcal{M}} \cdot (\bullet)$ of the mobility matrix on a given vector, which is computed efficiently in quasilinear time as described in the next section, the cost of each GMRES iteration will be also related to the action of $\boldsymbol{\mathcal{M}}^{1/2}$ on the random vector $\boldsymbol{\mathcal{W}}$, which is obtained through a preconditioned Lanczos iterative method (Chow and Saad, 2014) or a Positively-Split-Ewald (PSE) method (Fiore et al., 2017; see also Appendix A) in an unbounded or a triply periodic domain.

Accordingly, the solution to the constrained SDE (B.1) arises from the solution to the stochastic linear system (B.4), $\widetilde{\boldsymbol{U}}$, corrected by the stochastic drift term $k_BT(\nabla \cdot \boldsymbol{\mathcal{N}})$. The computation of the latter is challenging and is still an active area of research.

Fixman, 1978 proposed a method that avoids a direct computation of the drift term. However, this approach scales badly with the number of particles in the system (Delmotte and Keaveny, 2015; Sprinkle et al., 2017), and therefore can be computationally costly. A commonly-used approach to overcome this hurdle is the random finite difference (RFD). This approach has been introduced by Delong et al., 2014, and can be seen as a variant of Fixman's approach. In addition, efficient temporal schemes have been proposed for rigid particles to reduce significantly the number of operations while capturing the drift term through RFD (Usabiaga et al., 2017; Sprinkle et al., 2017). Finally, the drift-corrector (DC) method introduced by Delmotte and Keaveny, 2015, and recently generalized by Westwood et al., 2021, combines the two aforementioned approaches to capture the drift term. Therefore, the DC allows to carry out large Brownian simulations at a low computational cost compared to the RFD.

Since our constrained formulation is referred as "stiff", there is a need for an efficient temporal integrator to conduct large Brownian simulations. Indeed, this stiffness restricts the maximum possible time step size, and therefore increases significantly the wall times. The development of an efficient temporal integrator for constrained Brownian dynamics will be tackled in the future.

Appendix C

Weakly flexible fiber under sedimentation in a quiescent viscous fluid: lateral shift and trajectory

C.1 Lateral shift

Following Li et al., 2013, we perform a multiple-scale analysis to derive analytically the lateral shift for weakly flexible fibers. This approach was initially developed to solve the linear and nonlinear oscillator problems in a time domain $\mathcal{O}(t) \leq 1/\varepsilon^k$ (ε being a small parameter) under an asymptotic approximation in multiple scales t_0, t_1, ..., t_k, considered as independent variables (Hinch, 1991; Bender and Orszag, 1999).

We start with the local slender body theory (Hancock, 1953; Keller and Rubinow, 1976), scaled upon the settling timescale $8\pi L\eta/W$

$$\partial_t \boldsymbol{x}(s,t) = -\boldsymbol{\Lambda}[\boldsymbol{f}](s), \tag{C.1}$$

where $\boldsymbol{x}(s,t)$ is the position of a point s along the fiber centerline, and is given by

$$\boldsymbol{x}(s,t) = \boldsymbol{x}(1/2,t) + \left(s - \frac{1}{2}\right)\hat{\boldsymbol{t}} + \boldsymbol{\zeta}(s,t), \tag{C.2}$$

with $\boldsymbol{x}(1/2,t) = \boldsymbol{0}$, $\hat{\boldsymbol{t}} = \boldsymbol{x}_s(1/2,t)$ being the unit tangential vector at the fiber midpoint and $\boldsymbol{\zeta}(s,t)$ the time-dependent deflection defined such that at the midpoint $\boldsymbol{\zeta}(1/2,t) = \boldsymbol{0}$. $\boldsymbol{f}$ is the scaled fluid force acting on the fiber, and is defined as follows

$$\boldsymbol{f}(s) = -\boldsymbol{\omega}(s) - \left(T(s)\boldsymbol{x}_s\right)_s + \frac{1}{Be}\left(B(s)\boldsymbol{x}_{ss}\right)_{ss}, \tag{C.3}$$

with $\boldsymbol{\omega}(s)$ being the density of the gravitational forces, $T(s)$ the fiber centerline tension acting as a Lagrange multiplier to enforce the inextensibility condition and $B(s) = EI(s)$ the bending modulus. The local operator $\boldsymbol{\Lambda}$ in (C.1) is given by

$$\boldsymbol{\Lambda}[\boldsymbol{f}](s) = [(c(s)+2)\boldsymbol{I} + (c(s)-2)\hat{\boldsymbol{s}}\hat{\boldsymbol{s}}(s)] \cdot \boldsymbol{f}(s), \tag{C.4}$$

where $\hat{\boldsymbol{s}} = \boldsymbol{x}_s$, $\hat{\boldsymbol{s}}\hat{\boldsymbol{s}}$ is a dyadic product, and $c(s) = \ln\left(4s(1-s)/\varepsilon^2 r(s)^2 e\right)$, with $r(s)$ being dimensionless and $\varepsilon = 2a/L \ll 1$.

For small values of the elasto-gravitational number Be ($Be \ll 1$), Li et al., 2013 identified three independent timescales during the sedimentation of the fiber: the first one is the short elastic relaxation timescale of order $\mathcal{O}(Be)$, the second one is the time for the fiber to settle its own length, $\mathcal{O}(1)$, and the last one is the time for the fiber to reorient toward its equilibrium

configuration, $\mathcal{O}(Be^{-1})$. Introducing a new variable $t_1 = t_0 Be$, we assume the following perturbation expansions in power of Be, for the translational velocity $\boldsymbol{U}(t) = U(t)\hat{\boldsymbol{t}} + V(t)\hat{\boldsymbol{n}}$, the orientation angle $\theta(t)$, the line tension $T(s,t)$ and the time-dependent deflection $\boldsymbol{\zeta}(s,t)$,

$$U(t, Be) = U^{(0)}(t_0, t_1) + U^{(1)}(t_0, t_1)Be + \mathcal{O}(Be^2), \tag{C.5}$$

$$V(t, Be) = V^{(0)}(t_0, t_1) + V^{(1)}(t_0, t_1)Be + \mathcal{O}(Be^2), \tag{C.6}$$

$$\theta(t, Be) = \theta^{(0)}(t_0, t_1) + \theta^{(1)}(t_0, t_1)Be + \mathcal{O}(Be^2), \tag{C.7}$$

$$T(s, t, Be) = T^{(0)}(s, t_0, t_1) + T^{(1)}(s, t_0, t_1)Be + \mathcal{O}(Be^2), \tag{C.8}$$

$$\boldsymbol{\zeta}(s, t, Be) = (\zeta^{n(1)}(s, t_0, t_1)\hat{\boldsymbol{n}})Be + (\zeta^{n(2)}(s, t_0, t_1)\hat{\boldsymbol{n}} + \zeta^{t(2)}(s, t_0, t_1)\hat{\boldsymbol{t}})Be^2 + \mathcal{O}(Be^3). \tag{C.9}$$

In the following, we use the symbol t instead of t_0, for notation convenience.

We first solve the problem at the timescale $t = \mathcal{O}(1)$. By substituting the expansions defined above in (C.1), we end-up with

$$U^{(0)}(t, t_1) = 2c(s)\left[T_s^{(0)} + \cos\theta^{(0)}\right], \tag{C.10}$$

$$V^{(0)}(t, t_1) = -\left(c(s) + 2\right)\left[\zeta_{ssss}^{n(1)} + \sin\theta^{(0)}\right] - \left(s - \frac{1}{2}\right)\partial_t\theta^{(0)}. \tag{C.11}$$

The resulting equations (C.10) and (C.11) are obtained for a homogeneous fiber with uniform thickness, i.e., $r(s) = 1$, $\omega(s) = 1$ and $B(s) = 1$.

From here, as done in Appendix B of Li et al., 2013, we pursue the expansion at leading order in a small parameter $1/c_0 \ll 1$, where $c_0 = \ln(1/\varepsilon^2 e)$ such that $c(s) = \ln(4s(1-s)) + c_0$. Accordingly, we consider the following perturbation expansions

$$U^{(0)} = \sum_{k=0}^{+\infty} U_k c_0^{1-k}, \tag{C.12}$$

$$V^{(0)} = \sum_{k=0}^{+\infty} V_k c_0^{1-k}, \tag{C.13}$$

$$\theta^{(0)} = \sum_{k=0}^{+\infty} \theta_k c_0^{-k}, \tag{C.14}$$

$$T^{(0)} = \sum_{k=0}^{+\infty} T_k c_0^{-1-k}, \tag{C.15}$$

$$\zeta^{n(1)} = \sum_{k=0}^{+\infty} \zeta_k c_0^{-1-k}. \tag{C.16}$$

By inserting the above expansions up to $k = 1$ in (C.10) and (C.11), and using $\sin(c_0^{-1}\theta_1) = c_0^{-1}\theta_1 + \mathcal{O}(c_0^{-3})$, as well as $\cos(c_0^{-1}\theta_1) = 1 + \mathcal{O}(c_0^{-2})$, we obtain

$$U_0 = 2\cos\theta_0, \tag{C.17}$$

$$V_0 = -\sin\theta_0, \tag{C.18}$$

$$U_1 + 2\theta_1\sin\theta_0 = 2T_0' + 2\left[\ln(4s(1-s))\right]\cos\theta_0, \tag{C.19}$$

$$V_1 + \theta_1\cos\theta_0 = -\zeta_0'''' - \left[\ln(4s(1-s)) + 2\right]\sin\theta_0. \tag{C.20}$$

Applying the boundary conditions $T_0(0) = T_0(1) = 0$ and $\zeta_0'''(0) = \zeta_0'''(1) = 0$ to (C.19) and (C.20), we find

$$U_1 + 2\theta_1 \sin\theta_0 = 2\cos\theta_0 \int_0^1 \ln\left(4s(1-s)\right)\mathrm{d}s, \tag{C.21}$$

$$V_1 + \theta_1 \cos\theta_0 = -\sin\theta_0 \int_0^1 \left[\ln\left(4s(1-s)\right) + 2\right]\mathrm{d}s. \tag{C.22}$$

Thus, we can rewrite (C.19) and (C.20) as follows

$$T_0' = \left[2(\ln 2 - 1) - \ln\left(4s(1-s)\right)\right]\cos\theta_0, \tag{C.23}$$

$$\zeta_0'''' = \left[2(\ln 2 - 1) - \ln\left(4s(1-s)\right)\right]\sin\theta_0. \tag{C.24}$$

We solve the above ODEs with the suitable boundary conditions and deduce the following expressions of the tension and the deflection at the leading order in Be

$$T^{(0)} = c_0^{-1} p(s)\cos\theta^{(0)} + \mathcal{O}(c_0^{-2}), \tag{C.25}$$

$$\zeta^{n(1)} = c_0^{-1} q(s)\sin\theta^{(0)} + \mathcal{O}(c_0^{-2}), \tag{C.26}$$

with

$$p(s) = (1-s)\ln(1-s) - s\ln s, \tag{C.27}$$

and

$$q(s) = -\frac{1}{384}\left[16s^4\ln 2s + (2-2s)^4\ln(2-2s) - \left(\frac{13}{6} + 2\ln 2\right)(2s-1)^4 - (1+12\ln 2)(2s-1)^2\right]. \tag{C.28}$$

Now, we look at the next order $\mathcal{O}(Be)$ to derive the evolution of the orientation angle θ with respect to time. From (C.1), we obtain

$$\begin{aligned} V^{(1)}(t,t_1) = {} & (c(s)+2)\left[\left(T^{(0)}\zeta_s^{n(1)}\right)_s - \zeta_{ssss}^{n(2)} - \theta^{(1)}\cos\theta^{(0)}\right] \\ & + (c(s)-2)\left(T_s^{(0)} + \cos\theta^{(0)}\right)\zeta_s^{n(1)} - \left(s - \frac{1}{2}\right)\left(\partial_{t_1}\theta^{(0)} + \partial_t\theta^{(1)}\right). \end{aligned} \tag{C.29}$$

Multiplying by $(s-1/2)$ and integrating the above expression, we end-up with the following differential equation for the orientation angle, where the secular term has been removed by imposing $\partial_t\theta^{(1)} = 0$

$$\partial_t\theta = C\sin(2\theta)Be + \mathcal{O}(c_0^{-2}, Be^2), \tag{C.30}$$

with

$$C = 6\left[I_0 + c_0^{-1}(I_1 + I_2 + I_3)\right], \tag{C.31}$$

where

$$I_0 = \int_0^1 (s-1/2)q_s\mathrm{d}s, \tag{C.32}$$

$$I_1 = \int_0^1 (s-1/2)(pq_s)_s\mathrm{d}s, \tag{C.33}$$

$$I_2 = \int_0^1 (s-1/2)p_s q_s\mathrm{d}s. \tag{C.34}$$

$$I_3 = \int_0^1 (s-1/2)\left[\ln\left(4s(1-s)\right) - 2\right]q_s\mathrm{d}s. \tag{C.35}$$

Thus, by solving (C.30) for an arbitrary initial orientation $\theta(0)$, we obtain

$$\tan\left(\theta(t)\right) = \tan\left(\theta(0)\right)\exp\left((2CBe)t\right), \tag{C.36}$$

where C is given by

$$C = \frac{7}{400} + \ln\left(1/\varepsilon^2 e\right)^{-1}\left(\frac{1813 - 300\pi^2 + 630\ln\left(2\right)}{18000}\right). \tag{C.37}$$

The components of the settling velocity U_x and U_y in the laboratory frame are obtained by substituting (C.36) into the leading-order settling velocity $\boldsymbol{U} = 2c_0\cos(\theta)\hat{\boldsymbol{t}}(\theta) - c_0\sin(\theta)\hat{\boldsymbol{n}}(\theta)$, and then by multiplying the resulting expression respectively with the unit vectors $\hat{\boldsymbol{x}}$ and $\hat{\boldsymbol{y}}$ (see Fig. 5.4(a))

$$U_x = \boldsymbol{U}\cdot\hat{\boldsymbol{x}} = \frac{c_0 h}{1+h^2}, \tag{C.38}$$

$$U_y = \boldsymbol{U}\cdot\hat{\boldsymbol{y}} = -c_0\left(1 + \frac{1}{1+h^2}\right), \tag{C.39}$$

with

$$h(t) = \tan\left(\theta(0)\right)\exp\left((2CBe)t\right). \tag{C.40}$$

Finally, the lateral shift is obtained by integrating (C.38) and assuming $0 < \theta(0) \leq \pi/2$

$$\tilde{\delta}x = \int_0^\infty (\boldsymbol{U}\cdot\hat{\boldsymbol{x}})\mathrm{d}t = \frac{c_0}{2CBe}\left(\frac{\pi}{2} - \theta(0)\right). \tag{C.41}$$

C.2 Parametric equation of the trajectory

The time-dependent parametric equation of the path $\mathcal{L}$ described by the fiber midpoint (X, Y), is obtained by integrating (C.38) and (C.39) in time

$$\mathcal{L}: \begin{cases} \tan\left[(2CBe/c_0)X + \theta_0\right] = \tan\left(\theta_0\right)\exp\left[(2CBe)t\right], \\ Y = -c_0 t - \dfrac{c_0}{4CBe}\ln\left\{\dfrac{\left[1+\tan^2\left(\theta_0\right)\right]\exp\left[(4CBe)t\right]}{1+\tan^2\left(\theta_0\right)\exp\left[(4CBe)t\right]}\right\}, \end{cases} \quad t\in[0,+\infty). \tag{C.42}$$

Appendix D

Conformal mapping and parameter settings

D.1 Area-preserving conformal mapping

We use Riemann area-preserving map of the unit disk (Avron et al., 2004; Alonso-Matilla et al., 2019) to generate a class of cross-section shapes of the obstacle

$$\mathcal{F}(z) = \mathcal{W}z + \frac{\mathcal{Y}}{z} + \frac{\mathcal{K}}{\sqrt{2}z^2}, \tag{D.1}$$

where $z = e^{i\theta}$ with $\theta \in [0, 2\pi]$, $\mathcal{Y}$ and $\mathcal{K}$ respectively control the aspect ratio and the fore-aft asymmetry of the shape.

The shape parameter $\mathcal{W} > 0$ is defined as

$$\mathcal{W} = \sqrt{1 + \mathcal{Y}^2 + \mathcal{K}^2}. \tag{D.2}$$

Therefore, the coordinates of a given point in the physical xy plane derive from the mapping function (D.1)

$$\begin{cases} x = (\mathcal{W} + \mathcal{Y})\cos\theta + \dfrac{\mathcal{K}}{\sqrt{2}}\cos 2\theta \\ y = (\mathcal{W} - \mathcal{Y})\sin\theta - \dfrac{\mathcal{K}}{\sqrt{2}}\sin 2\theta \end{cases} \tag{D.3}$$

In our study, we take $\mathcal{Y} = 0$ and the resulting geometries are homogeneously dilated in order to have a constant obstacle width $\omega = 1$ for all the simulations.

D.2 Parameter sets

In the following table, we summarize the parameters used in our numerical simulations to compare with experiments. We recall that $\Delta s/\mathcal{C}$ is the obstacle cross-section shape resolution, where $\mathcal{C}$ is its contour length and Δs the centerline distance between two consecutive beads. $\varepsilon^{-1} = L/2a$ is the fiber aspect-ratio, which is equivalent to its number of beads N_F.

Parameter	Set I: "Gliding event".	Set II: "Trapping event".
ε^{-1}	75	91
$a[\mu\text{m}]$	257	257
$\Delta s/\mathcal{C}$	0.02	0.02
α	0.61	0.61
$\omega[\text{cm}]$	1	1
D_x/L	0.25	0.03
D_y/L	1.75	1.45
Be	200	210
ξ	7.71	9.35
$\mathcal{K}$	0	0
$W[\text{N/cm}]$	13×10^{-6}	11×10^{-6}
$\eta[\text{cP}]$	0.97	0.97

Table D.1: Parameter sets used for comparison with experiments in Section 5.4.1

References

Ahmed, D., Lu, M., Nourhani, A., Lammert, P. E., Stratton, Z., Muddana, H. S., Crespi, V. H., and Huang, T. J. (2015). Selectively manipulable acoustic-powered microswimmers. *Scientific Reports*, 5:9744.

Ahmed, S., Wang, W., Bai, L., Gentekos, D. T., Hoyos, M., and Mallouk, T. E. (2016). Density and Shape Effects in the Acoustic Propulsion of Bimetallic Nanorod Motors. *ACS Nano*, 10(4):4763–4769.

Alonso-Matilla, R., Chakrabarti, B., and Saintillan, D. (2019). Transport and dispersion of active particles in periodic porous media. *Physical Review Fluids*, 4(4):043101.

Anselmet, M.-C. (1989). *Contribution à l'étude Des Systèmes Fluide-Particules : Suspensions de Cylindres, Lits Fluidisés*. These de doctorat, Aix-Marseille 1.

Arkın, H. and Janke, W. (2013). Gyration tensor based analysis of the shapes of polymer chains in an attractive spherical cage. *The Journal of Chemical Physics*, 138(5):054904.

Audoly, B. and Pomeau, Y. (2010). *Elasticity and Geometry: From hair curls to the non-linear response of shells*. OUP Oxford, Oxford.

Avron, J. E., Gat, O., and Kenneth, O. (2004). Optimal Swimming at low Reynolds numbers. *Physical Review Letters*, 93(18):186001.

Balboa Usabiaga, F. and Delmotte, B. (2022). A numerical method for suspensions of articulated bodies in viscous flows. *Journal of Computational Physics*, 464:111365.

Bao, Y., Rachh, M., Keaveny, E., Greengard, L., and Donev, A. (2018). A fluctuating boundary integral method for Brownian suspensions. *Journal of Computational Physics*, 374:1094–1119.

Barratt, J., Chan, D., Sandaradura, I., Malik, R., Spielman, D., Lee, R., Marriott, D., Harkness, J., Ellis, J., and Stark, D. (2016). *Angiostrongylus Cantonensis* : A review of its distribution, molecular biology and clinical significance as a human pathogen. *Parasitology*, 143(9):1087–1118.

Batchelor, G. K. (1970). Slender-body theory for particles of arbitrary cross-section in Stokes flow. *Journal of Fluid Mechanics*, 44(3):419–440.

Bender, C. M. and Orszag, S. A. (1999). *Advanced Mathematical Methods for Scientists and Engineers I*. Springer New York, New York, NY.

Berg, H. C. and Turner, L. (1979). Movement of microorganisms in viscous environments. *Nature*, 278(5702):349–351.

Bhattacharjee, A., Jabbarzadeh, M., Kararsiz, G., Fu, H. C., and Kim, M. J. (2022). Bacteria-inspired magnetically actuated rod-like soft robot in viscous fluids. *Bioinspiration & Biomimetics*, 17(6):065001.

Bird, R. B., Curtiss, C. F., Armstrong, R. C., and Hassager, O. (1987). *Dynamics of Polymeric Liquids, Volume 2: Kinetic Theory, 2nd Edition*. Wiley.

Blavatska, V. and Janke, W. (2010). Shape anisotropy of polymers in disordered environment. *The Journal of Chemical Physics*, 133(18):184903.

Boal, D. (2012). *Mechanics of the Cell*. Cambridge University Press, Cambridge, 2 edition.

Bringley, T. T. and Peskin, C. S. (2008). Validation of a simple method for representing spheres and slender bodies in an immersed boundary method for Stokes flow on an unbounded domain. *Journal of Computational Physics*, 227(11):5397–5425.

Brinkman, H. C. (1949). A calculation of the viscous force exerted by a flowing fluid on a dense swarm of particles. *Flow, Turbulence and Combustion*, 1(1):27–34.

Broms, A. and Tornberg, A.-K. (2023). A Barrier Method for Contact Avoiding Particles in Stokes Flow.

Brown, P. N., Byrne, G. D., and Hindmarsh, A. C. (1989). VODE: A Variable-Coefficient ODE Solver. *SIAM Journal on Scientific and Statistical Computing*, 10(5):1038–1051.

Browne, M. A., Crump, P., Niven, S. J., Teuten, E., Tonkin, A., Galloway, T., and Thompson, R. (2011a). Accumulation of Microplastic on Shorelines Woldwide: Sources and Sinks. *Environmental Science & Technology*, 45(21):9175–9179.

Browne, M. A., Crump, P., Niven, S. J., Teuten, E., Tonkin, A., Galloway, T., and Thompson, R. (2011b). Accumulation of Microplastic on Shorelines Woldwide: Sources and Sinks. *Environmental Science & Technology*, 45(21):9175–9179.

Bukowicki, M. and L. Ekiel-Jeżewska, M. (2019). Sedimenting pairs of elastic microfilaments. *Soft Matter*, 15(46):9405–9417.

Butler, J. E. and Shaqfeh, E. S. G. (2002). Dynamic simulations of the inhomogeneous sedimentation of rigid fibres. *Journal of Fluid Mechanics*, 468:205–237.

Cappello, J., Bechert, M., Duprat, C., du Roure, O., Gallaire, F., and Lindner, A. (2019). Transport of flexible fibers in confined micro-channels. *Physical Review Fluids*, 4(3):034202.

Celli, J. P., Turner, B. S., Afdhal, N. H., Keates, S., Ghiran, I., Kelly, C. P., Ewoldt, R. H., McKinley, G. H., So, P., Erramilli, S., and Bansil, R. (2009). Helicobacter pylori moves through mucus by reducing mucin viscoelasticity. *Proceedings of the National Academy of Sciences*, 106(34):14321–14326.

Chakrabarti, B., Gaillard, C., and Saintillan, D. (2020). Trapping, gliding, vaulting: Transport of semiflexible polymers in periodic post arrays. *Soft Matter*, 16(23):5534–5544.

Chen, S. and Doolen, G. D. (1997). LATTICE BOLTZMANN METHOD FOR FLUID FLOWS. page 36.

Choi, C. E., Zhang, J., and Liang, Z. (2022). Towards realistic predictions of microplastic fiber transport in aquatic environments: Secondary motions. *Water Research*, 218:118476.

Chou, C.-F., Bakajin, O., Turner, S. W. P., Duke, T. A. J., Chan, S. S., Cox, E. C., Craighead, H. G., and Austin, R. H. (1999). Sorting by diffusion: An asymmetric obstacle course for continuous molecular separation. *Proceedings of the National Academy of Sciences*, 96(24):13762–13765.

Chow, E. and Saad, Y. (2014). Preconditioned Krylov Subspace Methods for Sampling Multivariate Gaussian Distributions. *SIAM Journal on Scientific Computing*, 36(2):A588–A608.

Claeys, I. L. and Brady, J. F. (1993). Suspensions of prolate spheroids in Stokes flow. Part 1. Dynamics of a finite number of particles in an unbounded fluid. *Journal of Fluid Mechanics*, 251:411–442.

Cortez, R. (2001). The Method of Regularized Stokeslets. *SIAM Journal on Scientific Computing*, 23(4):1204–1225.

Cortez, R., Fauci, L., and Medovikov, A. (2005). The method of regularized Stokeslets in three dimensions: Analysis, validation, and application to helical swimming. *Physics of Fluids*, 17(3):031504.

Cunha, L. H. P., Zhao, J., MacKintosh, F. C., and Biswal, S. L. (2022). Settling dynamics of Brownian chains in viscous fluids. *Physical Review Fluids*, 7(3):034303.

Dance, S. L., Climent, E., and Maxey, M. R. (2004). Collision barrier effects on the bulk flow in a random suspension. *Physics of Fluids*, 16(3):828–831.

D'Angelo, M. V., Semin, B., Picard, G., Poitzsch, M. E., Hulin, J. P., and Auradou, H. (2010). Single Fiber Transport in a Fracture Slit: Influence of the Wall Roughness and of the Fiber Flexibility. *Transport in Porous Media*, 84(2):389–408.

Darboux, G. (1896). *Leçons sur la théorie générale des surfaces et les applications géométriques du calcul infinitésimal: ptie. Déformation infiniment petite et réprésentation sphérique. Notes et additions: I. Sur les méthodes d'approximations successives dans la théorie des équations différentielles, par E. Picard. II. Sur les géodésiques à intégrales quadratiques, par G. Koenigs. III. Sur la théorie des équations aux dérivées partielles du second ordre, par E. Cosserat. IV-XI. Par l'auteur. 1896.* Gauthier-Villars.

de Gennes, P. G. (2003). Reptation of a Polymer Chain in the Presence of Fixed Obstacles. *The Journal of Chemical Physics*, 55(2):572–579.

Delmotte, B., Climent, E., and Plouraboué, F. (2015). A general formulation of Bead Models applied to flexible fibers and active filaments at low Reynolds number. *Journal of Computational Physics*, 286:14–37.

Delmotte, B. and Keaveny, E. E. (2015). Simulating Brownian suspensions with fluctuating hydrodynamics. *The Journal of Chemical Physics*, 143(24):244109.

Delong, S., Usabiaga, F. B., Delgado-Buscalioni, R., Griffith, B. E., and Donev, A. (2014). Brownian Dynamics without Green's Functions. *The Journal of Chemical Physics*, 140(13):134110.

Dillon, R., Fauci, L., Fogelson, A., and Gaver Iii, D. (1996). Modeling Biofilm Processes Using the Immersed Boundary Method. *Journal of Computational Physics*, 129(1):57–73.

Doi, M. and Edwards, S. F. (1988). *The Theory of Polymer Dynamics*. Clarendon Press, Oxford.

Dorfman, K. D., King, S. B., Olson, D. W., Thomas, J. D. P., and Tree, D. R. (2013). Beyond gel electrophoresis: Microfluidic separations, fluorescence burst analysis, and DNA stretching. *Chemical reviews*, 113(4):2584–2667.

Drescher, K., Shen, Y., Bassler, B. L., and Stone, H. A. (2013). Biofilm streamers cause catastrophic disruption of flow with consequences for environmental and medical systems. *Proceedings of the National Academy of Sciences*, 110(11):4345–4350.

Dreyfus, R., Baudry, J., Roper, M. L., Fermigier, M., Stone, H. A., and Bibette, J. (2005). Microscopic artificial swimmers. *Nature*, 437(7060):862–865.

Du Roure, O., Lindner, A., Nazockdast, E. N., and Shelley, M. J. (2019). Dynamics of flexible fibers in viscous flows and fluids. *Annual Review of Fluid Mechanics*.

Dykaar, B. B. and Kitanidis, P. K. (1996). Macrotransport of a Biologically Reacting Solute Through Porous Media. *Water Resources Research*, 32(2):307–320.

Engdahl, N. B. (2018). Simulating the mobility of micro-plastics and other fiber-like objects in saturated porous media using constrained random walks. *Advances in Water Resources*, 121:277–284.

Engstler, M., Pfohl, T., Herminghaus, S., Boshart, M., Wiegertjes, G., Heddergott, N., and Overath, P. (2007). Hydrodynamic Flow-Mediated Protein Sorting on the Cell Surface of Trypanosomes. *Cell*, 131(3):505–515.

Eriksen, M., Lebreton, L. C. M., Carson, H. S., Thiel, M., Moore, C. J., Borerro, J. C., Galgani, F., Ryan, P. G., and Reisser, J. (2014). Plastic Pollution in the World's Oceans: More than 5 Trillion Plastic Pieces Weighing over 250,000 Tons Afloat at Sea. *PLOS ONE*, 9(12):e111913.

Euler, L. (1744). *Methodus inveniendi lineas curvas maximi minimive proprietate gaudentes, sive Solutio problematis isoperimetrici latissimo sensu accepti...* apud Marcum-Michaelem Bousquet et socios.

Fauci, L. J. and McDonald, A. (1995). Sperm motility in the presence of boundaries. *Bulletin of Mathematical Biology*, 57(5):679–699.

Fiore, A. M., Balboa Usabiaga, F., Donev, A., and Swan, J. W. (2017). Rapid sampling of stochastic displacements in Brownian dynamics simulations. *The Journal of Chemical Physics*, 146(12):124116.

Fiore, A. M. and Swan, J. W. (2019). Fast Stokesian dynamics. *Journal of Fluid Mechanics*, 878:544–597.

Fixman, M. (1978). Simulation of polymer dynamics. I. General theory. *The Journal of Chemical Physics*, 69(4):1527–1537.

Gauger, E. and Stark, H. (2006). Numerical study of a microscopic artificial swimmer. *Physical Review E*, 74(2):021907.

Gidituri, H., Ellero, M., and Usabiaga, F. B. (2023). Swimming Efficiently by Wrapping.

Goetz, T. (2000). Interactions of Fibers and Flow: Asymptotics, Theory and Numerics.

Golestanian, R., Liverpool, T. B., and Ajdari, A. (2005). Propulsion of a Molecular Machine by Asymmetric Distribution of Reaction Products. *Physical Review Letters*, 94(22):220801.

Gompper, G., Ihle, T., Kroll, D. M., and Winkler, R. G. (2009). Multi-Particle Collision Dynamics – a Particle-Based Mesoscale Simulation Approach to the Hydrodynamics of Complex Fluids. pages 1–87.

Graham, M. D. (2018). *Microhydrodynamics, Brownian Motion, and Complex Fluids*. Cambridge Texts in Applied Mathematics. Cambridge University Press, Cambridge.

Guazzelli, É. and Hinch, J. (2011). Fluctuations and Instability in Sedimentation. *Annual Review of Fluid Mechanics*, 43(1):97–116.

Guix, M., Weiz, S. M., Schmidt, O. G., and Medina-Sánchez, M. (2018). Self-Propelled Micro/Nanoparticle Motors. *Particle & Particle Systems Characterization*, 35(2):1700382.

Gustavsson, K. and Tornberg, A.-K. (2009). Gravity induced sedimentation of slender fibers. *Physics of Fluids*, 21(12):123301.

Hall-McNair, A. L., Montenegro-Johnson, T. D., Gadêlha, H., Smith, D. J., and Gallagher, M. T. (2019). Efficient implementation of elastohydrodynamics via integral operators. *Physical Review Fluids*, 4(11):113101.

Hancock, G. (1953). The self-propulsion of microscopic organisms through liquids. *Proceedings of the Royal Society of London. Series A. Mathematical and Physical Sciences*, 217(1128):96–121.

Happel, J. and Brenner, H. (1981). *Low Reynolds Number Hydrodynamics*, volume 1 of *Mechanics of Fluids and Transport Processes*. Springer Netherlands, Dordrecht.

Hasimoto, H. (1959). On the periodic fundamental solutions of the Stokes equations and their application to viscous flow past a cubic array of spheres. *Journal of Fluid Mechanics*, 5(02):317.

Herzhaft, B. and Guazzelli, É. (1999). Experimental study of the sedimentation of dilute and semi-dilute suspensions of fibres. *Journal of Fluid Mechanics*, 384:133–158.

Herzhaft, B., Guazzelli, É., Mackaplow, M. B., and Shaqfeh, E. S. G. (1996). Experimental Investigation of the Sedimentation of a Dilute Fiber Suspension. *Physical Review Letters*, 77(2):290–293.

Hinch, E. J. (1991). *Perturbation Methods*. Cambridge Texts in Applied Mathematics. Cambridge University Press, Cambridge.

Ho, N., Leiderman, K., and Olson, S. (2019). A three-dimensional model of flagellar swimming in a Brinkman fluid. *Journal of Fluid Mechanics*, 864:1088–1124.

Ho, N., Olson, S. D., and Leiderman, K. (2016). Swimming speeds of filaments in viscous fluids with resistance. *Physical Review E*, 93(4):043108.

Howard, P. R., King, M. T., Morris, M., Feraud, J.-P., Slusher, G., and Lipari, S. (1995). Fiber/Proppant Mixtures Control Proppant Flowback in South Texas. In *SPE Annual Technical Conference and Exhibition*. OnePetro.

Jabbarzadeh, M. and Fu, H. C. (2020). A numerical method for inextensible elastic filaments in viscous fluids. *Journal of Computational Physics*, 418:109643.

Jiang, H.-R., Yoshinaga, N., and Sano, M. (2010). Active Motion of a Janus Particle by Self-Thermophoresis in a Defocused Laser Beam. *Physical Review Letters*, 105(26):268302.

Johnson, R. E. (1980). An improved slender-body theory for Stokes flow. *Journal of Fluid Mechanics*, 99(2):411–431.

Joung, C., Phan-Thien, N., and Fan, X. (2001). Direct simulation of flexible fibers. *Journal of Non-Newtonian Fluid Mechanics*, 99(1):1–36.

Juarez, G., Lu, K., Sznitman, J., and Arratia, P. E. (2010). Motility of small nematodes in wet granular media. *EPL (Europhysics Letters)*, 92(4):44002.

Jung, S. (2010). *Caenorhabditis Elegans* swimming in a saturated particulate system. *Physics of Fluids*, 22(3):031903.

Jung, S., Spagnolie, S. E., Parikh, K., Shelley, M., and Tornberg, A.-K. (2006). Periodic sedimentation in a Stokesian fluid. *Physical Review E*, 74(3):035302.

Kagan, D., Laocharoensuk, R., Zimmerman, M., Clawson, C., Balasubramanian, S., Kang, D., Bishop, D., Sattayasamitsathit, S., Zhang, L., and Wang, J. (2010). Rapid Delivery of Drug Carriers Propelled and Navigated by Catalytic Nanoshuttles. *Small*, 6(23):2741–2747.

Kalantari, I. and McDonald, G. (1983). A Data Structure and an Algorithm for the Nearest Point Problem. *IEEE Transactions on Software Engineering*, SE-9(5):631–634.

Kamal, A. and Keaveny, E. E. (2018). Enhanced locomotion, effective diffusion and trapping of undulatory micro-swimmers in heterogeneous environments. *Journal of The Royal Society Interface*, 15(148):20180592.

Kamarapu, S. K., Jabbarzadeh, M., and Fu, H. C. (2022). Modeling creeping flows in porous media using regularized Stokeslets. *Physical Review Fluids*, 7(10):104102.

Kane, I. A. and Clare, M. A. (2019). Dispersion, Accumulation, and the Ultimate Fate of Microplastics in Deep-Marine Environments: A Review and Future Directions. *Frontiers in Earth Science*, 7.

Katsamba, P., Michelin, S., and Montenegro-Johnson, T. D. (2020). Slender phoretic theory of chemically active filaments. *Journal of Fluid Mechanics*, 898:A24.

Kawale, D., Bouwman, G., Sachdev, S., J. Zitha, P. L., T. Kreutzer, M., R. Rossen, W., and E. Boukany, P. (2017). Polymer conformation during flow in porous media. *Soft Matter*, 13(46):8745–8755.

Keller, J. B. and Rubinow, S. I. (1976). Slender-body theory for slow viscous flow. *Journal of Fluid Mechanics*, 75(4):705–714.

Kim, S. (1985). Sedimentation of two arbitrarily oriented spheroids in a viscous fluid. *International Journal of Multiphase Flow*, 11(5):699–712.

Kim, S. and Karrila, S. J. (2005). *Microhydrodynamics: Principles And Selected Applications*. Dover Publications Inc., Mineola, N.Y.

Kim, S.-C., Wunsch, B. H., Hu, H., Smith, J. T., Austin, R. H., and Stolovitzky, G. (2017). Broken flow symmetry explains the dynamics of small particles in deterministic lateral displacement arrays. *Proceedings of the National Academy of Sciences*, 114(26):E5034–E5041.

Kirchhoff, G. (1850). Über das Gleichgewicht und die Bewegung einer elastischen Scheibe. *Journal für die reine und angewandte Mathematik (Crelles Journal)*, 1850(40):51–88.

Koch, D. L. and Shaqfeh, E. S. G. (1989). The instability of a dispersion of sedimenting spheroids. *Journal of Fluid Mechanics*, 209:521–542.

Koens, L. and Lauga, E. (2018). The boundary integral formulation of Stokes flows includes slender-body theory. *Journal of Fluid Mechanics*, 850:R1.

Kulrattanarak, T., van der Sman, R. G. M., Lubbersen, Y. S., Schroën, C. G. P. H., Pham, H. T. M., Sarro, P. M., and Boom, R. M. (2011a). Mixed motion in deterministic ratchets due to anisotropic permeability. *Journal of Colloid and Interface Science*, 354(1):7–14.

Kulrattanarak, T., van der Sman, R. G. M., Schroën, C. G. P. H., and Boom, R. M. (2011b). Analysis of mixed motion in deterministic ratchets via experiment and particle simulation. *Microfluidics and Nanofluidics*, 10(4):843–853.

KUMAR, P. and RAMARAO, B. (1991). Enhancement of the Sedimentation Rates of Fibrous Suspensions. *Chemical Engineering Communications*, 108(1):381–401.

Kurzthaler, C., Mandal, S., Bhattacharjee, T., Löwen, H., Datta, S. S., and Stone, H. A. (2021). A geometric criterion for the optimal spreading of active polymers in porous media. *Nature Communications*, 12(1):7088.

Lagomarsino, M. C., Pagonabarraga, I., and Lowe, C. P. (2005). Hydrodynamic induced deformation and orientation of a microscopic elastic filament. *Physical Review Letters*, 94(14):148104.

Lanczos, C. (1986). *The Variational Principles of Mechanics*. Dover Publications Inc., New York, new édition edition.

Landau, L. D., Pitaevskii, L. P., Kosevich, A. M., and Lifshitz, E. M. (1986). *Theory of Elasticity: Volume 7*. Butterworth-Heinemann, Amsterdam Heidelberg, 3rd edition edition.

Lauga, E. (2020). *The Fluid Dynamics of Cell Motility*. Cambridge University Press.

Lauga, E. and Powers, T. R. (2009). The hydrodynamics of swimming microorganisms. *Reports on Progress in Physics*, 72(9):096601.

Leal, L. G. (2007). *Advanced Transport Phenomena: Fluid Mechanics and Convective Transport Processes*. Cambridge Series in Chemical Engineering. Cambridge University Press, Cambridge.

Leiderman, K. and Olson, S. D. (2016). Swimming in a two-dimensional Brinkman fluid: Computational modeling and regularized solutions. *Physics of Fluids*, 28(2):021902.

Leshansky, A. M. (2009). Enhanced low-Reynolds-number propulsion in heterogeneous viscous environments. *Physical Review E*, 80(5):051911.

Li, L., Manikantan, H., Saintillan, D., and Spagnolie, S. E. (2013). The sedimentation of flexible filaments. *Journal of Fluid Mechanics*, 735:705–736.

Li, W., Wu, X., Qin, H., Zhao, Z., and Liu, H. (2016). Light-Driven and Light-Guided Microswimmers. *Advanced Functional Materials*, 26(18):3164–3171.

Lim, S., Ferent, A., Wang, X. S., and Peskin, C. S. (2008). Dynamics of a Closed Rod with Twist and Bend in Fluid. *SIAM Journal on Scientific Computing*, 31(1):273–302.

Liu, T. W. (1989). Flexible polymer chain dynamics and rheological properties in steady flows. *The Journal of Chemical Physics*, 90(10):5826–5842.

Llopis, I., Pagonabarraga, I., Lagomarsino, M. C., and Lowe, C. P. (2007). Sedimentation of pairs of hydrodynamically interacting semiflexible filaments. *Physical Review E*, 76(6):061901.

Loget, G. and Kuhn, A. (2011). Electric field-induced chemical locomotion of conducting objects. *Nature Communications*, 2(1):535.

Long, B. R., Heller, M., Beech, J. P., Linke, H., Bruus, H., and Tegenfeldt, J. O. (2008). Multidirectional sorting modes in deterministic lateral displacement devices. *Physical Review E*, 78(4):046304.

López, H. M., Hulin, J.-P., Auradou, H., and D'Angelo, M. V. (2015). Deformation of a flexible fiber in a viscous flow past an obstacle. *Physics of Fluids*, 27(1):013102.

Lundell, F., Söderberg, L. D., and Alfredsson, P. H. (2011). Fluid Mechanics of Papermaking. *Annual Review of Fluid Mechanics*, 43(1):195–217.

Mackaplow, M. B. and Shaqfeh, E. S. G. (1998). A numerical study of the sedimentation of fibre suspensions. *Journal of Fluid Mechanics*, 376:149–182.

Magdanz, V., Sanchez, S., and Schmidt, O. G. (2013). Development of a Sperm-Flagella Driven Micro-Bio-Robot. *Advanced Materials*, 25(45):6581–6588.

Majmudar, T., Keaveny, E. E., Zhang, J., and Shelley, M. J. (2012). Experiments and theory of undulatory locomotion in a simple structured medium. *Journal of The Royal Society Interface*, 9(73):1809–1823.

Makanga, U., Sepahi, M., Duprat, C., and Delmotte, B. (2023). Obstacle-induced lateral dispersion and nontrivial trapping of flexible fibers settling in a viscous fluid. *Physical Review Fluids*, 8(4):044303.

Malevanets, A. and Kapral, R. (1999). Mesoscopic model for solvent dynamics. *The Journal of Chemical Physics*, 110(17):8605–8613.

Malevanets, A. and Kapral, R. (2000). Solute molecular dynamics in a mesoscale solvent. *The Journal of Chemical Physics*, 112(16):7260–7269.

Manikantan, H., Li, L., Spagnolie, S. E., and Saintillan, D. (2014). The instability of a sedimenting suspension of weakly flexible fibres. *Journal of Fluid Mechanics*, 756:935–964.

Manikantan, H. and Saintillan, D. (2016). Effect of flexibility on the growth of concentration fluctuations in a suspension of sedimenting fibers: Particle simulations. *Physics of Fluids*, 28(1):013303.

Marchetti, B., Raspa, V., Lindner, A., du Roure, O., Bergougnoux, L., Guazzelli, É., and Duprat, C. (2018). Deformation of a flexible fiber settling in a quiescent viscous fluid. *Physical Review Fluids*, 3(10):104102.

Maxey, M. R. and Patel, B. K. (2001). Localized force representations for particles sedimenting in Stokes flow. *International Journal of Multiphase Flow*, 27(9):1603–1626.

Maxian, O., Mogilner, A., and Donev, A. (2021a). An integral-based spectral method for inextensible slender fibers in Stokes flow. *Physical Review Fluids*, 6(1):014102.

Maxian, O., Peláez, R. P., Mogilner, A., and Donev, A. (2021b). Simulations of dynamically cross-linked actin networks: Morphology, rheology, and hydrodynamic interactions. *PLOS Computational Biology*, 17(12):e1009240.

Maxian, O., Sprinkle, B., and Donev, A. (2023). Bending fluctuations in semiflexible, inextensible, slender filaments in Stokes flow: Towards a spectral discretization. *arXiv:2301.11123[math.NA]*.

McGrath, J., Jimenez, M., and Bridle, H. (2014). Deterministic lateral displacement for particle separation: A review. *Lab Chip*, 14(21):4139–4158.

Medina-Sánchez, M. and Schmidt, O. G. (2017). Medical microbots need better imaging and control. *Nature*, 545(7655):406–408.

Medina-Sánchez, M., Schwarz, L., Meyer, A. K., Hebenstreit, F., and Schmidt, O. G. (2016). Cellular Cargo Delivery: Toward Assisted Fertilization by Sperm-Carrying Micromotors. *Nano Letters*, 16(1):555–561.

Metzger, B., Butler, J. E., and Guazzelli, É. (2007a). Experimental investigation of the instability of a sedimenting suspension of fibres. *Journal of Fluid Mechanics*, 575:307–332.

Metzger, B., Butler, J. E., and Guazzelli, É. (2007b). On wavelength selection by stratification in the instability of settling fibers. *Physics of Fluids*, 19(9):098105.

Metzger, B., Guazzelli, É., and Butler, J. E. (2005). Large-Scale Streamers in the Sedimentation of a Dilute Fiber Suspension. *Physical Review Letters*, 95(16):164506.

Mirbagheri, S. A. and Fu, H. C. (2016). *Helicobacter Pylori* Couples Motility and Diffusion to Actively Create a Heterogeneous Complex Medium in Gastric Mucus. *Physical Review Letters*, 116(19):198101.

Mokhtari, Z. and Zippelius, A. (2019). Dynamics of Active Filaments in Porous Media. *Physical Review Letters*, 123(2):028001.

Montecucco, C. and Rappuoli, R. (2001). Living dangerously: How Helicobacter pylori survives in the human stomach. *Nature Reviews Molecular Cell Biology*, 2(6):457–466.

Montenegro-Johnson, T. D. (2018). Microtransformers: Controlled microscale navigation with flexible robots. *Physical Review Fluids*, 3(6):062201.

Moreau, C., Giraldi, L., and Gadêlha, H. (2018). The asymptotic coarse-graining formulation of slender-rods, bio-filaments and flagella. *Journal of The Royal Society Interface*, 15(144):20180235.

Münch, J. L., Alizadehrad, D., Babu, S. B., and Stark, H. (2016). Taylor line swimming in microchannels and cubic lattices of obstacles. *Soft Matter*, 12(35):7350–7363.

Muthukumar, M. and Baumgaertner, A. (1989). Diffusion of a polymer chain in random media. *Macromolecules*, 22(4):1941–1946.

Nagel, M., Brun, P.-T., Berthet, H., Lindner, A., Gallaire, F., and Duprat, C. (2018). Oscillations of confined fibers transported in microchannels. *Journal of Fluid Mechanics*, 835:444–470.

Nam, G., Johner, A., and Lee, N.-K. (2010). Reptation of a semiflexible polymer through porous media. *The Journal of Chemical Physics*, 133(4):044908.

Nazockdast, E., Rahimian, A., Zorin, D., and Shelley, M. (2017). A fast platform for simulating semi-flexible fiber suspensions applied to cell mechanics. *Journal of Computational Physics*, 329:173–209.

Nelson, B. J., Kaliakatsos, I. K., and Abbott, J. J. (2010). Microrobots for Minimally Invasive Medicine. *Annual Review of Biomedical Engineering*, 12(1):55–85.

Nourhani, A., Crespi, V. H., Lammert, P. E., and Borhan, A. (2015). Self-electrophoresis of spheroidal electrocatalytic swimmers. *Physics of Fluids*, 27(9):092002.

Olson, S. D., Lim, S., and Cortez, R. (2013). Modeling the dynamics of an elastic rod with intrinsic curvature and twist using a regularized Stokes formulation. *Journal of Computational Physics*, 238:169–187.

P. Bregulla, A. and Cichos, F. (2015). Size dependent efficiency of photophoretic swimmers. *Faraday Discussions*, 184(0):381–391.

Park, J., Metzger, B., Guazzelli, É., and Butler, J. E. (2010). A cloud of rigid fibres sedimenting in a viscous fluid. *Journal of Fluid Mechanics*, 648:351–362.

Patel, P. D. and Shaqfeh, E. S. G. (2003). A computational study of DNA separations in sparse disordered and periodic arrays of posts. *The Journal of Chemical Physics*, 118(6):2941.

Paxton, W. F., Kistler, K. C., Olmeda, C. C., Sen, A., St. Angelo, S. K., Cao, Y., Mallouk, T. E., Lammert, P. E., and Crespi, V. H. (2004). Catalytic Nanomotors: Autonomous Movement of Striped Nanorods. *Journal of the American Chemical Society*, 126(41):13424–13431.

Pérez Peláez, R. (2022). *Complex fluids in the Gpu era: Algorithms and simulations*. http://purl.org/dc/dcmitype/Text, Universidad Autónoma de Madrid.

Peskin, C. S. (2002). The immersed boundary method. *Acta Numerica*, 11:479–517.

Powers, T. R. (2010). Dynamics of filaments and membranes in a viscous fluid. *Reviews of Modern Physics*, 82(2):1607–1631.

Pozrikidis, C. (1992). *Boundary Integral and Singularity Methods for Linearized Viscous Flow*. Cambridge Texts in Applied Mathematics. Cambridge University Press, Cambridge.

Quennouz, N., Shelley, M., du Roure, O., and Lindner, A. (2015). Transport and buckling dynamics of an elastic fibre in a viscous cellular flow. *Journal of Fluid Mechanics*, 769:387–402.

Ralston, K. S., Kabututu, Z. P., Melehani, J. H., Oberholzer, M., and Hill, K. L. (2009). The Trypanosoma brucei Flagellum: Moving Parasites in New Directions. *Annual Review of Microbiology*, 63(1):335–362.

Ranjan, S., Zeming, K. K., Jureen, R., Fisher, D., and Zhang, Y. (2014). DLD pillar shape design for efficient separation of spherical and non-spherical bioparticles. *Lab on a Chip*, 14(21):4250–4262.

Re, V. (2019). Shedding light on the invisible: Addressing the potential for groundwater contamination by plastic microfibers. *Hydrogeology Journal*, 27(7):2719–2727.

Redlinger-Pohn, J. D., Liverts, M., and Lundell, F. (2021). Parameter regimes and rates of fibre collection on screens of various design. *Separation and Purification Technology*, 259:118053.

Ren, L., Zhou, D., Mao, Z., Xu, P., Huang, T. J., and Mallouk, T. E. (2017). Rheotaxis of Bimetallic Micromotors Driven by Chemical–Acoustic Hybrid Power. *ACS Nano*, 11(10):10591–10598.

Rojas-Pérez, F., Delmotte, B., and Michelin, S. (2021). Hydrochemical interactions of phoretic particles: A regularized multipole framework. *Journal of Fluid Mechanics*, 919:A22.

Rotne, J. and Prager, S. (1969). Variational Treatment of Hydrodynamic Interaction in Polymers. *The Journal of Chemical Physics*, 50(11):4831–4837.

Rusconi, R., Lecuyer, S., Guglielmini, L., and Stone, H. A. (2010). Laminar flow around corners triggers the formation of biofilm streamers. *Journal of The Royal Society Interface*, 7(50):1293–1299.

Rutllant, J., López-Béjar, M., and López-Gatius, F. (2005). Ultrastructural and Rheological Properties of Bovine Vaginal Fluid and its Relation to Sperm Motility and Fertilization: A Review. *Reproduction in Domestic Animals*, 40(2):79–86.

Sabrio, A. and Rasoulzadeh, M. (2022). Main modes of microfilament particles deformation in rough channels. *Physics of Fluids*, 34(1):013320.

Saggiorato, G., Elgeti, J., G. Winkler, R., and Gompper, G. (2015). Conformations, hydrodynamic interactions, and instabilities of sedimenting semiflexible filaments. *Soft Matter*, 11(37):7337–7344.

Saintillan, D., Darve, E., and Shaqfeh, E. S. G. (2005). A smooth particle-mesh Ewald algorithm for Stokes suspension simulations: The sedimentation of fibers. *Physics of Fluids*, 17(3):033301.

Saintillan, D., Shaqfeh, E. S. G., and Darve, E. (2006). The growth of concentration fluctuations in dilute dispersions of orientable and deformable particles under sedimentation. *Journal of Fluid Mechanics*, 553(-1):347.

Schlagberger, X. and Netz, R. R. (2005). Orientation of elastic rods in homogeneous Stokes flow. *Europhysics Letters (EPL)*, 70(1):129–135.

Schoeller, S. F., Townsend, A. K., Westwood, T. A., and Keaveny, E. E. (2021). Methods for suspensions of passive and active filaments. *Journal of Computational Physics*, 424:109846.

Sevick, E. M. and Williams, D. R. M. (2001). Long-lived states in electrophoresis: Collision of a polymer chain with two or more obstacles. *Europhysics Letters (EPL)*, 56(4):529–535.

Shaqfeh, E. S. G., McKinley, G. H., Woo, N., Nguyen, D. A., and Sridhar, T. (2004). On the polymer entropic force singularity and its relation to extensional stress relaxation and filament recoil. *Journal of Rheology*, 48(1):209–221.

Sharan, P., Maslen, C., Altunkeyik, B., Rehor, I., Simmchen, J., and Montenegro-Johnson, T. D. (2021). Fundamental Modes of Swimming Correspond to Fundamental Modes of Shape: Engineering I-, U-, and S-Shaped Swimmers. *Advanced Intelligent Systems*, 3(11):2100068.

Sprinkle, B., Usabiaga, F. B., Patankar, N. A., and Donev, A. (2017). Large Scale Brownian Dynamics of Confined Suspensions of Rigid Particles. *The Journal of Chemical Physics*, 147(24):244103.

Sridhar, V., Park, B.-W., and Sitti, M. (2018). Light-Driven Janus Hollow Mesoporous TiO $_2$ –Au Microswimmers. *Advanced Functional Materials*, 28(25):1704902.

Steigmann, D. J. and Faulkner, M. G. (1993). Variational theory for spatial rods. *Journal of Elasticity*, 33(1):1–26.

Stone, H. A. and Samuel, A. D. T. (1996). Propulsion of Microorganisms by Surface Distortions. *Physical Review Letters*, 77(19):4102–4104.

Sundararajan, S., Lammert, P. E., Zudans, A. W., Crespi, V. H., and Sen, A. (2008). Catalytic Motors for Transport of Colloidal Cargo. *Nano Letters*, 8(5):1271–1276.

Sutherland, B. R., DiBenedetto, M., Kaminski, A., and Van Den Bremer, T. (2023). Fluid dynamics challenges in predicting plastic pollution transport in the ocean: A perspective. *Physical Review Fluids*, 8(7):070701.

Swan, J. W. and Brady, J. F. (2007). Simulation of hydrodynamically interacting particles near a no-slip boundary. *Physics of Fluids*, 19(11):113306.

Swan, J. W. and Brady, J. F. (2010). Particle motion between parallel walls: Hydrodynamics and simulation. *Physics of Fluids*, 22(10):103301.

Swan, J. W., Brady, J. F., Moore, R. S., and ChE 174 (2011). Modeling hydrodynamic self-propulsion with Stokesian Dynamics. Or teaching Stokesian Dynamics to swim. *Physics of Fluids*, 23(7):071901.

Tasora, A. and Anitescu, M. (2013). A complementarity-based rolling friction model for rigid contacts. *Meccanica*, 48(7):1643–1659.

Tornberg, A.-K. and Shelley, M. J. (2004). Simulating the dynamics and interactions of flexible fibers in Stokes flows. *Journal of Computational Physics*, 196(1):8–40.

Turney, M. A., Cheung, M. K., Powell, R. L., and McCarthy, M. J. (1995). Hindered settling of rod-like particles measured with magnetic resonance imaging. *AIChE Journal*, 41(2):251–257.

Usabiaga, F. B., Delmotte, B., and Donev, A. (2017). Brownian Dynamics of Confined Suspensions of Active Microrollers. *The Journal of Chemical Physics*, 146(13):134104.

Usabiaga, F. B., Kallemov, B., Delmotte, B., Bhalla, A. P. S., Griffith, B. E., and Donev, A. (2016). Hydrodynamics of Suspensions of Passive and Active Rigid Particles: A Rigid Multiblob Approach. *Communications in Applied Mathematics and Computational Science*, 11(2):217–296.

Vakil, A. and Green, S. I. (2011). Flexible fiber motion in the flow field of a cylinder. *International Journal of Multiphase Flow*, 37(2):173–186.

Van Der Wee, E. B., Blackwell, B. C., Balboa Usabiaga, F., Sokolov, A., Katz, I. T., Delmotte, B., and Driscoll, M. M. (2023). A simple catch: Fluctuations enable hydrodynamic trapping of microrollers by obstacles. *Science Advances*, 9(10):eade0320.

Vutukuri, H. R., Bet, B., van Roij, R., Dijkstra, M., and Huck, W. T. S. (2017). Rational design and dynamics of self-propelled colloidal bead chains: From rotators to flagella. *Scientific Reports*, 7(1):16758.

Wajnryb, E., Mizerski, K. A., Zuk, P. J., and Szymczak, P. (2013). Generalization of the Rotne-Prager-Yamakawa mobility and shear disturbance tensors. *Journal of Fluid Mechanics*, 731:R3.

Wakiya, S. (1965). Mutual Interaction of Two Spheroids Sedimenting in a Viscous Fluid. *Journal of the Physical Society of Japan*, 20(8):1502–1514.

Walker, B. J., Ishimoto, K., and Gaffney, E. A. (2020). Efficient simulation of filament elasto-hydrodynamics in three dimensions. *Physical Review Fluids*, 5(12):123103.

Walther, A. and E. Müller, A. H. (2008). Janus particles. *Soft Matter*, 4(4):663–668.

Wandersman, E., Quennouz, N., Fermigier, M., Lindner, A., and du Roure, O. (2010). Buckled in translation.

Wang, Y., Hernandez, R. M., Bartlett, D. J., Bingham, J. M., Kline, T. R., Sen, A., and Mallouk, T. E. (2006). Bipolar Electrochemical Mechanism for the Propulsion of Catalytic Nanomotors in Hydrogen Peroxide Solutions. *Langmuir*, 22(25):10451–10456.

Westwood, T. A., Delmotte, B., and Keaveny, E. E. (2021). A generalised drift-correcting time integration scheme for Brownian suspensions of rigid particles with arbitrary shape. *arXiv:2106.00449 [physics]*.

Williams, B. J., Anand, S. V., Rajagopalan, J., and Saif, M. T. A. (2014). A self-propelled biohybrid swimmer at low Reynolds number. *Nature Communications*, 5(1):3081.

Wolgemuth, C. W. (2015). Flagellar motility of the pathogenic spirochetes. *Seminars in cell & developmental biology*, 46:104–112.

Wróbel, J. K., Lynch, S., Barrett, A., Fauci, L., and Cortez, R. (2016). Enhanced flagellar swimming through a compliant viscoelastic network in Stokes flow. *Journal of Fluid Mechanics*, 792:775–797.

Wu, Z., Chen, Y., Mukasa, D., Pak, O. S., and Gao, W. (2020). Medical micro/nanorobots in complex media. *Chemical Society Reviews*, 49.

Xu, H., Medina-Sánchez, M., Magdanz, V., Schwarz, L., Hebenstreit, F., and Schmidt, O. G. (2018). Sperm-Hybrid Micromotor for Targeted Drug Delivery. *ACS Nano*, 12(1):327–337.

Xu, H., Medina-Sánchez, M., Maitz, M. F., Werner, C., and Schmidt, O. G. (2020). Sperm Micromotors for Cargo Delivery through Flowing Blood. *ACS Nano*, 14(3):2982–2993.

Xu, X. and Nadim, A. (1994). Deformation and orientation of an elastic slender body sedimenting in a viscous liquid. *Physics of Fluids*, 6(9):2889–2893.

Xue, N., Nunes, J. K., and Stone, H. A. (2022). Shear-induced migration of confined flexible fibers. *Soft Matter*, 18(3):514–525.

Yamakawa, H. (1970). Transport Properties of Polymer Chains in Dilute Solution: Hydrodynamic Interaction. *The Journal of Chemical Physics*, 53(1):436–443.

Yamamoto, S. and Matsuoka, T. (1995). Dynamic simulation of fiber suspensions in shear flow. *The Journal of Chemical Physics*, 102(5):2254–2260.

Yan, W. and Blackwell, R. (2021). Kernel Aggregated Fast Multipole Method: Efficient summation of Laplace and Stokes kernel functions. *Advances in Computational Mathematics*, 47(5):69.

Yan, W. and Shelley, M. (2018). Universal image systems for non-periodic and periodic Stokes flows above a no-slip wall. *Journal of Computational Physics*, 375:263–270.

Yan, W., Zhang, H., and Shelley, M. J. (2019). Computing collision stress in assemblies of active spherocylinders: Applications of a fast and generic geometric method. *The Journal of Chemical Physics*, 150(6):064109.

Zhang, L., Abbott, J. J., Dong, L., Peyer, K. E., Kratochvil, B. E., Zhang, H., Bergeles, C., and Nelson, B. J. (2009). Characterizing the Swimming Properties of Artificial Bacterial Flagella. *Nano Letters*, 9(10):3663–3667.

Zuk, P. J., Wajnryb, E., Mizerski, K. A., and Szymczak, P. (2014). Rotne–Prager–Yamakawa approximation for different-sized particles in application to macromolecular bead models. *Journal of Fluid Mechanics*, 741:R5.

ECOLE
DOCTORALE

Titre : Transport et déformation des fibres flexibles en géométries complexes

Mots clés : Fibres flexibles, Environnements munis d'obstacles, Interactions fluide-structure, Ecoulements de Stokes, Sédimentation, Modélisation numérique.

Résumé : Les fibres flexibles se rencontrent dans diverses situations dans la nature et les applications industrielles. Parmi lesquelles on trouve des fibres de microplastiques, des fibres de cellulose et des structures filamenteuses résultant de colonies bactériennes dites "biofilms". Dans la plupart des cas, les fibres flexibles sont généralement immergées dans des environnements fluidiques qui sont munis d'obstacles. A titre d'exemple, les lave-linge rejettent un grand nombre de fibres de microplastiques (environ 1900 fibres par lavage) dans des eaux usées contenant plusieurs débris. Dans de tels environnements complexes, les fibres peuvent adopter différentes formes non triviales et se déplacer suivant différents modes à travers les obstacles environnants. Ces différents comportements résultent du couplage complexe entre la réponse élastique des fibres, les collisions et les interactions hydrodynamiques. Leur compréhension est par conséquent essentielle pour l'étude des systèmes biologiques, environnementaux et industriels, où des phénomènes similaires sont observés, de même que pour éviter des problèmes majeurs comme la pollution ou le colmatage. Au cours des dernières décennies, la modélisation des particules élancées immergées dans un fluide visqueux a été un domaine majeur de recherche en mécanique des fluides. Cependant, le développement des modèles numériques permettant de prendre en compte des environnements munis d'obstacles a été peu abordé. Le problème raide à résoudre sous contraintes qui en résulte en est une des raisons. Modéliser des fibres dans de tels environnements est un défi majeur pour les approches numériques actuelles.

Ainsi, dans cette thèse, nous proposerons une méthodologie pour simuler des fibres flexibles dans des environnements fluidiques munis d'obstacles. Notre implémentation permet de simuler des systèmes contenant un nombre considérable de fibres et d'obstacles en des temps raisonnables sur une seule carte graphique (GPU). Forts de cet outil, et d'expériences simples, nous étudierons ensuite le problème de sédimentation des fibres flexibles dans des environnements complexes. Nos résultats jettent les bases pour de futures expériences et fournissent des ingrédients physiques essentiels pour la conception des dispositifs de tri de particules sous l'action de la gravité.

Title : Transport and deformation of flexible fibers in structured environments

Keywords : Flexible fibers, Structured media, Fluid-structure interactions, Stokes flow, Sedimentation, Numerical modeling.

Abstract : Flexible fibers are encountered in various situations in nature and industrial applications. Examples include microplastic fibers, cellulose fibers, and biofilm streamers. In a wide range of such situations, flexible fibers are often immersed in a fluidic environment with embedded obstacles. For instance, laundry washing machines discharge a large number of microplastic fibers (around 1900 fibers per wash) into wastewaters which contain a significant amount of debris. In such complex media, flexible fibers can exhibit nontrivial conformations and different modes of transport through the surrounding obstacles. These dynamics result from the complex interplay between their elastic response, collisions and hydrodynamic interactions. Understanding of these phenomena is therefore essential to study the physics of biological, environmental and industrial systems, but also to prevent issues such as pollution or clogging. While modeling slender particles in viscous fluids has been a major area of research over the past few decades, methodologies involving surrounding environments are scarce. The resulting complex coupling leads to a constrained formulation of the problem in addition of being stiff. Therefore, modeling fibers in complex media is challenging and can be computationally costly.

In this thesis, we will propose a methodology to model flexible fibers in different environments that are made of rigid stationary obstacles. Our implementation enables dynamic simulations of large systems in reasonable wall times on a single modern Graphics Processing Unit (GPU). Using the capabilities afforded by our method, together with simple experiments, we will investigate the sedimentation of flexible fibers in structured environments. The resulting findings provide physical insight into future experiments and the design of gravity-based sorting devices.

Institut Polytechnique de Paris
91120 Palaiseau, France